

# **A multi-wavelength study of the evolution and pc-scale jet kinematics of active galaxies**

Inaugural-Dissertation

zur

Erlangung des Doktorgrades  
der Mathematisch-Naturwissenschaftlichen Fakultät  
der Universität Köln

vorgelegt von

**Marios Karouzos**

aus Athen, Griechenland

Berichterstatter: Prof. Dr. Andreas Eckart  
Prof. Dr. Anton Zensus

Tag der mündlichen Prüfung: 25. Oktober 2010

*...στην οικογένεια μου!*



# Contents

<b>Zusammenfassung</b>	<b>xiii</b>
<i>Περίληψη</i>	<b>xv</b>
<b>Summary</b>	<b>xvii</b>
<b>1 General Introduction</b>	<b>1</b>
1.1 Nuclear Activity in galaxies	1
1.2 A day in the AGN Zoo	4
1.2.1 Splitting hairs: An AGN Compendium	5
1.3 Making one out of many	8
1.3.1 Radio-quiet Unification	8
1.3.2 Radio-Loud Unification	10
1.4 AGN Jets	12
1.4.1 Synchrotron Radiation	12
1.5 Very Long Baseline Interferometry	14
1.5.1 Basic Formulas	14
1.5.2 Calibration	15
1.5.3 Imaging	16
1.5.4 VLBI arrays	17
1.6 The Caltech-Jodrell Bank flat-spectrum (CJF) sample	19
<b>2 Merger-driven evolution of active galaxies</b>	<b>23</b>
2.1 Introduction	23
2.1.1 The other side of the fence	25
2.2 Binary Black Hole Systems	26
2.2.1 Binary Black Hole System selection criteria	26
2.3 Motivation for this work	27
2.4 Evolution Criteria	29
2.4.1 Host galaxy signatures	29
2.4.2 AGN signatures	30
2.5 Multi-wavelength properties of the CJF sample	30
2.5.1 Radio emission	31
2.5.2 Infrared emission	32
2.5.3 Optical emission	32
2.6 Analysis and Results	33

2.6.1	Mergers in the CJF . . . . .	33
2.6.2	Luminosity Correlations . . . . .	34
2.6.3	AGN near-IR colors . . . . .	35
2.7	Tracing the evolution in the CJF . . . . .	35
2.7.1	Notes on individual sources . . . . .	40
2.8	Mrk 231: A Case Study of a late-merger . . . . .	44
2.9	Discussion . . . . .	46
2.9.1	Anticipated AGN properties . . . . .	46
2.9.2	Periodicities in the lightcurves . . . . .	49
2.9.3	Infrared emission, merging scenarios, and starburst . . . . .	50
2.9.4	Binary Black Holes in the CJF . . . . .	50
2.10	Conclusions . . . . .	53
<b>3</b>	<b>Jet Ridge Lines in the CJF</b> . . . . .	<b>57</b>
3.1	Introduction . . . . .	57
3.1.1	Relativistic Beaming and Projection Effects . . . . .	58
3.1.2	AGN Jet Kinematics . . . . .	59
3.1.3	Helical Jets . . . . .	62
3.1.4	Stationary components . . . . .	63
3.2	S5 1803+784: A Case Study . . . . .	64
3.3	Motivation . . . . .	69
3.4	Data . . . . .	69
3.4.1	Jet Length, $L$ . . . . .	71
3.4.2	Monotonicity Index, M.I. . . . .	71
3.4.3	Jet Width, $dP$ . . . . .	73
3.4.4	Jet Width Evolution, $\Delta P$ . . . . .	73
3.4.5	Jet Linear Evolution, $\Delta \ell$ . . . . .	74
3.5	Analysis and Results . . . . .	75
3.5.1	Jet Lengths in the CJF . . . . .	76
3.5.2	Jet Morphology in the CJF . . . . .	78
3.5.3	Jet Widths, $P$ , in the CJF . . . . .	80
3.5.4	Jet Width Evolution, $\Delta P$ , in the CJF . . . . .	86
3.5.5	Jet Linear Evolution, $\Delta \ell$ , in the CJF . . . . .	90
3.6	Summary of Results . . . . .	98
3.7	Discussion and Conclusions . . . . .	100
3.7.1	Identifying the pitfalls . . . . .	100
3.7.2	Comparison with previous studies . . . . .	102
3.7.3	A Helical Model and the Unification Scheme . . . . .	105
3.7.4	Conclusions . . . . .	111
<b>4</b>	<b><math>\gamma</math>-ray properties of the CJF sample</b> . . . . .	<b>113</b>
4.1	Introduction . . . . .	113
4.1.1	$\gamma$ -ray emission production . . . . .	114
4.1.2	$\gamma$ -rays and AGN phenomenology . . . . .	116
4.2	Motivation . . . . .	116
4.3	Data . . . . .	117

4.3.1	$\gamma$ -ray luminosities . . . . .	117
4.4	Analysis and Results . . . . .	119
4.4.1	Apparent VLBI Jet Component Velocities and $\gamma$ -ray emission . . .	122
4.4.2	$\gamma$ -ray Luminosities and Apparent Jet Component Velocities . . .	127
4.4.3	$\gamma$ -ray and jet ridge line properties . . . . .	128
4.4.4	TeV sources . . . . .	131
4.5	Discussion and Conclusions . . . . .	131
4.5.1	Summary . . . . .	131
4.5.2	Discussion . . . . .	133
4.5.3	Conclusions . . . . .	135
<b>5</b>	<b>Epilogue</b> . . . . .	<b>137</b>
5.1	Summary . . . . .	138
5.1.1	Active galaxies in the context of galaxy evolution . . . . .	138
5.1.2	Properties and evolution of AGN jet ridge lines . . . . .	139
5.1.3	$\gamma$ -rays and AGN kinematic properties . . . . .	141
5.2	Concluding Remarks . . . . .	143
5.3	Into the future... . . . .	143
	<b>Acknowledgements</b> . . . . .	<b>179</b>
	<b>A AGN Evolution Tables</b> . . . . .	<b>185</b>
	<b>B CJF Black Hole Masses</b> . . . . .	<b>195</b>
	<b>C CJF Jet Ridge Lines</b> . . . . .	<b>197</b>
	<b>D CJF <math>\gamma</math>-rays</b> . . . . .	<b>249</b>
	<b>Curriculum Vitae</b> . . . . .	<b>255</b>
	<b>Refereed Publications</b> . . . . .	<b>257</b>





# List of Figures

1.1	Black Hole collapse flow-chart . . . . .	2
1.2	Seyfert AGN Spectra . . . . .	5
1.3	AGN Unification Scheme . . . . .	10
1.4	Very Long Baseline Array . . . . .	18
1.5	Global VLBI Array . . . . .	19
1.6	Redshift Distribution for the CJF . . . . .	20
2.1	Cyclic Evolution Model (Hopkins et al. 2006) . . . . .	25
2.2	Halo Mass Driven Evolution (Hickox et al. 2009) . . . . .	28
2.3	Near-IR and Radio (5GHz) Luminosity Correlation . . . . .	34
2.4	CJF Near-IR Color-Color Diagram . . . . .	36
2.5	Equal Mass Merger Simulation (Lotz et al. 2008) . . . . .	37
2.6	Evolutionary Candidates Near-IR Color-Color Diagram . . . . .	43
2.7	Star-Formation Rate versus Time (Lotz et al. 2008) . . . . .	45
2.8	Mrk231 Radio Maps (5GHz) . . . . .	45
2.9	Mrk231 Optical and CO Maps . . . . .	46
3.1	Superluminal Motion . . . . .	58
3.2	Beaming Model . . . . .	60
3.3	Sketch of Jet regions . . . . .	61
3.4	0735+178 Jet Kinematics . . . . .	65
3.5	S5 1803+784 Multi-Wavelength Maps . . . . .	66
3.6	S5 1803+784 Core Separation versus Time . . . . .	67
3.7	S5 1803+784 Jet Ridge Line Evolution . . . . .	68
3.8	Jet Ridge Line M.I. Example . . . . .	72
3.9	Jet Ridge Line Width Example . . . . .	74
3.10	Jet Length Histogram ( $0 < z < 1$ ) . . . . .	76
3.11	Jet Length versus Redshift . . . . .	78
3.12	2200+420 Jet Ridge Line: M.I. example . . . . .	79
3.13	Jet M.I. distribution histogram . . . . .	80
3.14	QSO Jet Width versus Redshift . . . . .	83
3.15	Jet Width Distribution: $0 < z < 1$ . . . . .	84
3.16	Jet Width Distribution: Variable Sources . . . . .	86
3.17	Jet Width Evolution (max) Distribution: $0 < z < 1$ . . . . .	89
3.18	Jet Width Evolution (max) Distribution: Variable Sources . . . . .	91
3.19	Jet Linear Evolution Distribution: $0 < z < 1$ . . . . .	93

3.20	Jet Linear Evolution versus Redshift . . . . .	94
3.21	Jet Linear Evolution Distribution: Variable Sources . . . . .	95
3.22	Jet Linear Evolution: Radio luminosity correlation . . . . .	97
3.23	Jet $\beta_{app}$ to radio luminosity correlation . . . . .	104
3.24	Geometry of the helical jet model . . . . .	105
3.25	Helical trajectories examples . . . . .	107
3.26	Position Angle Distribution with Time . . . . .	108
3.27	Apparent Jet Width with Viewing Angle . . . . .	109
3.28	Jet Width Evolution with Viewing Angle . . . . .	110
3.29	Jet Linear Evolution with Viewing Angle . . . . .	111
4.1	Fermi-LAT 11-month map of the sky . . . . .	114
4.2	$\gamma$ -ray flux distribution . . . . .	118
4.3	$\gamma$ -detected CJF sources $z$ distribution . . . . .	119
4.4	$\gamma$ -ray luminosity and redshift . . . . .	120
4.5	$\gamma$ -to-radio ratio: QSOs vs. BL Lacs . . . . .	122
4.6	$\beta_{app,max}$ distribution: $\gamma$ -detected and non-detected sources . . . . .	124
4.7	$\beta_{app,max}$ distribution: Variable and non-variable $\gamma$ -detected sources . . . . .	125
4.8	$\beta_{app,max}$ distribution: Variable vs. Non-Variable / QSOs vs. BL Lacs . . . . .	126
4.9	$\beta_{app,max}$ and $\gamma$ -ray luminosity . . . . .	127
4.10	Jet ridge line properties ( $dP$ and $\Delta P$ ) and $\gamma$ -rays . . . . .	129

# List of Tables

1	Abbreviations . . . . .	xviii
1.1	CJF Selection Criteria . . . . .	19
2.1	Evolution Tracers in CJF . . . . .	38
2.2	CJF Multi-Wavelength Sub-Sample . . . . .	47
2.3	BBH Kinematics and Morphologies . . . . .	52
2.4	References for Table 2.3. . . . .	53
2.5	BBH Variability . . . . .	53
3.1	Jet Length Statistics . . . . .	77
3.2	Jet Length Statistics . . . . .	79
3.3	Jet Width Statistics: All . . . . .	81
3.4	Jet Width Statistics: $0 < z < 1$ . . . . .	82
3.5	Jet Width Statistics: Variable Sources . . . . .	85
3.6	Jet Width Evolution: Flags . . . . .	87
3.7	Jet Width Evolution Statistics: $0 < z < 1$ . . . . .	88
3.8	Jet Width Evolution (max) Statistics: $0 < z < 1$ . . . . .	89
3.9	Jet Width Evolution (max) Statistics: Variable Sources . . . . .	90
3.10	Jet Linear Evolution Statistics: $0 < z < 1$ . . . . .	92
3.11	Jet Linear Evolution Statistics: Variable Sources . . . . .	95
3.12	CJF Redshift Sampling . . . . .	101
3.13	Helical Model parameters . . . . .	106
4.1	$\gamma$ -detected CJF sources statistics . . . . .	121
4.2	TeV emitting CJF sources . . . . .	132
A.1	CJF Near-IR properties . . . . .	185
A.2	References for Table A.1. . . . .	188
A.3	CJF Cluster Members . . . . .	189
A.4	References for Table A.3. . . . .	190
A.5	CJF Morphology and Environment . . . . .	191
A.6	CJF Variability . . . . .	192
A.7	References for Table A.6. . . . .	194
B.1	CJF Black Hole Masses . . . . .	195
B.2	References for Table B.1. . . . .	196
C.1	CJF Jet Ridge Line Length . . . . .	197

## List of Tables

---

C.2	CJF Jet Ridge Line Width . . . . .	204
C.3	CJF Jet Ridge Line Width Evolution . . . . .	236
C.4	CJF Jet Ridge Line Linear Evolution . . . . .	242
D.1	CJF $\gamma$ -ray detected sources . . . . .	249

# Zusammenfassung

Aktive Galaxien zählen seit ihrer Entdeckung vor einigen Jahrzehnten zu den führenden Themen astronomischer Forschung. Das vermeintlich superschwere schwarze Loch (SMBH) in ihrem Zentrum charakterisiert ihre Eigenschaften und bestimmt die Entwicklung dieser Objekte. In dieser Arbeit untersuche ich die Entwicklung von aktiven galaktischen Kernen (AGN) im Rahmen eines auf Galaxienverschmelzungen (sog. 'Merger') basierenden Evolutionsschemas. Unter dieser Annahme erzeugen Galaxienverschmelzungen Aktivität in Galaxien sowohl in Form von intensiver Sternentstehung als auch als aktiver Kern. Diese Untersuchung verwendet das Caltech-Jodrell Bank Flat-Spectrum (CJF) Sample, ein statistisch vollständiges Sample von kompakten, radiolauten AGN. Ich habe Hinweise gefunden, die das auf Mergern basierende Evolutionsschema unterstützen und die Bedeutung von Verschmelzungen/Mergern für aktive Galaxien unterstreichen. Insbesondere zeigen fast 30% der CJF-Quellen im nahen Universum ( $z < 0.4$ ) Anzeichen für erst kurz zurückliegende, gegenwärtige oder mögliche zukünftige Merger. Das ist wichtig hinsichtlich der erwartungstreuen Auswahleffekte des CJF-Samples. Zusätzlich finden wir eine unterbrochene Korrelation zwischen der Helligkeit der CJF-Quellen im nahen Infrarotbereich (NIR) und ihrer totalen Radioleuchtkraft bei 5 GHz. Quellen mit geringer Leuchtkraft weisen einen Überschuss an Emission im nahen Infrarot auf im Vergleich zu Quellen mit starker Leuchtkraft. Eine Korrelation zwischen NIR-Farben und Multi-Wellenlängen-Variabilität wurde ebenfalls festgestellt. Schliesslich haben wir die unterschiedlichen Stadien der AGN-Entwicklung anhand einiger individueller Quellen verfolgt, die den jeweiligen Auswahlkriterien entsprachen. Dabei fanden wir 14 vielversprechende Kandidaten für Binäre Systeme schwarzer Löcher (BBH) im CJF.

Zu den wichtigsten Bestandteilen von radiolauten aktiven Galaxien gehören ihre Radiojets. Morphologie, Eigenschaften und Entwicklung der Kammlinie der CFJ-Jets (Jet Ridge Line) wurden im Hinblick auf ein kürzlich wieder aufgegriffenes Modell für BL Lac-Objekte untersucht. Es wurden verschiedene Messtechniken für die Breite, die Entwicklung der Breite, die lineare Entwicklung sowie die Krümmung der Jet Ridge Line entwickelt und darauf basierend eine statistische Analyse des gesamten Samples durchgeführt. BL Lac-Objekte haben wesentlich breitere Jets als Quasare. Sie weisen ausserdem grössere Änderungen in ihrer Breite auf, aber eine deutlich schwächere lineare Entwicklung der Jet Ridge Lines. Wir fanden Hinweise auf eine aktive Entwicklung der Jetlänge und lineare Entwicklung mit der Zeit (als Funktion der Rotverschiebung). Es ergibt sich eine Einschränkung für die Korrelation zwischen der totalen linearen Entwicklung der CJF-Jet Ridge Lines und der Radioleuchtkraft der entsprechenden Quellen. Die obigen Ergebnisse lassen sich als Kombination aus helikaler Struktur von AGN-Jets und Projektionseffekten erklären.

Verbunden mit der Kinematik von AGN-Jets ist die Emission von Gammastrahlung.

Aufgrund der ausgezeichneten Qualität der vom CJF erhältlichen kinematischen Daten sowie der Vielzahl von neuen Gammastrahlen-Informationen, die aus dem Fermi-LAT-Programm erhältlich sind, haben wir die Gammastrahlungs-Eigenschaften des CJF-Samples hinsichtlich ihrer Jet-Kinematik und Jet-Eigenschaften untersucht. Es zeigt sich, dass Quellen, die im Gamma-Bereich detektiert wurden, im Schnitt höhere scheinbare Geschwindigkeiten aufweisen als nicht-detektierte Quellen. Wir weisen allerdings auf eine bereits im Gamma-Bereich detektierte Population von CJF-Quellen mit niedriger Geschwindigkeit hin, was gegen das Argument spricht, dass 'Beaming' der alleinige Ursprung der Gammastrahlungsphotonen ist. Daher untersuchten wir die Möglichkeit einer Korrelation zwischen der Detektion von CJF-Quellen im Gammabereich, ihrer Gamma-Leuchtkraft und ihrer Jetmorphologie. Wir fanden eine Korrelation zwischen der Leuchtkraft im Gammabereich und der maximalen scheinbaren Geschwindigkeit der im Gammastrahlenbereich detektierten CJF-Quellen, die stärker ist für variable Quellen und für solche, die als BL Lacs identifiziert wurden. Weiterhin weisen im Gammabereich detektierte Quellen substantiell breitere und stärker entwickelte Jet Ridge Lines auf im Vergleich zu nicht-detektierten Quellen. Bezüglich der linearen Evolution der Jet Ridge Lines gibt es keine signifikanten Unterschiede zwischen im Gammabereich detektierten und nicht-detektierten Quellen. Das Nichtvorhandensein einer starken Korrelation zwischen den Gammastrahlungseigenschaften und der Jetkinematik der CJF-Quellen wird im Rahmen einer Spine-Sheath-Geometrie des Jets interpretiert: bei niedrigen Beobachtungsfrequenzen, wie sie für das CJF-Sample benutzt wurden, wird nur die äusseren Hülle des Jets sichtbar gemacht. Gammastrahlung stammt aber vermutlich aus den ultra-relativistischen inneren Schichten der AGN-Jets.

## Περίληψη

Οι ενεργοί γαλαξίες από την ανακάλυψη τους και μετά είναι στο κέντρο του ενδιαφέροντος της αστρονομικής έρευνας, δηλαδή εδώ και σχεδόν 50 χρόνια. Οι υπερμαζικές μαύρες τρύπες, οι οποίες φαίνεται να βρίσκονται στα κέντρα τους, επηρεάζουν τις ιδιότητες αυτών των γαλαξιών και καθορίζουν την εξέλιξη τους. Σε αυτή την εργασία ερευνήσα την εξέλιξη των ενεργών γαλαξιακών πυρήνων στο πλαίσιο ενός μοντέλου εξέλιξης, το οποίο βασίζεται στις γαλαξιακές συγκρούσεις και συγχωνεύσεις. Σύμφωνα με αυτή την θεώρηση, γαλαξιακές συγκρούσεις και συγχωνεύσεις σηματοδοτούν την έναρξη της δραστηριότητας στον γαλαξιακό πυρήνα, καθώς επίσης και την έντονη δημιουργία άστρων. Στην παρούσα έρευνα χρησιμοποιήθηκε το δείγμα Caltech Jodrell-Bank flat-spectrum (CJF), το οποίο αποτελεί ένα στατιστικά πλήρες δείγμα συμπαγών, ράδιο-φωτεινών ενεργών γαλαξιακών πυρήνων. Αποτέλεσμα αυτής της έρευνας είναι αποδείξεις που επιβεβαιώνουν την άποψη ότι οι ενεργοί γαλαξιακοί πυρήνες εξελίσσονται μέσω γαλαξιακών συγχωνεύσεων. Επίσης καταδείχτηκε η σημασία τέτοιων φαινομένων για τους ράδιο-φωτεινούς, ενεργούς γαλαξίες. Συγκεκριμένα, σχεδόν 30% των πηγών του CJF στο κοντινό Σύμπαν (ερυθρομετατόπιση μικρότερη του 0.4) δείχνουν δείγματα πρόσφατης, παρούσης, ή μελλοντικής σύγκρουσης ή συγχώνευσης με άλλον γαλαξία. Το αποτέλεσμα αυτό είναι ιδιαίτερα σημαντικό, δεδομένης της αμερόληπτης επιλογής του δείγματος CJF. Επιπλέον, βρέθηκε μια συσχέτιση μεταξύ της φωτεινότητας των πηγών του CJF στο κοντινό υπέρυθρο και της συνολικής φωτεινότητας των πυρήνων των πηγών του CJF στο ράδιο (5 GHz), η οποία εξαρτάται από την ράδιο φωτεινότητα των πηγών. Πηγές με χαμηλή φωτεινότητα (στο ράδιο) επιδεικνύουν περισσότερη εκπομπή στο κοντινό υπέρυθρο, σε σύγκριση με τις πηγές υψηλής φωτεινότητας. Εντοπίστηκε επίσης συσχέτιση μεταξύ των χρωμάτων στο κοντινό υπέρυθρο των πηγών CJF και την μεταβλητότητα της φωτεινότητας των πηγών αυτών σε διαφορετικά μήκη κύματος. Τέλος, καταγράφηκαν τα διαφορετικά στάδια της εξέλιξης των ενεργών γαλαξιακών πυρήνων, μέσω της επιλογής μεμονωμένων πηγών του CJF που εκπληρώνουν τα ανάλογα κριτήρια επιλογής για κάθε στάδιο. Βρέθηκαν δε 14 νέοι γαλαξίες υποψήφιοι για συστήματα διπλών μαύρων τρυπών.

Ένα από τα πιο σημαντικά χαρακτηριστικά των ράδιο-φωτεινών ενεργών γαλαξιών είναι οι πίδακες τους. Η μορφολογία, οι ιδιότητες, και η ανάπτυξη των κορυφογραμμών των πιδάκων του CJF μελετώνται, στα πλαίσια ενός νέου κινηματικού σεναρίου για τα αντικείμενα BL Lacs, όπως μελετήθηκε σε συγκεκριμένα αντικείμενα (π.χ., S5 1803+785, PKS 0735+178). Διαφορετικά εργαλεία για τη μέτρηση του εύρους, της αλλαγής του εύρους, της γραμμικής εξέλιξης, και της μορφολογίας και καμπυλότητας των κορυφογραμμών του CJF αναπτύσσονται και αναλύονται στατιστικά στα πλαίσια αυτού του καινούργιου κινηματικού σεναρίου. Βρέθηκαν σημαντικές ενδείξεις ότι η παρατηρηθείσα συμπεριφορά στα αντικείμενα S5 1803+784 και PKS

0735+178 εφαρμόζει σε όλους τους γαλαξίες αυτής της κλάσης. Οι γαλαξίες BL Lac επιδεικνύουν σημαντικά ευρύτερους πίδακες από τα κβάζαρς. Επίσης, επιδεικνύουν μεγαλύτερες αλλαγές στο εύρος των κορυφογραμμών των πιδάκων τους, αλλά μικρότερη γραμμική εξέλιξη. Προέκυψαν επίσης ενδείξεις για ενεργή εξέλιξη του μήκους και της γραμμικής εξέλιξης των κορυφογραμμών των πιδάκων του CJF. Επιπλέον, βρέθηκε μια συσχέτιση, σε μορφή περιβάλλοντος πλαισίου, μεταξύ της φωτεινότητας των πηγών στο ράδιο και της γραμμικής εξέλιξης των κορυφογραμμών του CJF. Τα παραπάνω αποτελέσματα εξηγούνται στα πλαίσια ενός συνδυασμού ελικοειδούς μορφολογίας των πιδάκων ενεργών γαλαξιών και προβολής αυτής της γεωμετρίας στο επίπεδο του ουρανού.

Άμεσα συνδεδεμένη με τις κινηματικές ιδιότητες των πιδάκων των ενεργών γαλαξιών είναι η εκπομπή από τους ενεργούς γαλαξίες ακτίνων  $\gamma$ . Με δεδομένα τα άριστα κινηματικά στοιχεία που είναι διαθέσιμα για το CJF, καθώς και τον πλούτο νέων παρατηρήσεων στις ακτίνες  $\gamma$  από το τηλεσκόπιο Fermi-LAT, μελετήθηκαν οι ιδιότητες των πηγών του CJF στις ακτίνες  $\gamma$ , με βάση τις κινηματικές και μορφολογικές ιδιότητες των πιδάκων τους. Βρέθηκε ότι οι πηγές του CJF που έχουν ανιχνευθεί στις ακτίνες  $\gamma$ , δείχνουν κατά μέσο όρο μεγαλύτερες φαινόμενες ταχύτητες στους πίδακες τους από αυτές που δεν έχουν ανιχνευθεί. Καταγράφηκε όμως παράλληλα η ύπαρξη ενός πληθυσμού  $\gamma$ -ανιχνευθέντων πηγών του CJF που επιδεικνύουν σχετικά χαμηλές φαινόμενες ταχύτητες στους πίδακες τους. Το γεγονός αυτό θέτει υπό αμφισβήτηση το φαινόμενο «beaming» ως την μοναδική πηγή παραγωγής ακτίνων  $\gamma$ . Διερευνήθηκε, για αυτό το λόγο, μια πιθανή συσχέτιση μεταξύ της ανιχνευσης μιας πηγής στις ακτίνες  $\gamma$ , με την φωτεινότητα της, και τις ιδιότητες του πίδακα της. Με αυτό τον τρόπο προέκυψε συσχέτιση μεταξύ της φωτεινότητας στις ακτίνες  $\gamma$  και της μέγιστης φαινόμενης ταχύτητας στους πίδακες των ανιχνευθέντων πηγών του CJF στις ακτίνες  $\gamma$ . Η συσχέτιση αυτή είναι εντονότερη για τα αντικείμενα BL Lacs και για τις μεταβλητές πηγές. Επίσης καταδείχτηκε ότι οι  $\gamma$ -ανιχνευθείσες πηγές επιδεικνύουν ευρύτερους πίδακες, με μεγαλύτερες αλλαγές στο εύρος τους, από ότι οι μη ανιχνευθείσες. Αντιθέτως δεν βρέθηκε καμία σημαντική διαφορά, σε ότι αφορά την γραμμική εξέλιξη των πιδάκων τους, μεταξύ των  $\gamma$ -ανιχνευθέντων και μη ανιχνευθέντων πηγών του CJF. Η απουσία στενής συσχέτισης μεταξύ των  $\gamma$  και κινηματικών ιδιοτήτων των πηγών του CJF ερμηνεύεται στα πλαίσια μιας γεωμετρίας «spine-sheath», όπου στις χαμηλές συχνότητες παρατήρησης του CJF, μόνο το εξωτερικό, αργό, περίβλημα (sheath) του πίδακα διαφαίνεται. Η ακτινοβολία  $\gamma$ , σε αυτό το πλαίσιο, εκπέμπεται από την υπερ-σχετικιστική στήλη στο κέντρο του πίδακα του ενεργού γαλαξία, η οποία περιβάλλεται από το αργό περίβλημα.



# Summary

Active galaxies have been in the forefront of astronomic research since their first discovery, at least 50 years ago . The putative supermassive black hole (SMBH) at their center characterizes their properties and regulates the evolution of these objects. I investigate the evolution of active galactic nuclei (AGN) in the context of a merger-driven evolution scheme. Under this assumption, galaxy mergers trigger activity in galaxies, both in the form of intense star-formation, as well as nuclear activity. This investigation uses the Caltech-Jodrell Bank flat-spectrum (CJF) sample, a statistically complete sample of compact, radio-loud AGN. I find evidence supporting the merger-driven evolution scheme of AGN, exhibiting the relevance of merger events in active galaxies. In particular, almost 30% of the CJF sources in the local Universe ( $z < 0.4$ ) show evidence of recent past, present, or possible future mergers. This is important in light of the unbiased selection effects of the CJF sample. In addition, I find a broken correlation between the near-infrared luminosity of the CJF sources and their total radio luminosity at 5 GHz. Low luminosity sources show an excess of near-infrared emission, compared to their high luminosity counterparts. A correlation between near-infrared colors and multiwavelength variability is also found. Finally, I trace the different stages of AGN evolution by selecting individual sources that fit the respective selection criteria, finding 14 promising candidates for binary black hole (BBH) systems in the CJF.

One of the most prominent constituents of radio-loud active galaxies are their radio jets. The morphology, properties, and evolution of the CJF jet ridge lines are studied, in light of a recently revisited kinematic paradigm for BL Lac objects. Different measures for the width, the width evolution, the linear evolution, and the curvature of the jet ridge lines are developed and a statistical analysis of the whole sample on that basis is conducted. BL Lac objects are found to have substantially wider jets than quasars. They are also found to show larger changes in their widths, but significantly weaker linear evolution of their jet ridge lines. We find indications of active evolution of the jet length and linear evolution with time (as a function of redshift). An envelope is found confining a correlation between the total linear evolution of the CJF jet ridge lines and the radio luminosity of the corresponding sources. The above results are explained in terms of the combination of helical structure for AGN jets and projection effects.

Coupled to the kinematics of the AGN jets is the emission of  $\gamma$ -ray radiation. In light of the excellent quality of kinematic data available for the CJF, as well as the wealth of new  $\gamma$ -ray information provided by the Fermi-LAT program, I investigate the  $\gamma$ -ray properties of the CJF sample, in terms of their jet kinematics and properties. I find that  $\gamma$ -ray detected sources show on average higher apparent velocities than their non-detected counterparts. I note however the existence of a low-velocity population of  $\gamma$ -ray detected CJF sources, that put the argument of beaming as the source of  $\gamma$ -ray photons under

debate. I study a possible correlation between the  $\gamma$ -ray detection of CJF sources, their luminosity, and their jet morphology. I find a correlation between the  $\gamma$ -ray luminosity and the maximum apparent jet speed for the  $\gamma$ -detected CJF sources. The correlation is stronger for variable sources and for those identified as BL Lacs. I find that  $\gamma$ -detected sources show substantially wider jet ridge lines, with stronger evolution of their widths compared to non-detected sources. I find no significant difference between  $\gamma$ -detected and non-detected sources concerning the linear evolution of their jet ridge lines. The absence of a strong correlation between  $\gamma$ -ray properties of the CJF sources and their kinematics is interpreted in the context of a spine-sheath geometry of AGN jet, where, at the low observing frequency used for the CJF, only the slow outer sheath of the jet is uncovered.  $\gamma$ -ray emission is assumed to originate in the ultra-relativistic spine of AGN jets.

### List of Abbreviations

Table 1: A list of abbreviations often used in this work for easy reference.

AGN	Active Galactic Nucleus
SMBBH	Super-massive Binary Black Hole
BL	BL Lac Object
CJF	Caltech-Jodrell Bank Flat-Spectrum
EGRET	Energetic Gamma Ray Experiment Telescope
FIR	Far Infrared
HST	Hubble Space Telescope
IRAS	Infrared Astronomic Satellite
ISO	Infrared Space Observatory
LAT	Large Area Telescope
mas	milliarcsecond
NIR	Near Infrared
NOT	Nordic Optical Telescope
pc	parsec
QSO	Quasi-Stellar Object / Quasar
RG	Radio Galaxy
SED	spectral energy distribution
SMBH	Super-massive Black Hole
ULIRG	Ultraluminous Infrared Galaxy
VLA	Very Long Array
VLBA	Very Long Baseline Array
VLBI	Very Long Baseline Interferometry

# 1 General Introduction

As one of the most prominent predictions of the theory of General Relativity, black holes have been in the center of astronomical research for many years. There is a large amount of indirect evidence supporting that most, if not all, galaxies host a supermassive black hole (SMBH) in their center (e.g., [Blandford 1986](#)). It is widely believed that this SMBH is the main constituent of activity in Active Galactic Nuclei (AGN) (for a review see e.g., [Begelman et al. 1984](#)). Although the mechanism that triggers this activity still remains unknown, it has been argued by many authors (e.g., [Hutchings and Campbell 1983](#); [Sanders et al. 1988](#); [Hopkins et al. 2006](#)) that galactic mergers should play a predominant role in such processes. Radio astronomy offers one of the most powerful tools to study the immediate vicinity of the SMBH at the centers of AGN, namely the radio jets. In this Chapter I will offer a short introduction to the physics of active galaxies, their demographics, and in particular focus on the radio-loud AGN. The physics of AGN relativistic jets will also be introduced. This Chapter is divided as follows: in Sect. 1.1 I introduce the concept of activity in galaxies, in Sect. 1.2 I describe the different types of active galaxies, in Sect. 1.3 I describe the unification scheme(s), in Sect. 1.4 some basic AGN jet physics is described, in Sect. 1.5 the basics of Very Long Baseline Interferometry (VLBI) is covered, and finally, in Sect. 1.6 I introduce the Caltech-Jodrell Bank Flat-spectrum (CJF) sample, used throughout this work.

## 1.1 Nuclear Activity in galaxies

Active galaxies are some of the brightest objects in the sky, rivalled only by transient events like  $\gamma$ -ray bursts. Together with the fact that these objects are often found at great distances from us (with the closest one being M87, at a distance of 0.073 Glyr), this puts active galaxies as one of the most energetic phenomena in the known Universe. Observed AGN monochromatic luminosities range from  $10^{42}$  to  $10^{48} \text{ erg s}^{-1}$ , making the most luminous members of the AGN family up to  $10^4$  times as bright as a normal field galaxy. The question of course arises, what the source of this energy is, especially since this activity appears to be sustainable at very long timescales, of the order of  $10^8$  years (as indicated by, for example, the extended radio lobes seen for specific types of AGN, e.g., [Fanti et al. 1995](#); [Bird et al. 2008](#)). Release of gravitational energy through the accretion of matter upon a central supermassive object can be shown to produce such enormous amounts of energy. With an efficiency of the order of 10% (larger for maximally rotating black holes), accretion is a much more efficient process than nuclear fusion (of the order of 0.7% for hydrogen burning). The concept of an accreting SMBH as the source of this energy output was first proposed already in 1964 ([Salpeter 1964](#); [Zel'Dovich 1964](#)), although at least 10

more years were needed for the theory to become more widely accepted.

There is now a wealth of (indirect) evidence supporting that these supermassive central objects are indeed black holes. Perhaps the most robust and direct piece of evidence comes from our own Milky Way, where the proper motion of the central stellar population has been studied extensively (e.g., [Genzel et al. 2000](#); [Schödel et al. 2002](#); [Genzel et al. 2003](#); [Eisenhauer et al. 2005](#)). The mass and spatial scales measured for our galaxy imply the existence of a supermassive black hole ( $\sim 10^6 M_{sol}$ ). [Rees \(1978\)](#) shows that the only stable structure for such large masses is a black hole (see Fig. 1.1), as any other astrophysical "species" would eventually collapse under its own gravitational pull. Other probes of the nature of these supermassive central objects include variability, stellar dispersions, and broad emission lines (see also, e.g., [Blandford 1986](#)).

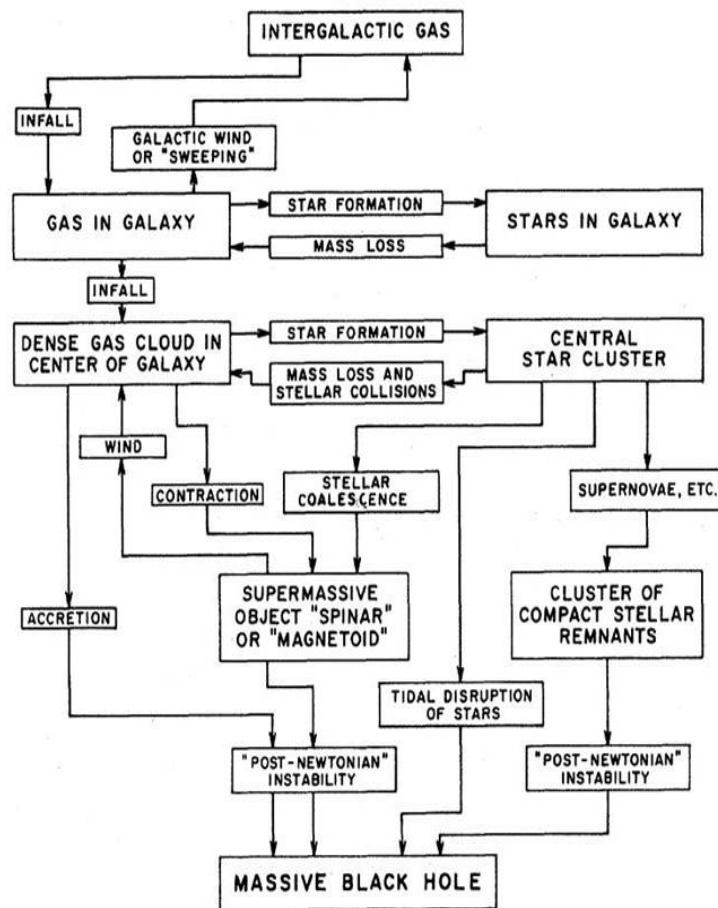


Figure 1.1: Schematic view of the processes leading to the ultimate creation of a supermassive black hole at the center of a galaxy. Figure reproduced from [Rees \(1978\)](#).

Delving a bit deeper into the accretion process, the accretion luminosity can be defined as:

$$L_{acc} = \eta \dot{M} c^2,$$

where  $\eta$  is the accretion radiative efficiency (of the order of 10%),  $\dot{M}$  is the accretion rate, and  $c$  is the speed of light. On first order, the energy output of an accreting SMBH does

not depend on the black hole mass itself. Of course, both  $\dot{M}$  and  $\eta$  are implicitly dependent on  $M$ , the mass of the central accreting object. In addition, the accretion onto the SMBH is regulated through the radiation pressure induced by the emitting matter itself. A limit can be defined, when the radiation pressure, pushing the matter outwards, counters the gravitational collapse and brings accretion to a halt. This is called the Eddington limit and in the form of a luminosity is given by the following formula (Eddington 1925):

$$L_E = 3.3 \times 10^{11} L_{sol} \frac{M_{BH}}{10^7 M_{sol}}.$$

The above equation assumes spherically symmetric accretion (Bondi accretion; Bondi 1952) and therefore is a simplification. Due to the angular momentum of the infalling matter, an accretion disk, rather than an accretion sphere, is formed around the SMBH. Viscous effects between slower and faster rotating material transfer angular momentum outwards and ultimately allow matter to be efficiently accreted on the SMBH. For given circumstances, leading to radiatively inefficient accretion, super-Eddington accretion rates can occur. Non-symmetric geometries, non-adiabatic accretion, inefficient cooling, or sufficiently optically thick disks can lead to super-Eddington accretion (e.g., Eggum et al. 1985; Blandford and Begelman 1999; Stone and Pringle 2001).

Accretion disks are one of the most important constituents of an active galaxy, being the main thermal emitters of these systems. At temperatures around  $10^6$  K or less, the accretion disk itself is relatively cool (compared to, for example, disks seen in X-ray binary systems), showing a peak of emission around 10 eV, a feature also called the Big Blue Bump (for more details see, e.g., Krolik 1999). In addition to the disk, a disk corona is also expected to be formed from electrons near their virial temperature (possible through magnetic extraction from the disk). Such a corona would up-scatter photons coming from either the accretion disk itself, or from another source (e.g., a jet) through inverse Compton (IC) scattering, producing a hard X-ray spectrum. This is indeed observed for most AGN and can be readily explained in the above manner (e.g., Haardt et al. 1997; Ross et al. 1999; Fabian et al. 2005).

Cold atomic gas found in the near vicinity of the SMBH can be excited by radiation coming from the accretion disk. The de-excitation of these atoms create the broad lines spectrum observed for a class of active galaxies. The width of these lines is a result of the large velocity dispersion of the gas, due to its close distance to the SMBH. In the same area, close to the SMBH and above the accretion disk, powerful outflows of matter can be produced. These, usually highly, collimated outflows form the radio jets, observed in radio-loud AGN. The physical properties of these structures will be discussed in a following section. These radio jets often encounter and ionize gas clouds orbiting the SMBH, essentially forming an ionization cone around them. This gas produces narrow emission lines, owing to the smaller velocity dispersion of the clouds at larger distances from the nucleus of the galaxy.

The final component needed is the torus. In order to have efficient accretion onto the SMBH, a large enough reservoir of cold gas and dust is needed. It can be calculated that for an average-luminosity AGN, one needs roughly  $10^9 M_{sol}$  to keep the nucleus shining for approximately  $10^8$  years. This translates to an accretion rate of  $\sim 1 M_{sol} \text{ yr}^{-1}$ . The mechanism of how such large amounts of gas flows into the nucleus of a galaxy is still under debate and models include bar instabilities, cooling flows, as well as minor and

major encounters or mergers with other galaxies (for more details on the latter see, Chap. 2). An obscuring structure of dense gas and dust will be formed around the nucleus of the galaxy, from which the accretion disk draws material. Evidence and signatures of all of the above mentioned components are still presently investigated. There is indeed a wealth of information supporting the existence of all the individual structures already mentioned. These shall be briefly reviewed in the following section (for an extensive treatment of this topic, see [Krolik 1999](#)).

### 1.2 A day in the AGN Zoo

One of the most characteristic attributes of active galaxies is their vast diversity in terms of both their emission and morphology properties. Characterized by their very broadband continuum spectrum, as well as their numerous emission and absorption lines, active galaxies have been categorized in different classes. In addition, different morphologies have been observed for AGN, leading to a further tier of classification with respect to that.

As early as 1908, the first emission lines from active galaxies were discovered by [Fath \(1908\)](#), who observed NGC 1068 during an effort to explain a peculiar faint light seen in the summer along the horizon. It was not until 1943 that the nature of these objects was studied in depth by Carl K. Seyfert ([Seyfert 1943](#)) and a new class of astrophysical objects was introduced. In the seminal paper of 1943, [Seyfert \(1943\)](#) studied the emission spectra of six sources, measuring their high velocity dispersions and noting that these should be created at the very center of these objects, from a point-like source. These objects are now classified as Seyfert galaxies (see Fig. 1.2 for examples of Seyfert AGN spectra).

On a parallel front, [Curtis \(1918\)](#) first observed a structure later understood as an outflow (jet) from the active galaxy M87 in the optical. It was however a discovery from Maarten Schmidt in 1963 that established active galaxies as one of the main fields of extragalactic astronomy. [Schmidt \(1963\)](#) measured the redshift of 3C 273, what was then known as a radio star, revealing that it is at a cosmological distance and thus should have an unprecedented rest-frame luminosity. Schmidt's results were at first questioned, triggering a debate in the astronomical community concerning the physical origin of the redshift observed in objects like 3C 273. The discovery of numerous such objects, as well as the advancement of the theoretical background to understand their nature, eventually established the idea of nuclear activity in galaxies.

The classification of AGN, as was mentioned above, is based on two broad sets of parameters, their emission properties and their morphology. One big dichotomy is introduced by whether the AGN is radio-loud or radio-quiet. The definition of radio loudness has a number of different interpretations, usually by means of ratio of fluxes in radio and another wavelength, most usually optical (e.g., [Kellermann et al. 1989](#)). The presence (or absence) of a strong, collimated, relativistic jet usually regulates the radio output of an AGN and therefore is the main deciding factor for which side of the fence an AGN is. Each of these two classes are further segregated into smaller groups. Radio-loud AGN can be divided in radio galaxies, quasars, and BL Lacs. Radio-quiet AGN are divided in LINER, Seyfert 1, Seyfert 2, and quasar galaxies. In addition, one can also divide radio-loud sources on the basis of their jet morphology, hence the Fanaroff-Riley ([Fanaroff and](#)

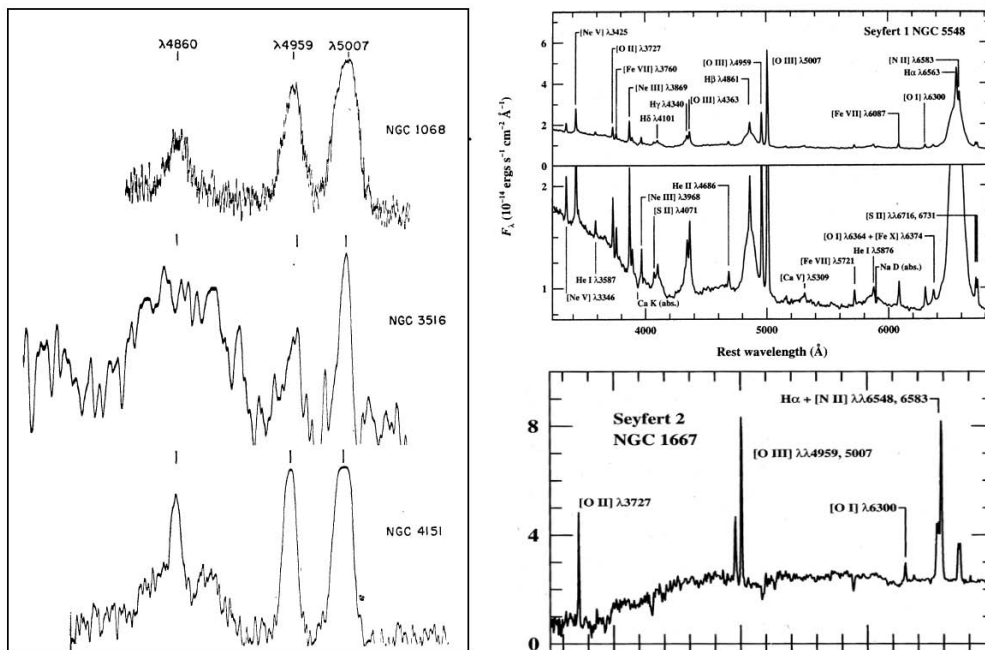


Figure 1.2: Examples of Seyfert galaxy spectra. In the left panel the original spectra from [Seyfert \(1943\)](#) are shown. Both broad and narrow emission lines are seen ( $H\beta$  and [OIII]). In the upper right panel a more contemporary spectrum of a Seyfert 1 galaxy is shown. For this class of objects both broad and narrow emission lines are seen. In contrast, in the lower right panel a spectrum of a Seyfert 2 galaxy is shown. For these objects, only narrow emission lines are detected. All spectra, in addition to the emission lines, also show strong absorption features. All spectra have been taken at the Lick Observatory. The left panel is reproduced from [Seyfert \(1943\)](#). The right panels are reproduced from [Ho et al. \(1993\)](#).

Riley [1974](#)) divided in Fanaroff-Riley Class I and Class II, AGN.

### 1.2.1 Splitting hairs: An AGN Compendium

Below I give a short description of the AGN classes and types most often used in the literature and in this work. A comprehensive listing of all the observational properties of the different types of objects is outside the scope of this work (for an extensive treatment of AGN physics and properties, I refer to [Krolik 1999](#)).

#### Quasars

Quasars (QSOs) are the most luminous active galaxies and the most energetic stable structures in the Universe. As already mentioned, QSOs can be either radio-quiet or radio-loud, with around a 5-10% of all QSOs being radio-loud (e.g., [Kellermann et al. 1989](#); [Padovani 1993](#); [Jiang et al. 2007](#)). Owing to their high luminosities, their host galaxies are often overshadowed and as a result, most QSOs appear as point-like sources (hence their name, quasi-stellar objects). They often show emission lines, with spectra similar to Seyfert

2 galaxies. Quasars appear to populate the most massive galaxies in the Universe and should therefore be integral in the cosmic structure formation. [Springel et al. \(2005\)](#) show in their Millennium Simulation that QSOs indeed end up at the centers of the most massive galaxies created in their simulation, often found at the centers of large concentrations of galaxies and the intersection of dark-matter cosmic filaments. Quasars might also be linked to the star-formation history of the Universe, as the peak of the number density distribution of QSOs with redshift coincides with that of star-formation activity (e.g., [Richards et al. 2006](#); [Hopkins et al. 2006](#); [Hopkins et al. 2007](#)).

### **BL Lac Objects**

BL Lac objects are named after the prototype object BL Lacertae, which was initially thought to be a variable star in the constellation of Lacerta ([Hoffmeister 1929](#)). BL Lac objects are characterized by their exceptionally featureless spectrum, exhibiting hardly any emission or absorption lines. BL Lacs are also known for their extreme variability throughout the electromagnetic spectrum, often showing correlated variability at different wavelengths. Closely related to BL Lacs are the Optically Violently Variables (OVVs), also sources with large amplitude variations of their fluxes. BL Lacs are all radio-loud AGN, with interesting jet properties (see Chap. 3), relatively flat spectrum, and highly polarized emission (up to  $\sim 20\%$ ). Compared to QSOs, BL Lacs appear to be less luminous. Blazars is a class that has been used to unify BL Lacs and radio-loud QSOs and usually refers to compact, flat-spectrum objects, with one-sided jets that are characterized by superluminally outward moving components. As sources, blazars are also characterized by intense variability over their whole spectrum.

### **Radio Galaxies**

Radio galaxies, as the name itself implies, are radio-loud AGN. They show two-sided extended jets that are usually not confined in the nucleus of the galaxy but rather go out to large distances (up to  $\sim$  Mpc scales). Their jets appear mostly symmetric and collimated, extending to opposite directions from the nucleus. These jets often end in a hot spot, which is usually surrounded by a radio lobe, or plume, that signifies a region where the jet interacts with the ambient medium, gets decollimated, and is ultimately diffused. The relative surface brightness of the radio jets and lobes gives rise to the classification introduced by [Fanaroff and Riley \(1974\)](#) to describe these objects. Radio galaxies with luminous, well collimated jets but invisible or faint radio lobes are categorized as Fanaroff-Riley (FR) Class I AGN. Class II Fanaroff-Riley AGN show on the contrary almost invisible or very faint inner jets but very prominent hot spots and radio lobes. Radio galaxies, although relatively less luminous than their BL Lac and QSO counterparts, show both emission and absorption features, either narrow (FR I) or also broad (FR II).

### **Seyfert Galaxies**

Seyfert galaxies are radio-faint (or quiet) AGN that show however a wealth of information in their emission and absorption spectra. These AGN are often found in gas and dust-rich spiral galaxies, with 3-5% of all galaxies estimated to host such an AGN (e.g., [Maiolino and Rieke 1995](#); [Maia et al. 2003](#)). No clear collimated outflow is seen for most objects



of this class, as is expected, given their faintness in radio. As was already mentioned, Seyfert galaxies can be divided into two subsequent main classes, with respect to the width of their emission lines:

- Seyfert 1 (Sy1) galaxies are characterized by both broad and narrow emission lines. In addition, absorption features are also found in their spectra. Measured velocities from the narrow and broad emission lines are calculated at  $\sim 10^2 \text{ km s}^{-1}$  and up to  $\sim 10^4 \text{ km s}^{-1}$ , respectively. An example can be seen in the upper right panel of Fig. 1.2.
- Seyfert 2 (Sy2), contrary to Sy1, show only narrow emission lines (see lower right panel of Fig. 1.2). There are about three times as many Sy2 galaxies as Sy1. Both Sy types are now believed to belong to the same family of objects, especially after the discovery of intermediate class objects, showing features similar to both classes. The nomenclature has thus changed to accommodate this, with objects classified in a fractional manner, depending on the relative strengths of the narrow and broad components of their spectra (e.g., type 1.5 or type 1.9).

### LINER Galaxies

Low-ionization nuclear emission-line region (LINER) galaxies are objects that show only weak nuclear emission lines (e.g. Heckman 1980), but no other signatures of AGN emission. They are the lowest-luminosity class of radio-quiet AGN. LINERs are found in up to  $\sim 35\%$  of all nearby galaxies (e.g., Ho et al. 1997) and in up to  $\sim 25\%$  of luminous infrared galaxies, systems linked to merger events (e.g., Veilleux et al. 1995). It is not clear whether the activity exciting the LINERs can be attributed to accretion (the AGN paradigm, e.g., Heckman 1980; Ho et al. 1993), or to star-formation (e.g., Terlevich and Melnick 1985; Shields 1992).

Apart from the above, additional classifications are used to describe the specifics of the radio jet structure of radio-loud AGN. In short there are:

- Core-dominated AGN (flat-spectrum AGN, luminous core and weak, often one-sided jet)
- Double-component AGN (core plus a one-sided jet)
- Triple-component AGN (core plus a two-sided jet)
- Compact Symmetric Objects (core plus a two-sided jet with lobe-like structure, resembling FR Class II AGN but at much smaller scales)
- etc.

There has been an ongoing effort to find a minimum set of parameters that can describe all the different properties of the numerous classes described above. Such a unification scheme would ultimately explain different types of objects as merely different sides of the same objects. Two such prevalent unification schemes exist presently. It should be noted here that a unification scheme can link different classes of objects together either in a spatial or a temporal manner. This means that the relevant importance of different properties

of the same object might change both as a function of space (i.e., where one looks an object from), but of time as well (i.e., which evolutionary phase an object is observed in). In the following section I shall briefly describe the currently accepted unification scheme. I postpone a detailed description of the temporal unification scheme of AGN for Chap. 2.

### 1.3 Making one out of many

Unlike stars, expected to be spherically symmetric and therefore appearing the same independent of the side you look them from, active galaxies are not expected to follow such a simplified notion. On the contrary, I have so far described different elements of an active nucleus that should be very much position dependent. One should underline and separate the two different effects at play here. Some processes are intrinsically anisotropic and therefore are expected to be "observable" only from certain positions in space (e.g., a radio jet is a highly oriented structure). On the other hand, there are other processes that are, in principle, isotropic in nature but are "collimated" by their environment, thus being allowed to be "observable" only at certain angles (e.g., an accretion disk emits, in first order approximation, isotropically). Both these effects appear to be important for AGN, modulating the appearance of active galaxies accordingly. It is therefore imperative to find a minimum set of parameters that would describe the observational differences between the AGN classes. These parameters could be summed up as follows: orientation (or the angle under which one views the AGN), the accretion disk luminosity (reflecting the accretion efficiency, as well as the accretion geometry), and the presence or not of a radio jet<sup>1</sup>. Orientation effects are considered to be the deciding factor in the currently accepted unified schemes (e.g., [Antonucci 1993](#); [Urry and Padovani 1995](#)).

#### 1.3.1 Radio-quiet Unification

There are two, rather distinct, unification schemes, regarding different aspects and properties of active galaxies. For both of these, the viewing angle to the object is the regulating factor. Concerning the radio-quiet side of the AGN spectrum, the unification scheme connects Seyfert galaxies (both types) and radio-quiet QSOs in one type. The key element for this unification is the assumption that there is an optically thick molecular torus, i.e., a cloud, or clouds, of matter containing gas and large amounts of dust, that is an extension of the accretion disk and obscures the central engine. Defining the inclination angle as the angle between the line of sight and the rotation axis of the accretion disk, then if one looks at an inclination angle of 90 degrees (edge on to the accretion disk), the line of sight encounters the dusty torus, an optically thick medium. Any radiation coming from gas clouds near the SMBH (and hence producing broad emission lines owing to their large velocities) is absorbed by the torus. As a consequence only narrow emission lines are observed, from clouds orbiting the SMBH at greater distances, effectively above

---

<sup>1</sup>It should be noted that the accretion disk luminosity and the presence of a radio jet are not completely independent effects. Accretion luminosity is dependent on the accretion rate. It has been considered that accretion rate plays a dominant role in regulating the evolution of an AGN. It is also to be expected that the creation of a radio jet would be closely connected to the rate with which material is funneled towards the nucleus of the system.

(or below) the torus. This produces a Sy2-like galaxy. If one looks at the AGN face on (meaning an inclination angle of 0 degrees), then the line of sight remains unobscured and emission from clouds both near and farther away from the SMBH is observable. This produces a Sy1-like galaxy. Radio-quiet QSOs are also included in this scheme as the higher-luminosity counterparts of Seyfert galaxies. Again, broad and narrow emission lines are observable (or obscured) depending on the viewing angle to the source.

The obscuring, molecular, dusty torus is assumed, in the simplest models, to have a donut like shape and have an homogeneous or, at least, continuous distribution of material. Alternatives include a clumpy torus or a warped disk. A torus-like geometry implies an energetic process counterbalancing the gravitational collapse of matter, providing support in the vertical direction (e.g., heating or magnetic turbulence). Given the presence of an accretion disk around the SMBH (e.g., [Shakura and Sunyaev 1973](#)), warping of the same disk at larger distances from the core is possible. Such warps can be radiatively, magnetically, or gravitationally induced (e.g., [Neufeld et al. 1995](#); [Pringle 1996](#)). Evidence for such an obscuration was given by polarized emission from the active nucleus. [Antonucci and Miller \(1985\)](#) observed NGC 1068, a Sy2 galaxy, in polarized light, unveiling a strong continuum spectrum superimposed by broad emission lines, characteristic of a Sy1 galaxy. The broad emission lines seen in the polarized light are believed to originate from clouds in the near vicinity of the SMBH that then get scattered and reflected to the observer by a hot, gaseous halo outside the torus, effectively circumventing its obscuring effect. This effect has now been observed in more than one Sy2 objects (e.g., [Tran 2001](#)), solidifying the above scenario.

In Fig. 1.3, a sketch of an AGN is shown, containing the following main structures:

- the central engine, a point-like and variable source. This includes a SMBH (with masses up to  $\sim 10^{10} M_{sol}$ ) and the accretion disk (usually assumed massless, i.e., the ratio of the accretion disc mass to the SMBH mass is close to zero). The SMBH radius is of the order  $\sim 10^{-3}$  parsecs, while the accretion disk extends out to  $\sim 1$  parsec. In terms of Schwarzschild radii, the accretion disk extends out to  $\sim 100R_s$  and emits the bulk of the optical to ultra-violet continuum radiation.
- the broad and narrow line regions, at scales of 0.1pc and 10-100pc, respectively. Ionized gas clouds orbit the SMBH at different distances. Those closer to the central engine (broad line region) are more compact and move at high velocities, producing wide emission lines. Narrow emission lines are produced by lower density clouds of ionized gas at larger distances, farther out from the core. The accretion disk and the possible jet are the sources that ionize these gas clouds.
- the dusty molecular torus, an optically and geometrically thick obscuring structure. This torus or puffy disk-like structure contains molecular gas and large quantities of dust, extending to sizes of order  $\sim 10$  pc. The torus is opaque to optical radiation coming from the nucleus of the system, absorbing it and reradiating it at infrared wavelengths. The inner radius of the molecular torus can be defined by the dust sublimation temperature ( $T_{sub} = 1500\text{K}$ ).
- jets, well collimated, probably magnetized outflows. These outflows can extend up to  $\sim \text{Mpc}$  scales out from the core, well outside the confines of the host galaxy of the

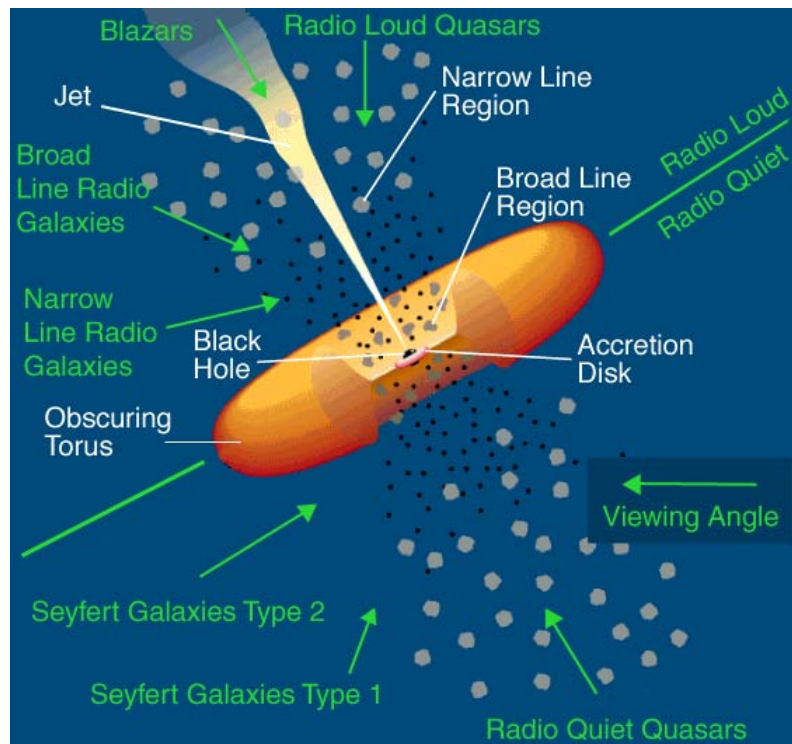


Figure 1.3: The main constituents of active galactic nuclei are shown in this sketch. A SMBH is in the center of the system, with an optically thick, geometrically thin accretion disk surrounding it. In the near vicinity of the SMBH the broad-line region is found, consisting of gaseous clouds orbiting the SMBH at high velocities and emitting due to excitation from the accretion disk and the base of a possible jet. The central area, including the broad-line region, is enclosed by a dusty, possible clumpy, geometrically and optically thick torus, that obscures the AGN and induces inclination-dependent effects. At larger distances, gaseous clouds are orbiting the SMBH at lower velocities. Narrow emission lines originate there (narrow-line region). For radio-loud AGN, a radio jet is also observed, in some cases stretching out to  $\sim$  Mpc scales. The figure is reproduced from [Urry and Padovani \(1995\)](#).

AGN. Jets are most probably anchored in the accretion disk or the ergosphere of the SMBH and they help transfer angular momentum away from the accreting matter. A continuous energy supply from the nucleus is necessary for collimating and ejecting these outflows at such distances. In the following section, more information on the radio jets will be given.

### 1.3.2 Radio-Loud Unification

The second part of the unification scheme of AGN pertains to those active galaxies loud in the radio waveband. Again the main constituent of this unification is the viewing angle, but this time in respect to the radio jet axis. It is assumed that AGN jets are axisymmetric structures, with their symmetry axis perpendicular to the accretion disk and aligned to the spin of the SMBH. Although this is not necessarily true (see Chap. 3 and

Sect. 3.7 in particular), it is a first order approximation that quite reasonably describes the observed properties. Relativistic effects are those that regulate what will be the observable properties of an AGN.

In this context, when looking at a radio-loud AGN at a very small angle to the jet axis (inclination angle  $< 5$  degrees), the observable emission is exclusively dominated by the jet component. Emission from the jet is mainly produced through the synchrotron mechanism (Alfvén and Herlofson 1950; Shklovsky 1953; also see the following section), with a considerable contribution of the inverse Compton scattering mechanism at higher frequencies (for an extensive treatment of both these mechanisms, see Rybicki and Lightman 1986). This emission is highly polarized and often quite variable. BL Lac objects are seen at these small inclination angles to the jet axis. The jet emission, boosted by relativistic effects (see Sec. 3.1), essentially covers any underlying emission coming from the accretion disk and the broad and narrow-line region, hence the featureless spectrum of BL Lacs, with no or very weak emission lines. Correlated variability, observed for this class of objects, can also be explained through propagation of "components" down the jet, their flux variation dominating the total source flux, through Doppler boosting.

Radio-loud quasars, on the other hand, are sources seen at intermediate inclination angles. A considerable jet component contributes to their total spectrum, but emission from the disk, as well as the line emitting regions (either narrow, or both narrow and broad, depending on the inclination angle and the extend of the dusty torus) is also important. Given the still mostly small inclination angles for these objects, they usually exhibit one-sided radio jets, owing to the Doppler dimming of the jet propagating to the direction opposite to the observer. Superluminal motions are observed in QSO jets, again a combination of relativistic and projection effects (e.g., Porcas 1983; Zensus and Pearson 1990; Zensus et al. 2003). In a similar fashion, radio galaxies are AGN that are observed at large inclination angles. For this class of objects relativistic and projection effects are the least important. They usually exhibit long, two-sided jets, often also with radio lobes (dependent on the exact inclination angle and the properties of the medium in which the jet is propagating). There is an overlap between radio galaxies and quasars, with radio galaxies being considered as lower-luminosity sources, usually associated with radiatively inefficient accretion modes. As for the case of quasars, radio galaxies also exhibit emission lines.

As can be seen, the unification scheme(s) can offer a fairly good explanation of the main differences observed for the different classes of active galaxies. It should however be noted that even for the same underlying physics and the modulations caused by the inclination angle and the internal luminosity of the nucleus, there is a large number of additional factors that affect the appearance of an object. These factors include the geometry of the individual parts described above, the type of the host galaxy, and the environment within which the active galaxy is embedded. One finally needs also to bear in mind that these factors might actually be dependent. Recently, the co-evolution of AGN and their host galaxies has come into focus, especially after the discovery of the correlation between the masses of the SMBHs at the centers of galaxies and the host galaxy bulge luminosity (e.g., Kormendy and Gebhardt 2001), or the velocity dispersion (e.g., Merritt and Ferrarese 2001).

This highlights another important point, only briefly mentioned before. Apart from any spatial unification achieved, one should also consider a possible temporal unification

of seemingly disparate objects. Chapter 2 will touch upon this topic and try to investigate such a possibility. Is there evidence that some active galaxies evolve into some other types of AGN with the course of time? How does the environment regulate such an evolution? Are merger events relevant to this process? Can one trace evolution in active galaxies? Can individuality of certain AGN, in terms of properties different from the average AGN, be attributed to such different evolutionary phases?

### 1.4 AGN Jets

It is important to spend a few more lines about the underlying physics and properties of AGN jets. As I have already mentioned, these extremely well collimated outflows give rise to radio-loud AGN and, for given inclination angles, even dominate the continuum spectrum of some active galaxies. The primary emission mechanism for jets is synchrotron radiation from a population of relativistic electrons gyrating in the magnetic field of the jet. The same magnetic field, anchored in the accretion disk, is most probably the driving force that ejects, collimates, and accelerates the outflow. This magneto-rotational process has been studied extensively both analytically as well as numerically (e.g., Lovelace 1976; Blandford and Znajek 1977; Blandford and Payne 1982; Königl 1989; Ferreira and Pelletier 1993; Sikora et al. 2005; Punsly et al. 2009; McKinney and Blandford 2009; for an overview, see Königl 2006). Radiation and gas pressure have also been employed to explain the creation of relativistic jets, however in both cases these mechanisms would not be sufficient to accelerate the outflow to the relativistic speeds observed in AGN jets.

An additional unknown for AGN jets is their composition. Two dominant scenarios are currently under debate, namely "heavy" proton-electron jets (e.g., Blandford and Rees 1974; Mannheim et al. 1991; Mannheim and Biermann 1992), or the "light" electron-positron jets (e.g., Kundt and Gopal-Krishna 1980; Wardle et al. 1998; Celotti and Blandford 2001), although a combination of the two is probably the closest to reality (e.g., Begelman et al. 1984; Sol et al. 1989; Sikora and Madejski 2000). Assuming a "heavy" jet configuration requires substantially higher energy pumped into the jet to accelerate the particles to relativistic speeds.

#### 1.4.1 Synchrotron Radiation

The synchrotron emission mechanism is responsible for the observable radiation from relativistic AGN jets. The basic principle includes a charged particle gyrating around a magnetic field line. Due to the continuous acceleration, the electron radiates. Synchrotron is a non-thermal emission mechanism (pertaining to the produced spectrum) and it is observed in diverse astrophysical environments beside AGN jets, e.g., supernova and supernova remnants, stars, galaxies, and cluster halos. One of the most prominent properties of synchrotron emission is its high fractional linear polarization (in the plane perpendicular to the radiation's propagation direction).

The emission for a particle with charge  $e$  and Lorentz factor  $\gamma$ , gyrating in a magnetic

field  $B$  has a characteristic frequency of:

$$\nu_c = \frac{\gamma^2 e B}{2\pi m c},$$

where the Lorentz factor is defined as  $\gamma = \frac{1}{\sqrt{1-\beta^2}}$ .  $\beta$  is the speed of the particle measured in units of the speed of light. A power-law energy distribution for a population of charged particles<sup>2</sup> will produce a superposition of the spectra of the individual charged particles. The resulting spectrum is a power-law that is described by a spectral index  $\alpha$ ,  $S_\nu \propto \nu^\alpha$ , where  $\alpha$  is defined as  $\frac{-(s-1)}{2}$ . At low frequencies the synchrotron emission is self-absorbed and below the turnover frequency it has a spectral index of 2.5 for a spatially homogeneous source, regardless of the energy distribution of the electrons. Assuming an isotropic distribution of angles between the injection velocity of the electron population and the magnetic field lines, the average power emitted by a particle is described as:

$$P_{syn} = \frac{4}{3} \sigma_T c \gamma 62 \beta^2 U_B,$$

where  $\sigma_T$  is the Thompson cross-section and  $U_B$  is the energy density of the magnetic field.  $P_{syn}$  can be used to estimate the cooling time of a synchrotron emitting particle as:

$$t_{syn} = \frac{E}{P_{syn}} = \frac{\gamma m c^2}{P_{syn}} \sim \frac{24.6}{B^2 \gamma} yr.$$

It can be seen that the higher energy particles cool faster, and therefore the spectral index decreases with time. As mentioned before, inverse Compton scattering also occurs in AGN jets and provides a further means for particle cooling. The inverse Compton scattering depends on the incident photon field and therefore the ratio of the radiation and magnetic energy density gives a measure of the relative importance of the two processes:

$$\frac{P_{syn}}{P_{Comp}} = \frac{U_B}{U_{ph}}.$$

The degree of synchrotron polarization can also be calculated as a function of the energy distribution power-law index  $s$  as follows:

$$n = \frac{s + 1}{s + \frac{7}{3}},$$

which, for a typical value of  $s=2$ , gives a fractional polarization of 69%. Depolarization effects, as well as polarization conversion effects, need first to be taken into account before the actual anticipated observable fractional polarization is estimated. On a final side note, the above energy output is modulated by the relativistic effects, effectively boosting (or de-boosting) the emission, as well as making the radiation field highly anisotropic. In principle, for a charged particle with a Lorentz factor  $\gamma$ , the radiation emitted is concentrated inside a cone of opening angle  $1/\gamma$  towards the direction of motion (beaming effect). The relativistic and projection effects with respect to the jet appearance will be discussed in more detail in Sect. 3.1.

<sup>2</sup>One can assume  $N(E)dE \propto E^{-s}dE$ , where  $N(E)$  is the number of charged particles with energies between  $E$  and  $E+dE$ .

## 1.5 Very Long Baseline Interferometry

In this section I will shortly describe the observation technique used to obtain the data analyzed in Chap. 3. Very Long Baseline Interferometry (VLBI, e.g., [Rogers et al. 1983](#); [Walker 1986](#); [Taylor et al. 1999](#)) is based on the simple concept of a two-element interferometer, by studying the mutual coherence function of the electric fields between two different points on the sky (a plane perpendicular to the direction of observation). A natural expansion of this concept is a multiple-element interferometer, with elements that are not directly linked to each other. In that case, the distance between each element (the baseline length) can be arbitrarily high, especially with the advent of space VLBI. It can be shown that the observing resolution of an interferometer,  $\theta$ , is proportional to the wavelength of the observations,  $\lambda$ , and inversely proportional to the length of the longest baseline of the interferometer,  $D$ :

$$\theta(\text{rad}) \propto \frac{\lambda}{D}.$$

For the global VLBI network (with baselines of the order of  $\sim 9000$  km) and radio frequencies, of the order of  $\sim 10^{10}$  Hz, a resolution of the order of milliarcseconds can be achieved, the highest angular resolution of all astronomical instruments. Increasing the baseline length (e.g., by space radio-antennas; VSOP2, [Tsuboi 2008](#)), or decreasing the observing wavelength leads to an improvement of the resulting resolution of observations. Currently, interferometers at infrared and optical frequencies exist, although observations of this kind are extremely difficult due to the short and variable coherence times for such high frequencies, induced by atmospheric effects. The most promising technique involves global millimeter VLBI observations (e.g., [Krichbaum et al. 2008](#)), with promise of resolving the event horizon of the black hole in the center of our galaxy, usually linked to the source SgrA\*, in the immediate future.

### 1.5.1 Basic Formulas

The most basic equation for interferometry is that of the spatial coherence function of the electromagnetic field radiated from an object on the sky. This formula relates the brightness distribution on the plane of the sky,  $I_\nu(x, y)$ , to the spatial coherence function relative to the phase tracking center measured in the  $uv$ -plane:

$$V_\nu(u, v) = \int \int I_\nu(x, y) e^{-2\pi i(ux+vy)} dx dy.$$

The  $uv$  plane is defined as  $\mathbf{r}_1 - \mathbf{r}_2 = \lambda(u, v, 0)$ , where  $\mathbf{r}_i$  is the position of antenna  $i$  and  $\lambda$  the observing wavelength. In other words, this equation relates plane-of-the-sky coordinates to antenna coordinates. This relation is a Fourier transform and as such it is reversible. One can therefore retrieve the true sky brightness distribution as a function of the information in the  $uv$  plane:

$$I_\nu(x, y) = \int \int V_\nu(u, v) e^{2\pi i(ux+vy)} du dv.$$

Unlike the sky brightness distribution, the  $uv$ -plane is only partially sampled, depending on the number of different baselines of the interferometer, as well as the duration of the



observation. This is described by a sampling function  $S(u,v)$ , and the resulting product is a "dirty" image, reflecting the convolution of  $B(u,v)$ , the dirty beam or point-spread-function of the instrument, with  $I(x,y)$ :

$$I_v^D(x, y) = \int \int V_v(u, v) S(u, v) e^{2\pi i(ux+vy)} dudv,$$

and

$$B(x, y) = \int \int S(u, v) e^{2\pi i(ux+vy)} dudv.$$

A deconvolution step is therefore needed, in order to extract the effect of the instrument sampling and recover the true sky brightness distribution  $I_v(x, y)$ . The point-spread-function (PSF), or dirty beam in the VLBI jargon, characterizes the instrument and reflects the resolution of a given observation.

## 1.5.2 Calibration

After the complex visibilities,  $V_v(u, v)$ , have been acquired, further steps are needed in order to account for errors stemming from the atmosphere, the assumed geometry of the observing array, as well as time-related errors. This procedure essentially constitutes the calibration of the instrument and consists of (1) the fringe-fitting, (2) the amplitude calibration, and (3) phase calibration (through self-calibration, i.e., phase and amplitude closure). In principle, all these errors can be traced back and divided to antenna-based and atmosphere-induced errors (for a thorough treatment of these procedures, see [Taylor et al. 1999](#)).

### Fringe-Fitting

The electromagnetic signals measured from an antenna are described by an amplitude and a phase. One can relate the interferometer phase,  $\phi_{l,v}$ , to the interferometer delay,  $\tau_l$ . The phase depends on both time and frequency. Fringe-fitting is the process of finding the residuals of the phase in frequency and in time. Once these residuals are removed, a coherent averaging over frequency and time is possible, thus effectively increasing the signal-to-noise ratio of the measurement (for a more detailed treatment of the fringe-fitting process, see [Cotton 1995](#)).

### Amplitude Calibration

During the amplitude calibration a gain function is derived for each antenna, depending on the antenna elevation. System and antenna temperatures are used for the amplitude calibration, with antenna temperatures being superior, but limited by larger errors and inadequate sensitivity of small antennas. At higher frequencies the atmosphere's opacity must also be taken into account (the simplest assumption for the atmosphere being a single parallel layer of absorbing gas, characterized by a temperature and a zenith opacity).

## Self-calibration

Self-calibration accounts for the sparse uv-sampling (i.e., missing spacings in the uv-plane) and the residual amplitude and phase errors, with the latter being the most crucial. One can define a complex gain factor  $G_i$  for antenna  $i$ , including the amplitude and phase errors induced by both the instrument, as well as the propagation of the signal from the source to the observer. By forming the sum of visibilities around a closed loop of 3 baselines one can exclude antenna-based errors and recover the true visibility and structure of the observed source. Similarly, one can form visibility amplitude ratios that are again independent of antenna gain factors. These are the so-called closure arguments for phase and amplitude and are used during the self-calibration process.

### 1.5.3 Imaging

The imaging process pertains to the deconvolution of the dirty beam (PSF) from the calibrated visibility data. This can be achieved in a non-linear way, requiring estimation of the visibility equation at positions in the uv-plane where no measurement is done. These estimations are provided by algorithms, most popular ones being CLEAN (e.g., Högbom 1974) and MEM (e.g., Frieden 1972). The simplest model one can assume is:

$$\hat{V}(u, v) = \sum_p \sum_q \hat{I}(p\Delta x, q\Delta y) e^{2\pi i(pu\Delta x + qv\Delta y)},$$

where the image-plane has been divided into a grid  $N_x \times N_y$  cells of surface  $\Delta x \times \Delta y$ . This model therefore has  $N_x N_y$  free parameters, and constrains equally the number of actual measurements. For the positions of the uv-plane where no measurement is taken, the model can assume any value. This translates to a convolution relation:

$$I_{p,q}^D = \sum_{p',q'} B_{p-p',q-q'} \hat{I}_{p',q'} + E_{p,q},$$

where (D) denotes the dirty image, B is the dirty beam,  $\hat{I}$  is the gridded true image, and E represents a noise function. The solution to this equation will provide us with the true image. This translates to finding the right (i.e., unique) combination of the principal solution of the convolution equation<sup>3</sup> and a subset of homogeneous solutions. This can only be done in a non-linear way. I now give a short description of two most often used deconvolution algorithms.

#### CLEAN algorithm

CLEAN<sup>4</sup> finds a solution to the convolution equation given above by progressively summing up point sources of non-constant strength, in an otherwise assumed empty field. An iterative process is followed to find the positions and strengths of these point sources, progressively removing (via deconvolution) the dirty beam from each respective position of the dirty image. Once the residuals have reached the noise level of the observations, the

---

<sup>3</sup>As principal solution is defined a solution for which all non-sampled uv-points are given a zero amplitude.

<sup>4</sup>For the data presented in Chap. 3 the CLEAN algorithm has been used.

image can be constructed. The final deconvolved image is the sum of the point components, found previously, convolved with a CLEAN beam, usually a Gaussian. The result of this process is an image consisting of a number of components<sup>5</sup>. For well known - extensively studied- sources, *a priori* models can be used before the CLEAN algorithm is applied to the dirty image.

### Model-fitting

After the fully calibrated CLEAN image has been acquired, further modeling of the map takes place (for a detailed treatment, see [Taylor et al. 1999](#)). In order to represent extended structures observed, the whole or part of the observed structure can be model-fitted using extended components, usually described by a 2-dimensional Gaussian distribution (either circular or elliptical). Each component used can be fitted to the image plane or is inverse-Fourier transformed into the uv-plane and is directly fitted to the observed visibilities. A number of parameters (depending on the quality of the available data and the aim of the investigation) such as the position, flux, and width of each of these components are obtained through this process. Therefore, an image of an extended object can be fitted by a number of such Gaussian components and characterized by their parameters. By cross-identifying these fitted components between different frequencies and epochs, one can follow their properties and kinematics. The CJF data used in Chaps. 3 and 4 have been analyzed in this way (see Sec. 3.4 for more information).

### Maximum Entropy Method (MEM)

Unlike the procedural, iterative way that CLEAN produces the final image, the maximum entropy method (MEM) algorithm selects the image that fits the data, to within the noise level, and also has maximum entropy. Entropy here should not be confused to the mechanical definition of Boltzman's entropy. Entropy here can be defined as something, which when maximized, produces a positive image with a compressed range in pixel values (e.g., [Narayan and Nityananda 1984](#)). Similarly to the CLEAN algorithm, one can also provide a "default" image for MEM, thus incorporating previous knowledge of the studied source. The model here is again constrained through a chi-square comparison of the resulting and expected values for each pixel. It is known that the MEM algorithm tends to fit the center of the uv-plane (short spacings) more poorly than longer spacings.

## 1.5.4 VLBI arrays

There is a number of different VLBI arrays currently around the globe. Of particular interest are the Very Long Baseline Array (VLBA) and Very Long Array (VLA) operated by NRAO, and the European VLBI network (EVN) operated by a consortium of European radio astronomical institutes. Of note is also the Effelsberg radio telescope, also part of the EVN, operated by the Max Planck Institute for Radio Astronomy. The EVN, the VLBA, the phased VLA, and a number of individual radio antennas can observe in unison,

<sup>5</sup>The number, exact position and strength of the components are not given by a unique solution. An error estimation (e.g., chi-square minimization) is necessary to constrain the model and recover a unique solution.

creating the global VLBI array, thus offering the highest possible resolution (due to the longest possible baselines). For the data analyzed in Chap. 3, VLBA and global VLBI observations have been conducted.

### Very Large Baseline Array

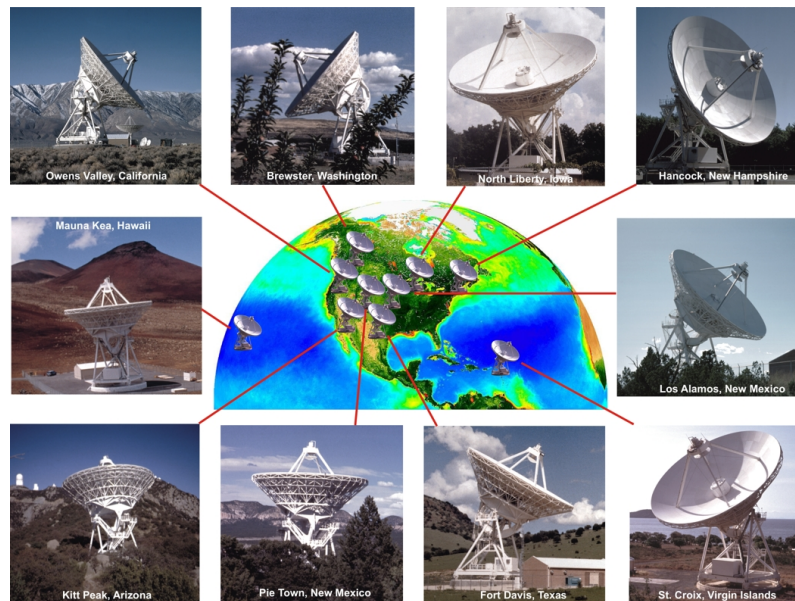


Figure 1.4: The Very Long Baseline Array (VLBA) operated by NRAO. It consists of 10 radio antennas, seen on the picture. Picture courtesy of NRAO.

The VLBA (see Fig. 1.4) is the largest dedicated interferometric instrument in the world. It is comprised by 10 25-meter antennas, with the longest baseline between Mauna Kea (in Hawaii) and St. Croix (in the US Virgin Islands) measuring 8611 kilometers. The array operates in 14 different frequency bands from 0.3 to 90 GHz and can achieve nominal resolutions of 22 to 0.32 milliarcseconds, respectively.

### Global VLBI Network

The global VLBI array (see Fig. 1.5) is the highest resolution radio interferometer currently available for observations<sup>6</sup>. It is not a dedicated instrument but rather comprises of a number of individual antennas and arrays that can, on occasion, conduct coordinated observations. Observations can be carried out at frequencies above 5 GHz, while for a smaller subset of the global VLBI network, millimeter observations are also possible. Resolutions achieved from the global VLBI array are sub-milliarcsecond.

---

<sup>6</sup>It should be noted that the global mm-VLBI network (e.g., [Krichbaum et al. 2008](#)) offers even higher resolutions, given its higher observing frequency, although currently transatlantic baselines are still in the experimental phase.

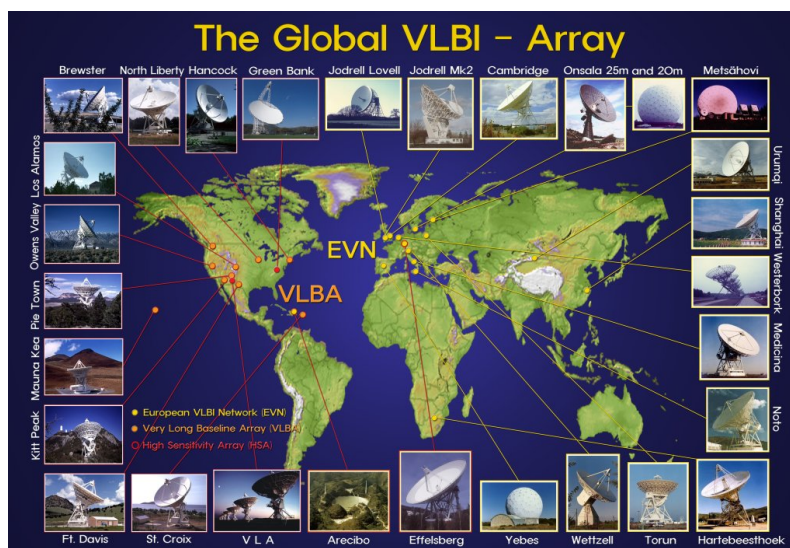


Figure 1.5: The Global VLBI Array coordinated by a consortium of international radio astronomy institutes. It consists of the 18 EVN radio antennas, the VLBA, the VLA, and the GBT. Picture courtesy of NRAO.

## 1.6 The Caltech-Jodrell Bank flat-spectrum (CJF) sample

Due to the complex nature of the topics investigated in this work, I use a statistical approach in order to average out the individual characteristics that might otherwise hinder the study of single sources. For this analysis I use a statistical sample of radio-selected active galaxies, the Caltech-Jodrell Bank flat-spectrum (CJF) sample.

The CJF sample (Table 1.1) has been selected in the radio (at 5 GHz) and therefore has been most extensively studied in the radio regime (e.g., Taylor et al. 1996; Pearson et al. 1998; Britzen et al. 1999a; Vermeulen et al. 2003; Pollack et al. 2003; Lowe et al. 2007; Britzen et al. 2007b; Britzen et al. 2007b; Britzen et al. 2008).

Table 1.1: Selection criteria and consistency of the Caltech-Jodrell Bank flat-spectrum sample.

<b>Frequency(MHz)</b>	4850
<b>Spectral Index</b>	$\alpha_{1400}^{4850} \geq -0.5$
<b>Declination</b>	$\delta \geq 35^\circ$
<b>Galactic latitude</b>	$ b  \geq 10^\circ$
<b># Quasars</b>	198
<b># BL Lac</b>	32
<b># Radio Galaxies</b>	52
<b># Unclassified</b>	11
<b># Total</b>	293

The CJF sample (Taylor et al. 1996) consists of 293 radio-loud active galaxies selected

(see Table 1.1) from three different samples (for details see, Britzen et al. 2007b), forming a statistically complete, flux-density limited sample. The sources span a large redshift range (see Fig. 1.6), with the farthest object being at a redshift  $z = 3.889$  (1745+624; Hook et al. 1995) and the closest one at  $z = 0.0108$  (1146+596; de Vaucouleurs 1991). The average redshift of the sample is  $z_{avg} = 1.254$ , with  $z_{BL Lac, avg} = 0.546$ ,  $z_{RG, avg} = 0.554$ , and  $z_{QSO, avg} = 1.489$  for BL Lac objects, radio galaxies, and quasars, respectively. All the objects have been observed with the VLBA and/or the global VLBI network. Each source has at least 3 epochs of observations and has been imaged and studied kinematically (Britzen et al. 1999a; Britzen et al. 2007b; Britzen et al. 2008). The X-ray properties have been studied and correlated with their VLBI properties (Britzen et al. 2007a).

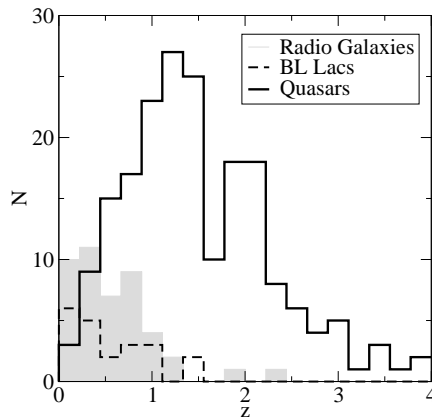


Figure 1.6: Redshift distribution for the CJF sample, for quasars (continuous line), BL Lacs (dashed line), and radio galaxies (grey blocks). CJF sources extend out to a redshift of  $\sim 4$ .

This sample has been created to study the kinematics of relativistic AGN jets on a statistical basis and the CJF sources have been selected accordingly. In addition, among the original goals of the study of the CJF sample are a study of the evolution of compact radio sources with cosmic time, as well as placing significant limits on the mass of compact objects through the search for gravitational lenses (see Taylor et al. 1996). The flatness of the CJF sources spectrum ensures the selection of compact, core-dominated, sources that usually exhibit superluminal motions in their jets.

The following data are available for the CJF sample:

- single dish total flux observations at 4.85 and 1.6 GHz (Gregory and Condon 1991 and White and Becker 1992, respectively) and a radio spectral index calculated between these
- VLA core flux densities at 4.85 and 1.6 GHz
- VLBA flux densities again at 4.85 and 1.6 GHz (both VLA and VLBA flux densities compiled in Taylor et al. 1996)
- optical identification and redshift information for 97% of the CJF sources (see Britzen et al. 2007a for references)

- VLA images with polarization information
- VLBA images with model fitting component parameters over several epochs ([Britzen et al. 2007b](#); [Britzen et al. 2008](#))
- proper motions and apparent speeds for all cross-identified components from the VLBA maps
- soft X-ray flux densities from the ROSAT satellite (detections or upper-limits, [Britzen et al. 2007b](#))

Interestingly, the kinematics of the CJF sources ([Britzen et al. 2008](#)) are characterized by sub-luminal or mildly superluminal motions, in contrast to the generally accepted scenario (see Chap. 3). In addition, inwardly moving components complicate the global picture. [Britzen et al. \(2008\)](#) develop a localized method for calculating the bending of the jet associated with individual components. The maximum of the distribution of local angles is at zero degrees, although a substantial fraction shows some bending (0 – 40 degrees). A few sources exhibit sharp bends of the order of > 50 degrees (see Fig. 13 in [Britzen et al. 2008](#)). Such morphologies in pc-scales (for a detailed discussion see [Britzen et al. 2008](#)) can be explained in the context of a BBH system. In Chap. 3 I will study the morphologies of the jets of the CJF sources and their evolution.

This work is structured in the following way: in Chap. 1 I gave a brief introduction on activity in galaxies, jet physics, and the VLBI technique and I described the Caltech-Jodrell Bank flat-spectrum (CJF) sample of sources used throughout this work, in Chap. 2 I study the role of activity in galaxies in the context of the merger-driven evolution scheme, in Chap. 3 I present results from the investigation of the jet ridge line properties and evolution of the CJF sample, in Chap. 4 the kinematics of the same sample is studied in the context of the  $\gamma$ -ray properties of the sources, finally I conclude with an epilogue summarizing my findings and offering an outlook for the future in Chap. 5.





## 2 Merger-driven evolution of active galaxies

According to the current paradigm of structure formation in the Universe (e.g., [Frenk et al. 1988](#)), gravitational interactions, ultimately leading to mergers, between individual galaxies play a predominant role in regulating the evolution of that structure. The relevance of merger events to activity in galaxies has been investigated by a number of authors (see Sect. 2.1) both theoretically and observationally, indeed finding a strong link between the two. A direct result of that link is the prediction of the formation of binary black hole systems in the centers of merging, or recently merged, galaxies. In this chapter I use the Caltech-Jodrell Bank flat-spectrum (CJF) sample to investigate the evolution of active galaxies in the frame of merger-driven evolution. In the same context, an evolution sequence, including the final stage of a binary black hole system, is traced using individual sources from the CJF sample as examples.

This chapter is organized as follows: in Sect. 2.1 I will shortly present the frame in which this work is placed, in Sect. 2.2 I will discuss BBH systems and the criteria used here to identify potential candidates, in Sect. 2.3 the motivation of this work is discussed, Sect. 2.4 discusses the criteria and tools used in the present investigation, Sect. 2.5 describes the multi-wavelength data collected for the CJF, in Sect. 2.6 I discuss the methods used in this investigation and show the results that they yielded, in Sect. 2.7 the merger-driven evolution is traced by means of individual sources examples. Finally, the chapter is concluded with Sects. 2.9 and 2.10, a discussion and conclusions based on the results are presented respectively.

### 2.1 Introduction

In the context of the hierarchical model for structure formation in the Cosmos, it is believed that structure, namely galaxies, are formed in a bottom-up manner (first suggested by [Searle and Zinn 1978](#)) where smaller proto-structures interact gravitationally and eventually merge forming progressively larger structures. [Sanders et al. \(1988\)](#) presented the first large-scale compelling evidence from the IRAS "minisurvey" in the far-infrared (precursor to the all-sky survey of the same telescope, [Rowan-Robinson et al. 1984](#)) that linked merging systems to active galaxies. These merging galaxies, identified by IRAS as ultraluminous in the far infrared (ULIRGs;  $L_{far-IR} > 10^{12}L_{sol}$ ), were found to contain large quantities of molecular gas (as traced by CO molecules). Their extreme infrared luminosity was attributed to a mixture of intense star-formation events (starburst) and an active core (AGN).

This link has since then been further explored by a number of authors (e.g., [Veilleux et al. 1995](#); [Veilleux et al. 1999](#); [Nagar et al. 2003](#); [Bennert et al. 2008](#); [Urrutia et al. 2008](#); [Yuan et al. 2010](#)). The advent of the Hubble Space Telescope (HST), as well as higher resolution infrared surveys (e.g., 2MASS; [Kleinmann 1992](#)) allowed the observation and imaging of the host galaxies of both ULIRGs and AGN. Almost 100% of ULIRGs were found to undergo a merger (e.g., [Sanders and Mirabel 1996](#)). In addition, a considerable fraction (of the order of 30%) of AGN in the local Universe were also found to show signs of interaction or close companions (e.g., [Hutchings and Campbell 1983](#), [Surace 1998](#)). Already in 1988, [Sanders et al. \(1988\)](#) proposed that QSOs indeed are the evolutionary descendants of ULIRGs, with the merger event supplying the necessary material (in the form of gas) to be accreted onto a central SMBH. [Canalizo and Stockton \(2001\)](#) put this hypothesis to test. By both imaging and spectroscopic investigation of the host-galaxies of nine QSOs, compelling evidence are found linking tidal interactions/merger events, intensive star-formation, and QSO activity.

Aside from the observational efforts to test the merger-driven evolution scheme, on the theoretical front intensive efforts have been undertaken to both analytically, as well as numerically, model the process of a merger under different circumstances and for different properties of the parent galaxies. With the substantial progress of computer technology, the numerical simulations have seen a leaping increase in both sensitivity and resolution. Recent theoretical work has shown that indeed merger events lead to both intense star-formation episodes and the triggering of AGN (e.g., [Barnes and Hernquist 1991](#); [Cattaneo et al. 2005](#), [Bekki et al. 2006](#); [Lotz et al. 2008](#)).

Individual objects have been found exhibiting a number of different properties characteristic of different phases in such an evolutionary scenario (e.g., [Boller et al. 2002](#); [Riechers et al. 2008](#); [Braitto et al. 2009](#)). These and other objects (e.g., NGC 6240; [Kommossa et al. 2003](#), Mrk 231; [Gallagher et al. 2002](#), etc.) have been used as pathfinders, as well as robust evidence, for the relevance of merger events and their effects in the evolutionary track of a galaxy.

All of the above, different aspects of evolution of active galaxies, have been combined into self-consistent models, offering a plausible scheme as to how galaxies evolve (e.g., the cyclic model of [Hopkins et al. 2006](#); see Fig. 2.1).

The current paradigm, in broad terms, would entail a merger event between two late-type "spiral" galaxies that form a star-forming merging system. Through dynamical friction large amounts of gas and dust are funneled towards the center of the merging system. Further loosing angular moment, the material forms an accretion disk, ultimately feeding the central core and therefore triggering an AGN. Eventually, through feedback processes, the originally obscured AGN pushes out the remaining dust, revealing the central core, but on the same time essentially quenching the star-formation (e.g., [Silk and Rees 1998](#)). Given the finite amount of fuel available to the AGN, core activity should die out after  $\sim 10^8$  yrs (assuming a standard luminosity of  $10^{12}L_{\star}$ , an accretion efficiency of 0.1, and a typical availability of gas  $\sim 10^9 M_{sol}$ ). The result would be a non-active "late-type" elliptical galaxy. A new merger event would re-initialize the same cycle.

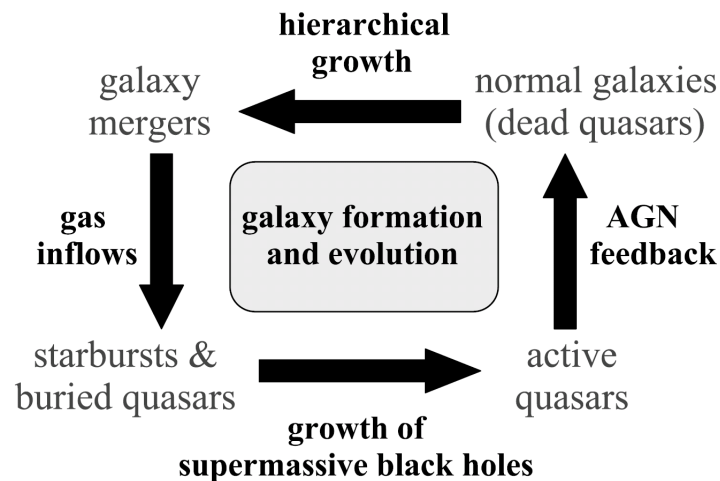


Figure 2.1: A cyclic model for the evolution of galaxies through successive merger events, starburst, and activity episodes. The figure is reproduced from [Hopkins et al. \(2006\)](#)

### 2.1.1 The other side of the fence

Although the above presented scenario enjoys wide recognition as the current paradigm for galaxy evolution and the role of AGN in it, there is a number of open questions and problems with it, as well as some alternative models addressing them.

The merger-driven evolution scheme and in particular the significance of active galaxies in it have been challenged on grounds of different points. Several authors find no apparent correlation between close companions (hence gravitational interactions) and nuclear activity (e.g., [Virani et al. 2000](#); [Schmitt 2001](#); [Li et al. 2008](#)). Additionally, the connection between AGN activity and induced increased star-formation rate has also come under question (e.g., [Miller et al. 2003](#)). Finally, the formation of a BBH system in the center of merging galaxies is still under heavy debate, mainly due to a lack of an efficient way of bringing the binary close enough for the gravitational radiative losses to kick in - the so called "final parsec" problem (e.g., [Rajagopal and Romani 1995](#); [Milosavljević and Merritt 2001](#); [Lodato et al. 2009](#)), as well as the absence of enough observational evidence.

[Elbaz et al. \(2009\)](#), basing their investigation on the peculiar object HE0450-2958 (first discovered by IRAS), propose a different paradigm for galaxy formation and evolution. In the suggested scheme, QSOs are created and fueled by accretion of intergalactic cold gas filaments (e.g., [Dekel et al. 2009](#)). In a bit more detail, a massive BH can form in a low-mass galaxy and switch on its activity, forming a radio jet. Rapid star-formation is induced through jet interaction with the ambient intra- or intergalactic medium (e.g., [Rees 1989](#)). The star-forming cloud will eventually coalesce with the galaxy, effectively increasing its mass and on the same time providing the QSO with additional fuel. There is a number of evidence supporting this model: the common presence of extended emission line regions around radio quasars (as candidate seeds for jet-induced star-formation), the positional offset of molecular gas concentrations with respect to QSOs, and indications

that the  $M_{BH}/M_{\star}^{bulge}$  ratio was larger in the past (for a more complete discussion of these see [Elbaz et al. 2009](#) and references therein).

## 2.2 Binary Black Hole Systems

According to the above scheme, given the assumed ubiquity of SMBHs in the center of each galaxy, galaxies with a binary black hole (BBH) in their center should be common systems (e.g., [Milosavljević and Merritt 2001](#); [Merritt and Ekers 2002](#); [Haehnelt and Kauffmann 2002](#)). These systems, although predicted in theory ([Begelman et al. 1980](#); for a review on the evolution of BBH see [Merritt and Milosavljević 2005](#)), have been difficult to study. Only a few of them have been directly observed (e.g., [Hudson et al. 2006](#); [Komossa et al. 2003](#); [Rodriguez et al. 2006](#)), while in a number of galaxies the presence of a BBH is discussed (for an overview see [Komossa 2006](#)). Active galaxies hosting BBHs will be primary candidates for the future gravitational wave space interferometer L.I.S.A. (e.g., [Sesana et al. 2005](#)).

Unlike the relative infancy of BBH systems observational studies, extensive work has been done theoretically in order to predict the different properties and characteristics of such systems. An analytical treatment of such a system and its evolution, although possible, is not realistic. Several authors have treated the problem of the creation and evolution of a BBH system numerically (e.g., [Mayer et al. 2007](#); [Dotti et al. 2009](#); [Dotti et al. 2010](#)). Even more phenomenological approaches to the BBH problem has been done, usually tailored to individual systems exhibiting peculiar properties (e.g., 3C 345, [Lobanov and Roland 2005](#); OJ 287, [Lehto and Valtonen 1996](#); PKS 0420-014, [Britzen et al. 2001](#); S5 1803+784, [Roland et al. 2008](#)).

The relative absence of observational data on BBH systems is a direct reflection of the rarity of such objects, as well as the limited observational capabilities of current instruments. At the same time, absence of a large enough number of such sources limits the potency of individual results and, ultimately, hampers our ability to efficiently identify new BBH candidates. It is therefore important to identify further new BBH candidates. BBH systems, according to the above, are the final step in the evolutionary path of a merging system and therefore could provide crucial information concerning the whole evolution process (e.g., see [Dotti et al. 2010](#) and [Merritt and Milosavljević 2005](#)), merging history, and the potential AGN triggering of such systems.

### 2.2.1 Binary Black Hole System selection criteria

Binary black hole systems are anticipated as an intermediate evolutionary stage for, possibly all ([Britzen et al. 2001](#)), active galaxies, as the result of a prior merger (e.g., [Merritt and Milosavljević 2005](#)). The evolutionary track of bound BBH systems has been studied extensively and is divided in three major phases:

- as the two host galaxies merge, the two black holes sink towards the center of the merging system through dynamical friction,
- the two black holes form a bound binary system and continue losing energy through gravitational interaction with the central stellar population, and surrounding gas

- and finally, after reaching a critical separation, the systems rapidly lose energy through gravitational radiation, leading to the actual coalescence of the two black holes.

As bound (or "hard") BBH systems, I consider a system of two black holes for which its binding energy per unit mass exceeds the kinetic energy of the stellar population in the nucleus of the system. It becomes apparent from the above that BBH properties would be directly linked to the properties of the host galaxy and the activity of the resulting AGN.

Given the distance of active galaxies and the timescales involved, one can expect to observe BBH systems in the first two phases of their evolution, before or just after they have formed a bound pair. I am therefore interested in identifying and classifying systems recently or currently undergoing a merger phase. Such systems, according to simulations (e.g., [Mayer et al. 2007](#)), exhibit complex morphologies, due to the tidal forces exerted on the merging galaxies.

ULIRGs are likely to host an early, unbound BBH system (as is the case of NGC 6240 and 3C 75, [Komossa et al. 2003](#); [Hudson et al. 2006](#)). Almost half of the ULIRGs observed so far exhibit nuclear emission lines, typical of LINER and Seyfert nuclei (e.g., [Nagar et al. 2003](#)). These exhibit the connection of galaxy evolution, and AGN in particular, to the BBH research.

Mergers are not the only systems where BBH systems have been searched for. Binary black holes in the second stage of their evolution, would reside in the nuclei of relaxed active galaxies, resembling, in first order, a single black hole AGN. Very Long Baseline Interferometry (VLBI) techniques have been used to map sources with complicated structures, that have been explained by the presence of a BBH (e.g., 0420-014, [Britzen et al. 2001](#); 3C345, [Lobanov and Roland 2005](#); 1803+784, [Roland et al. 2008](#)). A BBH system could lead to a precessing jet base (e.g., [Yokosawa and Inoue 1985](#); [Romero et al. 2003](#); [Roland et al. 2008](#); [Kaastra and Roos 1992](#)) and thus to a bent jet. Periodicities in the light curves can also be connected to a BBH (e.g., [Lehto and Valtonen 1996](#); [Sillanpaa et al. 1988](#); [Qian et al. 2007](#); [Caproni and Abraham 2004](#)). There is finally a number of further evidence more weakly connected to such systems (e.g., [Komossa 2006](#)).

## 2.3 Motivation for this work

Many authors have previously investigated the link between activity in galaxies and merger events (see references above). However, most of such investigations have concentrated on samples biased by their selection criteria towards merging systems. [Hutchings and Campbell \(1983\)](#) use an optically selected sample of active galaxies to investigate the percentage of mergers in active galaxies. [Sanders et al. \(1988\)](#) use extreme far-IR luminosities to investigate the connection between ULIRGs and AGN activity. Similarly, [Surace \(1998\)](#) use a far-IR selected sample. [Canalizo and Stockton \(2001\)](#) use far-IR color criteria to select their sample of *bona fide* QSOs studying the same connection.

Unlike the aforementioned efforts, in this chapter I use the Caltech Jodrell-Bank Flat-spectrum (CJF) flux-limited sample of 293 radio-loud active galaxies to study the evolution of AGN and identify AGN in different evolutionary stages, including the elusive BBH systems. In this way, I essentially conduct a "backwards" investigation, starting from the final result of the evolution process, active galaxies, and looking for evidence for merger

events. This is done by means of a multi-wavelength analysis of the sample. In contrast to other samples, the CJF sample contains AGN well into their activity cycle since it was originally created to study the kinematics of AGN jets. Combined with the selection criteria for flat-spectrum sources, it is ensured that a population of active galaxies with very compact cores and prominent radio jets is probed.

In the context of the evolution scheme described in Sect. 2.1, compact core AGN with powerful jets would be found in the very end of the evolutionary track of a merging system, when the gas has settled in an accretion disk and efficient feeding of the central SMBH (or BBH) has begun (e.g., [Hickox et al. 2009](#); see Fig. 2.2). However, one should also note the possibility of multiple mergers for individual galaxies ([Conselice et al. 2008](#) find a merger rate of  $4.3 \pm 0.8$  for galaxies with  $M_\star > 10^{10} M_{sol}$ ). In this case, one would find active cores in systems that otherwise show evidence of a previous evolutionary phase (e.g., tidal disruptions, companions, etc.). This of course complicates the effort of correctly identifying sources in different stages of their evolution.

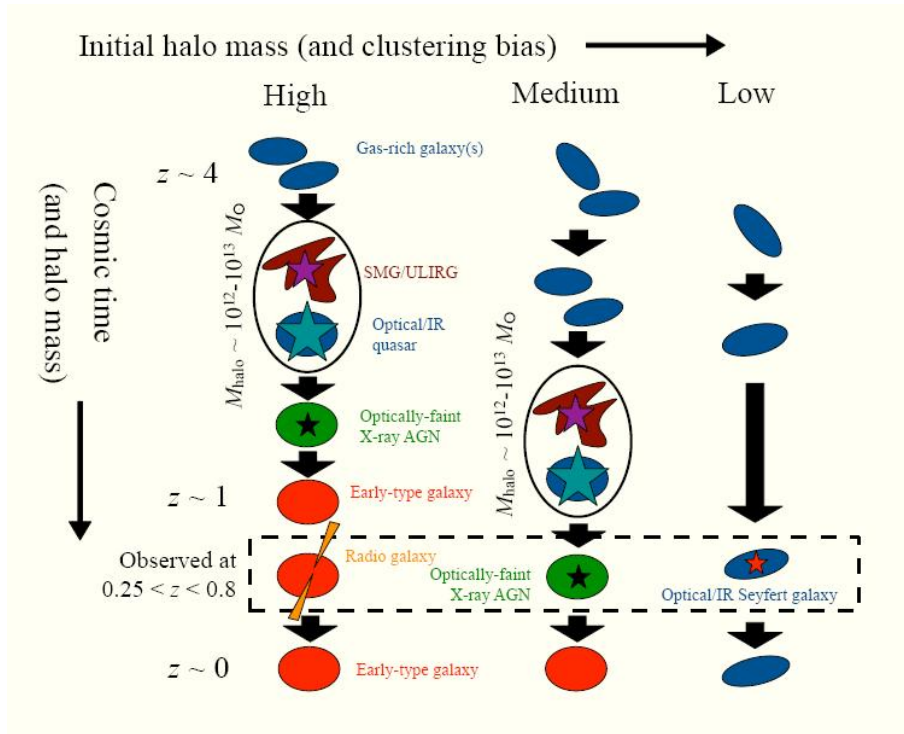


Figure 2.2: A qualitative model for different evolution paths depending on halo masses. For a massive enough halo ( $M_{crit} \sim 10^{12} - 10^{13} M_{sol}$ ) efficient accretion on a SMBH leads to the formation of a radio-loud AGN. The figure is reproduced from [Hickox et al. \(2009\)](#)

By using the CJF sample I ensure that I conduct an unbiased investigation of the evolution of AGN. I want to investigate the true percentage of AGN connected to merging or merger-remnant systems. I am also interested in finding out the significance and occurrence of different evolutionary phases in the CJF sample, including possible BBH systems.

Throughout this chapter I assume the following cosmological parameters:  $H_0 = 71$

$\text{km s}^{-1} \text{Mpc}^1$ ,  $\Omega_M = 0.27$ , and  $\Omega_\Lambda = 0.73$ .

## 2.4 Evolution Criteria

I look for evidence supporting the connection between activity in galaxies and merger events. I also identify and classify candidate systems in different evolutionary stages using the following criteria:

- merger signs (morphological distortions, tidal tails, companions etc.)
- excess infrared fluxes and starburst activity
- color information

In addition I look for BBH candidates. The basic assumption is made that BBH systems are created in systems that have undergone a merger. It is expected that unrelaxed (morphologically disturbed) systems host still unbound BBH systems, whereas bound pairs of black holes are expected to be found in more evolved systems (of the order of  $10^6 - 10^7$  years after the merger, [Begelman et al. 1980](#)). I use variability as a tracer for these evolved systems. Although the above do not provide robust evidence for the existence of a BBH system, they can be used as strong filters for selecting possible candidates.

### 2.4.1 Host galaxy signatures

Merger signs - I look for morphological information that would characterize a system that is about, is currently, or has recently undergone a merger event. I use this information to show the connection between activity in galaxies and merger events. Systems with close companions are the precursors of merging systems and present the earliest evolutionary stage of such systems. In this context, I additionally collect clustering information of the CJF sources, as sources in clusters present a higher probability of taking part in galaxy interactions and mergers. Tidal tails and other morphological distortions are used as explicit signs of current or recent merger activity.

Star-formation - Increased star-formation rate can be an effect of merger events (e.g., [Barnes and Hernquist 1991](#)). It is known that ULIRGs ([Sanders et al. 1988](#)) are considered to be a direct result of merger events (e.g., [Sanders and Mirabel 1996](#)) and are systems that are powered by a strong starburst component (e.g., [Genzel et al. 1998](#)), although higher luminosity ULIRGs appear to be dominated by a nuclear component. I use starburst activity, as well as extreme infrared luminosities induced by intensive star-formation, as a further piece of evidence for systems possibly undergoing a merger.

Color information - I use the available near-infrared (HJK photometry) information to identify systems possibly associated to merger events. Merging systems, owing to the high concentration of dust, appear redder in color than their non-merger counterparts or simple evolved stellar populations. This effect is used to identify evolutionary transitory systems.

Infrared Emission - Infrared emission coming from active galaxies originates partly from the host galaxy of the AGN, as a result of thermal emission processes (thermal radiation from heated dust grains and gas). Part of the infrared emission also stems from non-thermal processes, namely synchrotron emission, originating from the same seed population of electrons that produces the radio emission in the compact core and jets of AGN. Infrared emission can be, partially, used as a tracer for the thermal emission of the AGN host galaxy. High resolution infrared observations can potentially resolve the AGN host and reveal any peculiar morphological features, signs of tidal interactions.

Optical Emission - The optical and UV continuum observed in AGN originate from the inner part of the galaxy, mostly from the accretion disk and its photosphere, and partly from the jet. The emission is predominantly thermal (as implied by the observation of the big blue bump, Krolik 1999) and, under certain assumptions, the radiation resembles that of a black body, affected however by different absorption mechanisms. The non-thermal jet component can however dominate the total emission due to beaming effects. As in the infrared, any morphological disruptions can also be seen in the optical.

### 2.4.2 AGN signatures

Variability - Although variability can be induced by a number of different effects, almost periodical, multi-wavelength variations in the lightcurves of objects point towards a periodical modulation in the nucleus of the system, although a wavelength dependence also exists (i.e., variability at different wavelengths might arise in different places). Assuming that a hard BBH system is possibly the origin of such variations, I use multi-wavelength variability as a tracer for hard BBH systems and thus late-merger (or merger-remnant) systems.

Radio Emission - Radio emission originates mostly in the compact core and jet of the active galaxy. It is produced by relativistic electrons, gyrating in a magnetic field, through synchrotron radiation. Radio properties of a source provide direct information about the properties of the AGN (e.g., compactness, brightness temperature, etc.). The radio luminosity of an active galaxy can be used as a measure for its non-thermal, AGN, component.

A more detailed discussion of the above can be found later on in Sect. 2.9.

## 2.5 Multi-wavelength properties of the CJF sample

In this section I present multi-wavelength information for the CJF sources gathered from an extensive search in the available literature. I focus on the radio, infrared, and optical parts of the spectrum. Please note that complete information are available for the CJF in both the radio and X-ray wavelength regimes.



### 2.5.1 Radio emission

The CJF is a flux limited radio-selected sample of flat-spectrum radio-loud AGN (see Sect. 1.6). Although originally created to study, among other topics, the kinematics of pc-scale jets and superluminal motion, the CJF represents an ideal sample for an unbiased study of the evolution of active galaxies. Unlike previously used samples in the same context, the fact that the CJF is radio-selected allows us to exclude biases towards transitory systems (as is the case for infrared selected samples).

As described in Sect. 1.6 the CJF sample has been predominantly observed in the radio regime. In particular all CJF sources have single-dish observations at 1.5, 5, and 30 GHz (Kuehr et al. 1981; Gregory and Condon 1991; Taylor et al. 1996; White et al. 1999; Lowe et al. 2007). Similarly, 83.6% and 62.8% of the sources have been observed with the Very Long Array (VLA) at 5 and 1.5 GHz respectively. Finally, all sources have been observed with either the global VLBI or VLBA array for at least 3 epochs (Britzen et al. 2007b).

Although the CJF sample consists mostly of blazars, presumably highly beamed sources, the kinematical study of the sample shows a large number of sources having stationary, subluminal, or, at best, mildly superluminal outward velocities (e.g., see Fig. 15 in Britzen et al. 2008). Combined with a number of sources exhibiting inward moving components (e.g., 0600+422, 1751+441, 1543+517, Britzen et al. 2007b), these sources do not fit into the regular paradigm of outward, superluminally moving components in blazar jets. One possible explanation for such peculiar kinematic behaviors can be a precessing, or helical, jet (e.g., Conway and Murphy 1993) as a result of a BBH system (see Sect. 3.7 for a detailed discussion). Other explanations include standing or recollimation shocks, as well as trailing shocks induced by a primary perturbation propagating down the jet (e.g., Agudo et al. 2001).

#### Variability

As an observational tool, variability of an AGN can relate information about both the structure and the evolution of a source. I should note that a stringent definition of periodicity requires a repetition of a behavioral pattern with a constant step, the period of the phenomenon (i.e.,  $f(t+T) = f(t)$ , where  $T$  is the period in this case). In order to convey a stable period from astronomical data, it is required that several periods of a phenomenon are observed. Additionally, the sampling of the observations, as well as potential gaps in the data, can introduce spurious effects or affect the calculated period. Most of the astronomical objects observed, especially given the limitations of the instruments, can not be called periodic in an absolute sense. A more appropriate definition would be that of quasi-periodicity, (i.e.,  $f(t+T) = \exp(\alpha t + \beta)f(t)$ ), or almost periodicity (i.e., a function of a real number that is periodic to within any desired accuracy, given suitably long "almost-periods"). For the sake of simpleness of writing, from now on I will use the term periodic or periodicity more loosely, reflecting mainly the meaning of almost-periodicity.

Fan et al. (2007), using the power spectral analysis method, study the lightcurves of a large number of AGN in three different frequencies (4.8, 8.0, and 14.5 GHz), showing that there are different periodicities in them. There are 19 CJF sources included in the Fan et al. sample (see Table A.6) with periodical behavior in their radio lightcurves. There are 7 further sources reported exhibiting periodical variability in their radio lightcurves,

as found in the literature (in total 26 sources, 8.9% of the sample; Table A.6 and A.7 for references). Intra-day variability is not considered here (see Sect. 2.9 for a discussion on why variability in such short scales is assumed to be not relevant to this study).

### 2.5.2 Infrared emission

One should here make the distinction between the near (1.25-2.20  $\mu\text{m}$ ), mid (5-25  $\mu\text{m}$ ), and far-infrared (25-100  $\mu\text{m}$ ). When observing the near-IR, one sees thermal emission from dust in the source. The far-IR emission from galaxies is dominated by the light of stars, therefore giving a measure for the star-formation rate (the ratio of far-IR colors is usually used). One should also not forget the additional non-thermal component of IR emission produced from the active core through the synchrotron mechanism. CJF sources have been mostly observed in the near-IR, with only a few of them having mid- or far-IR information. This presents a limitation to the extent to which I can investigate the thermal component from the host galaxies of the sources.

Given the ongoing discussion concerning the evolutionary connection between ULIRGs and AGN, with ULIRGs being the predecessors of active galaxies as a result of a merger, I search for ULIRGs in the CJF sample. I find one source in the CJF sample classified as an ULIRG (Mrk 231, Cao et al. 2008; Kim et al. 2002). There are 101 sources (34.5% of the sample; Table A.1) that have been observed and detected (it should be noted that the data presented here are not statistically complete) in the near to far infrared by the Infrared Astronomical Satellite (IRAS, Clegg 1980) and the 2 Micron All Sky Survey (2MASS, Kleinmann 1992), as well as other earth-bound telescopes.

Only a few blazars have extensive light curves in the infrared. I find 12 sources (4.1% of the sample) showing infrared variability (Table A.6).

### 2.5.3 Optical emission

Almost all CJF sources (285 sources, 97.3% of the sample) have been detected in the optical (see Table 1 in Britzen et al. 2007a for magnitudes and redshifts).

I find 16 sources (5.5% of the sample, 11 radio galaxies, 4 BL Lac objects, and 1 quasar) exhibiting distortions in the optical and infrared (see Table A.5). I find 14 sources (4.8% of the sample, 9 RG, 3 BL, and 2 Q) having one or more close companions (Table A.5).

I also investigate the CJF sample for the number of sources that belong to a cluster or a group of galaxies. Due to the large redshift span of the CJF, it is not possible to have cluster information for sources at high  $z$  ( $z > 1.5$ , e.g., Blakeslee et al. 2003; Brodwin et al. 2008). I find 54 sources (18.4% of the sample) belonging to a cluster or group of galaxies (see Table A.3). From these, 5 are BL Lac objects (1.7% of the sample), 14 are radio galaxies (4.8%), and 35 are quasars (11.9%). These percentages are biased by the fact that high- $z$  quasars dominate the CJF. For  $z < 1$  I calculate that 25.0% of the QSOs ( $z_{\text{avg}} = 0.60$ ), 33.3% of the radio galaxies ( $z_{\text{avg}} = 0.27$ ), and 29.4% of the BL Lac objects ( $z_{\text{avg}} = 0.25$ ) are found in clusters. Radio galaxies are more often members of clusters. Hill and Lilly (1991) find a similar trend in their redshift range (e.g. see Fig. 11 of Hill and Lilly 1991).

Twenty-two sources (7.5% of the sample) show variable fluxes in the optical (intra-day variability has not been taken into account). Some of these sources have extensive enough lightcurves to calculate the timescales of this variability (see Table A.6).

## 2.6 Analysis and Results

### 2.6.1 Mergers in the CJF

Assuming that activity in galaxies is indeed triggered by mergers, it is expected to observe morphological distortions in the optical or infrared maps of the CJF sources. If such structures are observed, the system must have recently (100-200 Myr, Lotz et al. 2008) undergone a merger, with typical merger lifetimes being of the order of a few billion years. Lotz et al. (2008), through simulations, find that the peak in the morphological disturbances of the merging system happens just after the first pass of the two galaxies and after the actual merging of the nuclei of the merging galaxies. In between the system does not exhibit any quantitatively appreciable asymmetry. Merger-induced star formation can be used as evidence for merging systems in such an intermediate phase.

I find 16 sources (5.5% of the sample, 11 radio galaxies, 4 BL Lac objects, and 1 quasar) exhibiting distortions in the optical and infrared (see Table A.5). I find 14 sources (4.8% of the sample, 9 RG, 3 BL, and 2 Q) having one or more close companions (Table A.5). The percentage of distorted and, or, sources with companions is in good agreement with Hutchings and Campbell (1983) and Surace (1998) who find that, for  $z < 0.4$ , a 30% of quasars show such properties (28.6% of the CJF). **This underlines the ubiquity of such morphologically distorted systems and the relevance of mergers to AGN.** The angle to the line of sight assumed for radio galaxies (Urry and Padovani 1995) allows the investigation of the host galaxy, unlike in the case of BL Lacs and quasars, where the jet dominates the emission. This could explain the higher percentage of radio galaxies in the distorted sources. Their lower average redshift, compared to the quasar sample, additionally contributes to the above effect. Finally, with lower nuclear luminosity, radio galaxy cores do not outshine their host galaxies, thus facilitating such morphological studies. As previously stated, the percentages described here can only constitute lower limits, as not all sources have been observed in the optical and/or infrared, while many of them remain unresolved due to their high redshifts.

Given the small number of CJF sources observed in the far-IR, information on the star-formation rates of these objects is scarce. Nevertheless, I find four sources showing signs of starburst activity (0316+413, Richer et al. 1993; 1254+571, Richards et al. 2005; 1652+398, 1807+698, Condon et al. 2002) and one more possible candidate (0248+430, Dudik et al. 2005).

Finally, given that one ULIRG (Mrk 231) is found, one can infer a percentage for the content of ULIRGs in the CJF sample. Counting only the IR detected sources, 1.0% of the sample is found exhibiting very high luminosities in the far-IR ( $> 10^{12} L_{sol}$ ). It should be stressed that this number is a lower limit, given that not all CJF sources have been observed in the far-IR or are observable at their respective redshifts.

## 2.6.2 Luminosity Correlations

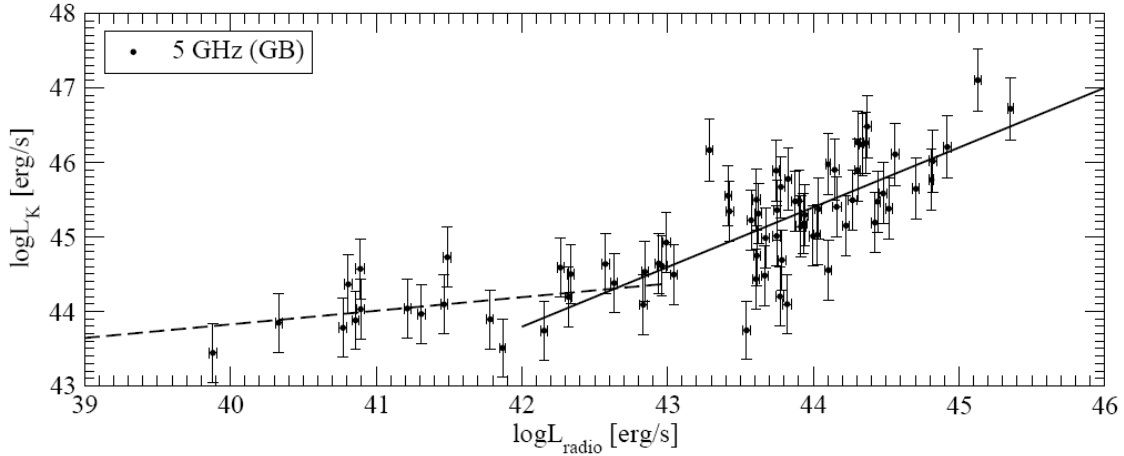


Figure 2.3: Luminosities in the near-infrared as a function of the radio luminosity at 5 GHz, from single dish observations with the Green Bank radio telescope (data from [Gregory and Condon 1991](#)).

In Fig. 2.3 I plot the near-infrared (K band) luminosity against the K-corrected radio luminosity obtained by single dish observations at 5 GHz for 76 CJF sources with available information.

The infrared luminosity of a source probes the stellar light of the active galaxies, as well as radiation from the dust and gas component of the sources. I am interested in the relation of this thermal component to the non-thermal one, as expressed by the radio luminosity of the AGN. I find a "broken" correlation between these two quantities. The lower luminosity sources appear to have a near constant NIR luminosity independent of the radio core luminosity. A standard linear regression gives a slope of  $0.18 \pm 0.12$  with a correlation coefficient of 0.35. For higher luminosities a linear dependence is seen. A slope of  $0.80 \pm 0.11$  with a correlation coefficient of 0.79 is given by standard linear regression. Following [Browne and Murphy \(1987\)](#) I additionally examine the correlation of the ratio  $L_{radio}/L_{NIR}$  to  $L_{radio}$  and to  $z$ . I find a stronger correlation to  $L_{radio}$  luminosity, with a correlation coefficient of 0.788, as opposed to  $z$  (correlation coefficient 0.498). This leads us to believe that the correlation is not an artifact of luminosity evolution. The large scatter of the data in Fig. 2.3 is expected, given the highly variable nature of active galaxies and the fact that the radio and infrared observations are not contemporaneous.

[Rieke \(1978\)](#) first confirmed a correlation between NIR and radio continuum for a sample of Seyfert galaxies. This indicates that the infrared output of Seyfert galaxies is dominated by reradiation by dust in the host galaxy. In this context, I find higher luminosity sources to be dominated by their AGN component (as traced by the radio luminosity). In contrast, lower luminosity sources exhibit an excess NIR luminosity (considering the anticipated luminosity implied by the linear dependency seen for higher luminosity sources). This points towards a significant infrared output from star formation regions that dominates over nuclear infrared emission. Therefore, higher redshift detected (effectively, higher luminosity) sources are less likely to be found in a transitional evolutionary stage,

since their spectrum is exclusively dominated by their nucleus, effectively outshining and hiding any effects of an ongoing merger. Moreover, it appears that a considerable thermal component exists in active galaxies, although becoming observable for lower luminosity ones.

### 2.6.3 AGN near-IR colors

In the same context as above, I am interested in investigating the interplay between the star-formation and nuclear component in the sources of the CJF sample. For this reason, I calculate the near-infrared colors of the sources with available data, after correcting all magnitudes (HJK bands) for galactic extinction (from [Schlegel et al. 1998](#)). From these I construct the near-IR color-color diagram seen in Fig. 2.4. The lines for a black body and a power-law emitting body divide the color-color parameter space in three regions. Sources situated above the black body line are predominantly thermal emitters. Sources beneath the power-law line are dominated by non-thermal emitting mechanisms. For sources between the two lines both components are important.

In Fig. 2.4 I have separated blazars from radio galaxies given the different nature of these objects. It is anticipated that radio galaxies are dominated by emission originating in their host galaxies. Indeed 8 out of the 11 radio galaxies depicted in Fig. 2.4 are situated above the black body line. Radio galaxies appear significantly redder in both J-H and H-K colors with  $(J - H)_{avg, RG} = 2.2 \pm 1.1$  and  $(H - K)_{avg, RG} = 1.8 \pm 1.1$ . With the exception of nine sources, the rest of the blazars are situated beneath that same line, with most of them situated around and beneath the power-law line.

I am particularly interested in the sources found in the space between the two lines, hence showing transitory properties from a thermal emission dominated state to a non-thermal dominated one. Indeed blazars in this transition area, with an average H-K color of  $(H - K)_{avg} = 0.814 \pm 0.027$ , are considerably redder than their equivalents found above the black-body line ( $(H - K)_{avg} = 0.19 \pm 0.05$ ), sign of an excess of dust leading to the observed reddening.

In the previous section I have inferred on the possible connection between multi-wavelength variability, binary black holes, and hence post-merger or merger-remnant systems. This connection is tested using the near-IR color properties of the CJF sources. I divide the sources in three groups, as defined by the two lines seen in Fig. 2.4. I find that 42.9% of the sources situated between the black body and power-law lines, sources assumed in a transition from a merger (a system that is dominated by its thermal emission) to an active galaxy (a system that is dominated by its non-thermal emission), are variable in different wavelengths. Only 11.1% and 10.5% of the sources above the black body line and below the power law line respectively show variability.

## 2.7 Tracing the evolution in the CJF

One aim of this work is to study the possible evolutionary stages of the AGN in the CJF sample. Different sub-samples of the CJF, and individual sources within them, can probe these different evolutionary stages. Mergers, starburst activity, and BBH systems are integral parts of such a study.

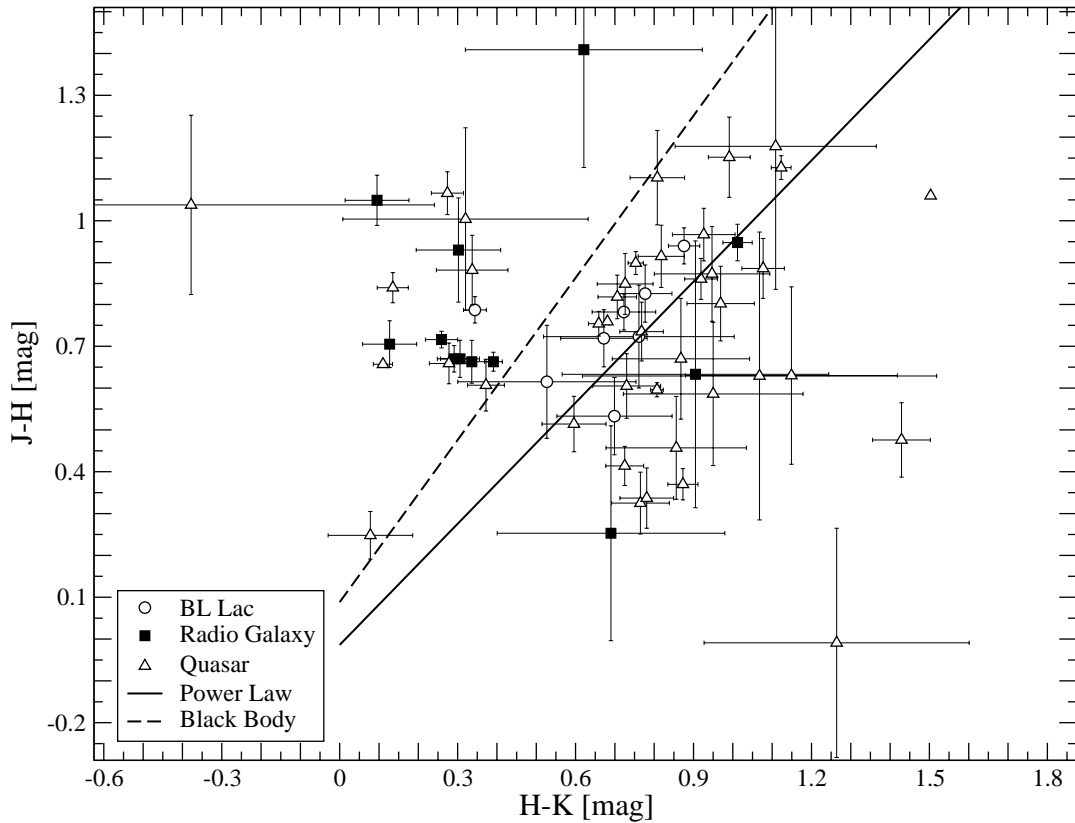


Figure 2.4: Near-infrared color-color diagram for all CJK sources with available information. The lines for a power-law emitting body (continuous line) and for a black body (dashed line) are plotted. Blazars are denoted with open symbols (circles for BL Lac objects and triangles for the quasars) and radio galaxies with filled ones (see text for details).

One of the most prominent examples supporting the link between starburst and BBH systems is NGC 6240, one of the few sources that have directly been observed to have a binary core (Komossa et al. 2003). This system is an ULIRG, hosts two AGN, and also presents strong evidence for ongoing starburst activity, making it an archetype of the evolutionary scenario discussed here.

By selecting the sources that show a companion, one can investigate the earliest stages of a merging process. Accordingly, by selecting the sources with disturbed morphologies and large infrared fluxes, an intermediate phase (e.g., Mrk 231) is probed. Finally, sources with relaxed morphologies but with almost periodical variability in multiple wavelengths present good candidates for systems where an assumed BBH has sunk into the center of the system.

Lotz et al. (2008) conducted simulations of equal-mass gas-rich mergers, classifying the sources in six distinct merging phases: pre-merger, first pass, maximal separation, merger, post-merger, and remnant (see Fig. 2.5). Using this classification scheme for the CJK sources, objects are classified in pre and post-merger stages.

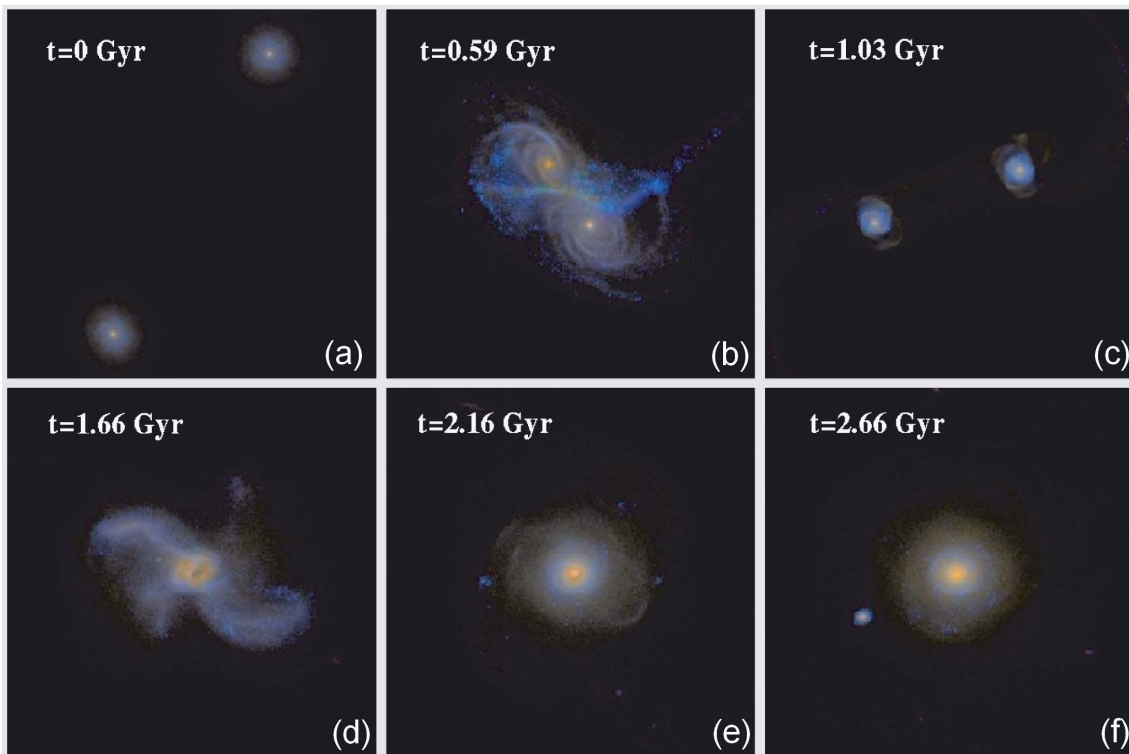


Figure 2.5: Composite color images (in u, r, and z SDSS photometric bands) with dust extinction for the high-resolution prograde-prograde merger of equal mass, gas rich mergers, as viewed face-on (for details see [Lotz et al. 2008](#)). In the upper-left corner of each image the time passed since the onset of the simulation is shown. In a sequence from (a) to (f) the initial pre-merger galaxies, the first pass, the maximal separation after the first pass, the merger of the nuclei, the post-merger at 0.5 Gyr after the merger ( $t=2.16$  Gyr), and the remnant at 1 Gyr after the merger are shown ( $t=2.66$  Gyr). The field of view for the initial galaxies and the maximal separation is 200 kpc, while the field of view for the other images is 100 kpc. The merger morphologies are most disturbed at the first pass and merger. Star-forming regions in the initial discs, tidal tails and outer regions of the remnant appear blue, while the dust-enshrouded star-forming nuclei appear red. Figure and caption reproduced from [Lotz et al. \(2008\)](#).

The incompleteness of the information available for the CJF sample does not allow to make unambiguous claims for the classification of some sources (especially when differentiating between, for example, pre-merger and maximal separation, or post-merger and remnant classes). Of the distorted sources, those with companions can be classified either in the pre-merger or in the maximal separation phase, while those with no companions can be categorized as either in the first pass or in the post-merger phase. This translates, for the latter group, roughly to an age of 2-4 Gyr after the initial approach of the progenitor systems. Exception to the above constitute four sources (3C 84, Mrk 231, 3C 371, and Mrk 501) that exhibit both distorted morphologies and considerable starburst activity (e.g., [Richards et al. 2005](#); [Condon et al. 2002](#)). These characteristics put them in the merger phase and would constrain their age to  $< 2$  Gyr after the initial approach.

Table 2.1: CJF sources categorized in different evolutionary phases of AGN (following Lotz et al. 2008, for details see text). Columns (1)-(4) give the source IAU name, other name, type (BL=BL Lac, Q= Quasar, G= Radio Galaxy), and redshift respectively, Col. (5) gives information on the presence of companions, Col. (6) gives morphology information, Col. (7) gives the number of wavelength regimes the source has been observed and detected as variable, and Col. (8) gives information on the presence of starburst activity. For references see previous tables.

Source [1]	Other Name [2]	Type [3]	z [4]	Companion [5]	Morphology [6]	Variability [7]	Starburst [8]
<b>Pre - merger</b>							
0954+658		BL	0.368	yes	-	2	-
2021+614	OW 637	Q	0.227	yes	-	-	-
2352+495	OZ 488	G	0.237	yes	-	-	-
<b>First Pass</b>							
0018+729		G	0.821	-	disturbed	-	-
0108+388	OC 314	G	0.669	-	disturbed	-	-
0804+499	OJ508	Q	1.432	-	tidal tail	1	-
1146+596	NGC3894	G	0.011	-	interacting	-	-
<b>Max Separation</b>							
0402+379	4C 37.11	G	0.055	yes	interacting	1	-
0710+439	OI+417	G	0.518	yes	disturbed	-	-
0831+557	4C +55.16	G	0.240	yes	disturbed	-	-
1031+567		G	0.460	yes	disturbed	-	-
1823+568	4C 56.27	BL	0.664	yes	non-relaxed isophotes	-	-
1843+356		G	0.764	yes	disturbed	-	-



Table 2.1 – Continued

Source [1]	Other Name [2]	Type [3]	z [4]	Companion [5]	Morphology [6]	Variability [7]	Starburst [8]
1946+708		G	0.101	yes	non-relaxed isophotes	-	-
<b>Merger</b>							
0248+430		Q	1.310	-	-	-	possible
0316+413	3C 84	G	0.018	yes	twisted isophotes	3	yes
1254+571	Mrk 231	Q	0.042	yes	disturbed	3	yes
1652+398	Mrk 501	BL	0.034	-	extra nuclear component	5	yes
1807+698	3C 371.0	BL	0.051	yes	interacting	2	yes
<b>BBH/ Post-merger</b>							
0219+428	3C066A	BL	0.444	-	-	3	-
0716+714		BL		-	-	5	-
0814+425	OJ425	BL	0.245	-	-	3	-
0923+392	4C 39.25	Q	0.699	-	-	3	-
1101+384	Mrk 421	BL	0.031	-	-	5	-
1418+546	OQ530	BL	0.151	-	extra nuclear component	3	-
1633+382	4C 38.41	Q	1.807	-	-	3	-
1641+399	3C345	Q	0.595	yes	-	4	-
2200+420	BL Lac	BL	0.069	-	-	4	-

In Table 2.1 the 28 best candidates for different evolutionary phases are given (following Lotz et al. 2008). Sources with companions, but no sign of disturbed morphologies, are selected as pre-merger systems. Sources with disturbed morphologies, but no companions and no apparent starburst activity, are assigned to the first pass phase, when the two systems are at a minimum separation for the first time. The next phase is described by the maximal separation between the merging systems. For this phase, sources with disturbed morphologies and detected companions are selected. Sources identified as undergoing the first pass could also be merger remnants. More information is needed to make such a distinction.

In the context of BBH systems, the last two categories shown in Table 2.1 are the most interesting ones, as it is expected that the SMBHs at the centers of the merging systems are close enough for the gravitational pull to bind them together. For the merger phase, I select sources that have disturbed morphologies and also show signs of ongoing starburst activity (similar to Mrk 231). For the final category sources are selected that appear extremely variable across their spectrum (variable in at least 3 different wavelength regimes), in an almost periodical manner. These sources do not show signs of ongoing interaction, merging (apart from 1418+546, see *Individual Sources*), or starburst activity. These are likely candidates for BBH systems. In the context of the above categorization, these sources can be identified as possible post-merger systems.

At least three of the sources in Table 2.1 (0954+658; 0108+388; 0248+430) can not be unambiguously categorized in one evolutionary phase, as they exhibit properties common to more than one stages of evolution as they have been presented here. Sources selected in the last two categories (merger and post-merger) are the best BBH candidates in the CJF sample. I plot their NIR colors in Fig. 2.6. As expected, most candidate sources are found above the power law line, while most post-merger classified sources (selected solely by their variability properties) are found just above the power law line, in the transitory area of the color-color diagram. This provides us with a further selection tool for transitory systems (see *Individual sources*).

### 2.7.1 Notes on individual sources

Here I present additional information on individual sources from the sub-sample in Table 2.1. For references see the respective tables.

#### Pre-merger:

As pre-merger sources I classify those systems that have a companion but do not exhibit distorted morphologies:

**0954+658** - (BL Lac,  $z = 0.368$ ) Besides its companion (projected separation 474 kpc), this source exhibits periodicity in the optical and variability in the  $\gamma$ -rays. It shows a bent jet both on VLA and VLBA scales. This is a misaligned source. The nature of this object is ambiguous, as it could also be classified in the post-merger phase.

**2021+614 (OW 637)** - (quasar,  $z = 0.227$ ) Has a companion at a projected distance of 36 kpc. Its VLBA jet exhibits peculiar morphology, while its VLA jet is unresolved.

**2352+495 (OZ 488)** - (radio galaxy,  $z = 0.237$ ) Has a companion at a separation of 47 kpc. Its VLBA jet is bent, and the VLA jet is unresolved.

First Pass:

As first pass sources I classify those systems that exhibit distorted morphologies without a visible companion and no signs of ongoing starburst activity:

**0018+729** - (radio galaxy,  $z = 0.821$ ) This object appears distorted in the optical. On VLA scales there is no jet resolved, while on VLBA scales the jet appears bent.

**0108+388 (OC 314)** - (radio galaxy,  $z = 0.669$ ) Source with disturbed morphology in the optical. Exhibits a straight jet both in VLBA and VLA scales.

**0804+499 (OJ 508)** - (quasar,  $z = 1.432$ ) Distorted morphology in the NIR. This source is variable in the radio. Exhibits bent VLBA jet and diffuse emission on VLA scales.

**1146+596 (NGC 3894)** - (LINER,  $z = 0.011$ ) Disturbed morphology in the optical. This source is positioned in the thermal regime on the NIR color-color diagram (see Fig. 2.6), confirming its transitional phase. The above indicates that the system has possibly undergone, or is undergoing, a merger. The radio jet appears straight. The VLA jet is unresolved.

Max Separation:

In this phase, I classify sources that show distorted morphologies along with the existence of a companion, but no ongoing starburst activity. Distinguishing between pre-merger, first-pass, and max separation phases can be ambiguous:

**0402+379 (4C 37.11)** - (radio galaxy,  $z = 0.055$ ) This object is both disturbed (in the optical) and has a close companion galaxy (projected distance 29 kpc). Its VLBI jet is bent. Diffuse radio emission is seen on VLA scales. Variable in the radio. It is positioned in the thermal regime of the color-color plot. This object can also be classified as a transitory object between the max separation and merger phase.

**0710+439 (OI 417)** - (Seyfert,  $z = 0.518$ ) Disturbed optical morphology source with companion (projected distance 53 kpc). Bent VLBA jet.

**0831+557 (4C 55.16)** - (LINER,  $z = 0.24$ ) Possibly optically disturbed source with a companion (at a separation of 81 kpc). On VLBA scales the jet appears bent, while on VLA scales the jet and counter-jet appear misaligned.

**1031+567** - (Seyfert 2,  $z = 0.46$ ) Disturbed morphology in the NIR. A companion has been found in the optical (projected separation of 65 kpc). Shows straight VLBA jets. Unresolved VLA jet.

**1823+568 (4C 56.27)** - (BL Lac,  $z = 0.664$ ) Source exhibiting non-relaxed isophotes in the NIR, indirect sign of past merger activity. A possible close companion is also observed (projected distance of 46 kpc, no redshift information). The source is variable in the radio and has been claimed to show almost periodicity. On VLBA scales the jet appears fairly straight, while on VLA scales the jet appears to be misaligned to the inner jet.

**1843+356** - (radio galaxy,  $z = 0.764$ ) Disturbed morphology source (optical) with companion (projected distance 129 kpc). Straight VLBA jet, unresolved on VLA scales.

**1946+708** - (radio galaxy,  $z = 0.101$ ) This object appears to be disturbed in the optical. A possible companion galaxy (no redshift information available) is also observed at a projected distance of  $\sim 67$  kpc and thus I classify it as a max separation object. Its VLBA jet is highly bent. It is positioned in the non-thermal regime of the NIR color-color diagram. This can be due to a misclassification. The source being a merger remnant is the most plausible alternative.

Merger:

In the merger phase, I classify sources that exhibit distorted morphologies and also ongoing starburst activity:

**0248+430** - (quasar,  $z = 1.31$ ) This source exhibits signs of starburst activity (e.g., [Dudik et al. 2005](#)), while at the same time it is very luminous both in the optical and the X-rays.

At a redshift  $z = 1.31$  the source is not optically resolved.

**0316+413 (3C 84)** - (radio galaxy,  $z = 0.018$ ) Disturbed morphology source (optical) with companion (projected distance 600 kpc). This source is positioned in the thermal region of the color-color plot and shows ongoing starburst activity. Both the VLBA and VLA jet of this source appear bent. This is a primary candidate for a merging system. It is periodically variable in the radio, optical, and X-rays.

**1254+571 (Mrk 231)** - (quasar,  $z = 0.042$ ) This object is an ULIRG and is positioned in the transitory region of the color-color diagram. It exhibits starburst activity (see Sect. 2.9 for more details). There is no jet resolved in either VLBA or VLA scales. Mrk 231 fits well into the evolutionary scenario proposed by [Sanders et al. \(1988\)](#) occupying a transitory phase between a merging system and an active galaxy. Combined with its variability (radio, optical, and X-rays), it can be argued that this is a late merger object, moving to the post-merger phase.

**1652+398 (Mrk 501)** - (BL Lac,  $z = 0.034$ ) This source is almost periodically variable in all wavelengths checked. It exhibits a disturbed morphology (optical) and is positioned in the thermal region of the color-color diagram. This system appears to be undergoing a series of mergers, supported by the fact that it is a member of a cluster. Its VLBI jet is bent, with diffuse emission on VLA scales.

**1807+698 (3C 371)** - (BL Lac,  $z = 0.051$ ) Optically disturbed source with a companion (projected separation 81 kpc). It is almost periodical in the optical. Variable in the infrared. The VLBA jet of this object appears straight. The VLA jet however appears bent and diffuse emission is present.

### BBH / Post-merger Candidates:

Here I select sources that exhibit variability in at least three wavelength regimes (almost periodical in at least one wavelength). Correlated variabilities are one of the strongest evidence for the existence of a BBH. Such systems could possibly be also identified as post-merger systems, as it would be anticipated in such systems the existence of a hard BBH system in their nuclei:

**0219+428 (3C 66A)** - (BL Lac,  $z = 0.444$ ) This object is positioned in the transitory region of the color-color diagram, thus is classified as an early post-merger system. Both the VLBI and VLA jet appear straight (with the VLBA jet exhibiting one sharp bend). Almost periodical variability in the optical, variability in radio and X-rays.

**0716+714** - (BL Lac, unknown  $z$ ) This source is variable in all wavelength regimes observed, with correlated variability on longer timescales in the radio and the optical. It is a misaligned source with a bent jet both at VLBA and VLA scales.

**0814+425 (OJ 425)** - (BL Lac,  $z = 0.245$ ) Almost periodical variability in the radio and optical. Variable in the infrared. This system is positioned in the transitory region of the color-color diagram. Its VLBA jet appears bent.

**0923+392 (4C 39.25)** - (quasar,  $z = 0.699$ ) This source exhibits variability in different wavelengths (almost periodicity in the radio). Its VLBI jet is bent. No jet is resolved at VLA scales. It is positioned in the non-thermal region of the color-color diagram.

**1101+384 (Mrk 421)** - (BL Lac,  $z = 0.031$ ) VLBA jet appears straight. The VLA jet

appears bent. It is almost periodically variable in the radio, optical, and X-rays. It is variable in the infrared.

**1418+546 (OQ 530)** - (BL Lac,  $z = 0.151$ ) This object has a disturbed morphology. The fact that it is positioned in the transitional region of the color-color diagram and that it exhibits periodicities in different wavelengths points more to a post-merger galaxy. Its VLBI jet does not exhibit bends. It shows almost periodical variability in the radio. It is also variable in the infrared and optical.

**1633+382 (4C 38.41)** - (quasar,  $z = 1.807$ ) Misaligned source with bent jet both on VLBA and VLA scales. Almost periodical in radio. Variable in optical and  $\gamma$ -rays.

**1641+399 (3C 345)** - (quasar,  $z = 0.595$ ) This source appears to have a close companion (at a projected separation of 47 kpc) and is also member of a cluster, implying the possibility of multiple mergers. This source has already been modeled for a BBH (Lobanov and Roland 2005). The bent jet agrees well with the presence of a BBH system. Almost periodical in radio, optical, and X-rays. Variable also in the infrared.

**2200+420 (BL Lac)** - (BL Lac,  $z = 0.069$ ) This system is positioned in the non-thermal regime of the color-color diagram and appears almost periodical in radio (Fan et al. 2007) and optical (Smith and Nair 1995; Hagen-Thorn et al. 1997; Fan et al. 1998). It is also variable in infrared (Takalo et al. 1992) and  $\gamma$ -rays (Fan et al. 2002).

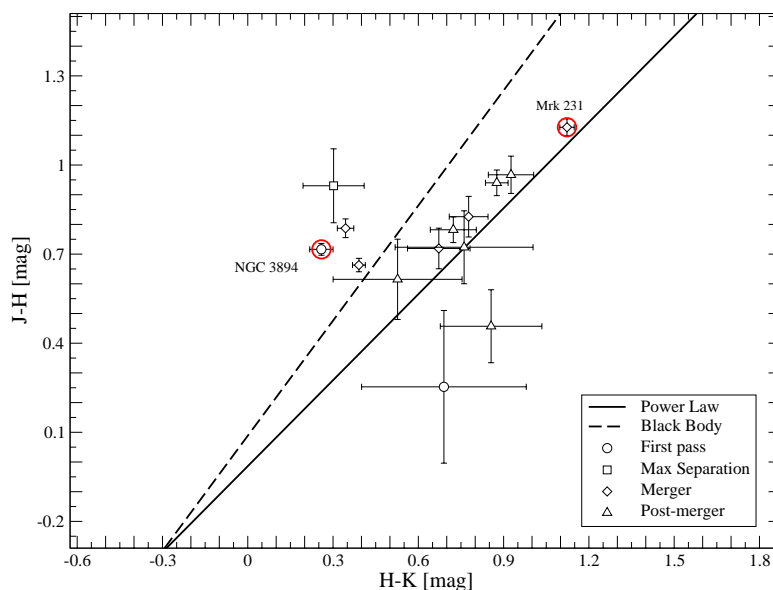


Figure 2.6: Near-infrared color-color diagram for the sources included in Table 2.1 with available information. The lines for a power-law emitting body (continuous line) and for a black body (dashed line) are plotted. Two objects are noted (Mrk 231, NGC 3894) of interest due to their transitional nature (see text for details).

## 2.8 Mrk 231: A Case Study of a late-merger

UGC 08058, also known as Mrk 231, is an active galaxy in the local Universe ( $z=0.042$ ). It has been classified as an ULIRG due to its extreme luminosity in the far-IR, as well as a broad line quasar (BLQ) and a type 1 Seyfert. The system shows signs of an ongoing interaction and merger (Canalizo and Stockton 2001; Petrosian et al. 2002; also see Fig. 2.9). The source shows strong starburst activity, also a sign of a system that has undergone a merger. Davies et al. (2004) study the nucleus of Mrk 231 using NIR high resolution spectroscopy. They uncover a young star-formation region ( $< 120 Myr$ ), accounting for up to 40% of the bolometric luminosity of this object, co-planar with a gas disk, result of the recent merger. The young age of the starburst component is in agreement with the simulations from Lotz et al. (2008). The authors find that the peak in star-formation occurs in the merger phase (also see Fig. 2.5 and Fig. 2.7), almost 2 Gyr after the initial approach. Assuming Mrk 231 is seen in a late merger (e.g., Murphy et al. 2001) or a post-merger phase (onset at  $\sim 2.2$  Gyr after initial approach), then this is consistent with the age derived for the star-formation region ( $\sim 10^{-1} Gyr$ ). The authors explain the quasar classification of the source as result of the superposition of a Seyfert 1 core and a strong starburst component. Richards et al. (2005) also study Mrk 231 in the radio, concluding the existence of a starburst component. Papadopoulos et al. (2007) also conduct IR spectroscopy revealing a dense molecular gas component, in which more than 50% of the molecular gas of the galaxy resides. The authors suggest this to be the fuel for the rigorous star-formation in Mrk 231. James et al. (1999) study the morphology of a sample of 11 merger systems, among which Mrk 231, finding that all galaxies resemble elliptical galaxies (from K-band photometry and central velocity dispersions), fitting well the assumption that elliptical galaxies are formed as the result of mergers.

The source has been studied in the X-ray (e.g., Imanishi and Ueno 1999; Franceschini et al. 2003), where it exhibits extended emission (e.g., Turner 1999; Ptak et al. 2003; Huo et al. 2004), in addition to a hard spectrum central source which remains unresolved and is off-center to the extended X-ray halo. An off-nuclear source has been detected in the X-rays in a distance of  $6''$  (Gallagher et al. 2002). Mrk 231 has been studied for variability in different wavelengths. It has been found to be variable in the X-ray (Gallagher et al. 2002), optical (in the absorption lines; Kollatschny et al. 1992), and radio (Ulvestad et al. 1999b).

Mrk 231 has been observed in three epochs (Sep 1992, Sep 1994, and Aug 1996) with the VLBA, in the frame of the CJF sample. The source remains unresolved for all three epochs (see Fig. 2.8, data from Britzen et al. 2008). Taylor et al. (1999) detect sub-kiloparsec structure with the VLBA and VLA that they interpret as a jet plus some diffuse emission attributed to a central starburst component. No jet-like structure is seen on VLA scales. Ulvestad et al. (1999b) and Ulvestad et al. (1999a) however find a pc-scale jet consisting of one component that moves at sub-luminal speeds. Carilli et al. (1998) present strong arguments for the existence of a sub-kpc molecular disk formed in Mrk 231 (also see Bryant and Scoville 1996; also see Fig. 2.9).

Mrk 231 provides a perfect example of an evolutionary transitory system between two distinct phases of evolution, that of a merger and an active galaxy. Indeed the above properties point to a young AGN (e.g., Lípari and Terlevich 2006), created by a recent merger that has formed a molecular disk fueling gas into the nucleus of the newly formed

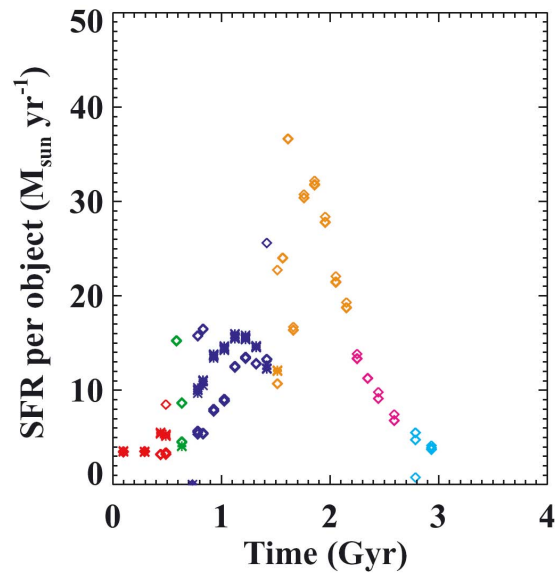


Figure 2.7: Time versus star-formation rate for the high-resolution prograde-prograde Sbc merger with stiff supernova feedback, including the effects of dust. Each merger state is marked with a different color (pre-merger: red, first pass: green, maximal separation: blue, final merger: orange, post-merger: magenta, remnant: cyan). Open diamonds are for the one merging galaxy and the merger remnant; crosses are for the other merging galaxy. The mergers show strong morphological disturbances and peaks in the star formation rate at the first pass (green points) and final merger (orange points). Figure and caption reproduced from [Lotz et al. \(2008\)](#).

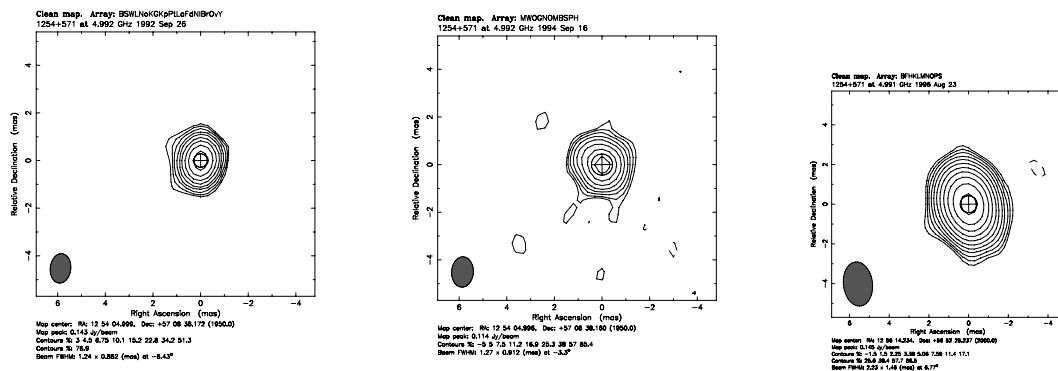


Figure 2.8: Three epochs of VLBI observations at 5 GHz of the object 1254+571, Mrk 231. Contour maps with maximum flux at 0.143 Jy/beam. Figures reproduced from [Britzen et al. \(2008\)](#).

active core and a young radio jet at VLBI scales, fitting well in the evolution scenario (see also, [Hickox et al. 2009](#)).

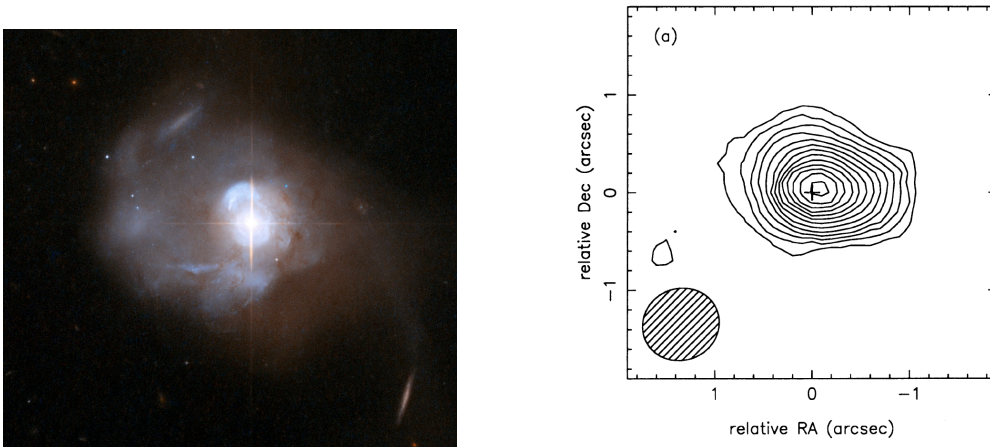


Figure 2.9: Left: Composite HST image of Mrk 231 using B and I filters, taken with ACS and WFC instruments. The disrupted morphology of the galaxy is apparent. Right: Velocity-integrated CO ( $2 \rightarrow 1$ ) emission of Mrk 231 from the Owen Valley millimeter array. The map reveals a resolved disk-like structure at scales of 1 arcsec ( $\sim 840$ pc). Map reproduced from [Bryant and Scoville \(1996\)](#).

## 2.9 Discussion

In the previous sections I have presented the accumulated literature information available for the CJF sources and have presented a sample of CJF sources that trace AGN evolution, along with the best BBH candidates. In this section I first qualitatively assess the completeness of the information presented in the previous sections and extrapolate the results to a sample with complete multi-wavelength data. I then investigate the criteria used as tags for identifying candidates for BBH systems. It is interesting to discuss which subset of these criteria can provide a robust enough argument for the existence of a BBH.

### 2.9.1 Anticipated AGN properties

I am interested in assessing the completeness of the information for the CJF sample presented here, as these were collected from the available literature and are not a result of a uniform observational campaign. To reach this goal, two sub-samples of CJF sources are formed. For the first one, I select sources with available NIR information, as this is the information primarily presented and analyzed in this chapter. I further exclude sources without redshift information. I find 74 sources fulfilling the above criteria, with the number of sources explicitly controlled by the availability of infrared information (see [Table A.1](#)). For the second sub-sample, those CJF sources are selected that have been observed and have available information across the whole spectrum (radio to  $\gamma$ -rays). Only 10 such sources are found, with the number of sources mainly regulated by availability of  $\gamma$ -ray information (see [Table 2.2](#)).



Table 2.2: The CJF source with available information across the electromagnetic spectrum (radio, near-infrared, optical, X-ray, and  $\gamma$ -ray).

Source	Other Name	Type	Redshift
0133+476	OC 457	HPQ	0.86
0219+428	3C066A	BL Lac	0.44
0316+413	3C 84	G	0.02
0650+453		Q	0.933
0814+425	OJ425	BL Lac	0.53
0836+710	4C 71.07	LPQ	2.18
1101+384	Mrk 421	BL Lac	0.03
1633+382	4C 38.41	LPQ	1.81
1652+398	Mrk 501	BL Lac	0.03
1803+784		BL Lac	0.68
2200+420	BL Lac	BL Lac	0.07

### Near-IR sub-sample

This sub-sample, having been selected on the basis of detection in the near-IR, is expected to be more sensitive to infrared bright sources and consequently presents a higher probability of containing sources associated to merger events. This bias should be accounted for. I start off by investigating if this sub-sample is fundamentally different compared to its parent sample, from which it was selected. The sub-sample has an average redshift of  $z_{avg,sub} = 0.864$ , effectively probing more near-by sources than the CJF ( $z_{avg,CJF} = 1.254$ ). I also check the radio spectral index  $\alpha_{1400}^{4800}$  as a measure of the compactness of the sources. The sub-sample has lower average and median values for the index compared to the whole sample. This indicates that this sub-sample contains less compact objects. Finally I check the range of luminosities where almost complete information for the CJF is available (in radio, optical, and X-ray) for both the sub-sample and the CJF as a whole. I find that in both samples the ranges are the same for all three wavelength regimes. I also apply a Kolmogorov - Smirnov (K-S) test for both the distribution of redshifts and radio spectral indices for the CJF sample and the NIR sub-sample. I find a probability of 0.3% and 0% that the two samples are drawn from the same parent sample. I conclude that this sub-sample likely contains sources that are closer and more extended, making it substantially different from the original sample.

For this sub-sample, 18.9% of the sources exhibit morphological distortions and starburst activity. 11 sources (14.9%) are found to have companions. Compared to the CJF sample in total (5.5% of sources with distortions; 4.8% with companions) merger effects appear to be more prominent in this sub-sample, as was expected. However, the more than three times higher percentage of distorted sources and sources with companions compared to the CJF as a whole indicates that the actual number of such sources might be higher than currently believed.

It is also interesting to check the variability properties of this sub-sample. 22.7% of the sources are variable in the radio, 13.3% in the infrared, 18.7% in the optical, 6.7% in the X-rays, and 12.0% in the  $\gamma$ -rays. For most of these sources and wavelength regimes

(with the exception of infrared and  $\gamma$ -rays) almost periodicities have been found in their lightcurves (see Tables A.6 and A.7 for timescales and references). Compared to the total CJF sample, these sources appear significantly more variable. This is an unexpected result, as nothing in the selection criteria and the properties of this sub-sample implies a bias towards more variable sources.

### Multi-wavelength sub-sample

This second sub-sample has been selected in order to assess how my results (concerning the importance and relevance of merging events and variability for active galaxies) is affected by the availability of multi-wavelength information (or lack thereof). Given the very small number of the sources included in this sub-sample, a statistical comparison to the whole sample is difficult. The K-S test for the redshift and spectral index distributions gives a probability of 3.3% and 97.6% respectively, that the two samples are drawn from the same parent sample. The average redshift of this sub-sample is  $z_{avg,sub} = 0.689$  and contains almost exclusively blazars (with the exception of 3C 84).

For this sub-sample, 17.6% of the sources (all of which at  $z < 0.05$ ) exhibit morphological distortions and starburst activity. One source (9.1%) is found to have companions. Compared to the CJF sample in total merger effects appear to be more prominent in this sub-sample. One must again take into account that the average redshift of the CJF sample is  $z_{avg,CJF} = 1.254$ , much higher than this sub-sample. However, the more than three times higher percentage of distorted sources compared to the CJF as a whole indicates that the actual number of such sources is higher than what was uncovered by the original analysis of the whole CJF sample. This illustrates the fact that the numbers uncovered from this investigation of the whole CJF sample are lower limits rather than absolute numbers.

I am also interested in the variability properties of this sub-sample. 81.8% of the sources are variable in the radio, 45.4% in the infrared, 72.7% in the optical, 27.3% in the X-rays, and 81.8% in the  $\gamma$ -rays (see Tables A.6 and A.7 for timescales and references). Compared to the total CJF sample, these sources appear highly variable, in an almost periodical manner. This can be explained as a bias effect, as sources that are highly variable in one waveband are more likely to be targeted for observations in other wavelengths. Alternatively, one can argue that (periodical) variability is an ubiquitous phenomenon for a large portion of active galaxies. The latter is supported further by the high percentages of variable sources seen also for the first sub-sample. Multi-wavelength variability, however, can only be revealed through extensive (and therefore time-costly) monitoring of a source, thus effectively reducing the number of known sources with such properties.

It is interesting to note that for both sub-samples I find rather high percentages for sources showing signs of past, present, or future merger events, as well as sources with variable fluxes at different wavelengths. Although the criteria used for the selection of these two sub-samples were different, the resulting percentage concerning merger signs are the same for both sub-samples, significantly larger than the percentage for the whole CJF. **This implies that due to the incompleteness of the available information (due to both lack of observations and instrumental limitations), the percentage of active galaxies linked to a merger event that was uncovered in the CJF sample reflects only a portion of the actual number. If the percentage calculated for the two sub-samples is closer to the true percentage, I expect approximately 50 CJF sources to have been**

**found taking part in a merger event and 31 sources having close companions.** From the available information I have found 15 and 11 sources respectively.

## 2.9.2 Periodicities in the lightcurves

Having concluded that this statistical analysis of the CJF can provide us only with lower limits for, e.g., the percentage of mergers in the CJF sample of active galaxies, I can now move on to the discussion of the criteria used to identify BBH systems.

Periodicities in the lightcurves can be linked to a periodical process in the center of an AGN, presumably a binary system with a quasi-stable orbit which produces periodical perturbations in the accretion disk and in the jet of the AGN (e.g., [Britzen et al. 2001](#); [Rieger 2004](#); [Lobanov and Roland 2005](#); [Qian et al. 2007](#); [Roland et al. 2008](#); [Britzen et al. 2010a](#)). However this is not the only possibility.

Precession of the jet has been employed to explain a variety of phenomena including the variability that AGN show in different wavelengths (e.g., [Caproni and Abraham 2004](#); [Roland et al. 1994](#)). An intrinsically helical jet can also exhibit the same morphological and kinematical results (for a study of the different kind of helicities in AGN jets see [Steffen 1997](#)). Helicity in AGN jets can be the result of internal Kelvin-Helmholtz (K-H) instabilities and in particular the  $m = 2$  helical mode of the K-H instabilities (for a 2-D treatment of the problem see e.g., [Baty et al. 2003](#); alternatively, [Perucho et al. 2006](#); [Meier and Nakamura 2006](#)).

Doppler beaming can also be the origin of the observed variability in the lightcurves of AGN. [Camenzind & Krockenberger \(1992\)](#) first described the, so called, lighthouse effect. This model has been successfully applied to different sources (e.g., 3C 273, [Camenzind and Krockenberger 1992](#); 3C 345, [Schramm et al. 1993](#)).

Different physical phenomena have different characteristic times describing them. BBH and precessing jets can describe periodicities of the order of  $\sim 10$  years (see references above), whereas lighthouse models tend to explain the intra-day variability, also observed in many blazars (for a review see [Wagner and Witzel 1995](#)). Intra-day variability can also be explained by interstellar scintillation (for a review see e.g., [Rickett 1990](#); also see [Melrose 1994](#)), although also BBH models have been recently invoked ([Roland et al. 2009](#)).

Correlated variability in different wavelengths implies that the same population of particles produces this variability, thus pointing to an intrinsic effect, rather than, for example, a turbulent screen between the observer and the observed source. One of the most prominent sources that shows correlated variability in different wavelengths is 0716+714 (radio and optical) ([Quirrenbach et al. 1991](#); [Wagner et al. 1996](#)). OJ287 is another famous example of such a source, with correlated variability in the radio, optical, and infrared (see e.g., [Fan and Lin 1999](#)). OJ287 is a prominent candidate for a BBH system ([Sillanpaa et al. 1988](#); [Lehto and Valtonen 1996](#); [Pietilä 1998](#); [Valtonen et al. 1999](#); [Liu and Wu 2002](#); [Valtonen 2007](#)).

I have categorized sources that exhibit almost periodic variabilities in their lightcurves as possible post-merger candidates (Table 2.1), assuming the existence of a BBH as the origin of variability in different wavelengths. Indeed, I find that variability is connected to transitory systems as they are defined on the near-IR color-color diagram. In Table A.6 I give the variability timescales where available. Four out of 9 post-merger classified

sources (0716+714, 1101+384, 1641+399, 220+420) show almost periodical variability with similar timescales (of the order of 10 years) in the radio and in the optical. These are candidates for hard BBH systems. More detailed investigations of their radio jet morphology can provide further information.

### 2.9.3 Infrared emission, merging scenarios, and starburst

The infrared emission from an AGN consists of different components, coming from different parts of the nucleus. Distinguishing and separating these constituents (accretion disk, thermal, and jet, non thermal) is not straightforward. Both components would be affected by a BBH system, since both would precess under the gravitational influence of the binary, although probably on different timescales.

In light of the evolutionary scenario, I investigate whether there is a connection between an excess in the infrared regime and sources with companions or sources that exhibit disrupted morphologies. For 16 sources with peculiar morphologies I calculate an average infrared (K band) luminosity  $\log(\nu L_\nu)_{NIR,avg} = 44.17 \pm 0.14$  erg/s for an average redshift of  $z_{avg} = 0.41$ . I also calculate the average luminosity in the NIR for the sources that are found to have companions  $\log(\nu L_\nu)_{NIR,avg} = 44.61 \pm 0.21$  erg/s, for 11 sources with a  $z_{avg} = 0.34$ . Defining a sub-sample of the CJF sources with similar average and median redshifts ( $z_{avg} = 0.38$ ) I find  $\log(\nu L_\nu)_{NIR,avg} = 44.5 \pm 0.1$  erg/s. Sources with disturbed morphologies exhibit below average near infrared luminosity, contrary to sources with companions which, on average and within errors, are equally luminous to the rest of the sample. The available data do not show a prominent near-IR excess for AGN with perturbed morphologies as would be expected. The lack of mid- and far-infrared data does not allow me to extend this over the whole infrared range.

I note 1146+596 as an object somewhat similar to Mrk 231. This low redshift ( $z=0.011$ ) radio galaxy appears to be extremely luminous in the near infrared (Skrutskie et al. 2006). It shows signs of ongoing interaction (Pustilnik et al. 2001), to which the infrared excess can be attributed. Moreover, Peck and Taylor (1998) detect redshifted H I gas in absorption, implying infall of gas towards the central engine.

In the above context, for the merger phase (in Table 2.1) I select sources that appear disturbed and also show signs of ongoing starburst activity (Mrk 231, 3C 84, Mrk 501, 3C 371). These are primary candidates for BBH that have not yet sunk into the center of the merging system (similar to NGC 6240). Most of these sources exhibit variability in different wavelengths. Three sources (0316+413, 1418+546, 1652+398) show almost periodical variability in the radio. 0316+413 and 1652+398 are additionally members of clusters and therefore are good candidates for multiple merger systems.

I note here the ambiguity of the classification of sources in the different pre-merger stages (Table 2.1). Starburst activity is the defining, although not unambiguous, property for identifying systems that are currently undergoing a merger, with the other evidence discussed above being weaker selection criteria.

### 2.9.4 Binary Black Holes in the CJF

There are 9 sources in the CJF sample that have been previously argued to be good BBH candidates. These sources are presented in Table 2.3 and Table 2.5, along with the relevant

references.

I compare the luminosities of these systems individually with the average luminosities in different wavelengths of a sub-sample of the CJF with similar median redshift. All 9 sources are found to be significantly more luminous in the X-ray. Two of these 9 sources (4C 37.11, BL Lac) are found to have above average K-band luminosity, possibly indicating a younger age for these sources. These two sources are less luminous in the X-rays than the rest 7 sources. According to [Sanders et al. \(1988\)](#), after a merger has taken place, the peak of the SED of the system is pushed towards higher frequencies, as the AGN blows away any obscuring material, remnant from the merging phase. This is a further indication that 4C 37.11 and BL Lac are indeed in an earlier evolutionary stage than the other BBH candidates.

Additionally, I note that all BBH candidates exhibit periodicities across the spectrum. I find that 7 out of the total of 9 sources have bent VLBA jets. Out of the sources in [Table 2.3](#), 6 sources belong to a cluster or have a companion, showing the higher probability of such sources to harbor a BBH system.

Returning to the original point, that is assessing the criteria used in this investigation, it is seen that different tools provide different insights. Given the selection criteria of the CJF sample (flat-spectrum sources), it is expected that hard BBH candidate systems are among the CJF sources. Indeed, the 9 already BBH candidate systems found in the CJF exhibit extreme variability across the spectrum and are very luminous in X-rays, in accordance to [Sanders et al. \(1988\)](#) predictions. For the current generation of telescopes however, resolving such systems is impossible. Instead, the only two examples of directly observed and resolved BBH systems are harbored in merger-remnant systems and therefore probably still unbound. A compromise is, as always, needed. Since unbound BBH systems do not allow us to dynamically model them (very large timescales are involved), variability studies are the most robust way to look for close (bound) BBH systems. Together with the radio jet morphology and kinematics, these two groups of indirect evidence can provide enough information to infer the presence of a BBH system. In this context, in the next chapter I am going to investigate the morphology and kinematics of the CJF jets.

Table 2.3: Kinematic and morphological information for CJF sources already considered to be BBH candidates. Columns (1)–(4) as in previous tables, Col. (5) shows the sources with X-ray detected jet, Col. (6) gives the misalignment angle between the pc and the kpc-scale jet of the source, Col. (7) gives the bending as calculated in Britzen et al. (2008) for the inner-most component identified in the jet, Col. (8) gives references related to the ambient of the source such as companion, and interaction with other systems, Col. (9) comments on the general kinematics of the pc-scale jet, Col. (10) gives the reference for possible precession models for the source, and Col. (11) gives the references in regard to possible BBH. For the references see Table 2.4.

Source	Other Names	Type	z	X-ray Jet	APA ( $^{\circ}$ )	Bending ( $^{\circ}$ )	Environment	Kinematics	Precession	BBH
[1]	[2]	[3]	[4]	[5]	[6]	[7]	[8]	[9]	[10]	[11]
0316+413	3C 84	G	0.018		20	51.9	53	inward <sup>101</sup>		108
0402+379	4C 37.11	G	0.055		27 / 12		54	stationary <sup>102</sup>		54, 102
0716+714		BL	0.300		75	2.6		stationary <sup>103</sup>	106	109
1101+384	Mrk 421	BL	0.031		13	1.9	44	slow <sup>104</sup>		110
1641+399	3C345	Q	0.595	knot	98	46.8	50, 63		107	111
1652+398	Mrk 501	BL	0.034		83	10.5	51, 61	stationary <sup>104</sup>	106	110
1803+784		BL	0.680		70	18.0	61	stationary <sup>105</sup>		112
1928+738	4C 73.18	Q	0.302	knot	22	23.4		stationary <sup>101</sup>	106	113
2200+420	BL Lac	BL	0.069		30	24.8	100			114

Table 2.4: References for Table 2.3.

Symbol	Reference	Symbol	Reference
100	Disney (1974)	108	Pronik (1988)
101	Britzen et al. (2007a)	109	Nesci et al. (2005)
102	Maness et al. (2004)	110	De Paolis et al. (2003)
103	Britzen et al. (2006)	111	Lobanov and Roland (2005)
104	Kellermann et al. (2003)	112	Roland et al. (2008)
105	Britzen et al. (2008)	113	Roos et al. (1993)
106	Lu and Zhou (2005)	114	Zier (2007)
107	Caproni and Abraham (2004)		

Table 2.5: Variability information and, if available, timescales concerning CJF sources already considered to be BBH candidates, Col. (4) in the radio, Col. (5) in the infrared, Col. (6) in the optical, Col. (7) in the X-rays, and Col. (8) in the  $\gamma$ -rays. Columns (1)-(3) as before. For references see previous tables.

Source	Type	$z$	$\text{Var}_{\text{Radio}}$ (yr)	$\text{Var}_{\text{IR}}$	$\text{Var}_{\text{Opt}}$ (yr)	$\text{Var}_x$ (days)	$\text{Var}_\gamma$ (days)
[1]	[2]	[3]	[4]	[5]	[6]	[7]	[8]
0316+413	G	0.018	9.7				
0402+379	G	0.055	yes				
0716+714	BL	0.300	5.4-15	yes	3.3		yes
1101+384	BL	0.031	3.7-8.0	yes	6.2	62	
1641+399	Q	0.595	5.1, 3.5-4	yes	5.6, 11.4, 10.1, 1.9		
1652+398	BL	0.034	6.8-12.3	yes	yes	23	23.2
1803+784	BL	0.680	7.0-11.3		0.003		
1928+738	Q	0.302	7.7-8.2		yes		
2200+420	BL	0.069	3.9-7.8	yes	7.8, 0.6, 0.88, 14, 7.7		

## 2.10 Conclusions

The focus of this work is twofold, investigating the evolutionary connection between active galaxies and merger events, as well as identifying AGN candidates at different evolutionary stages, including binary black hole system candidates. To this end, I collect and present multi-wavelength information of the CJF sources.

From the previous analysis it becomes apparent that mergers or merger induced effects (starburst activity) have an ubiquitous presence in active galaxies. **With almost 30% of the CJF sample showing evidence of interactions at  $z < 0.4$  and with indications that, although not yet observed, more such systems exist, mergers appear to play a predominant role in the evolution not only of galaxies but AGN as well. Please note here**

**the importance of the absence of any biases towards transitory systems in the selection criteria of the CJF sample. This supports a direct link between merger events and active galaxies in general. Furthermore, I show that multi-wavelength variability can be linked to transitory systems. Assuming that multi-wavelength variability originates in binary black hole systems, this provides a further link between merger events, binary black holes, and active galaxies, as well as a possible identifier for such sources.**

Additionally, following the merger-driven evolution scheme, I present a sub-sample of 28 CJF sources that are good tracers of evolution in AGN. I find at least 14 promising BBH candidates at different phases of their evolution (5 in an unbound and 9 in a hard state). Classification of these sources can not be unambiguous, given the lack of complete information. Further observations are needed to clarify their true nature.

Following arguments both from analytical and numerical simulations, it is anticipated that binary black holes should be formed during merger processes. I show that at least 13.6% of the CJF sources exhibit variability in different wavelengths (not including IDV), with most of them being almost periodical. I show that most of the previous BBH candidates are highly variable across the spectrum, showing the tight connection between the two phenomena. The morphology and evolution properties of the AGN jets can also be linked to the evolution scheme and BBH systems. The exact morphology of CJF jets and its evolution will be studied in detail in the following chapter.

More specifically, I find that:

- one CJF source (Mrk 231) has been classified as an ULIRG. Its properties fit well in the merging paradigm of AGN. I also note the similar source 1146+596, which shows high luminosity in the near-infrared, as a probable candidate for a merging system. Both sources are primary BBH candidates.
- a correlation between radio luminosity and NIR luminosity exists. This is qualitatively explained in terms of reradiation of the non-thermal AGN emission. Low luminosity AGN appear to have a near-constant NIR luminosity.
- based on incomplete multi-wavelength observations, 4.4% of the CJF sources exhibit distortions in their optical images, signs of ongoing or recent interaction. 3.1% have been identified as possibly having a companion. For  $z < 0.4$ , 28.6% of the CJF sources exhibit distortions or have a companion, in excellent agreement with [Hutchings and Campbell \(1983\)](#) and [Surace \(1998\)](#).
- from the assessment of the incompleteness of the available multi-wavelength data (see Sect. 2.9.1) I find that the actual percentage of AGN linked to a merger event could be up to three times the one found for the whole CJF sample.
- the above item, combined with the unbiased selection criteria of the CJF sample towards transitory systems, argues for the importance of merger events in the evolution of active galaxies
- multi-wavelength variability appears to be linked to systems undergoing a transition from thermal to non-thermal emission dominated spectrum. This can be connected to the presence of a bound binary black hole in the nucleus of such systems.



- multi-wavelength variability appears to be ubiquitous to active galaxies, as seen from the study of the two sub-samples described in Sect. 2.9.1. Assuming that this variability is indeed linked to BBH systems, then the occurrence of these systems in active galaxies is higher than implied so far.
- following the categorization of [Lotz et al. \(2008\)](#), I select the best candidate sources from the CJF sample for different evolutionary phases. I also select sources as the best candidates in the CJF sample for BBH systems.



## 3 Jet Ridge Lines in the CJF

For the first time observed in the optical for the nearest active galaxy to us (M87, [Curtis 1918](#)), jets are found in a plethora of astrophysical environments, among which, young stellar objects, massive X-ray binaries, possibly pulsars,  $\gamma$ -ray bursts, and AGN. As such, astrophysical jets research has been a booming field of astronomy, especially after the advent of high-resolution imaging instruments and techniques (like that of VLBI). Although observed in the minority of active galaxies ( $\sim 15\%$ ; [Krolik 1999](#)), extragalactic jets are some of the most pronounced morphological features in AGN research. Their, presumably direct, connection to the active core and the SMBH residing there, makes them invaluable tools in the effort to characterize the properties and the underlying physics of activity in galaxies. VLBI observations enabled the direct imaging of AGN jets and thus the study of their properties. In this chapter I use the CJF sample to study the kinematic properties of active galaxies and in particular a possible dichotomy between QSOs and BL Lacs. Using a statistical analysis of this sample, I make inferences on the nature of AGN jets and their underlying structure.

This chapter is organized as follows: in Sect. [3.1](#) I give a short overview of AGN jet research and set up the stage for the analysis to follow, in Sect. [3.2](#) I introduce the BL Lac object S5 1803+784, which has been one of the primary examples of BL Lac objects with peculiar kinematic behavior, in Sect. [3.3](#) I sketch out the motivation of this work, Sect. [3.4](#) deals with the observations that resulted in the data used here, as well as the data itself, Sect. [3.5](#) contains the main part of the work presented here, the analysis of the data and the results, in Sect. [3.6](#) I summarize the results from this chapter. Finally, the chapter is concluded with Sect. [3.7](#), a discussion of the methods used, as well as the implications of the results obtained.

### 3.1 Introduction

The close connection of jets to the active core in AGN makes them of outmost importance to any study of activity in galaxies. In Chap. [1](#) the physics of jets were briefly outlined. It is still unclear what processes launch, accelerate, and collimate extragalactic jets (e.g., [Blandford 2008](#); also see Chap. [1](#)). Constraints to these processes can be derived by either theoretical or observational work. VLBI techniques have allowed the mapping of jets in the radio (see below). A result of this was the discovery of the knotty nature of AGN jets. A consecutive series of brightness maxima and minima was found to comprise the observed jets. Observations at different times revealed that these brightness maxima actually move and thus began the investigation of extragalactic jet kinematics. One of the most prominent discoveries, related to jet kinematics, was that of the superluminal move-

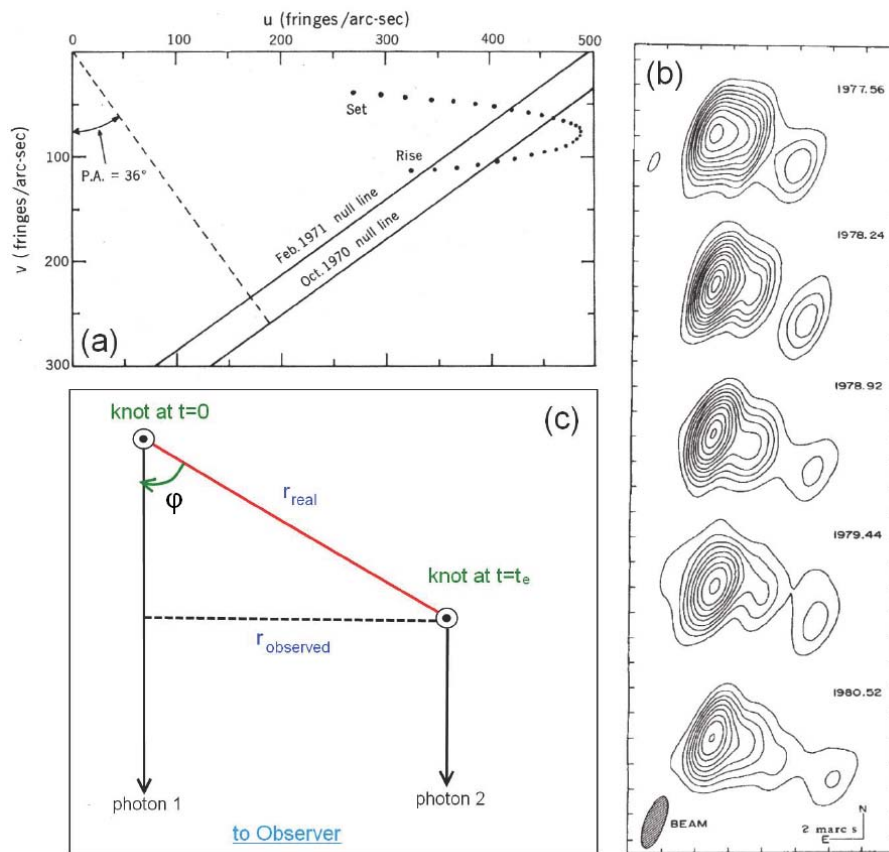


Figure 3.1: Superluminal motion detected through single baseline VLBI technique at 7.8 GHz (a; reproduced from [Whitney et al. 1971](#)). The source is 3C 279 and an apparent superluminal speed of  $10 \pm 3 c$  was derived. In 1981, the jet of 3C 273 was mapped, finding a superluminal speed of  $9.6 \pm 0.8 c$  (b; reproduced from [Pearson and Readhead 1981](#)). In (c) a sketch of the geometry of the effect is shown. The apparent speed is calculated in terms of the internal speed, the speed of light, and the angle to the line of sight.

ment of these jet components, which was first theoretically predicted by [Rees \(1966\)](#). The effect is a combination of relativistic expansion speeds (close to the speed of light) and the projected geometry onto the plane of the sky. Superluminal movement was indeed detected, first indirectly ([Whitney et al. 1971](#)), and then by direct imaging ([Pearson and Readhead 1981](#); see Fig. 3.1).

### 3.1.1 Relativistic Beaming and Projection Effects

As mentioned before, superluminal motion is a result of the combination of relativistic and geometric effects. The formalism of special relativity applied to extragalactic relativistic jets was first described by [Blandford and Konigl \(1979\)](#). As seen from the geometry presented in Fig. 3.1, the apparent speed of a jet component moving outwards, along the

jet axis, can be derived as:

$$\beta_{app} = \frac{\hat{n} \times (\boldsymbol{\beta} \times \hat{n})}{1 - \boldsymbol{\beta} \cdot \hat{n}},$$

$$\beta_{app} = \frac{\beta \sin(\phi)}{1 - \beta \cos \phi},$$

where  $\beta_{app}$  is the apparent velocity measured in the observer's frame,  $\boldsymbol{\beta}$  is the actual velocity of the component in the rest-frame of the jet (both speeds in units of speed of light,  $c$ ), and  $\hat{n}$  the unity vector along the line of sight. With  $\phi$  I indicate the angle between the line of sight and the jet axis. In the above formula, both projection and relativistic effects are taken into account (see Fig. 3.2).

Due to time aberration, the frequency  $\nu$  of a photon emitted from a relativistically moving jet component arrives as  $\nu' = \delta\nu$ . This is the Doppler effect, and is characterized by the Doppler factor:

$$\delta = \frac{1}{\Gamma(1 - \beta \cos \phi)},$$

where  $\Gamma$  is the Lorentz factor, described as  $\Gamma = (1 - \beta^2)^{-1/2}$ . Given a known viewing angle  $\phi$ , one can derive the Doppler factor as:

$$\delta = \sqrt{1 - \beta_{app}^2 + 2\beta_{app} \cot \phi}.$$

It can be shown that the observed flux density can be related to the Doppler factor as:

$$S_{app}(\nu) = S(\nu)\delta^{3+\alpha},$$

where  $\alpha$  is the spectral index ( $S \propto \nu^{-\alpha}$ ). The shift of the radiation to the observed frequency introduces the spectral index into the calculation of the apparent flux density. The above formula holds for optically thin sources and spherical optically thick sources (Blandford and Konigl 1979). One can, in addition, calculate a flux ratio between jet and counter-jet, taking into account the above equations:

$$R = \left( \frac{1 + \beta \cos \phi}{1 - \beta \cos \phi} \right)^{2-\alpha}.$$

The  $(2-\alpha)$  dependence comes from later calculations done by Lind and Blandford (1985). It becomes obvious that Doppler beaming, or the considerable brightening of sources moving towards the observer and the significant dimming of sources moving in the opposite sense, drastically alters one's perception of relativistic jets. One direct result of this effect is the core-jet morphology most often seen, with the counter-jet being dimmed below detection levels (see Fig. 3.2).

### 3.1.2 AGN Jet Kinematics

Studying the kinematics of AGN jets has been one of the main focuses of extragalactic radio astronomy. The supreme resolution offered by radio interferometers allows us to resolve the complicated structure of AGN jets and measure both their structural and flux evolution. A number of important phenomena are linked to the AGN jet research; the

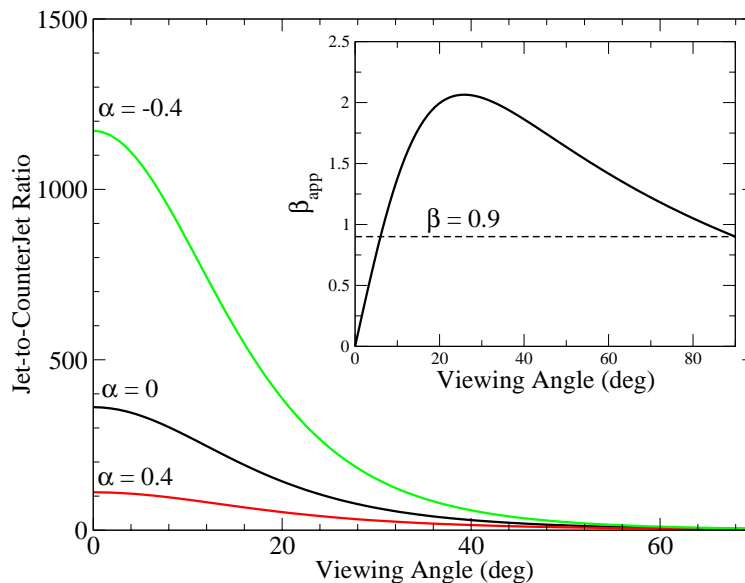


Figure 3.2: Jet to counter-jet ratio (see text for details) as a function of the viewing angle. The apparent speed of a component moving relativistically with  $v = 0.9c$  again as a function of the viewing angle is shown in the inlay.

properties of the accretion onto the SMBH at the center of AGN, the physical processes responsible for the efficient acceleration of the jet, the role of magnetic fields, the interaction of the jet with the ambient medium (and the equilibrium between internal and external pressure), as well as the fact that radio jets are some of the most bright objects in the radio sky illustrate the importance and relevance of such studies to astrophysics in general. One should also note the critical role that AGN jets have played in the unification effort of the different flavors of active galaxies.

Jet kinematics, as investigated through the study of distinct components, is currently explained in terms of the shock-in-jet model (e.g., [Marscher and Gear 1985](#)), where the observed jet knots are manifestations of shocks propagating at relativistic speeds down the jet. As discussed above, beaming and projection effects regulate the observed properties of the jets. Analysis of statistically important samples (large number of sources and/or stringent selection criteria) of active galaxies have been of fundamental importance to this end (e.g., [Ghisellini 1993](#); [Vermeulen and Cohen 1994](#); [Vermeulen 1995](#); [Taylor et al. 1996](#); [Hough et al. 2002](#); [Lister and Homan 2005](#); [Britzen et al. 2007b](#)). There has been a continuous effort to distinguish whether the different types of active galaxies (e.g., QSOs, BL Lacs, etc.) are due to just an orientation effect, or these objects have intrinsically different properties. The current paradigm is that the differences observed can be attributed to geometrical effects, although some indications to the contrary also exist (e.g., [Gabuzda 1995](#); [Gabuzda et al. 2000](#); [Britzen et al. 2009](#); [Britzen et al. 2010b](#)). For example, [Ghisellini et al. \(1993\)](#) find no appreciable difference for a sample of 39 superluminal sources between the distribution of Doppler factors between BL Lacs and QSOs, with RGs showing smaller values.

Such studies are hindered by the usually limited number of observations per object.

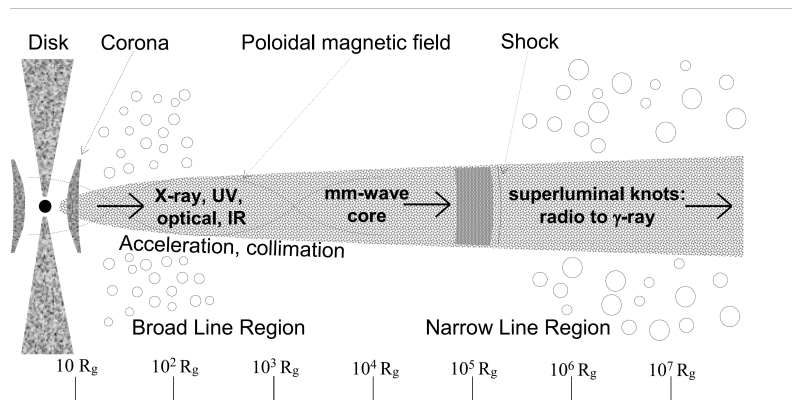


Figure 3.3: Basic sketch of a radio-loud AGN featuring a relativistic jet and a shock propagating down the jet, giving rise to the observed superluminal components. Different jet regions emit at different wavelengths. Figure reproduced from [Lobanov \(2007\)](#) (adapted from [Marscher 2005](#)).

Given a small number of epochs per source, certain assumptions are usually made, e.g., that components follow ballistic trajectories at constant speeds. More detailed studies of individual objects has however shown that this is rarely the case (e.g., see Sect. 3.2). Components appear to move along bent trajectories. Consequently, component speeds have also been seen to vary as a function of time and separation from the core, with both acceleration and deceleration observed. One well-studied example of a curved jet is that of the QSO 3C 345 (e.g., [Caproni and Abraham 2004](#)). 3C 345 has been modeled for a BBH system, explaining the complicated morphology and kinematics of its jet ([Lobanov and Roland 2005](#)). There is however a large number of sources found to exhibit bent jets, as reflected in the curved trajectories followed by their jet components (e.g., 4C 39.25, [Alberdi et al. 1997](#); S5 1803+784, [Krichbaum et al. 1994](#); 3C 454.3, [Krichbaum et al. 1995](#)). In general, there appears to be a trend for jets to appear more bent close to the core (e.g., [Krichbaum et al. 1994](#)) and show higher apparent speeds at larger core separations (e.g., [Zensus and Pearson 1990](#); [Abraham et al. 1996](#)).

The jet kinematics can also be related to the broadband properties of a source. There have been several examples where the emergence of a new component from the VLBI core, as well as its propagation down the jet (e.g., in a helical pattern) is accompanied by a broadband flare, with respective lags for different wavelength regimes, from radio to  $\gamma$ -rays (e.g., [Wagner et al. 1995](#); [Denn and Mutel 1996](#); [Britzen and Krichbaum 1997](#); [Britzen et al. 1999b](#); [Jorstad et al. 2001a](#); [Britzen et al. 2001](#)). This speaks in favor of the jet properties being exclusively regulated by beaming effects, with broadband flares occurring when the trajectory of a component passes the line of sight. Time lags between these flares, usually associated with the expansion velocity of a presumed "plasmon" propagating down the jet, or, equivalently, with the emergence of the shock front through progressively optically thinner regions of the jet (see Fig. 3.3), are model-specific and can be used to distinguish between different physical schemes.

### 3.1.3 Helical Jets

There is a growing number of sources for which helical models are employed for explaining their kinematic, flux, and evolution properties (e.g., 3C 273, [Lobanov and Zensus 2001](#); 1803+784, [Roland et al. 2008](#); 3C454.3, [Qian et al. 2007](#); 0605-085, [Kudryavtseva et al. 2010](#); 1632+382, [Liu et al. 2010](#), etc.). A helical, bent, trajectory has been employed for 3C345, showing that a constant Lorentz factor of about 10 can explain the observations. Apparent acceleration of the components is an effect of the change of the viewing angle ([Zensus et al. 1995](#)). Further evidence supporting an intrinsic helical structure for AGN jets (as traced by the magnetic fields threading them) is given by polarization studies, and in particular Faraday rotation gradients and circular polarization found in several sources (e.g., [Gabuzda 2005](#); [Gabuzda et al. 2008](#)).

Such helical structures/trajectories have been explained by a number of different models. An often employed concept is that of a precessing jet, combined with the non-ballistic motion of ejected components. Two different scenarios concerning the central engine that feeds the jets can explain the observed curvature.

#### Models relying on a single central black hole

In the first scenario, the core that ejects the jet is considered to be a single object (usually a supermassive black hole, SMBH). Precession can then occur due to the Bardeen-Petterson effect through Lense-Thirring precession of the accretion disk (e.g., [Caproni et al. 2006](#)). However, this model assumes a rigid body configuration between the accretion disk and the jet, an assumption not readily verifiable. A magnetic torque mechanism has also been proposed (e.g., [Lai 2003](#)), driven by the large-scale magnetic field threading the accretion disk, leading to precession of the disk and consequently of the jet. In the same frame, a group of models attribute the curving and wiggling of the jet to magnetohydrodynamic (MHD) instabilities, most prominently Kelvin-Helmholtz (K-H) instabilities (e.g. [Hardee and Norman 1988](#); [Birkinshaw 1991](#); [Camenzind and Krockenberger 1992](#); [Zhao et al. 1992](#); [Hardee et al. 1994](#); [Hardee and Stone 1997](#); [Meier and Nakamura 2006](#); [Perucho et al. 2006](#)). [Meier and Nakamura \(2006\)](#) consider the instability to be driven by current, related to the strong-field pinch, rather than by K-H instabilities. All models mentioned above strongly depend on the jet-to-environment density ratio. [Gong \(2008\)](#) considers a precessing jet, with relativistic components following non-ballistic trajectories, also taking into account the density of the medium external to the jet, essentially imposing a deceleration timescale for components due to interaction with the ambient medium.

#### Binary black hole models

In the second scenario, models have been built under the assumption that a binary system can be found in the centers of AGN. The most popular idea concerns binary black hole systems (BBH) as a product of galaxy merging (see Chap. 2). The problem is complex and each of the models makes a number of assumptions to explain the observed structures. In such systems, the primary black hole is considered to have an accretion disk and jets, whereas the secondary black hole is in orbit around the primary. Gravitational perturbations associated with this orbiting secondary black hole can disrupt the accretion disk of the primary black hole and lead to precession. [Lobanov and Roland \(2005\)](#) argue



that in light of the two-fluid model, the orbital motion and the disk precession can lead to curving and wiggling of the jet. A modified model has also been successfully applied to S5 1803+784 (Roland et al. 2008). Furthermore, they propose that for strong enough magnetic fields, the K-H instabilities can be considered negligible. Roos et al. (1993) argue that the orbital motion of the binary is responsible for the change of the jet-ejection direction and thus leads to a wiggling structure (the jet is treated ballistically). Kaastra and Roos (1992) argue that the precession angle is determined by the angle between the primary black hole spin axis and the angular momentum of the binary system. As before, the jet is treated ballistically. Similar models have been proposed by Katz (1997) (a gravitational torque induced by the secondary black hole onto the accretion disk) and Romero et al. (2000) (near-rigid body configuration). A number of BBH models have also been developed for OJ 287 (see Chap. 2, Sect. 2.9 for some references).

### External causes of jet curvature

Finally I mention another group of models that rely on external causes for explanation of the curving and wiggling of jets. The bending of the jet could be attributed to interaction with the surrounding medium. This however can not fully explain cases such as S5 1803+784 (see Sect. 3.2), since such periodic and fine structure within the jet would imply an equally finely structured surrounding medium, for which there is no evidence. Blandford and Icke (1978) attributed the structure of the jet of 3C 31 to dynamical interaction with a nearby galaxy (again treating the jet ballistically). Jaegers and de Grijp (1985), based on the latter model, proposed a similar model for 3C 10, while studying the movement of discrete blobs along the jet. Lupton and Gott (1982) proposed that the curving of the jet of 3C 449 is due to the orbital motion of the central engine around the hosts center of gravity. Yokosawa and Inoue (1985) combine some of the above models for the case of 3C 75, which has a double radio source with two pairs of jets that seem to intertwine. Again treating the jets ballistically, the authors take into account the pressure of the surrounding medium, assuming a time-dependent ejection velocity for the jets, and accounting for the orbital motion of the central engines of the jets.

### 3.1.4 Stationary components

Of special interest for this work is the apparent stationarity observed for several AGN jet components. These components appear to stay at similar core separations for long time spans. Such components are observed in a growing number of AGN (see e.g., Gómez et al. 2001; Jorstad et al. 2005; Britzen et al. 2007b). Different physical models and scenarios have been invoked to explain the phenomenon of stationarity in AGN jets. A prominent example is the superluminal radio source 4C39.25, in which a stationary component was observed by Alberdi et al. (2000). They explain this in geometrical terms, proposing that the stationary component is at a 90 degrees bend in the jet away from the observer. They disfavor the case of a recollimation shock based on polarization data. Gómez et al. (2001) find three quasi-stationary components in the jet of 0735+178 in a quiescent state of the source, and attribute them to recollimation shocks and differential Doppler boosting. Britzen et al. (2007b) and Kellermann et al. (2004) find stationary components in the, respective, 6 and 2cm AGN surveys. I also note the case of the quasar 3C 395 (Simon

et al. 1988; Lara et al. 1994; Lara et al. 1999), whose jet exhibits a possible stationary component due to possible bending of the jet. Unlike these cases, detailed investigation of two sources, 180+784 (Britzen et al. 2010a) and 0716+714 (Britzen et al. 2009), showed that the parsec-scale jets of these sources are actually dominated by components that remain stationary throughout all the available epochs of observations. In addition, as was exhibited for the case of 1803+784 (Britzen et al. 2010a), stationary and superluminal components can co-exist in the same jet. This appears to be a different phenomenon as it results to a predominantly stationary (with respect to the distance from the core) jet, as opposed to an outwards evolving jet with an apparent stationary component at some fixed distance from the core.

Martí and Müller (2003) model AGN jets and find that pressure mismatches exist between the jet and the surrounding medium. These lead to the production of reconfinement shocks and energy density enhancements downstream of these shocks, which in turn give rise to stationary radio knots. Numerical simulations by Agudo et al. (2001) of an expanding relativistic jet show that the injection of a superluminal component into the jet can trigger instabilities that give rise to stationary components (shocks) in the wake of the superluminal component, especially in the near vicinity of the core. It should be noted however, that recent simulations of the same authors (Mimica et al. 2009) show a frequency dependence of this effect, predicting that at lower frequencies (e.g., 5 and 15 GHz) such stationary features would be blended out due to the low resolution of the convolving beam. Geometric projection effects can also, partially, explain such stationary features.

Perhaps in one of the most interesting case of stationary AGN jet components, Britzen et al. (2010b) show that 0735+178 is a hybrid in the sense that the kinematic properties change simultaneously with morphological changes. At times when the pc-scale jet is straight, the jet components appear to be stationary. At times when the pc-scale jet appears to be strongly bent, the jet components show apparent superluminal motion (see Fig. 3.4). This implies that 0735+178 is at a critical angle to the line of sight, such that small ejection angle changes result to markedly different kinematic behaviors for the components.

## 3.2 S5 1803+784: A Case Study

S5 1803+784 is an active galaxy at a moderate redshift of  $z=0.68$  (Hewitt and Burbidge 1989). It has been classified as a BL Lac object. Being a member of the complete S5 sample (Witzel 1987) it has been extensively studied in the radio, at different wavelengths and with different instruments (see Britzen et al. 2010a for a detailed recounting of the source's radio observations history). As an active galaxy, 1803+784 has also been observed in different wavelengths including the FIR (IRAS; Moshir et al. 1990), the NIR (space-based: Padovani et al. 2006, ground-based: Kotilainen et al. 2005; Heckman et al. 1983), the optical (e.g., HST; Urry et al. 2000), the X-ray (ROSAT, Britzen et al. 2007b; BeppoSAX, Donato et al. 2005), and recently in the  $\gamma$ -rays by the Fermi-LAT space telescope (Abdo 2009). The host galaxy of 1803+784, although observed in the highest available resolution by the HST, still remains unresolved in the optical. Kotilainen et al. (2005) resolve the host galaxy of 1803+784 at the NIR with an effective scale length of

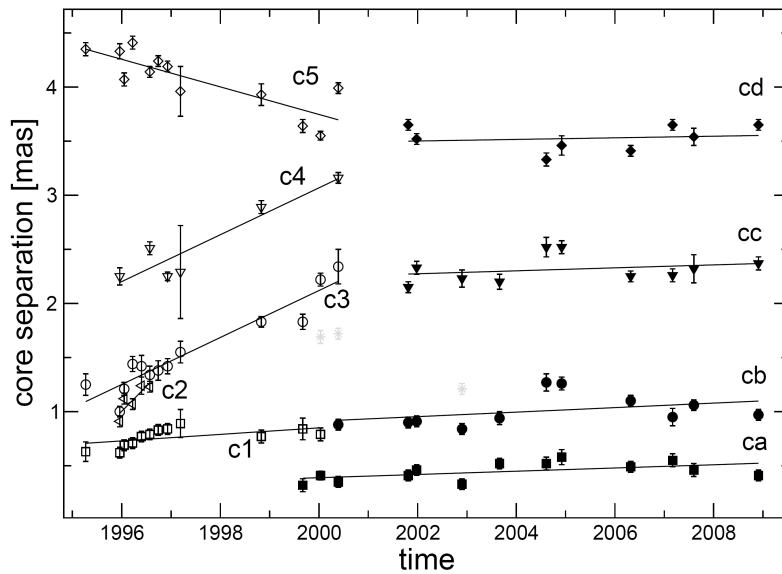


Figure 3.4: Core separation evolution of 0735+178 jet components with time. A change of mode can be seen around 2001, after which all components appear to remain stationary. Figure reproduced from [Britzen et al. \(2010b\)](#).

the bulge at 7.4 kpc (see Fig. 3.5). Typical for this class of objects, 1803+784 has been observed to be variable in the radio and the optical for both long and short-timescales (e.g., [Wagner and Witzel 1995](#); [Heidt and Wagner 1996](#); [Nesci et al. 2002](#); [Fan et al. 2007](#)).

1803+784 has however become famous due to its peculiar jet morphology and kinematics. The milli-arcsecond jet of this source shows a number of prominent components at separations of 1.4, 5, and 12 mas. Interestingly, the inner-most component at 1.4 mas has been found to be stationary with respect to the core. [Britzen et al. \(2005b\)](#) instead showed that that component is indeed moving, but with a strongly subluminal speed ( $\beta_{app} < 0.74h^{-1}$ ), performing an oscillatory movement. The morphology of the jet is also of interest. The jet of 1803+784 shows curvature on all scales probed (see Fig. 3.5), with evidence for a helical trajectory for its components from mm observations (e.g., [Krichbaum 1990](#)). Additionally, 1803+784 is one of the misaligned AGN as described by [Antonucci et al. \(1986\)](#), where the pc- and kpc-scale jets are seen to be aligned almost perpendicular to each other.

[Britzen et al. \(2010a\)](#), having collected an unprecedented amount of VLBI data for 1803+784, have conducted a detailed investigation of the morphology and kinematics of the source at different frequencies (1.6 - 15GHz). In particular, 94 epochs of observations with different arrays - global VLBI, VLBA, etc. - have been collected and uniformly re-analyzed by the authors. From this investigation, a new kinematic scheme for 1803+784 was revealed. All components in the inner part of the jet (up to 12mas) appear to remain stationary with respect to the core (for an example of this see Fig. 3.6). This behavior is seen at all frequencies studied by the authors. In contrast to this, the components show strong changes in their position angles, implying a prevailing movement perpendicular to the jet axis.

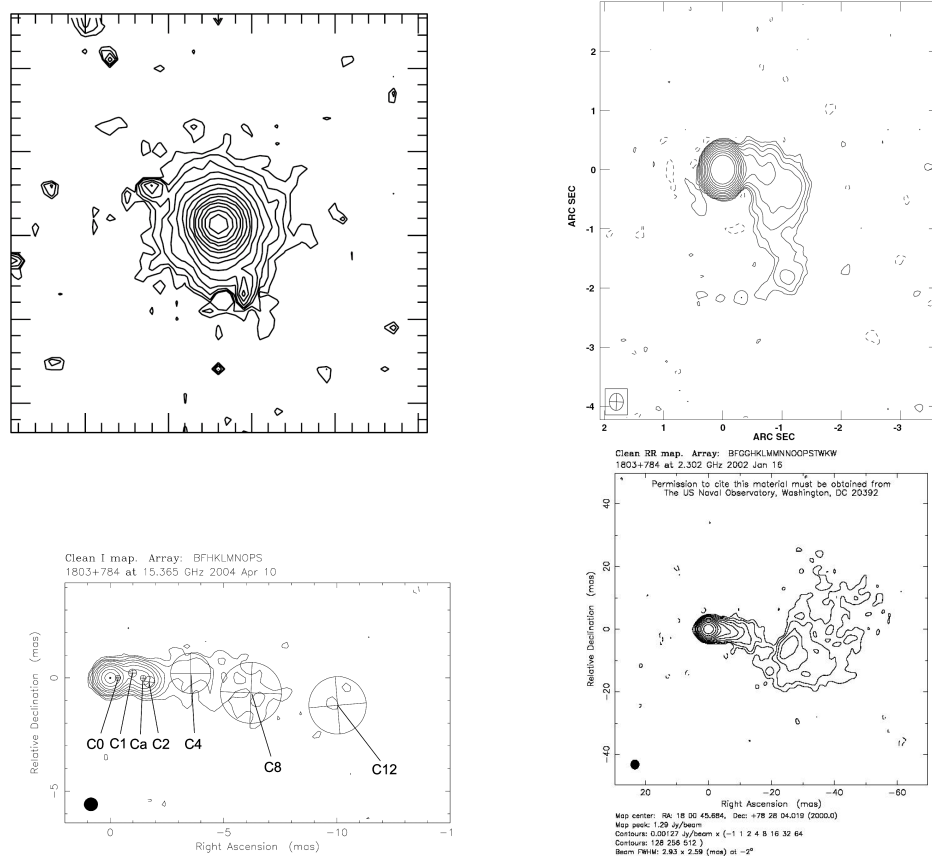


Figure 3.5: S5 1803+784 at different wavelengths. Upper left: An image of the host galaxy of 1803+784 in the NIR (K band), taken with the Nordic Optical Telescope (NOT). The host galaxy appears to be resolved. Upper right: Radio map of 1803+784 at 18cm with the MERLIN interferometric array. The bending of the jet at large scales can be seen. Lower left: Core and jet of 1803+784 as observed with the VLBA at 15GHz. Jet components up to 12mas are shown. Lower right: Lower frequency (2.3GHz) VLBA map of 1803+784 taken within the frame of the Radio Reference Frame Image Database (RRFID) managed by the United States Naval Observatory (USNO). Figures reproduced from [Kotilainen et al. 2005](#), [Britzen et al. 2005b](#), and [Britzen et al. 2005a](#).

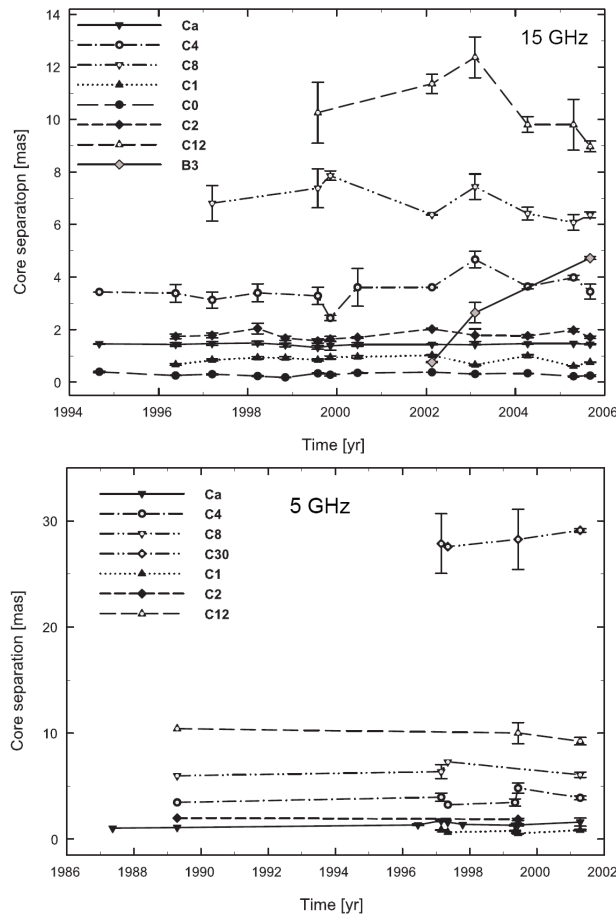


Figure 3.6: Core separation versus time plots for 1803+784 at two different frequencies (15GHz left and 5GHz right). It can be seen that all components remain stationary with respect to the core (within error-bars). Figures reproduced from [Britzen et al. \(2010a\)](#).

[Britzen et al. \(2010a\)](#) however also studied the jet ridge line morphology and evolution of S5 1803+784. A jet ridge line at a given epoch is defined as the line that linearly connects all component positions at that epoch. The morphology of the jet ridge line, essentially tracing the flux maxima along the jet at a certain moment in time, is independent of the identification of individual components and is thus an unbiased way of studying the properties of the jet as a whole. As already implied by the movement of single components, the jet ridge line of 1803+784 appears to change strongly between epochs. The authors find that the jet ridge line changes in an almost periodic manner, starting resembling a straight line, evolving into a sinusoid-like pattern, and finally returning to its original linear pattern (see Fig. 3.7), although slightly displaced from its original position. The authors calculate a period of  $\sim 8.5$  years for the evolution of the jet ridge line.

Of interest to this work is also the investigation of the evolution of the jet width, as reflected by the distribution of the positions of the identified components at a certain epoch. The authors find that the jet changes its width (in a range between a few and a few tens of degrees) in an almost periodic way with a timescale similar to the one found from

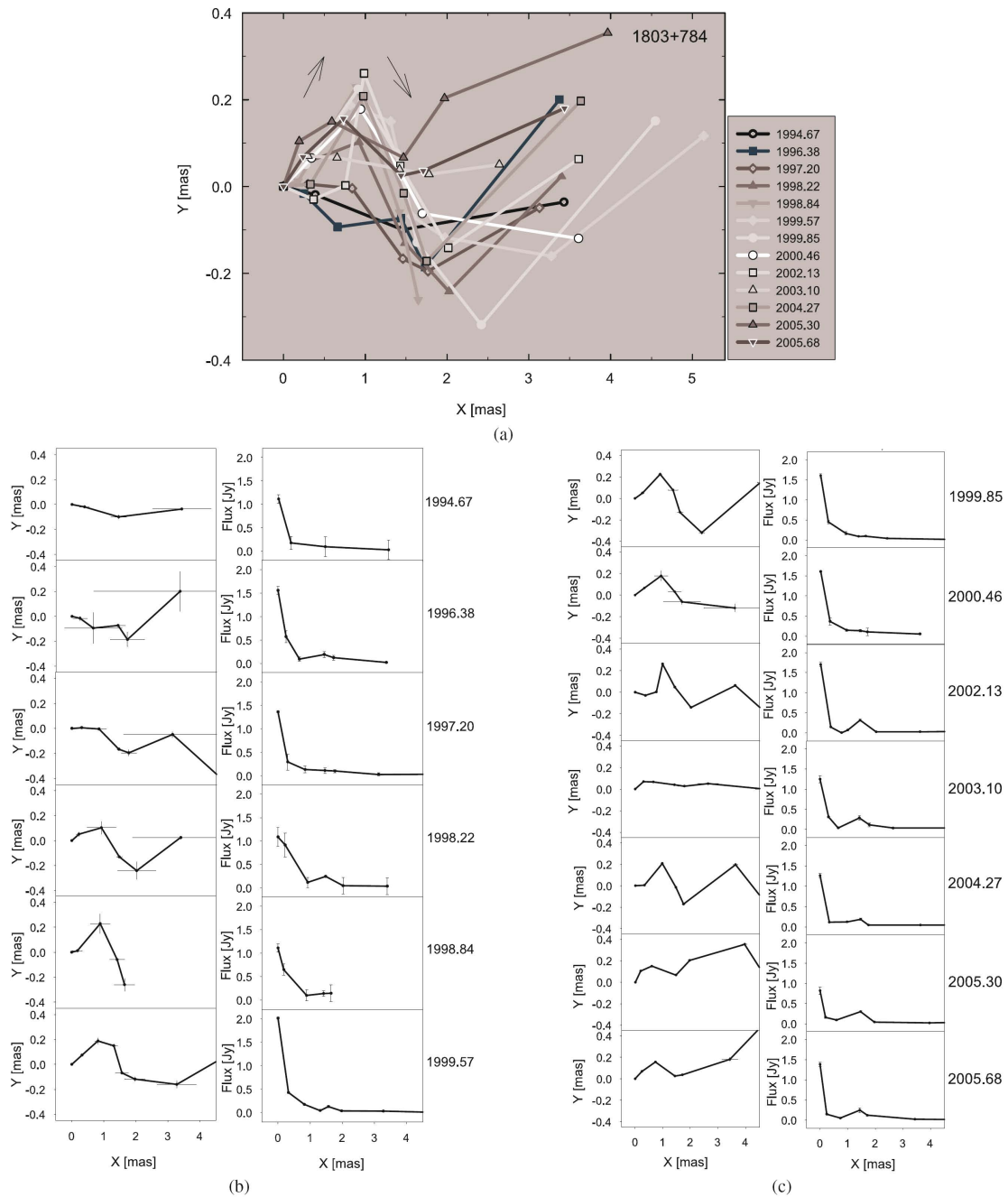


Figure 3.7: Jet ridge lines of S5 1803+784 constructed by the component positions at 15GHz for different epochs. In panel (a) the cumulative evolution of the jet ridge line is shown. In panels (b) and (c) the jet ridge lines in Cartesian coordinates (left columns) at individual epochs, along with the corresponding fluxes of the components along the jet (right columns), are shown. The figure is reproduced from Britzen et al. (2010a).

the evolution of the jet ridge line. All of the above properties support a new kinematic scheme for 1803+784, where components follow oscillatory-like trajectories, with their movement predominantly happening perpendicular to the jet axis rather than along it. **Moreover, the jet appears at times to form a wide channel of flow, while changing its width considerably across time.**

### 3.3 Motivation

S5 1803+784 is not the only object exhibiting such behavior. 0716+714 has been shown to behave in a similar way (Britzen et al. 2009), with most of its components being stationary with respect to the core while changing their position angles considerably. PKS 0735+178 is another example of a source with similar, but rather more complicated, kinematic properties (Britzen et al. 2010b). It is interesting to note here that all three objects, recently found to deviate from the currently accepted kinematic paradigm of relativistic superluminal blazar jets, have been classified as BL Lac sources. Under the unification scheme of active galaxies (as described in Sect. 3.1 of this work), BL Lac objects are believed to be active galaxies for which the viewing angle to their jets is very small, leading to strong relativistic effects. In the last several years, the classification of active galaxies between the quasar and BL Lac classes has been osmotic in nature, with the general classification of blazars often used to describe members of both classification groups. However, this phenomenological unification of QSOs and BL Lacs comes into question in light of the recent investigation of sources like S5 1803+784 and 0716+714.

The work in this chapter focuses on exactly this apparent division between BL Lac and QSO jet kinematics. As valuable as single source studies are to an in-depth understanding of particular phenomena, there are a number of biases and unaccounted factors that alter and ultimately hinder a universal application of their results. In this context, I use the CJF sample to statistically investigate and assess the similarity, or divergence, of the kinematic and morphological properties between the two distinct sub-samples of QSOs and BL Lac objects in the CJF. I want to test whether BL Lac objects indeed show stationarity with respect to their cores compared to their QSO counterparts. Furthermore I am interested in the phenomenon exhibited in S5 1803+784 of an, at times, very wide jet, as well as a strong evolution of that width. For this investigation I use tools that extract information from the jet ridge line of the sources, instead of focusing on individual components. In Sect. 3.7 I shall discuss the advantages, as well as the drawbacks, of such a method.

### 3.4 Data

The work presented in this chapter is heavily based on the kinematic analysis of the CJF sample (Britzen et al. 2007b; Britzen et al. 2008). As already mentioned in Sect. 1.6, an extensive observing campaign of all 293 CJF sources was undertaken using both the VLBA and the global VLBI array at 5GHz (in a time span of 10 years between March 1990 and December 2000). The observational strategy was to observe each source 8 times in 5.5 min snapshots in each observing session. The data were recorded with a 32MHz total bandwidth broken up into four baseband channels, with 1 bit sampling. The data correlation was done in Socorro. There was an aim of a minimum of three epochs per source

(Britzen et al. 2007b note that 3 epochs spread over a period of 4 years are necessary for an unambiguous treatment of the jet kinematics<sup>1</sup>). All sources have been model-fitted independently (directly to the observed visibilities), starting from a point source and using circular Gaussian components (see Sec. 1.5 for an explanation on model-fitting) with parameters flux density ( $S$ ), position in Cartesian coordinates ( $x, y$ ), and major axis ( $M$ ). Specific information for all observation runs, data reduction procedure, uncertainties calculation, and information on individual sources can be found in Britzen et al. (2007b). I note that five CJF sources were initially excluded from any further analysis due to problematic observations (0256+424, 0344+405, 0424+670, 0945+664, 1545+497) and therefore are also omitted here. In total, 288 sources are considered and analyzed in the following sections. Of these 196 are classified as quasars (68.05%), 49 as radio galaxies (17.01%), 33 as BL Lac objects (11.46%), and 10 (3.47%) are not classified.

Due to the scope of the CJF program, the identification and analysis of jet component kinematics has been focused on the part of the jet that is beamed towards us. For a number of sources, several components belonging to the counter-jet have been identified. However, cross-identification over epochs has not been carried out. For this reason, and given the nature of the analysis that I undertook (see below), I have excluded all counter-jet components in the following investigation. In a total number of 2468 components, 82 (3.32%) counter-jet components have been identified and excluded from this analysis. On average, radio galaxies have 3.6 components identified per jet, 2.7 components are identified per quasar jet, and 2.9 components per BL Lac jet (Britzen et al. 2007b). This reflects the relative difference of projected jet length for the different types of objects. This shall be discussed more thoroughly in Sect. 3.7.

In the following, I am going to describe the tools that were used for the analysis of the jet ridge lines of the CJF sample in the context described in Sects. 3.2 and 3.3. In short, I used the following measures:

- apparent (projected) jet length,  $L$ ,
- monotonicity index, M.I.,
- apparent jet width,  $dP$ ,
- apparent jet width evolution,  $\Delta P$ , and
- apparent jet linear evolution,  $\Delta \ell$ .

I note that all the above measures, as their names imply, refer strictly to values projected onto the plane of the sky. Although it is possible to constrain, or in some cases have an exact value of, the viewing angle of each source, this is outside the scope of this current work. For the following analysis, and for the sake of brevity, I shall drop the characterization of apparent for each of these values, although this will be implied throughout unless otherwise stated. In the following subsections, each of the above named terms are going to be described in more detail.

---

<sup>1</sup>However, as the case of 1803+784 exhibits, a larger number of epochs allows for more complicated kinematic behaviors to be uncovered. For the case of a uniform sample investigation, as is the case of CJF, a large number of observing epochs is prohibitive.



### 3.4.1 Jet Length, L

As has been already described, under the currently accepted unification scheme (Urry and Padovani 1995), BL Lac objects are believed to be seen under a very small angle to the jet axis. Accordingly, QSOs have slightly larger viewing angles, with radio galaxies having the largest viewing angles and their jets being viewed "edge on". In this context, and due to projection effects, I expect that the apparent length of the jet as observed in the different classes of objects behaves accordingly, with radio galaxies having the apparently longest jets and the BL Lac objects the shortest ones.

I am interested in quantifying this relation. I define the apparent jet length of a source at an epoch  $i$ ,  $L_i$ , as the distance of the component farthest from the core, measured in parsecs. This is in principle a simplified treatment of the problem and is susceptible to the larger errors of the identification and fitting of components near the borders of the field of view. I also find the maximum jet length,  $L_{max}$ , across all available epochs for each individual source. I should point out here that the jet length derived by this method is limited, or regulated, by the resolution and sensitivity of the instrument used and reflects the extend of the *observable* jet in parsec scales. It is to be expected that, if observed with higher sensitivity and dynamic range, every individual jet would extend farther away from the identified core than currently seen, in addition to being broader and with much more complex structure. Relative jet length differences between the separate classes of objects (QSOs, BL Lacs, radio galaxies) should, in first order, not be affected by this observational effect.

### 3.4.2 Monotonicity Index, M.I.

It is known that a large number of active galaxies exhibit bent or otherwise non-linear jet morphologies in different scales. Individual sources like S5 1803+784 and PKS 0735+178 (see references above), as well as others (e.g. 3C 345; Lobanov and Zensus 1999), have been extensively studied to understand the origin of these bends. Britzen et al. (2008) calculate the "bends" between successive components for all CJF sources, finding large local variations of the position angles of the sources. In this context, I am interested in quantifying the bending of the whole jet ridge line. Moreover, I want to differentiate between a simple bend or straight jet (see Fig. 3.8, right), as opposed to a more sinusoid-like morphology (similar to what is seen for some epochs of S5 1803+784, also see Fig. 3.8, left). This is done by means of the monotonicity index, M.I.

I quantify a sinusoid-like morphology of a jet by identifying the local extrema in a given jet ridge line, in the core separation - position angle plane ( $r, \theta$ ). For an epoch  $i$ , a component  $m$  consists a local extremum under the following definition:

$$\theta_{m;extr} : |\theta_m - \theta_{m\pm 1}| \geq 10(d\theta_m + d\theta_{m\pm 1}).$$

Having calculated the number of extrema for a given jet ridge line at an epoch  $i$ , I define the M.I. as:

$$M.I. = \frac{\text{number of extrema}}{N - 1},$$

where  $N$  is the total number of components at that given epoch. This is a crude calculation, but can give us a handle on how the bending of the jet behaves along the jet. For M.I.

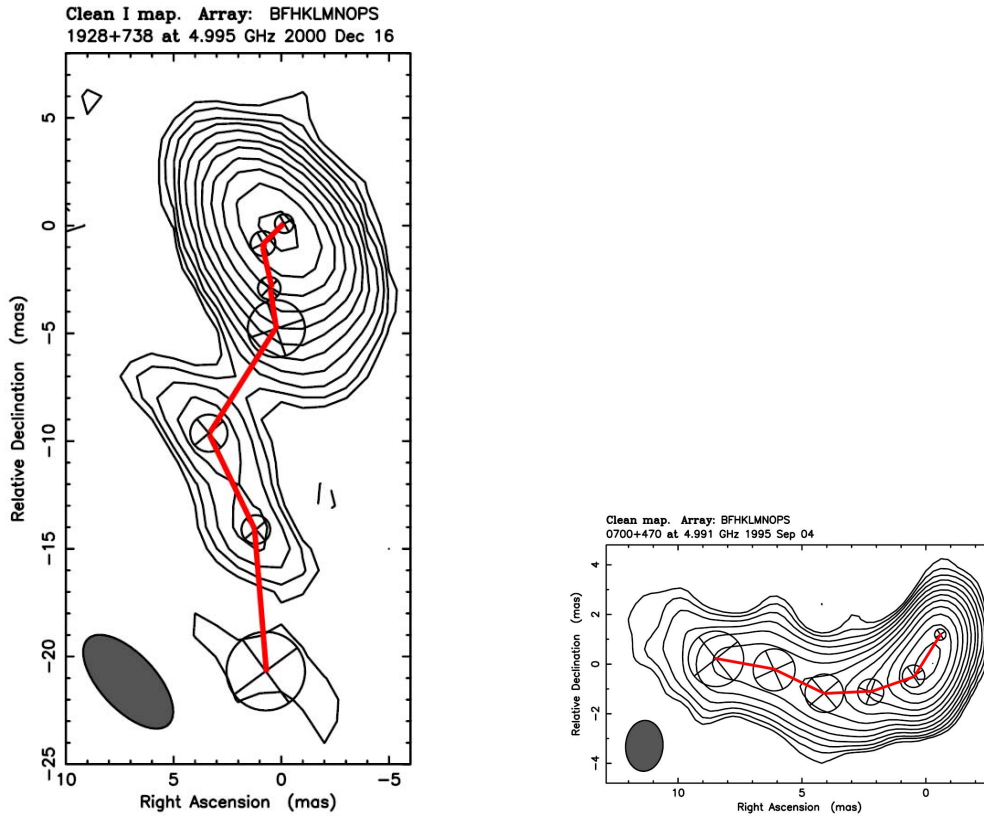


Figure 3.8: Radio maps at 5GHz of 1928+738 (left) and 0700+470 (right, with jet ridge lines superimposed). Two examples of a sinusoid-like jet morphology (left) and a single-bend one (right). I am interested in distinguishing between the two. Figures adapted from Britzen et al. (2007b).

values close to one, the jet resembles more a sinusoid. An M.I. value close to zero reveals a monotonous, single-bend or straight, jet morphology. I normalize for the number of components  $N$  to account for longer, or shorter, jets and to enable comparison between different sources. As an example, for the sources shown in Fig. 3.8, 1928+738 is found to have an M.I. value of 0.4, compared to 0700+470, that gives an M.I. value of 0.

As is the case for most of the tools described in this section, the value of M.I. heavily depends on the resolution of the observations. Given that the resolution is not the same across all epochs and sources, an uncertainty is introduced when comparing two M.I. values of two different sources. A final remark pertains to the definition of an extremum. I use a  $10\sigma^2$  value as the lower limit for flagging an extremum. A different level of significance (e.g.,  $5\sigma$ ) would result in different values of M.I.. The choice of the  $10\sigma$  significance is a conservative approach to the identification of extrema in the jet ridge line. Therefore, in the following, M.I. shall be used as more of a qualitative tool rather than a quantitative measure of the actual jet morphology.

<sup>2</sup>Here  $\sigma$  is defined as the sum of the position angle errors for  $\theta_m$  and  $\theta_{m\pm 1}$ . The choice of this  $\sigma$  reflects an original underestimation of the position angle errors during the component fitting.

### 3.4.3 Jet Width, $dP$

As was discussed in Sect. 3.2, one of the characteristics of the evolution of the 1803+784 jet is the fact that its jet ridge line at times becomes very wide, resembling a channel rather than a narrow flow. I therefore need to define a measure of the CJF jet widths in order to study this behavior. For an epoch  $i$  and a jet consisting of  $N$  components characterized by their core separation and position angle  $(r_i, \theta_i)$ , I identify the components with the maximum and the minimum position angles<sup>3</sup>. The apparent width of the jet  $dP$ , measured in degrees, is then calculated as (also see Fig. 3.9):

$$dP_i = \theta_i^{max} - \theta_i^{min},$$

while the uncertainty is calculated by error propagation:

$$\delta dP = \sqrt{(d\theta_i^{max})^2 + (d\theta_i^{min})^2}.$$

There is a number of factors that should be considered at this point. The most obvious drawback for the above definition is the non-localized nature of this measure. Using two different components, at different core separations, gives us only an approximate notion of the width of the flow. Higher resolution investigations might resolve the structure of the jet perpendicular to the jet axis and provide us with a more real estimate of the local width of the jet. Alternatively, one can calculate a localized value of the jet width by using the FWHM of the fitted Gaussian components (e.g., [Pushkarev et al. 2009](#)). In this case, however, the width is heavily dependent on the beam size and therefore on the resolution. Instead, by using the definition above, I seek to quantify the opening of the jet flow and identify the effect of a channel-like jet, as seen in the case of S5 1803+784. In the context of the localization problem, I have implemented in my calculations a constrain in the maximum allowed distance between the two components identified with the minimum and maximum position angles. The value of this limit depends on the jet length and shall be discussed in Sect. 3.5.

### 3.4.4 Jet Width Evolution, $\Delta P$

I want to investigate how the jet width, as defined previously, changes with time. The jet width evolution  $\Delta P$ , measured in degrees per unit time, is defined between two successive epochs  $i$  and  $(i-1)$ . It is calculated as follows:

$$\Delta P = \frac{dP_i - dP_{i-1}}{T_i - T_{i-1}},$$

where  $T_i$  denotes the time at epoch  $i$ , measured in years. I can also define the maximum jet width evolution as:

$$\Delta P^{max} = \max\{\Delta P_{1...i}\}.$$

This value is characteristic for each source and reflects the maximum potential in the width evolution of the jet flow for that source. I should note here that the jet width evolution does not reflect an angular speed (given the units of degrees per unit time). Instead,

<sup>3</sup>The original data are given in a  $[-180, 180]$  format. I transform all position angles into the  $[0, 360]$  range for simplicity and clarity of results.

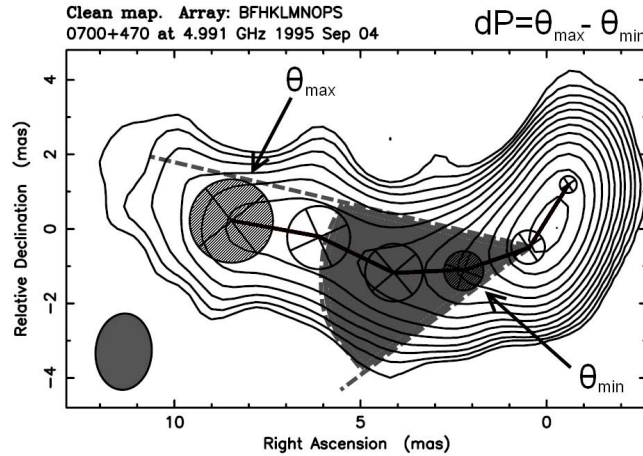


Figure 3.9: Example of the definition of the jet width for the source 0700+470. With filled circles I denote the components with the minimum and maximum position angles at that epoch.

the per unit time reflects a normalization for time that ensures a comparison between sources that have been observed during different time spans. The currently available data are too sparse to allow us a calculation of a real angular speed for how the jet width (and orientation) changes with time.

For both the width  $dP$  and the width evolution  $\Delta P$ , the sensitivity and dynamic range of the observations play a regulating role. Given that I need at least two components to define the width, a dimming of one of these components across epochs can result to a false or altered value for both the calculated width and width evolution. A more detailed discussion of this can be found in Sect. 3.7.

### 3.4.5 Jet Linear Evolution, $\Delta \ell$

Having introduced two different measures pertaining to the investigation of the angular evolution of the jet, I need a measure reflecting the total linear displacement of the jet. Such a measure is dictated by the need to investigate a possible stationarity of components, as seen in S5 1803+784. I calculate this linear evolution across all available epochs and for all components, ultimately acquiring a value reflecting the total linear displacement of the whole jet ridge line. I use plane-of-the-sky coordinates  $(X_i, Y_i)$  to calculate the linear displacement of a component  $m$  between epochs  $i$  and  $(i+1)$ :

$$l_i^m = \sqrt{\Delta X_i^2 + \Delta Y_i^2}.$$

To calculate the total displacement of the whole jet ridge line I then need to sum up over all components and all available observing epochs:

$$\ell = \sum_{i=1} \sum_m l_{(i)}^m.$$

Again, given that I want to compare  $\ell$  in different sources, I need to account for differences in both the time span of observations, as well as in the number of components. Therefore

I define the jet linear evolution  $\Delta\ell$ , measured in parsecs per unit time and per component, as follows:

$$\Delta\ell = \frac{\sum_{i=1} \sum_m l_{(i)}^m}{N(T_i - T_1)} = \frac{L}{NdT},$$

where  $N$  is the total number of components used through all the epochs. I need to underline a fundamental difference between the way the jet linear evolution,  $\Delta\ell$ , is calculated, compared to the measures described previously. For the calculation of the displacement of an individual component  $\ell$  between two consecutive epochs, and consequently of  $\Delta\ell$ , the cross-identification of components across epochs is necessary. Therefore, for  $\Delta\ell$ , unlike the previously discussed jet ridge line characteristic values, the actual individual identification of components is important.

The reason for normalizing this value over the time span of observations is the same as for the jet width evolution. In this case however, I also need to account for the number of components for each individual jet. As [Britzen et al. \(2007b\)](#) find, radio galaxies have more components per jet identified than QSOs and BL Lacs. I therefore divide the total displacement of the whole jet ridge line by the actual number of components used for the calculation (hence the number of components cross-identified across each pair of observation epochs).

I should note here that  $\Delta\ell$  essentially reflects the apparent speed distribution of all cross-identified components of the jet and therefore represents a value characteristic for the whole jet, rather than for individual components. By summing up all components and epochs I trade temporal and positional resolution for a universal treatment of the whole jet. In this way I can test whether the kinematics of BL Lac objects is fundamentally different than that of QSOs while averaging out localized properties of individual components.

There is one last point concerning all the tools described above that should be mentioned. Given the large span of redshifts that the CJF sources cover, it is imperative to account for the different linear scales probed for sources at different distances from us. It is known that the jet structure and behavior changes with the distance from the core. By comparing sources at different redshifts, one implicitly studies a different part of their jet. To counter this effect, I define a maximum core separation limit<sup>4</sup>, above which components are not included in this investigation. In this way I ensure that I probe the same linear scales for all CJF sources, albeit with different resolution. The latter effect can be counteracted by using redshift bins throughout. Additionally, through use of redshift bins, I can probe a possible evolution of the studied properties with redshift, if any.

## 3.5 Analysis and Results

Having presented the tools that I am going to use for my investigation, as well as implications of their application to the data, I am now ready to move to the analysis and the results of this investigation. As the jet length and its morphology (as expressed by the M.I.) are used as a basis for the further analysis, I am going to discuss these first.

<sup>4</sup>The definition of this limit and a justification for that definition will be given in Sect. 3.5.

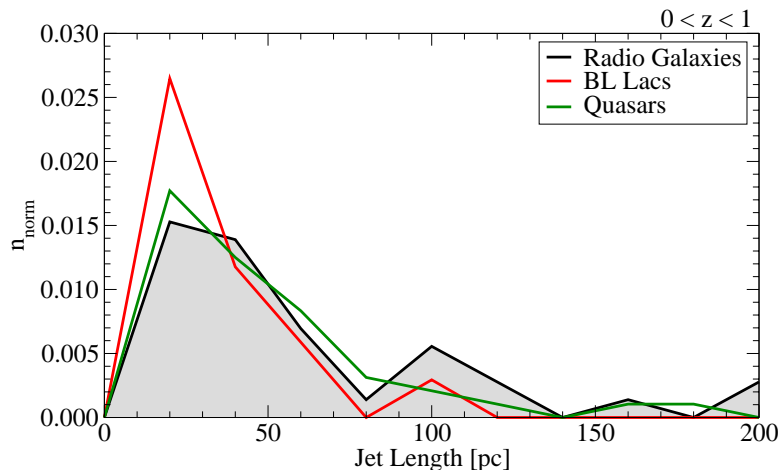


Figure 3.10: Distribution of jet lengths for the three classes of objects and for a redshift bin from 0 to 1: BL Lacs (red), QSOs (green), RGs (black). The histogram has been normalized to unity area for easier comparison of the different distributions.

### 3.5.1 Jet Lengths in the CJF

As was already described in the previous section, I anticipate RGs to have the longest jets and in turn, QSOs to have longer jets than BL Lacs. This is indeed what is observed. I note that in the following I use the maximum value of jet length for each source across all available epochs. In Fig. 3.10 I show a histogram of the distribution of jet lengths for QSOs, BL Lacs, and RGs with redshift lower than 1. The histogram has been normalized to unity area. **It is obvious that the BL Lac distribution is dominated by short-length jets.** In comparison, RGs appear to have a wider distribution, extending to higher values than their BL Lac counterparts. It should be however noted that the majority of all three classes have jets with lengths in the bins from 0 to 50 parsecs. A two-sample K-S test between pairs of the three classes does not give significant differences between them. This is in accordance with the line-of-sight effect and reflects the homogeneity of the distribution of the angles to the line-of-sight.

I can calculate the statistical properties of these three sub-samples. In Table 3.1 I give the average values for each class, along with the median, maximum, and minimum values (for sources with  $z \in [0, 1]$ ). One can immediately see that BL Lac objects indeed have the lowest average jet length. The high values of the uncertainties imply an uneven distribution of values. In this case the median values might be more representative of the samples. Again the BL Lacs show significantly lower median values<sup>5</sup> than both QSOs and RGs. Interestingly enough, QSOs appear to have on average longer jets, even compared to RGs. This is a redshift induced effect. The QSO sub-sample has a higher average redshift (0.64) compared to the BL Lacs (0.39) and the RGs (0.40). Accounting for this, I get an average jet length for QSOs of  $43 \pm 7$  pc, a value lower than that of RGs.

Having calculated the average jet lengths for the CJF objects, it is possible to define a

<sup>5</sup>The uncertainty for the median values is calculated as the median of the absolute deviation of the median from the measurements, divided by the square root of the number of measurements.

Table 3.1: Characteristic statistic values for the jet length of QSOs, BL Lacs, and RG. A redshift bin from 0 to 1 is used.

<b>Jet Length (pc)</b>	<b>QSO</b>	<b>BL</b>	<b>RG</b>
<b>#</b>	48	17	36
<b>Average</b>	51	35	50
<b>Error</b>	6	7	6
<b>Median</b>	27.1	17.3	31
<b>Error</b>	2.4	2.7	4
<b>Max</b>	284.7	203.5	195.7
<b>Min</b>	4.7	3.6	1.7

maximum core separation limit (for the reasons discussed in Sect. 3.4). As I am interested in the behavior of BL Lacs, I use them as the basis of this decision (see Table 3.1). I adopt a limit of 40 parsecs. All components at separations larger than 40 parsecs with respect to the core are not included in the following analysis. There is a further reasoning for this limit: for 1803+784, peculiar kinematics of the components is observed for the innermost part of its jet (up to 12 mas), with most robust effects out to 6 mas. For this source's redshift, this translates roughly to (82 pc) 41 pc. For a limit of 40 pc I probe the whole jet for a 60% of the CJF sources, while for approximately 17% of the CJF sources more than half of the jet is excluded from further analysis.

### Jet Length Evolution with $z$

The calculation of the same values for higher redshifts is unfortunately not robust. For a redshift bin between 1 and 2 there are only 4 BL Lac objects and 5 radio galaxies (compared to 85 QSOs). However, I can use smaller redshift bins and see whether the jet length changes as a function of redshift. In Fig. 3.11 I show the jet length as a function of  $z$  for QSOs, BL Lacs, and RGs. I use differential bins (widths range from 0.05 to 0.4) and calculate the corresponding average values. In addition, I plot the cosmological distance scale<sup>6</sup> (using the cosmological parameters given in Sec. 2.3) for a jet with an average length of  $8.5 \pm 1.0$  mas (value calculated from 14 QSOs with  $z \in [0, 0.5]$ ). The cosmological distance scale gives the intrinsic jet length for a jet of fixed apparent length that is observed at different redshifts. It reflects the expansion of the Universe and therefore indicates a passive evolution curve. Any deviation from this curve would indicate active evolution of the length of AGN jets.

From Fig. 3.11 one can draw a number of conclusions. For the redshift range  $[0, \sim 1]$  QSOs follow the cosmic distance scale line quite closely, with RGs consistently above the line and BL Lacs beneath (two values are above the line but exhibit very large errors). For  $z > 1$  reliable QSO points (small errors) appear to be consistently below the line and outside the  $1\sigma$  uncertainty margin. BL Lacs and RGs also are found below the cosmic

<sup>6</sup>To calculate the cosmological distances I use the simple relation  $d(AU) = \theta(mas)D_A(pc)$ , where in parentheses I put the units of each parameter. For the used system of units (pc and mas) the relation can be written as  $d(pc) \simeq 4.848\theta(mas)D_A(pc)$ .  $d$  is the distance,  $\theta$  the angular distance, and  $D_A$  the angular size distance (calculated from the redshift by Ned Wright's Cosmology Calculator; Wright et al. 1998).

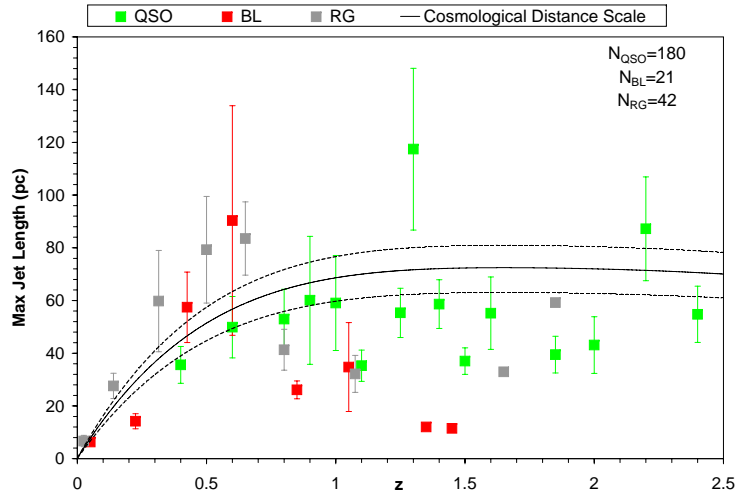


Figure 3.11: Average jet length as a function of redshift for QSOs (green), BL Lacs (red), and RGs (grey). The cosmological distance scale for a jet with an average length of  $8.47 \pm 1.03$  mas is shown (continuous line denotes the actual values, dashed lines show a  $1\sigma$  uncertainty deviation). In the upper right corner, the number of objects for each of the three classes -QSOs, BL Lacs, RGs- is given.

distance scale line<sup>7</sup>. The deviation of the average values of QSO jet lengths at higher redshifts from the ones anticipated by the cosmic distance scale line points towards an active evolution of the jet length with redshift. Jets of active galaxies at higher redshifts (possible younger AGN) appear to be intrinsically shorter than their counterparts in the local Universe.

### 3.5.2 Jet Morphology in the CJF

As I already discussed in Sect. 3.4, I qualitatively assess the jet morphology of the CJF sources by means of the monotonicity index. I investigate how, if at all, a jet resembles a sinusoid (as in the case of S5 1803+784). In order to do this I calculate the M.I. from the jet ridge lines of the CJF sources. The M.I. is calculated for the whole jet (I do not apply the core separation limit of 40 pc), as I am interested in the morphology of the entire jet, rather than a localized property. In addition, a large number of components is needed for a robust interpretation of the M.I.. For a jet consisting of 2 components, a high M.I. does not reflect a sinusoid-like morphology (see Fig. 3.12 for an example). In order to study the morphology of the jets, I therefore take into account only epochs with at least three components identified. Furthermore, I define the maximum M.I. value for each source across the available epochs. In this way an evolution of the jet morphology with time is taken into account, that would possibly mask the effect I am looking for.

<sup>7</sup>Most points for BL Lacs and RG at  $z > 1$  reflect the values of individual objects rather than an average value, as a result of the absence of enough identified high-redshift objects of these two classes. This is denoted by the absence of an error for these points.



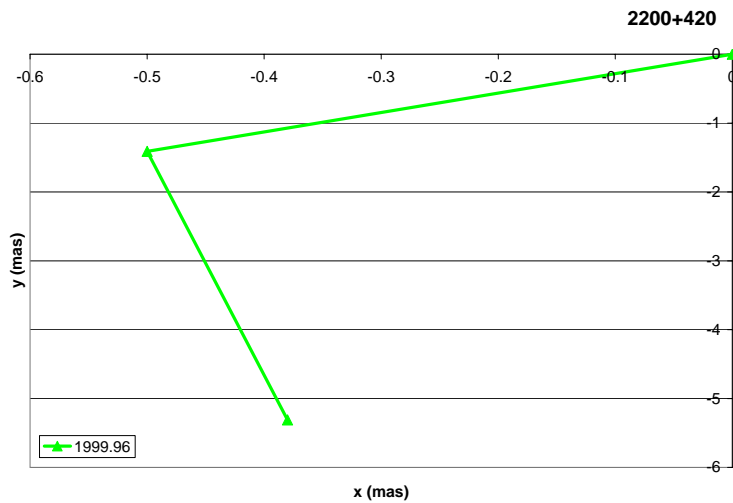


Figure 3.12: Jet ridge line of 2200+420 for epoch 1999.96. Only two components (C1, C4) are identified in this epoch. C1 is identified as an extremum. This results in a M.I. value of 1.

**Under the above constrains, I find that BL Lacs show more often jets with sinusoid-like morphologies, compared to both QSOs and RGs** (see Table 3.2 for average and median values). In addition to this, more than half of the QSOs ( $\sim 51\%$ ) have an M.I. value of 0, while two thirds ( $\sim 66\%$ ) have an M.I. value lower than 0.5. For RGs the respective percentages are  $\sim 41\%$  and  $\sim 66\%$ . In contrast to this, only one third of the BL Lacs ( $\sim 33\%$ ) have M.I.=0 and less than half ( $\sim 44\%$ ) of them have M.I.< 0.5. In Figure 3.13 I show the normalized M.I. distributions of the three different classes. BL Lacs show a strong maximum in the  $[0.6,0.8)$  bin. In contrast, both QSOs and RGs have their maxima in the  $[0,0.2)$  bin. Interestingly, for the highest bin of  $[1,1.2)$ , BL Lacs appear to show a lower occurrence than both QSOs and RGs.

Table 3.2: Characteristic statistic values for the jet length of QSOs, BL Lacs, and RG. A redshift bin from 0 to 1 is used.

M.I.	QSO	BL	RG
#	77	18	29
<b>Average</b>	0.29	0.36	0.35
<b>Error</b>	0.03	0.06	0.06
<b>Median</b>	0	0.5	0.33

High resolution VLBI observations have revealed that the curvature of jets is ubiquitous, especially for the inner parts closer to the core. Several authors have studied such bent jets (e.g., Krichbaum et al. 1994; Britzen et al. 1999b; Britzen et al. 2000; Walker et al. 2001; Lister 2001; Britzen et al. 2005b; Britzen et al. 2005a). For the CJF, Britzen et al. (2008) find a surplus of BL Lac objects exhibiting larger bents, of the order of

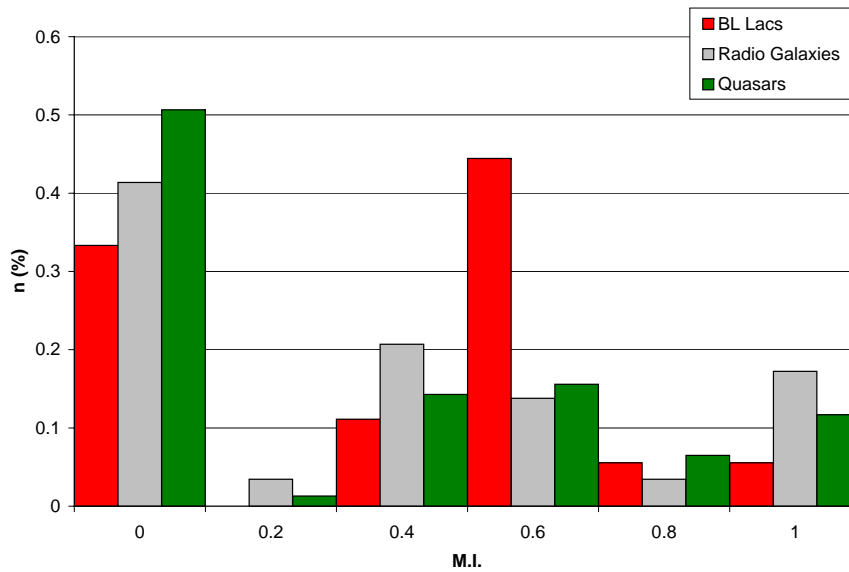


Figure 3.13: Normalized histogram of the M.I. distribution for BL Lacs (red), QSOs (green), and RGs (grey). Only the maximum M.I. values per source across all available epochs is taken into account here. I exclude epochs with less than 3 components identified.

90 degrees, significantly more than QSOs and RGs (21% compared to 5% and 7% respectively). The M.I., although including the effects of localized bending calculated by Britzen et al. (2008), infers information about the whole jet, in essence differentiating between a monotonic jet (either straight, or single bent) and a sinusoid-like jet (with multiple bends along its length). **In this sense and context, BL Lacs indeed are found to show sinusoid-like curved jets, as seen for S5 1803+784 and 0716+714.** In Sect. 3.7 the implications of these results will be discussed in more detail.

### 3.5.3 Jet Widths, $P$ , in the CJF

I am interested in studying the width of the CJF jet ridge lines and comparing between the three different classes of objects. In Sect. 3.4, I briefly discussed the concept of localized width and how this relates to the measure I am going to investigate here. In order to better understand this relation, I study how the distribution of the widths of the CJF jet ridge lines<sup>8</sup> relates to the maximum distance between the two components used to calculate this width. For this step, I do not use any redshift bins, in order to maximize the number of available sources used to investigate the effect of localization.

Using a total of more than 500 epochs, I calculate an average jet ridge line width for the CJF sources. Without imposing any constraints on the maximum distance between the components used<sup>9</sup>, **I find that BL Lacs show significantly wider jet ridge lines (average**

<sup>8</sup>The width of the jet ridge line is defined as the difference in position angle between the two components with the maximum and the minimum position angle at each individual epoch.

<sup>9</sup>Here a universal limit of 40 pc in core separation from the core is imposed to all the available data.

Table 3.3: Characteristic statistic values of the whole CJF sample concerning the width of the jet ridge line. I give average and median values with uncertainties, maximum, and minimum values for QSOs, BL Lacs, and RGs. The noted distance pertains to the maximum distance between the two components used to calculate the jet ridge line width (see text for details).

<b>Jet Width (<math>^{\circ}</math>)</b>									
<b>Distance (pc)</b>	All			< 20			< 5		
<b>Types</b>	QSO	BL	RG	QSO	BL	RG	QSO	BL	RG
<b>#</b>	353	77	111	251	45	72	18	15	22
<b>Average</b>	11.9	22.6	16.7	10.8	18.2	16.5	17	17	25
<b>Error</b>	0.4	1.9	1.0	0.5	2.1	1.2	3	3	3
<b>Median</b>	8.7	16.5	13.0	7.00	10.6	13.2	8.9	12.9	18.2
<b>Error</b>	0.3	1.2	0.7	0.28	1.1	0.9	1.5	1.5	2.2
<b>Max</b>	86.4	96.9	72.8	86.4	51.9	72.8	47.7	51.2	72.8
<b>Min</b>	0.1	0.7	0.2	0.1	0.9	0.2	0.1	1.6	3.0

**value of  $22.6 \pm 1.9^{\circ}$ , compared to both QSOs ( $11.9 \pm 0.4^{\circ}$ ) and RGs ( $16.7 \pm 1.0^{\circ}$ ).** The same behavior is seen when median values are taken into account (for all parameters see Table 3.3). I can now impose a constrain of 20 pc for the maximum distance at which the width is calculated. The BL Lacs still show wider jet ridge lines (average value of  $18.2 \pm 2.1^{\circ}$ ), compared to RGs ( $16.5 \pm 1.2^{\circ}$ ) and QSOs ( $10.8 \pm 0.5^{\circ}$ ). It is interesting that within errors BL Lacs and RGs show similar average values. When looking at median values, although BL Lacs show higher values than QSOs, RGs appear to show the highest median value. This reversal of relative widths becomes even more prominent if I assume a more stringent constrain of 5 pc for the distance. Radio galaxies show wider jets (average values of  $25 \pm 3^{\circ}$ ), while BL Lacs and QSOs show the same average values ( $17 \pm 3^{\circ}$  and  $17 \pm 3^{\circ}$ , respectively). In median values RGs appear wider, with BL Lacs remaining wider than QSOs. Please note that there is a heavy loss of information when narrowing down the selection through the distance constraints. This becomes obvious by the absolute number of epochs used for each case (Table 3.3). When going from using no distance constraint to a constraint of 5 pc, I discard more than 80% of information for BL Lacs and RGs, while almost 95% of the QSO epochs are discarded. Low number statistics does not allow us to draw a robust conclusion for the localized width of the CJF jet ridge lines.

However, distance is only one parameter affecting the results. As I already discussed, redshift also introduces spurious effects in this comparison. This effect needs to be assessed. To this end, I investigate sources in the redshift bin  $[0,1]$ . Although the redshift span of the CJF goes out to almost 4, only 19 of the BL Lacs included in the CJF have redshift information. Of these, 17 are below redshift 1. Therefore for the following I will

---

Any components at larger core separations are disregarded. This translates to an implicit maximum distance between the components used for the calculation of width to 40 pc.

Table 3.4: Characteristic statistic values concerning the width of the jet ridge line of sources with measured redshifts. I give average and median values with uncertainties, maximum, and minimum values for QSOs, BL Lacs, and RGs. The noted distance pertains to the maximum distance between the two components used to calculate the jet ridge line width (see text for details).

Jet Width ( $^{\circ}$ ), $0 < z$						
Types	QSO		BL		RG	
Distance (pc)	All	< 20	All	< 20	All	< 20
#	343	251	55	45	95	72
<b>Average</b>	12.0	10.8	19.8	18.2	16.3	16.5
<b>Error</b>	0.4	0.5	2.1	2.1	1.0	1.2
<b>Median</b>	8.7	7.00	11.7	10.6	13.0	13.2
<b>Error</b>	0.3	0.28	1.1	1.1	0.7	0.8
<b>Max</b>	86.4	86.4	93.2	51.9	72.8	72.8
<b>Min</b>	0.1	0.1	0.7	0.9	0.2	0.2

Jet Width ( $^{\circ}$ ), $0 < z < 1$						
Types	QSO		BL		RG	
Distance (pc)	All	< 20	All	< 20	All	< 20
#	91	76	50	43	83	62
<b>Average</b>	11.1	10.5	21.1	18.4	16.6	16.4
<b>Error</b>	0.8	0.9	2.3	2.1	1.2	1.4
<b>Median</b>	7.5	6.5	13.4	10.6	12.3	10.8
<b>Error</b>	0.5	0.5	1.3	1.1	0.7	0.8
<b>Max</b>	47.7	47.7	93.2	51.9	72.8	72.8
<b>Min</b>	0.1	0.1	0.9	0.9	0.2	0.2

focus my investigation to sources up to redshift 1. In Table 3.4 I show the characteristic statistical parameters for the CJF jet ridge line widths for all sources with available redshift, as well as sources in the redshift bin  $[0,1]$ . Given the above analysis concerning the distance constraints, in Table 3.4 I give values also for the case where a 20 pc constrain for the distance is assumed<sup>10</sup>.

The jet ridge line width appears to be independent of redshift. To test this further, I use the sub-sample of CJF QSOs to calculate average and median width values for different redshift bins. The values are shown in Fig. 3.14. It can be seen that out to  $z=2.5$  the jet ridge line width remains fairly stable, with the median value showing larger changes than the average. For the last two bins, the number of sources contained drops drastically (as

<sup>10</sup>I note that, when using the 20 pc distance constraint, I exclude on average around 35% of the available epochs.

reflected by the much larger error bars) and therefore it is difficult to conclude whether the strong increase in both average and median values is a true or a spurious effect. It should be noted that this sharp increase coincides with the epoch of maximum nuclear and star-formation activity in the Universe (at  $z \sim 2-3$ , e.g., [Hasinger 1998](#); [Madau et al. 1996](#)). Focusing on the redshift bin  $[0,1]$ , from Table 3.4, I find that **BL Lac jet ridge lines appear significantly wider ( $\sim 5\sigma$ ) than their QSO counterparts ( $21.1 \pm 2.3^\circ$ , compared to  $11.1 \pm 0.8^\circ$ ). The same behavior is seen when looking at the median values.** Considering the values when the distance limit is assumed, BL Lacs remain substantially wider (at a  $\sim 4\sigma$  significance level). Radio galaxies appear to have narrower jet ridge lines than BL Lacs, but at a lower significance level ( $2\sigma$ ).

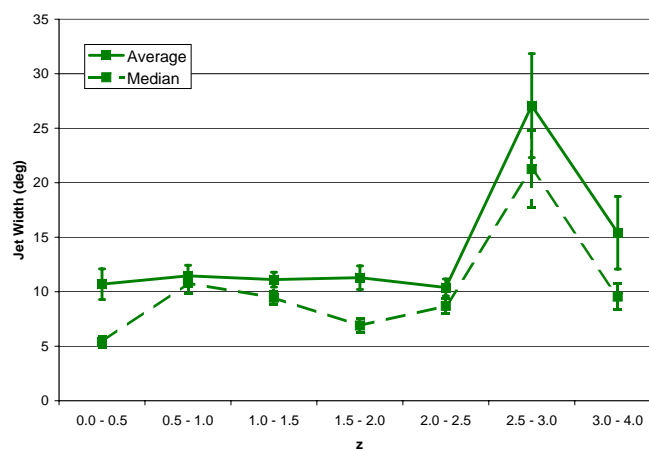


Figure 3.14: Jet width for CJF QSOs, as a function of redshift. I use 0.5 redshift binning to calculate averages (continuous line) and median values (dashed line). Number of sources per bin: 38 (0-0.5), 53 (0.5-1), 106 (1-1.5), 61 (1.5-2), 55 (2-2.5), 18 (2.5-3), 12 (3-4).

In Fig. 3.15 I show the distribution of jet ridge line widths for BL Lacs, QSOs, and RGs, in the redshift bin  $[0,1]$ . It can be seen that all three classes show similar distributions, with their maxima situated at around 10 degrees. **The distribution of BL Lac appears to be wider and extending to larger widths compared to QSOs.** Comparing the secondary maxima for BL Lacs and QSOs, I find that BL Lacs show a secondary maximum at 60 degrees with a ratio of secondary to primary of 0.35. In comparison, QSOs show their secondary maximum at around 50 degrees with a ratio of 0.1, showing a distribution much more contained to lower width values. Radio galaxies appear similar to BL Lacs, also showing a more extended distribution, with a weak secondary maximum also at 60 degrees (secondary to primary ratio of 0.07).

I apply the two-sample K-S test to the data to see whether the three classes of AGN, BL Lacs, QSOs, and RGs, are indeed different in their jet ridge line widths. Comparing the jet ridge line widths of BL Lacs and QSOs (no redshift binning or distance constraints)

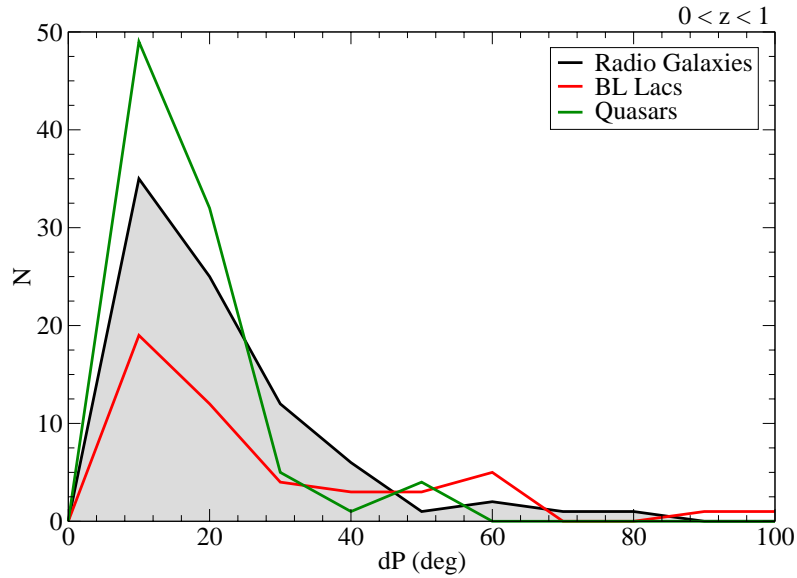


Figure 3.15: Jet ridge line width (absolute) distribution for BL Lacs (red), QSOs (green), and RGs (black). For this histogram sources with redshifts in the  $[0,1]$  bin are used.

the K-S test gives a probability of  $0.7 \cdot 10^{-5}$  that these two sub-samples originate from the same parent distribution. Comparing QSOs with RGs, I get a similar probability of  $0.7 \cdot 10^{-2}$ . The K-S test gives a 22.1% probability that BL Lacs and RGs come from the same sample. Given that BL Lac and RG jets are markedly different in appearance and properties, it is interesting to investigate whether this apparent similarity with regard to this feature is true or not. I also compare the sub-samples of BL Lacs, QSOs, and RGs in the redshift bin  $[0,1]$ . In this case the K-S test gives a probability of 1% that BL Lacs and QSOs are drawn from the same parent sample. For BL Lacs and RGs the probability is again of the order of 22.1%. Finally, I also apply the K-S test after assuming the 20 pc distance constraint. In this case I get a 4.4% probability for BL Lacs and QSOs, and 41.7% for BL Lacs and RGs. This indicates that indeed the jet width distributions for BL Lacs and RGs are somewhat similar. Whether this is a true similarity or some data effect can not yet be addressed here. I shall return to this point in Sect. 3.7. **I can conclude however that BL Lacs show a significantly different distribution of jet ridge line widths compared to QSOs. In both average and median values, BL Lacs show substantially wider jets than both QSOs and RGs.**

### Jet Widths and Variability

In Chap. 2, Sect. 2.9, I discussed the origins of long-timescale variability in AGN. I explained such variability in the context of jet precession (possibly as a result of a binary core) and Doppler beaming effects. I am now interested in exploring this connection, namely a possible link between variability and the jet kinematics as investigated in this chapter. I therefore create a sub-sample that includes the 40 CJF sources shown to exhibit variability (see Table A.6) and study its properties relating to their jet ridge line

Table 3.5: Characteristic statistic values concerning the width of the jet ridge lines of sources identified as variable (see Table A.6 and Sect. 2.5, Chap. 2). I give average and median values with uncertainties, maximum, and minimum values for the whole sub-sample, QSOs, BL Lacs, and RGs.

<b>Jet Width (<math>^{\circ}</math>)</b>				
	<b>All</b>	<b>QSO</b>	<b>BL</b>	<b>RG</b>
<b>#</b>	81	28	44	9
<b>Average</b>	18.3	22.0	17.1	12.9
<b>Error</b>	1.3	2.7	1.7	2.1
<b>Median</b>	15.7	17.8	13.5	13.4
<b>Error</b>	0.9	1.6	1.3	1.9
<b>Max</b>	86.4	86.4	51.6	28.1
<b>Min</b>	0.9	1.3	0.9	1.2

widths. In Table 3.5 I show the parameters of this sub-sample. Given the small number of sources/epochs for this investigation, I impose no redshift or distance constraints on this sub-sample.

Compared to the parent sample, the sub-sample of variable sources exhibits both higher average and median values than the whole sample ( $18.3 \pm 1.3^{\circ}$  and  $15.7 \pm 0.9^{\circ}$ , compared to  $14.4 \pm 0.4^{\circ}$  and  $9.70 \pm 0.26^{\circ}$  respectively). In Fig. 3.16 I plot the jet ridge line width distribution for the sub-sample of variable sources, as well as for the rest of the CJF. I see that the parent (non-variable<sup>11</sup>) CJF sample shows a strong maximum in the lowest bin  $[0^{\circ}, 8^{\circ}]$  with a decreasing trend. In contrast, the sub-sample of variable sources shows two maxima in bins  $[0^{\circ}, 8^{\circ}]$  (main) and  $[16^{\circ}, 24^{\circ}]$  (secondary), with a secondary to primary ratio of  $\sim 0.9$ . A third, weak, peak is seen around 50 degrees. **Variable CJF sources indeed show a more extended distribution of jet ridge line widths, shifted towards higher values compared to the parent CJF sample.** A K-S test gives a very low (0.3%) probability that the two sub-samples are drawn from the same parent population.

I also check the average and median values for the individual classes. Although BL Lacs appear to maintain the same average width as their parent sample (within errors), they show higher median value ( $13.5 \pm 1.3^{\circ}$ , compared to  $10.6 \pm 1.1^{\circ}$ ). In addition QSOs appear to have both much higher average ( $> 4\sigma$  difference) and median values than their parent sample ( $22.0 \pm 2.7^{\circ}$  and  $17.8 \pm 1.6^{\circ}$ , compared to  $10.8 \pm 0.5^{\circ}$  and  $7.00 \pm 0.28^{\circ}$  respectively). Variable RGs show equally interesting behavior, with lower average ( $12.9 \pm 2.1^{\circ}$ , compared to  $16.5 \pm 1.2^{\circ}$ ) but similar median value. **There seems to be a strong connection between variability and jet kinematics.** I will discuss this link more extensively in Sect. 3.7.

<sup>11</sup>The number of variable sources is explicitly regulated by the availability, or lack thereof, of the appropriate observations (long-timescale variability can be uncovered only by means of extensive monitoring of a source). Some of the sources labeled here as "non-variable" are probably variable but not observed as such.

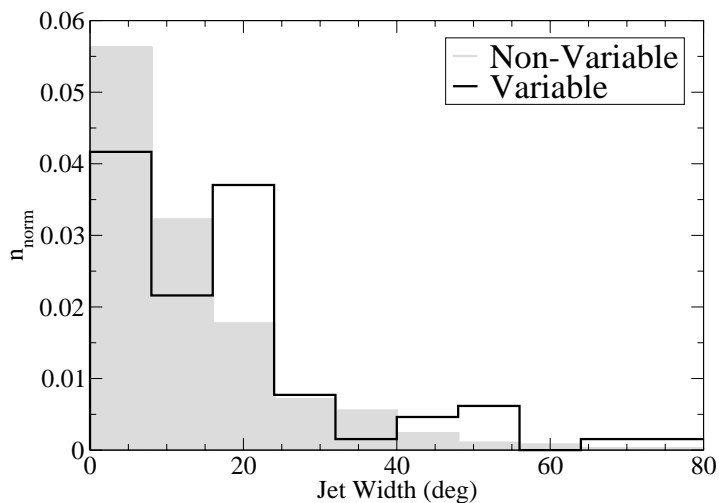


Figure 3.16: Jet ridge line width distribution for the sub-sample of variable sources from Table A.6 (black line) and for the rest (non-variable) CJF sample (grey blocks). Due to the big difference in absolute numbers for the two samples, I normalized to unity surface area. No redshift or distance constraints are assumed.

### 3.5.4 Jet Width Evolution, $\Delta P$ , in the CJF

One of the characteristics seen in S5 1803+784 (as well as in 0716+714) is the significant change of the jet ridge line morphology and width. As Britzen et al. (2010a) demonstrated (see Fig. 3.7 and Fig. 10 of that paper), the width of that source changes with a period of  $\sim 8.5$  years. I want to investigate whether this kind of behavior is common for all AGN and whether BL Lacs differentiate themselves from the rest of the sample. Before I move on to the results, there is one effect that needs to be discussed. I have mentioned before that component identification is unimportant when working with jet ridge lines. While this is true, the actual detection of the same number of components across different epochs does have some importance to the results. The effect of a vanishing component (either due to diminishing flux, bad observing conditions, or otherwise flawed data) will induce a spurious width change, affecting the overall statistics of the sample. Although, in the case of diminishing flux, one could argue that this change is indeed intrinsic and therefore important, often the latter two effects dominate. Moreover, as I already mentioned in Sect. 3.4, the given sensitivity and dynamic range of the observations define my results. For much more sensitive observations, jets would probably appear rather wider than what I find here.

To take this effect into account, I flag the data accordingly. The best quality data are those for which a width change is calculated between epochs with the same number of components identified per source. Width changes calculated between epochs with  $\pm 1$  number of identified components are flagged as moderate quality data. If the number of components varies by 2 or more, the data are flagged as bad. In Table 3.6 the number of



Table 3.6: Three different types of flagging for the CJF data, along with their definition. For each category the corresponding number for each class of object is shown.

	Definition	# of epochs		
		QSO	BL	RG
<b>OK</b>	$N_l = N_{l+1}$	173	26	54
<b>!</b>	$N_l = N_{l+1} \pm 1$	53	21	15
<b>NO</b>	$N_l \geq N_{l+1} \pm 2$	2	2	5

epochs for each class of object with each of the corresponding flags is shown. As can be seen, QSOs and RGs have the best quality of data, with only 24% and 27% respectively of the data flagged as mediocre ("!" and "NO" flag). In contrast BL Lacs have almost half their data (47%) flagged accordingly. This reflects the difficulty of a consistent component model-fitting of BL Lac jets across epochs. This is a result of (1) the variable nature of these objects, (2) the shorter length of their jets, combined with the higher number of components per jet, that leads to confusion effects between components (compared for example to QSO jets), and (3) the fact that BL Lacs are intrinsically fainter than QSOs. The effect of this shall be discussed in more detail later on.

As I described in Sect. 3.4, I use both individual jet ridge line width evolution values across two successive epochs, as well as the maximum values between these for each source. The first approach offers a larger number of values to work with, effectively pushing down the uncertainty levels of the final results. Conversely, the second method offers a more characteristic distribution of values, undiluted, for example, by the varying number of epochs for different sources.

In Table 3.7, I show the statistical properties of the jet width evolution distribution for the different classes of objects. As before, I employ redshift binning to see whether values change considerably with redshift. Unlike with the previous section, here I do not assume any separation constraints between the components used to calculate the individual widths, simply because then a very large part of the data would have to be excluded. I only consider values flagged as OK, or ! (see Table 3.6). The results are ambiguous. Perhaps surprisingly, RGs appear to show larger variations of their jet ridge line width both in average and median values. Comparing between BL Lacs and QSOs, BL Lacs show on average larger variations than QSOs (although only marginally). When studying the [0,1] redshift bin, BL Lacs appear to differentiate more clearly from QSOs (at a  $2\sigma$  level). In contrast to that, both for all sources, as well as for those in the [0,1] redshift bin, QSOs show higher median values than their BL Lac counterparts.

As the above results are non-conclusive, I turn to the distribution of maximum jet ridge line width evolution. The same constraints as above hold. I use redshift binning, no separation constraints, and I exclude values flagged as "NO". For the whole sample, I see that RGs still show the largest width evolution between the three classes, with QSOs showing the lowest. The same holds for median values. When using a redshift bin of [0,1], the situation changes substantially. BL Lac objects show the higher average and median

Table 3.7: Statistical properties of the jet width evolution distribution for QSOs, BL Lacs, and RGs. Average, median, maximum, and minimum values are calculated for both all sources with available redshifts ( $0 < z$ ), as well for sources in the redshift bin  $[0,1]$ . Sources flagged as "NO" are excluded.

<b>Jet width evolution (<math>deg/yr</math>) - Flag: "OK", "!"</b>						
<b>Types</b>	$0 < z$			$0 < z < 1$		
	<b>QSO</b>	<b>BL</b>	<b>RG</b>	<b>QSO</b>	<b>BL</b>	<b>RG</b>
<b>#</b>	220	33	59	58	30	51
<b>Average</b>	2.50	3.2	3.4	2.41	3.1	3.7
<b>Error</b>	0.13	0.5	0.3	0.25	0.5	0.4
<b>Median</b>	1.56	1.53	2.37	1.65	1.61	2.42
<b>Error</b>	0.06	0.21	0.20	0.14	0.23	0.23
<b>Max</b>	27.11	18.32	20.74	24.39	18.32	20.74
<b>Min</b>	0.05	0.09	0.06	0.15	0.09	0.06

values ( $4.7 \pm 0.8^\circ/yr$  and  $3.6 \pm 0.5^\circ/yr$ , compared to  $3.5 \pm 0.4^\circ/yr$  and  $2.42 \pm 0.20^\circ/yr$ , and  $3.7 \pm 0.4^\circ/yr$  and  $2.73 \pm 0.27^\circ/yr$  for QSOs and RGs, respectively). When checking the maximum and minimum values of each sub-sample, it becomes obvious that QSOs and BL Lacs show much more extended distributions compared to RGs. I however note the substantial drop in the available data for this last comparison (71, compared to a total of 288). This is reflected in the high relative uncertainties for the average values for all three sub-samples ( $\sim 13\%$  for QSOs and RGs, and  $\sim 17\%$  for BL Lacs).

In Fig. 3.17 the distributions for the maximum jet ridge line width evolution is shown for QSOs, BL Lacs, and RGs. I use a redshift bin of  $[0,1]$  and exclude all data flagged as "NO" (this corresponds to the right part of Table 3.8). BL Lac objects show a wide distribution of jet width evolution values, with a primary maximum at 3 degrees/yr, with several secondary maxima (at 6 and 10 degrees/yr, with secondary to primary ratio of 0.84 and 0.39, respectively). Radio galaxies show a somewhat similar behavior with a plateau between 2 and 4 degrees/yr and a secondary maximum at 8 degrees (secondary to primary ratio 0.35). Quasars, in contrast, show a confined distribution with a strong maximum around 3 degrees/yr and all values contained between 0 and 10 degrees/yr. I apply the K-S test to see whether these differences are significant or not. Concentrating on the comparison in the  $[0,1]$  redshift bin, the K-S test gives a probability of 33.8% that QSOs and BL Lacs are drawn from the same parent sample. Although this result is not as conclusive as the one seen in the previous subsection, I can tentatively say that indeed BL Lacs show on average larger changes in their jet ridge line width, as compared to QSOs.

### Jet Width Evolution and Variability

I am interested in investigating a possible link between long-time scale variability and the kinematics of the jet, as studied here. I therefore use again the sub-sample of the 40 CJF

Table 3.8: Statistical properties of the maximum jet width evolution distribution for QSOs, BL Lacs, and RGs. Average, median, maximum, and minimum values are calculated for both all sources with available redshifts ( $0 < z$ ), as well for sources in the redshift bin  $[0,1]$ . Sources flagged as "NO" are excluded.

<b>Jet width evolution (max) (<i>deg/yr</i>)</b>						
<b>Types</b>	$0 < z$			$0 < z < 1$		
	<b>QSO</b>	<b>BL</b>	<b>RG</b>	<b>QSO</b>	<b>BL</b>	<b>RG</b>
<b>#</b>	111	18	30	29	16	26
<b>Average</b>	3.48	4.8	3.6	3.5	4.7	3.7
<b>Error</b>	0.23	0.8	0.4	0.4	0.8	0.4
<b>Median</b>	2.27	3.6	3.05	2.42	3.6	2.73
<b>Error</b>	0.13	0.5	0.26	0.20	0.5	0.27
<b>Max</b>	27.11	18.32	11.84	24.39	18.32	11.84
<b>Min</b>	0.16	0.34	0.51	0.41	0.34	0.51

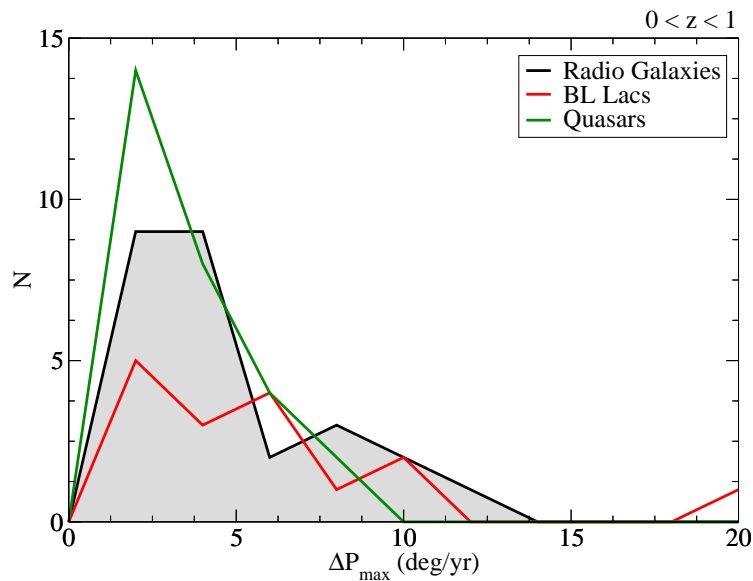


Figure 3.17: Maximum jet ridge line width evolution distribution for QSOs (green), BL Lacs (red), and RGs (black). Sources with redshift lower than 1 are used. Sources flagged as "NO" (see text for detail) are excluded.

sources shown to exhibit variability (see Table A.6) and study its properties relating to their maximum jet ridge line width evolution. In Table 3.9, I show the parameters of this sub-sample. Given the small number of sources/epochs for this investigation, I impose no redshift constraints on this sub-sample. As previously explained, data flagged as "NO"

are excluded.

Table 3.9: Characteristic statistic values concerning the width evolution of the jet ridge lines of sources identified as variable (see Table A.6 and Sect. 2.5, Chapter 2). I give average values with errors, median, maximum, and minimum values for the whole sub-sample, QSOs, BL Lacs, and RGs. Data flagged as "NO" are excluded.

<b>Jet Width Evolution (max) (<math>^{\circ}</math>)</b>				
	<b>All</b>	<b>QSO</b>	<b>BL</b>	<b>RG</b>
<b>#</b>	26	9	14	3
<b>Average</b>	5.5	8.4	4.5	1.9
<b>Error</b>	0.9	2.3	0.9	0.6
<b>Median</b>	3.1	5.0	2.5	1.6
<b>Error</b>	0.4	1.0	0.5	1.0
<b>Max</b>	24.39	24.39	18.32	3.35
<b>Min</b>	0.34	0.74	0.34	0.69

Compared to the parent sample, the sub-sample of variable sources exhibits both higher average and median values ( $5.5 \pm 0.9^{\circ}/yr$  and  $3.1 \pm 0.4^{\circ}/yr$ , compared to  $3.51 \pm 0.18^{\circ}/yr$  and  $2.37 \pm 0.11^{\circ}/yr$  respectively). In Fig. 3.18 I plot the maximum jet ridge line width evolution distribution for the sub-sample of variable sources, as well as for the rest (non-variable) CJF sources. Both samples show a similar distribution for bins up to 7.5 deg/yr. For both samples, the total maximum of the distribution occurs in the [0,2.5] bin, with the variable CJF sources showing a weaker maximum compared to the non-variable sample (as well as lower values for the bins [2.5,5] and [5,7.5]), while extending to the highest values, up to 25 deg/yr. Applying the K-S test to the two sub-samples I get a 17.6% probability that they are drawn from the same parent population.

I can also check average and median values for the individual classes. BL Lacs appear to maintain both the same average width as their parent sample (within errors), as well as the same median value ( $2.5 \pm 0.5^{\circ}/yr$ , compared to  $2.3 \pm 0.3^{\circ}/yr$ ). In addition, QSOs appear to have both higher average ( $> 2\sigma$  difference) and median values than their parent sample ( $8.4 \pm 2.3^{\circ}/yr$  and  $5.0 \pm 1.0^{\circ}/yr$ , compared to  $3.44 \pm 0.22^{\circ}/yr$  and  $2.26 \pm 0.13^{\circ}/yr$  respectively). Variable RGs show equally interesting behavior, with lower average ( $1.9 \pm 0.6^{\circ}/yr$ , compared to  $3.3 \pm 0.3^{\circ}/yr$ ) and median values ( $1.6 \pm 1.0^{\circ}/yr$ , compared to  $2.48 \pm 0.20^{\circ}/yr$ ). It should be noted that, especially for RGs, this comparison is problematic due to the small number of sources (3 RGs). However, there seems to be a connection between variability and jet kinematics, as is seen for QSOs, that exhibit significantly stronger changes of their jet widths. I will discuss this link more extensively in Sect. 3.7.

### 3.5.5 Jet Linear Evolution, $\Delta\ell$ , in the CJF

Focusing on the final measure of the jet ridge line kinematics, as studied in this work, I want to investigate whether the stationarity of components, as observed in the case of S5

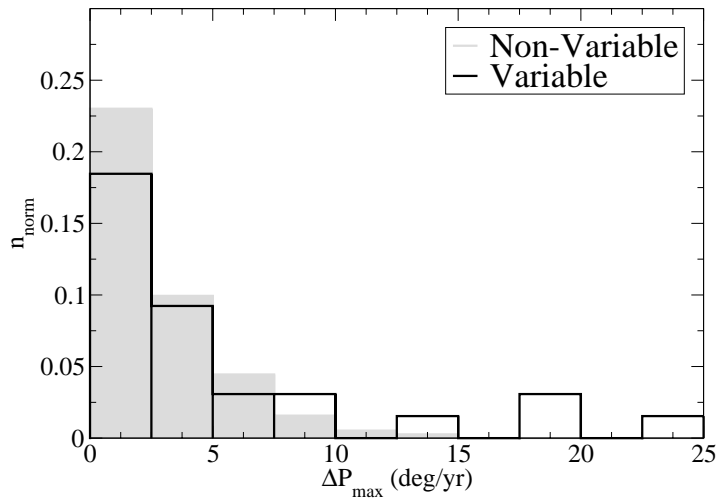


Figure 3.18: Maximum jet ridge line width evolution distribution for the whole (non-variable) CJF (parent) sample (grey blocks) and for the sub-sample of variable sources from Table A.6 (black line). Due to the big difference in absolute numbers for the two samples, the histogram is normalized to unity surface area. No redshift or distance constraints are assumed. Data flagged as "NO" are again excluded.

1803+784, is commonplace among other BL Lacs or it amounts to a peculiarity of that source. I use the linear evolution measure<sup>12</sup>, as described in Sect. 3.4, to do this. I follow the same procedure as in the previous subsections, to check the statistics of the individual classes.

In Table 3.10 I give the statistical properties of the total linear evolution of the jet ridge line distributions for QSOs, BL Lacs, and RGs (measured in parsecs per unit time and component). On average, BL Lacs show weaker evolution of their jet ridge lines compared to QSOs ( $0.38 \pm 0.05$  pc/yr/comp and  $0.470 \pm 0.016$  pc/yr/comp, respectively). Radio galaxies show even weaker evolution ( $0.34 \pm 0.03$  pc/yr/comp), although, within errors, this is of the same order as for the BL Lacs. Looking at the median values, BL Lacs show the least evolution compared to both QSOs and RGs ( $0.236 \pm 0.026$ ,  $0.414 \pm 0.012$ , and  $0.281 \pm 0.024$  pc/yr/comp respectively). In order to exclude any redshift induced effects, I also study the statistics of the sub-sample of CJF sources in the [0,1] redshift bin (also in Table 3.10). The behavior remains the same as before, with differences between BL Lacs and QSOs becoming more pronounced (however the errors also increase, given the smaller number of sources).

I now turn to the actual distribution of the total jet linear evolution for the three types of objects, shown in Fig. 3.19. Once again only sources in the redshift bin [0,1] are taken into account. Quasars show a pronounced maximum around 0.63 pc/yr/comp, with

<sup>12</sup>For the total linear evolution of each jet ridge line, I take into account only components at core separation smaller than 40 pc, cross-identified across each pair of successive epochs (see Sect. 3.4). Only sources with available redshifts are taken into account.

Table 3.10: Statistical properties of the total jet linear evolution distribution for QSOs, BL Lacs, and RGs. Average, median, maximum, and minimum values are calculated for both all sources with available redshifts ( $0 < z$ ), as well as for sources in the redshift bin  $[0,1]$ . These numbers pertain to the inner part of the jet ( $< 40$  pc).

<b>Jet linear evolution (<math>pc/yr/comp</math>)</b>						
<b>Types</b>	$0 < z$			$0 < z < 1$		
	<b>QSO</b>	<b>BL</b>	<b>RG</b>	<b>QSO</b>	<b>BL</b>	<b>RG</b>
<b>#</b>	171	21	41	44	17	35
<b>Average</b>	0.470	0.37	0.34	0.51	0.38	0.32
<b>Error</b>	0.016	0.05	0.03	0.04	0.06	0.03
<b>Median</b>	0.414	0.236	0.281	0.495	0.236	0.249
<b>Error</b>	0.012	0.026	0.024	0.027	0.029	0.021
<b>Max</b>	1.910	1.081	0.989	1.910	1.081	0.989
<b>Min</b>	0.028	0.038	0.028	0.028	0.038	0.028

a secondary maximum around  $0.37$  pc/yr/comp (secondary to primary ratio  $\sim 0.62$ ) and a weaker third one around  $0.87$  pc/yr/comp (ratio to primary  $\sim 0.23$ ). In contrast, both BL Lacs and RGs show their distribution maxima around  $0.25$  pc/yr/comp, with secondary maxima around  $0.63$  (ratio to primary  $\sim 0.3$ ) and  $0.87$  pc/yr/comp (ratio to primary  $\sim 0.3$ ) for RGs, and around  $0.87$  pc/yr/comp for BL Lacs (ratio to primary  $\sim 0.33$ ). Quasars appear to have a wider distribution of total linear evolution values, also showing the highest maximum values among all three types (see Table 3.10). Interestingly, RGs and BL Lacs, in total, show very similar distributions. Once again I employ the K-S test to compare the distributions. For the whole sample (independent of redshift constraints), the K-S test gives a probability of 4.3% that BL Lacs and QSOs are drawn from the same parent population. For BL Lacs and RGs this probability raises to 49.5%. Focusing on the  $0 < z < 1$  sub-sample, I get a 5.4% probability from the K-S test that BL Lacs and QSOs stem from the same parent sample (46.1% for BL Lacs and RGs). These results, although giving a positive answer as to whether BL Lacs show less absolute linear evolution of their jets compared to their QSO counterparts, are somewhat surprising concerning the comparison between BL Lacs and RGs. Possible insight to this result is given by Fig. 3.2, although one would nevertheless expect RGs to show stronger evolution than BL Lacs, although still lower than QSOs. I will discuss this further in Sect. 3.7.

### Jet Linear Evolution, $\Delta\ell$ , and $z$

In Sect. 3.5.1 I investigated how the jet length of the CJF sources might depend on their redshift, finding indications for a possible evolution of the jet length beyond that induced by the cosmic scale evolution. As  $\Delta\ell$  is measured in absolute distance, I can use it to further investigate this possible evolution. I want to see whether  $\Delta\ell$  shows any kind of dependency on  $z$ . In Fig. 3.20 I show the total linear jet ridge line evolution as a function

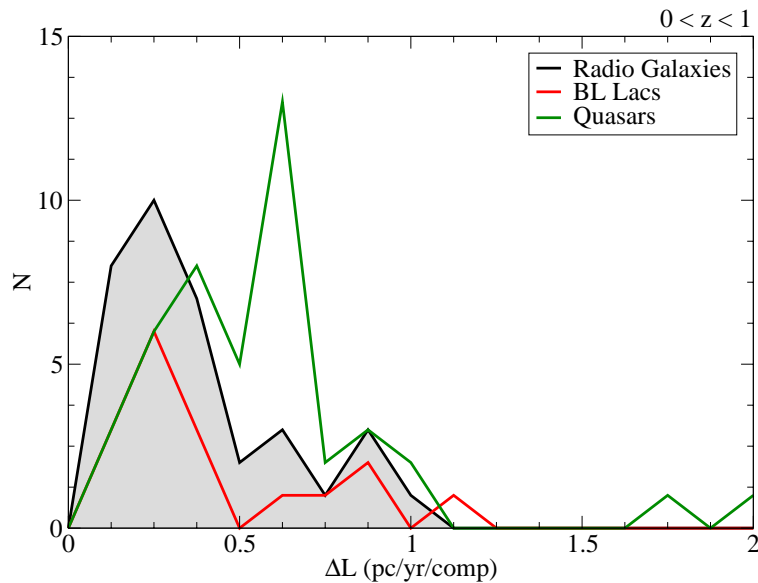


Figure 3.19: Distribution of the total linear evolution of the CJK jet ridge lines for QSOs (green line), BL Lacs (red line), and RGs (grey filled line). Sources with redshift lower than 1 are used.

of redshift for QSOs, BL Lacs, and RGs. Similarly as in Sect. 3.5.1, I use differential bins (widths range from 0.05 to 0.4) and calculate the corresponding average values. In addition, I plot the cosmological distance scale (using the cosmological parameters given in Sect. 2.3) for a jet with an average linear evolution of  $0.357 \pm 0.052$  pc/yr/comp (value calculated from 13 QSOs with  $z \in [0, 0.5]$ ) (for details on the cosmological distance scale calculations see Sect. 3.5.1).

A peculiar behavior is seen in Fig. 3.20. Although the cosmic distance scale curves are calculated for the average value of linear evolution of QSOs in the bin  $[0, 0.5]$ , there seems to be large scatter in the values, reflected by the fact that the first redshift bin ( $[0, 0.4]$ ) is found above the cosmic distance scale line, whereas the next bin ( $[0.4, 0.6]$ ) is situated below it. For  $z > 1$  reliable QSO points (small errors) appear to be consistently below the line and outside the  $1\sigma$  uncertainty margin. BL Lacs and RGs are also found below the cosmic distance scale line<sup>13</sup>. This is partly expected, as both BL Lacs and RGs show on average less total linear evolution of their jet ridge lines. Two redshift bins should be noted ( $[0.5, 0.7]$  and  $[0.7, 1]$ ), for which the average values of BL Lacs lie above the cosmic distance scale line, showing similarly strong evolution as their QSO counterparts at similar redshifts. The large errors for these two points indicate large scatter of the values in these bins and therefore argue for peculiar behavior of individual objects, rather than a general trend. The deviation of the average values of QSO jet linear evolution at higher redshifts from the ones anticipated by the cosmic distance scale line points towards an internal evolution of the linear evolution of the jet ridge line with redshift. **Jets of active**

<sup>13</sup>Most points for BL Lacs and RG at  $z > 1$  reflect the values of individual objects rather than an average value, as a result of the absence of enough identified high-redshift objects of these two classes. This is denoted by the absence of an error for these points.

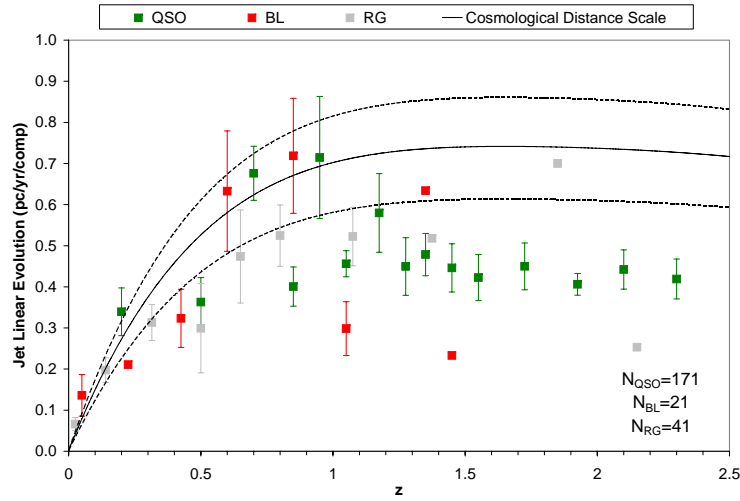


Figure 3.20: Average jet total linear evolution as a function of redshift for QSOs (green), BL Lacs (red), and RGs (grey). The cosmological distance scale for a jet with an average linear evolution of  $0.357 \pm 0.052$  pc/yr/comp is shown (continuous line denotes the actual values, dashed lines show a  $1\sigma$  uncertainty deviation). In the lower right corner the number of objects for each class -QSOs, BL Lacs, and RGs- is shown.

**galaxies at higher redshifts (possible younger AGN) appear to be intrinsically slower than their counterparts in the local Universe.**

### Jet Linear Evolution, $\Delta\ell$ , and Variability

As in previous sections, I am interested in investigating if long timescale variability can be linked to jet ridge line properties. In Table 3.11 I show the parameters of the sub-sample of variable CJF sources (from Table A.6). Given the small number of sources/epochs for this investigation, I impose no redshift constraints on the sub-sample. Quasars, BL Lacs, and RGs of this sub-sample are divided and studied separately.

Compared to the parent sample, the sub-sample of variable sources exhibits both higher average and median values ( $0.49 \pm 0.05$  and  $0.38 \pm 0.03$  pc/yr/comp, compared to  $0.435 \pm 0.014$  and  $0.381 \pm 0.011$  pc/yr/comp respectively). In Fig. 3.21 the total jet ridge line linear evolution distribution is plotted for the sub-sample of variable sources, as well as for the rest (non-variable) CJF sources. Both samples show a similar distribution for bins up to 0.8 pc/yr/comp. For both samples the total maximum of the distribution occurs in the [0.2,0.4] bin, with the variable CJF sources however showing a less strong maximum compared to the non-variable sample (as well as lower values for the bins [0.4,0.6] and [0.6,0.8]). In contrast to the non-variable sources, the variable sample shows a secondary maximum in the bin [0.8,1] pc/yr/comp (ratio 0.45). The K-S test gives a probability of 23.8% that the two sub-samples are drawn from the same parent distribution.

I also check average and median values for the individual classes. BL Lac objects appear to maintain the same average linear evolution as their parent sample (within er-



Table 3.11: Characteristic statistic values concerning the total linear evolution of the jet ridge lines of sources identified as variable (see Table A.6 and Sect. 2.5, Chapter 2). The average and median values with uncertainties, maximum, and minimum values are given for the whole sub-sample, QSOs, BL Lacs, and RGs. No redshift constraints are assumed.

<b>Jet Linear Evolution (pc/yr/comp)</b>				
	<b>All</b>	<b>QSO</b>	<b>BL</b>	<b>RG</b>
<b>#</b>	35	18	14	3
<b>Average</b>	0.49	0.62	0.36	0.35
<b>Error</b>	0.05	0.06	0.07	0.17
<b>Median</b>	0.38	0.53	0.23	0.135
<b>Error</b>	0.03	0.04	0.03	0.003
<b>Max</b>	1.64	1.642	1.081	0.79
<b>Min</b>	0.04	0.153	0.038	0.13

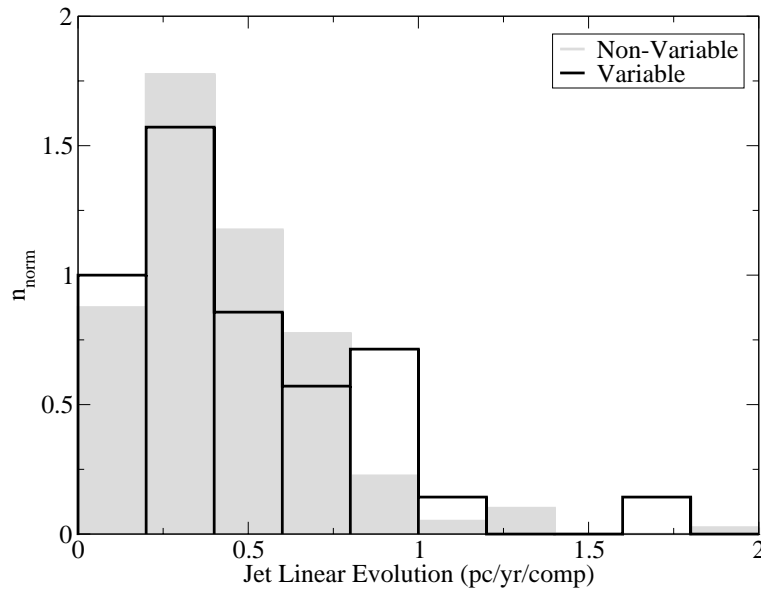


Figure 3.21: Distribution of the total linear evolution of the jet ridge lines for the whole (non-variable) CJF (parent) sample (filled grey line) and for the sub-sample of variable sources from Table A.6 (open black line). Due to the big difference in absolute numbers for the two samples, I have normalized to unity surface area. No redshift constraints are assumed.

rors), however the median value of the variable sample is considerably smaller than the non-variable one ( $0.23 \pm 0.03$  pc/yr/comp, compared to  $0.36 \pm 0.05$  pc/yr/comp). This

indicates a much more concentrated distribution of values for the variable BL Lacs. Variable quasars appear to have both higher average ( $> 4\sigma$  difference) and median values than their parent sample ( $0.62 \pm 0.06$  and  $0.53 \pm 0.04$  pc/yr/comp, compared to  $0.453 \pm 0.017$  and  $0.409 \pm 0.012$  pc/yr/comp respectively). Variable RGs show equally interesting behavior, with same average values (within errors) but lower median value ( $0.135 \pm 0.003$  pc/yr/comp, compared to  $0.294 \pm 0.028$  pc/yr/comp). It should be noted that, especially for RGs, this comparison is problematic due to the small number of sources (3 RGs). However, there seems to be a connection between variability and jet kinematics, as it is seen for QSOs, that exhibit significantly stronger linear evolution of their jet ridge lines. This link shall be discussed more extensively in Sect. 3.7.

### Jet Linear Evolution, $\Delta\ell$ , and Radio Luminosity

Britzen et al. (2008) for the CJF, as well as Cohen et al. (2007) and Lister et al. (2009b) for the MOJAVE/2cm sample, uncover a correlation between apparent jet speeds and source luminosity. Britzen et al. (2008) use all best quality components of the CJF sources and the best quality, brightest component per source to show this correlation. Cohen et al. (2007) uses the fastest component per source to the same end. Both authors conclude that this apparent correlation between apparent speeds and apparent luminosity is indeed true, not an effect of redshift. They also conclude that intrinsically faster components tend to populate the more luminous sources, essentially linking the energy output of the AGN with the kinematics of its jet. In the same context, I am interested in seeing whether this behavior is inherent to the entire jet or is rather connected to individual components. I therefore use the total linear evolution of the jet ridge line to test this correlation.

In Fig. 3.22, I show the total linear evolution of the CJF jet ridge lines as a function of the total luminosity of the source at 5 GHz (from single dish observations). **It can be immediately seen that the same correlation reported previously for apparent speeds still holds for the measure of total linear evolution of the jet ridge line. This is seen as an upper envelope, above which no sources are found. More strongly evolving jets inhabit brighter sources. Conversely, low luminosity sources appear to show the smallest values of linear displacement of their jets.** Britzen et al. (2008) discuss the correlation between apparent speeds and luminosity as an effect caused by redshift. As can be seen in Fig. 3.22, there are indications that this is not a redshift induced effect. The CJF sources at the highest redshifts ( $> 3$ ) all appear to have rather weak linear evolution of their jet ridge lines. Conversely, several sources with intermediate redshifts ( $1 < z < 2$ ) are found to exhibit rather strongly evolving jet ridge lines. Further arguments against a redshift induced effect dominating this correlation can be found in Britzen et al. (2008) (e.g., the absence of a similar envelope for the apparent speeds as a function of redshift). It should be noted that low-number statistics might be affecting my results. Both for low luminosity sources, as well as high redshift sources, I have a small number of objects available. That hinders the global validity of what is seen in Fig. 3.22.

Concerning differences between QSOs, BL Lacs, and RGs, no strong effects can be seen in this context. The low-luminosity tail of the distribution is predominantly populated by RGs and BL Lacs, with QSOs mainly dominating the higher luminosities. Cohen et al. (2007) use Monte Carlo simulations to show that such an envelope can be explained

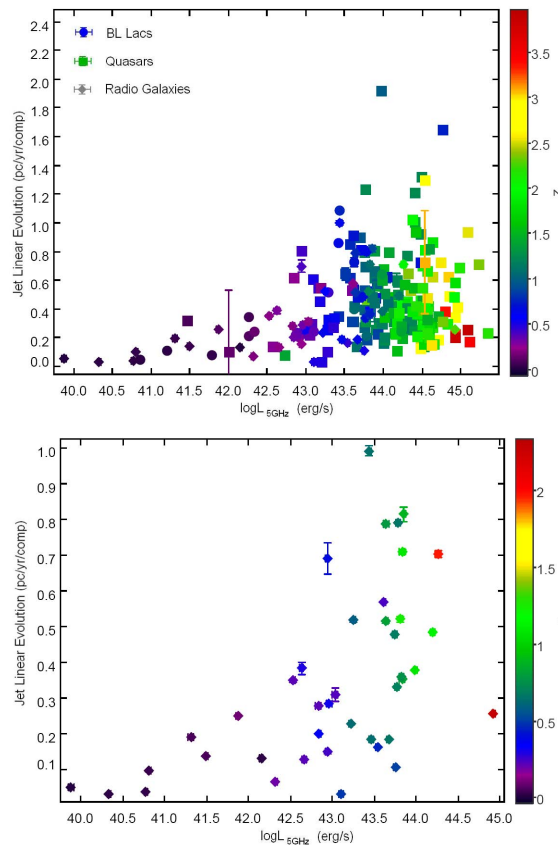


Figure 3.22: Total linear evolution of the jet ridge lines for the whole CJK sample (left) and the RG sub-sample (right) as a function of the total source luminosity at 5 GHz. Quasars are shown with squares, BL Lacs with circles, and RGs with diamonds. I use a color scale to denote different redshifts.

in terms of "aspect curves"<sup>14</sup>, essentially supporting the beaming model of relativistic jets as an explanation for this effect. In Fig. 3.22 (right) I also plot the same correlation but only for the RGs in the CJK sample. They form the same upper envelope, with more strongly evolving jets appearing in more luminous RGs. **In the context of the unification scheme, where RGs are believed to be observed at large angles to their jet axes, this effect indicates that the correlation between total linear evolution of the jet ridge line and the luminosity can not be attributed only to geometric effects.** I shall discuss this in more detail in Sect. 3.7.

<sup>14</sup>An "aspect" curve shows all possible observable pairs  $(\beta_{app}, L)$  for a certain source, result of viewing angle variation. The aspect curve is parametric in the viewing angle, its height is fixed by the Lorentz factor, while the position on the x-axis is constrained by the combination of the Lorentz factor and the intrinsic luminosity of the jet. For more details, see Cohen et al. (2007).

## 3.6 Summary of Results

In this chapter, I have focused on the kinematics and morphology of the jet ridge lines in the CJF sample. As discussed in Sect. 3.3, I am particularly interested in the relative behavior between BL Lacs objects and quasars, especially given the indications of differences between the two classes recently published, as often these two classes of objects are fused into a single group of blazars. Before I move on to the discussion and concluding remarks, let me summarize the results I presented in this chapter.

- I develop a number of tools to investigate both the morphology and kinematics of the CJF jet ridge lines:
  1. Jet Length: I calculate the maximum length of each CJF source. I use this information to further constrain the final results.
  2. Monotonicity Index: I define an index that offers a measure of how much a jet ridge line's morphology resembles that of a sinusoid curve. This is done in terms of identifying maxima across the jet ridge line.
  3. Jet Width: I define the width of the jet ridge line at a given epoch as the difference in position angle between the components with the maximum and minimum position angle.
  4. Jet Width Evolution: I calculate the evolution of the jet ridge line width. I characterize each source with its maximum value across all epochs.
  5. Jet Linear Evolution: I calculate the total absolute displacement of all components and across all epochs. This measure characterizes the overall linear evolution of the jet ridge line.
- In accordance with the unification scheme, I find BL Lacs to have the shortest jets, with QSOs and RGs having, on average, similarly long jets. In median values however, RGs appear to have the highest values, with QSOs second, and BL Lacs showing the lowest median values.
- The distribution of jet lengths for all three classes is fairly similar, with most jets having jet lengths in the range [0,50] pc. Radio galaxies exhibit a much more extended distribution of lengths.
- I find indications that the jet length of the CJF sources evolves with  $z$ , finding an additional component of evolution to the cosmic scale evolution with redshift. The relative behavior between classes is maintained as a function of the redshift.
- Using the M.I., I find that BL Lacs jet ridge lines more often resemble a sinusoidal curve compared to both QSOs and RGs. In contrast, 2/3 of the QSOs have an M.I. lower than 0.5 (indicating fairly monotonous jets).
- BL Lacs exhibit substantially wider jets. This effect persists under several constraints (e.g., redshift bins, core separation limits). Quasars show the least wide jets among the three classes. This supports the effects seen in individual BL Lac objects (i.e., 1803+784, 0716+714, etc.).

- No indication is found for a change of jet width with redshift, at least out to  $z \sim 2$ .
- The distribution of jet ridge line widths for BL Lacs is extended towards higher values, with QSOs mainly contained at lower values. Radio galaxies show a somewhat wider distribution of widths than QSOs. A K-S test indicates a  $0.7 \cdot 10^{-5}$  probability that QSOs and BL Lacs are drawn from a single parent population.
- Variable CJF source are, on average, found to exhibit wider jets than the non-variable ones. Indeed the width distribution of the variable sub-sample is extending to higher values, with a maximum at 20 degrees. A K-S test gives a 1% probability that these two sub-samples stem from the same parent distribution.
- When taking into account the maximum values of width evolution for the CJF sources, BL Lacs are found to show stronger evolution of their jet widths, with QSOs and RGs showing similar values (within errors). This behavior holds for a smaller redshift bin.
- BL Lac objects show a somewhat broader distribution of jet width evolution values, with its maximum shifted, with respect to the QSO and RG maxima, to higher values. A K-S test does not however give a conclusive result, with a 33.8% probability for BL Lacs and QSOs to be drawn from the same parent sample.
- In the context of variability, variable sources in the CJF show, on average, stronger angular evolution than the non-variable ones. This is reflected in the fairly wider distribution of jet width evolution angles compared to the parent (non-variable) sample. Again a K-S test appears inconclusive (17.6% probability for BL Lacs and QSOs to stem from the same parent sample).
- BL Lac objects, on average, show weaker linear evolution of their jet ridge lines compared to QSOs. Interestingly, RGs show even weaker linear evolution. BL Lac objects and radio galaxies show slower moving jets than quasars.
- BL Lac objects show a fairly contained distribution of linear evolution values, with a maximum around 0.25 pc/yr/comp. Quasars, on the other hand, have their maximum shifted to higher values ( $\sim 0.6$ ) and their distribution extends to the highest values seen in the CJF sample. A K-S test gives a 4.3% probability for BL Lacs and QSOs to belong to the same distribution.
- Again a dependence is found between redshift and the absolute total evolution of the CJF jet ridge lines. In particular, at higher redshifts, jets appear to evolve more weakly.
- The sub-sample of variable sources exhibits stronger linear evolution. This is seen also in the distributions of the two sub-samples. A K-S test gives an inconclusive result (a probability of 23.8%). There are indications that variable BL Lacs show lower values than their non-variable counterparts. Interestingly, QSOs show the opposite behavior, with variable QSOs showing substantially more strongly evolving jet ridge lines. As I will discuss, this is probably connected to the beaming mechanism.

- A correlation, in the form of an upper envelope, is found between total linear evolution of the CJF jet ridge lines and their radio (single dish, 5 GHz) luminosities. Although partly attributed to relativistic effects, there are indications of a further, intrinsic effect additional to the geometric one.

**Indeed, the indications seen in the case of S5 1803+784 (see Sect. 3.2) and other sources - i.e., slow jets, wide flows, etc.-, have a more universal character than originally thought.** In the following section I shall discuss the methods used in this chapter and their robustness and I will try to bring all of the above results into a consistent picture, as well as their relevance and implications with regard to the currently accepted scheme of AGN jet kinematics.

## 3.7 Discussion and Conclusions

Having summarized the results of this chapter in the above section, I now move on to the discussion of the results and their implications. I start the discussion with the restrictions and limitations of the above method, I follow this with a comparison of the results with studies of other samples of active galaxies. I finish the discussion with the implications of the results in the context of the beaming model as well as the unification scheme.

### 3.7.1 Identifying the pitfalls

There is a number of limitations to the methods presented here. Most of these are associated to the CJF sample itself, as well as the particular types of objects included. As I have already mentioned before, the CJF sample is dominated by QSOs ( $\sim 70\%$ ), with only a small fraction of the sample being RGs ( $\sim 18\%$ ) and BL Lacs ( $\sim 12\%$ ). This reflects the occurrence of each class of active galaxies in the Universe, enhanced by the selection criteria of the CJF. With flux-limited sample and no volume constraints, high-redshift/high-luminosity QSOs are preferentially included, rather than low-luminosity RGs. Additionally, assuming that the unification scheme is true, there are far more QSOs than BL Lacs (BL Lacs are sources oriented towards us in very small angles) in the Universe. This inadvertently affects the statistics presented here. The small number of BL Lacs introduces larger uncertainties to the corresponding values, and therefore makes the comparisons more difficult. In this sense, I have only drawn comparisons between sub-samples that have a sufficient number of sources, or when this is not the case, it is clearly noted as such.

Another effect that needs to be noted here is the large redshift span of the CJF, as well as the uneven sampling of that range with regard to the three types of AGN<sup>15</sup>. I calculate an average content of sources per a 0.1 redshift bin. This is shown in Table 3.12. BL Lac objects are overdense in the redshift range 0 to 2. Radio galaxies follow a similar behavior, with most sources in the redshift range [0,1], but a few sources at higher redshifts. Contrary to that, QSOs show an overdensity in the redshift bin [1,2] and extending to the highest redshift values of the sample.

---

<sup>15</sup>This of course is, in some context, positive, as it allows the investigation of the kinematic properties of active galaxies over that large redshift range and enables, in principle, the investigation of their evolution.

Table 3.12: Percentage of each type of object per 0.1 redshift range in each respective redshift bin. The absolute numbers along with the distribution histogram of redshifts in the CJF can be seen in Sect. 1.6. The values shown here are averages. The coverage of each redshift bin is not uniform.

		Type		
		QSO	BL	RG
$z$	[0,1]	2.9	8	8.7
	[1,2]	4.6	2	1.1
	[2,3]	2	0	0.2
	[3,4]	0.5	0	0

As I briefly discussed before, the fixed sensitivity and resolution of the arrays used lead us to essentially observe different scales of the jet for objects at different redshifts. It is expected that the properties, kinematics, and morphology of the jets are a strong function of the separation from the core. As I am interested in comparing between different groups of sources, it is essential to account for this effect. I therefore adopt redshift bins for all of the comparisons I do. Given the distribution of redshifts for the CJF (see Fig. 1.6 and Table 3.12) the only bin that can be used without losing most of the BL Lacs is the [0,1] one<sup>16</sup>. The unevenness of the relative distribution is accounted for by using differential binning, essentially spreading out the overdensities and summing up redshift ranges with only a few sources (this is used, e.g., in Fig. 3.20 and in Fig. 3.11).

The next point that should be addressed is the sensitivity, or lack thereof, of the method presented here to the identification of individual components. One of the major advantages of studying the jet ridge line, is the fact that it is independent of component identification. Kinematical studies of individual sources have often caused debate over the specifics of component identification. Indeed, different identification schemes inadvertently lead to different kinematic scenarios and jet properties. In this context, the way that I study the width and width evolution of the jet is completely independent of component identification. The linear evolution of the jet ridge line is an exception to this. For this measure I am forced to follow the given identification of components (from Britzen et al. 2007b) as some reference point is needed to calculate absolute displacements. This, although potentially biasing, does not compromise my results. Despite the inevitable coupling of prior component identification and the  $\Delta\ell$  measure, the fact that all components and all epochs are included in this measure ensures a treatment of the jet as a whole, evening out peculiarities or possible misidentifications of individual components.

However, these measures are sensitive to the number of components identified at a certain epoch. A vanishing component (due to it dropping below the sensitivity limit of the instrument or due to flawed data) will lead to a change of both the width of the jet at

<sup>16</sup>It should also be noted that given the featureless spectrum for which BL Lacs are famous for leads to more than 36% of the CJF BL Lacs to not have available redshift information. When using redshift bins these objects are obviously excluded.

that epoch, as well as the jet width evolution. Also in the case of  $\Delta\ell$ , a vanishing component will lead to a zero contribution to the sum of individual component displacements, altering the final result for that source. It is easy to see that this effect is artificial, not reflecting any essential physical change in the kinematics or morphology of the jet, at least not in the sense discussed here. I account for this effect by identifying the number of components per epoch and then flagging the data according to how this number changes across epochs (this is described in Sect. 3.5.4). For the case of the jet linear evolution this is implicitly accounted for in the inclusion only of components that are cross-identified between epochs.

The last and perhaps most critical point concerns the nature of BL Lac jets. As I discussed previously, BL Lacs are known to be extremely variable sources. In part, this is due to the presumably small angle to the line of sight, resulting to beaming effects that lead to abrupt changes of both the core and the jet flux. Secondly, I have shown that BL Lacs have substantially shorter jets than both QSOs and RGs. This translates to a higher difficulty of consistently model-fitting the jets of BL Lacs, as blending effects become more prominent as the viewing angle decreases. Moreover, given the strong variability of both core and jet, components might simply vanish as a result of diminishing luminosity or insufficient dynamic range of the observations. A further way to demonstrate this is by using the quality classification for jet components used by Britzen et al. (2008). Jet component proper motions are classified as Q1 for the best quality data, and Q2 and Q3 for diminishing quality. The ratio  $N(Q1)/(N(Q2) + N(Q3))$ , where  $N(x)$  is the number of  $x$  quality components of that type of source, is 0.63 for QSOs, 0.80 for RGs, and 0.41 for BL Lacs. BL Lac objects indeed appear to be the most difficult to model-fit. Returning to the previous point, I see therefore, that the number of components across epochs in BL Lac jets is more variable than both QSOs and RGs. Ultimately, this effect is the limiting factor of my method, essentially regulating the uncertainties of my results.

### 3.7.2 Comparison with previous studies

It is interesting to make a comparison between the work presented here and previous studies of similar scope. **It should be noted that this is the first time the jet ridge lines of a sample of AGN this size have been explicitly and exclusively studied in a statistical manner.** While the ridge line of a jet is not a new concept, so far only the jet ridge lines of individual sources (both galactic and stellar) have been studied (e.g., Condon and Mitchell 1984; Steffen et al. 1995b; Lister et al. 2003; Lobanov et al. 2006; Britzen et al. 2009; Perucho et al. 2009; Lister et al. 2009b; Britzen et al. 2010a). It should also be noted, that the definition of the jet ridge line can differ from study to study. As it was previously discussed, I define the ridge line of a jet at a certain epoch as the line that linearly connects the projected position of all components at that epoch. Alternatively, one can use an algorithm to more directly extract the jet ridge line from the VLBI map of each epoch (e.g., Pushkarev et al. 2009). By fitting the intensity with a Gaussian curve (in the transverse sense to the jet axis) at different distances from the core, one can build the ridge line as a line comprising the consecutive maxima of these Gaussian fits. In this sense, one can build a much denser jet ridge line. One should however be careful of oversampling effects, in effect extracting information that is not actually there. The method followed here, although perhaps simpler, is more robust in the quality of information used.



The one obvious direct comparison that can be drawn is to the MOJAVE / 2cm sample (Lister and Homan 2005; Paper I of a series of 6 papers). The MOJAVE sample is a statistically complete sample of 133 radio-loud AGN, selected by position criteria on the sky, as well as a flux limit at 15 GHz VLBA measurements of 1.5 Jy (or 2 Jy for southern sources). Unlike the CJF, no spectral index selection criteria were imposed. As in the case of the CJF, all data have been uniformly analyzed and therefore offer a very good statistical tool for the investigation of AGN kinematics. The MOJAVE sample offers higher resolution observations (given the higher frequency), as well as a larger number of epochs per source (a median value of 15 epochs per source). On the other hand, CJF offers more than double the number of sources (due to the lower flux-limit). Moreover, by imposing the spectral index criterion, compact, core-dominated sources are selected, ideal for the kind of kinematic studies the CJF was built for. There is a significant overlap of 24 sources between the CJF and the MOJAVE sample.

As the work presented here is prototype in its conception, it is difficult to draw direct comparisons to the MOJAVE sample. It is of interest to compare the apparent velocity distributions for the MOJAVE and the CJF, as the apparent velocities are in a sense reflected in the measure of the total jet ridge line linear evolution. The CJF sources appear to be significantly slower than what is seen in the MOJAVE sample (e.g., compare Fig. 7 from Britzen et al. 2008 and Fig. 7 from Lister et al. 2009b). In the distribution of apparent speeds, for the CJF there is a maximum at around  $4c$  and then a turn down, with very few sources above  $15c$ . In contrast, the distribution for the MOJAVE sources shows a maximum at  $10c$  with a fair number of sources showing speeds greater than  $20c$ . This can be explained in terms of the higher temporal resolution of the MOJAVE sample (owning to the larger number of epochs per source) that might allow the detection of such faster motions. It should be noted that no clear distinction has been made in the MOJAVE sample between BL Lacs and QSOs, probably due to the relatively small number of BL Lacs. Lister et al. (2009b), however, do mention that BL Lacs are more often found to exhibit "low-pattern speeds", i.e., components with slow motions, significantly smaller than others in the same jet. That is in tentative agreement with CJF BL Lacs showing on average weaker linear evolution than QSOs.

As was previously mentioned, a correlation between apparent speeds and luminosity has been studied for the MOJAVE sample too (Cohen et al. 2007; Lister et al. 2009b). A similar correlation was observed also for the CJF sample, as was shown in Britzen et al. (2008). It should be noted that for both samples, these correlations were between luminosity and either the maximum apparent speed per source (in the case of MOJAVE), or only for the best quality (Q1) data (for the CJF). In this chapter, I presented a similar correlation between 5 GHz core luminosity (as derived from VLA measurements) and the total linear evolution of the jet ridge line. In this sense, I include speed information for all components identified across-epochs and therefore treat the jet as a whole, rather than singling out the fast component. The result is however remarkably similar to what was previously found. Cohen et al. (2007) and Lister et al. (2009b) discuss possible interpretations of the upper-envelope that is observed in this correlation, in terms of the beaming model. They conclude that there is no apparent argument as to why such an envelope should exist. They instead offer an alternative interpretation in terms of a link between the energy output of the AGN and the intrinsic Lorentz factor of a jet. They conclude however that the shallow flux limit of the MOJAVE sample does not allow for a

robust conclusion. The deeper flux-limit of the CJF (and the resulting more than double number of sources) allow us to re-address the same issue. The fact that this correlation remains in the CJF sample, both in the sense of a maximum apparent jet speed, as well as that of the linear evolution measure, argues in favor of a link between the intrinsic luminosity and Lorentz factor. A definite answer would come by the inclusion of low-luminosity sources in such an investigation. It would then become obvious whether this envelope holds and potentially differs between a beaming model signature and that of an intrinsic connection of the energy output and the jet kinematics.

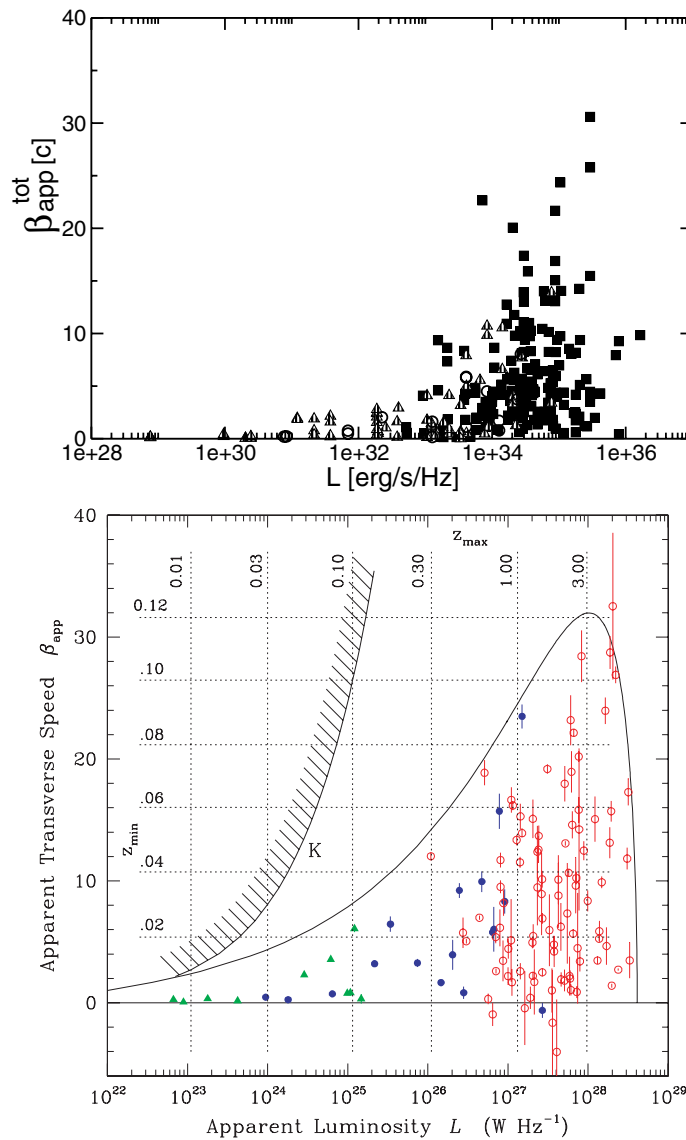


Figure 3.23: Apparent total transverse speed as a function of radio luminosity for the CJF at 5 GHz (up) and for the MOJAVE sample at 15 GHz (down). Figures reproduced from Britzen et al. (2008) and Lister et al. (2009b), respectively.

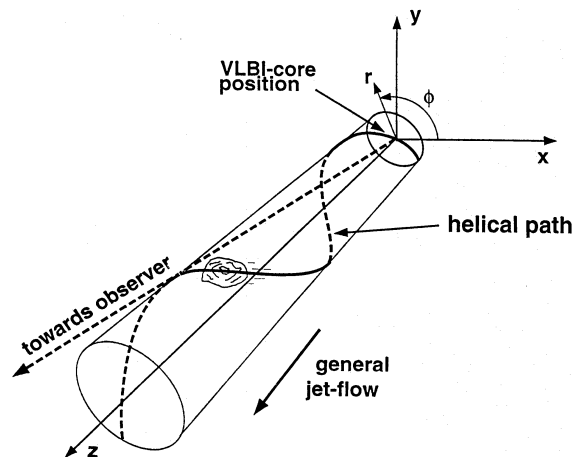


Figure 3.24: The geometry of the helical jet model of [Steffen et al. \(1995b\)](#). The VLBI jet core is put at the origin of the cylindrical coordinates system  $(r, \phi, z)$ . The jet axis (parallel to the  $z$ -axis) forms an angle  $\theta$  to the line of sight. Figure reproduced from [Steffen et al. \(1995b\)](#).

### 3.7.3 A Helical Model and the Unification Scheme

Having discussed all of the above, I am now ready to offer an interpretation of the results shown here. As already mentioned before, helicity of AGN jets has been employed for a number of sources, to explain peculiar kinematic properties of their components. I employ a simple helical jet model and try to see whether a helical geometry, combined with projection effects, can account for the results of the above statistical analysis above, namely that BL Lacs are expected to have wider jets, change their jet widths stronger than QSOs, and also show weaker total linear displacement of their jets than the two other classes of AGN.

I use the helical model of [Steffen et al. \(1995b\)](#), applied in that case to the QSO 3C345 (the same model has also been applied to the BL Lac source S5 1803+784, [Steffen et al. 1995a](#); QSO B3 1633+382, [Liu et al. 2010](#); etc.). The motion of a component down the jet is determined by the conservation of a number of quantities (e.g., specific kinetic energy, specific angular momentum, etc.). In particular, [Steffen et al. \(1995b\)](#) find that the best fit to 3C345 provides a case where the specific kinetic energy of the component, the specific angular momentum, as well as the opening half-angle of the jet are conserved (Case 3 in that paper). The geometry of the model can be seen in Fig. 3.24.

The equations describing the motion of a VLBI component are derived from the conservation equations and, for this specific case, can be written as follows:

$$r(t) = \sqrt{(at + b)^2 + c^2},$$

$$z(t) = \frac{r(t) - r_0}{\tan \psi},$$

$$\phi(t) = \phi_0 + \frac{1}{\sin \psi} \left[ \arctan \frac{at + b}{c} - \arctan \frac{b}{c} \right],$$

where a, b, and c are given by these expressions:

$$a = u \sin \psi,$$

$$b = \sqrt{r_0^2 - \frac{L^2}{u^2}},$$

$$c = \frac{L}{u}.$$

The symbols and their explanation are given in Table 3.13.

$\gamma$	Lorentz factor of the component
$\psi$	opening half-angle of the jet
$\theta$	inclination angle of the jet axis
$r(t)$	distance from the jet axis
t	time in the rest-frame of the source
$z, r, \phi$	cylindrical coordinates
u	velocity in units of the speed of light
L	angular momentum of the component

Table 3.13: The parameters used in the equations for the helical jet model. For more details, see [Steffen et al. \(1995b\)](#).

For the purposes of this work, I have changed the model accordingly to calculate the trajectory of a jet component for a given  $\psi$ , but with changing  $\theta$ . In this way, I can study the projection effects on the apparent evolution of the component as it moves down the jet. I note here, that the opening half-angle  $\psi$  regulates the helicity of the trajectory, with small values ( $\sim \psi < 2$ ) denoting a fairly helical jet, while large values result in a straight trajectory (with an initial bent). By changing  $\psi$ , I can therefore determine whether a more strongly helical jet behaves substantially different from a straight jet, in the context of the measures described in the previous sections.

In Fig. 3.25, I give examples of component trajectories (in sky coordinates) for 6 different values of  $\psi$ . For each  $\psi$  I allow for three different values of the inclination angle  $\theta$ . Both helicity and projection effects can be seen. A relativistic component with a speed  $u = 0.995c$  is assumed.

Returning to the goal of this exercise, I want to test whether BL Lacs show wider jets, if they change their widths more strongly than QSOs, and if they evolve less in absolute (linear) scales. I adopt the helical model accordingly, so that the behavior of the above measures can be assessed as a function of the inclination angle  $\theta$  of the jet axis, and the opening half-angle  $\psi$  of the jet.

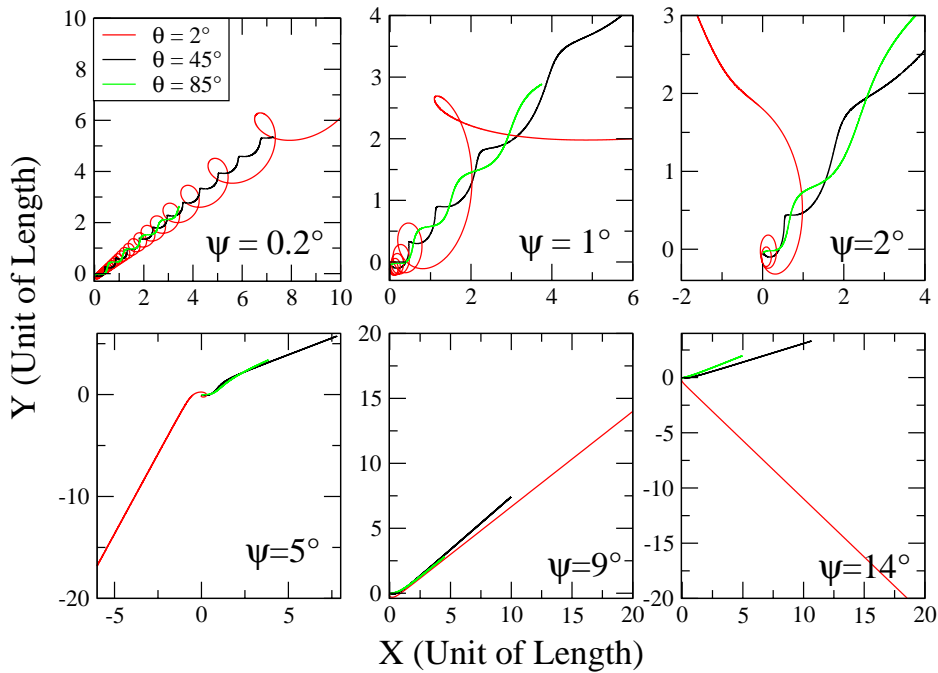


Figure 3.25: Examples of different component trajectories for different opening half-angles: (a)  $\psi = 0.2$ , (b) 1, (c) 2, (d) 5, (e) 9, and (f) 14 degrees, as well as three different inclination angles  $\theta$  of the jet axis: (red) 2, (black) 45, and (green) 85 degrees. X and Y are sky coordinates, the plane perpendicular to the observer's line of sight.

### Jet Width

By definition, this model calculates the evolution of a single component. This is of course not the case of what is observed for most sources. The width of the CJF jet ridge lines is calculated as the difference (in degrees) between the components with the maximum and minimum position angle at a given epoch. Making the simplifying assumption that all components follow the same path (therefore implicitly assuming that  $\psi$ ,  $\theta$ , and  $u$  do not change between different components), this is equivalent to finding the maximum and minimum position angle for one component across different epochs.

In Fig. 3.26 I show the evolution of the position angle as a function of time, for a helical jet ( $\psi = 1$ ) and for 4 different viewing angles. It is obvious that for smaller viewing angles, the modulations of the position angle become stronger, resulting in substantially wider position angle distributions than for the case of large viewing angles.

I calculate the projected width of each loop of the helix. The maximum value of these widths (for a given viewing angle) is representative of that helix and therefore I am interested in seeing its behavior as a function of  $\theta$  and  $\psi$ . This is shown in Fig. 3.27. The  $\phi$  cylindrical coordinate describes the phase of the helix. One loop of the helix equals to a full rotation of the  $\phi$  unity vector and thus I can trace the projected width of the jet

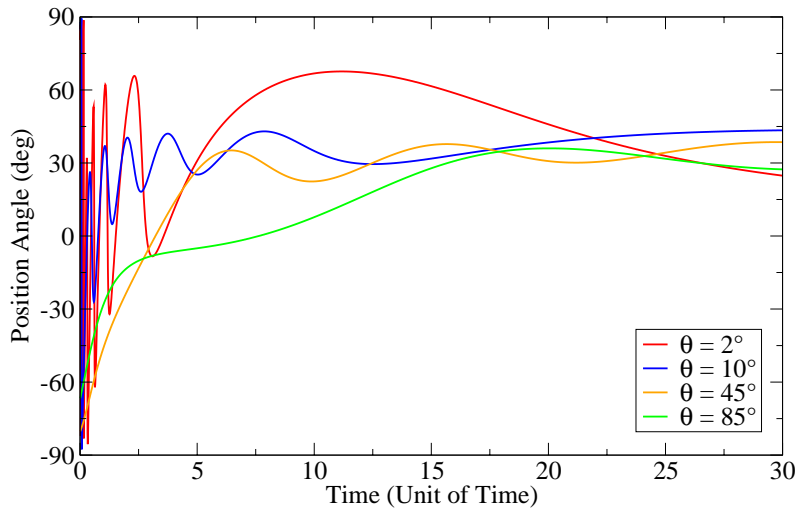


Figure 3.26: Position angle as a function of time for a helical jet ( $\psi = 1$ ) and for 4 different viewing angles: (red) 2, (blue) 10, (orange) 45, and (green) 85 degrees.

after each loop by following the rotation of  $\phi$ . As expected, for highly helical jets, smaller viewing angles produce substantially wider jets. The highest value of apparent width at the smallest viewing angle is produced by the  $\psi = 1$  jet, while for slightly larger viewing angles (up to  $\sim 15$  degrees) the  $\psi = 2$  jet appears wider. For  $\psi > 2$  I get zero values for the apparent jet width. This is because of the method used to calculate the apparent width and reflects the fact that for these jets no single loop is produced in the rest-frame of the jet (the  $\phi$  unity vector does not complete a full rotation).

In conclusion, helical jets appear to reproduce well the effects seen for the width of the CJF jet ridge lines. A combination of a highly bent trajectory of the components, together with the effects of the projected geometry can explain the extremely wide jets seen for BL Lacs. As is seen in Fig. 3.27, QSOs are anticipated to show narrower jets, given a helical structure of their jets and their expected larger viewing angles. However, this is probably not the whole picture. According to my results, radio galaxies show intermediate jet ridge line widths. Given their fairly extended jets and their large angles to the line of sight, it would be expected that RGs show relatively narrow jets. It is possible that due to the overall lower luminosities of these sources, their jets appear more extended, in contrast to QSOs and BL Lacs, whose jets are dominated by the relativistic inner-jet, therefore effectively overshadowing the more extended structure of the outflow (given the finite dynamical range of the observations). This effect can not be reproduced with the model described here. Given the relatively small number of both BL Lacs and RGs, as well as the rather simple model used, one can not offer a definite answer.

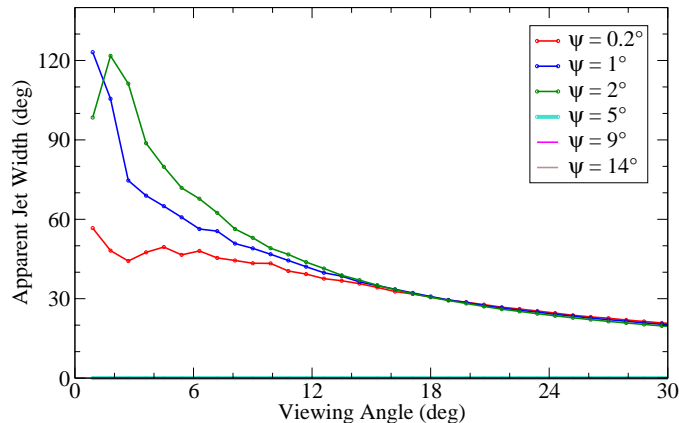


Figure 3.27: Apparent jet width as a function of the viewing angle, for different opening half-angles: (red) 0.2, (blue) 1, (green) 2, (turquoise) 5, (fuchsia) 9, and (brown) 14.

### Jet Width Evolution

For calculating the width evolution of the jet I do the following: for each set of jet parameters ( $\theta$  and  $\psi$ ), a mean value of the position angle distribution is calculated. Then, for each time  $t$ , the difference between the actual position angle and the mean value is derived. Finally, the differences are summed up and divided by the total time. That gives therefore a measure of the position angle deviation of the jet components from the mean value, per unit time. This is described by this formula:

$$\frac{\Delta P}{\Delta t} = \frac{\sum(|PA(t) - \bar{PA}|)}{\Delta t}.$$

The results can be seen in Fig. 3.28. The behavior of this measure is strongly dependent both on the viewing angle and the opening half-angle of the helix. For low values of  $\psi$  (0.2 and 1), the position angle varies strongly for small viewing angles, weakly for intermediate viewing angles, and picks up again for large viewing angles. For  $\psi = 5$  the maximum of the curve is shifted towards higher viewing angle values, with the position angle varying less for the smallest viewing angles, showing a maximum around  $\theta \sim 5$ , a minimum around  $\theta \sim 50$  and then rising again. Interestingly, for the largest opening half-angle ( $\psi = 14$ ) a different behavior is seen: up to viewing angles of  $\sim 20$  degrees, the position angle variation remains constant and then rises, showing a maximum at  $\theta \sim 60$  degrees.

According to the previous statistical analysis, I find that BL Lacs show the strongest changes in their jet widths, QSOs the weakest, and RGs in between. This agrees very well with the curves for  $\psi = 0.2$  and  $\psi = 1$  degrees of opening half-angle, where at the smallest viewing angles (BL Lacs) one has the strongest variation of position angles, for slightly larger viewing angles (QSOs) weaker variation are seen, while for the largest viewing angles (RGs) the position angle variations begin to become stronger again. As in the case

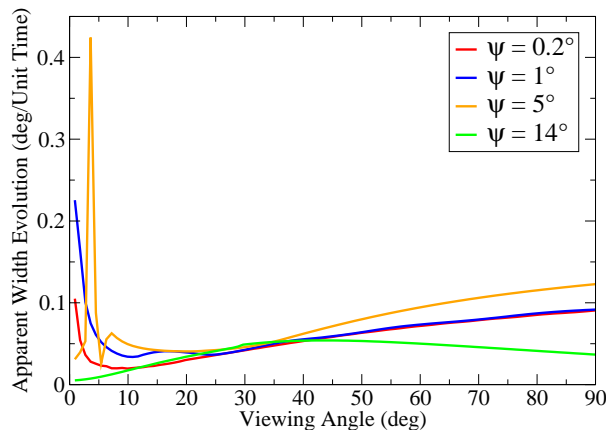


Figure 3.28: Apparent jet width evolution as a function of the viewing angle, for different opening half-angles: (red) 0.2, (blue) 1, (orange) 5, and (light green) 14.

of the jet width, the combination of a helical jet and a projected geometry can explain the results from Sect. 3.5.

### Jet Linear Evolution

The last point of interest is the linear evolution of the jet. I want to test whether a helical jet can also account for the slower linear evolution of a component. I follow the same steps as for the analysis of the CJF jets. The displacement of each modeled jet component is calculated between two successive epochs ( $t$  and  $t+dt$ ) and summed up for all epochs. The total linear evolution (per component) of the jet is then calculated as the total displacement of the jet component divided by the total time  $\Delta t$ . This is the equivalent of what was calculated for the CJF jet ridge lines, if the assumption that all components follow the same trajectory in the jet holds.

The results are shown in Fig. 3.29. Again, there is a strong dependence of the measure of the linear evolution on both the viewing angle and the opening half-angle of the jet. For the smallest values of  $\psi$  (0.2 and 1) and for small viewing angles, the linear evolution of the jet is weak, showing a maximum around  $\theta = 6$  and then decreasing slowly. The opposite behavior is seen for the less helical jets: for  $\psi = 5$ , the linear evolution becomes maximum for the smallest viewing angles, shows a deep minimum around  $\theta = 7$  and then rises slowly. For  $\psi = 14$  (fairly straight jet), a very strong maximum is seen at the smallest viewing angles, a steep decline leads to a minimum around  $\theta = 20$  degrees, and then the curve rises slowly. All curves converge at around  $\theta = 45$  degrees.

Once more I refer to the results of the previous statistical analysis. It was shown that BL Lacs and RGs show on average weaker linear evolution of their jet ridge lines than QSOs. In particular, BL Lacs and RGs show similar values (within the errors). This is well reproduced by the helical jets shown in red ( $\psi = 0.2$  degrees) and blue ( $\psi = 1$  degree) in Fig. 3.29. For the case of the measure of the linear evolution of the jet, I again conclude



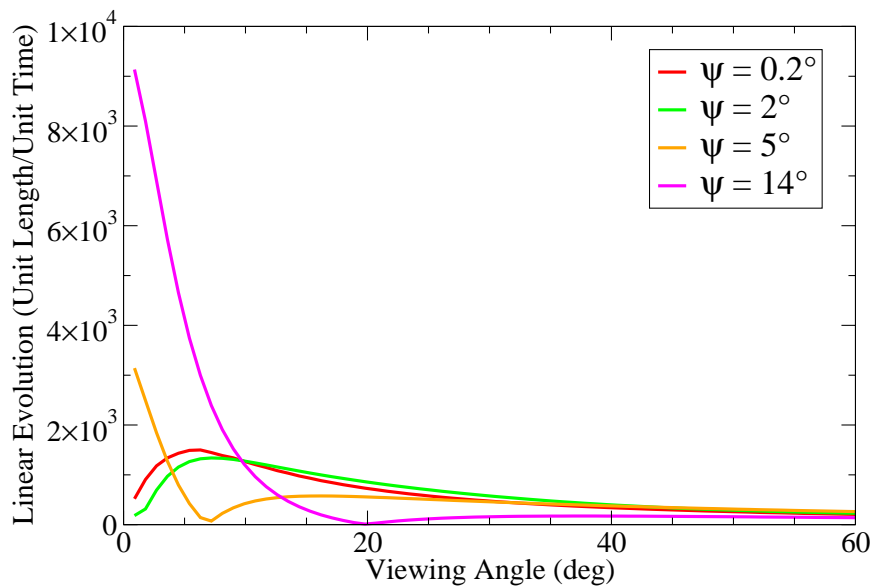


Figure 3.29: Apparent jet linear evolution as a function of the viewing angle, for different opening half-angles: (red)  $0.2^\circ$ , (light green)  $2^\circ$ , (orange)  $5^\circ$ , and (fuchsia)  $14^\circ$ .

that helical jets projected onto the plane of the sky can explain the results of this chapter.

### 3.7.4 Conclusions

In the previous section I have used a model for a helically moving component to explain the statistical results that I obtained from the study of the CJF sample. The combination of a helical jet or, more precisely, a helically moving component, combined with projection effects can very well explain the relative widths, width evolution, and linear evolution between BL Lacs, QSOs, and RGs. It should be noted that the jet model employed here is quite simple and accounts for a fairly static jet. It is known (see Sect. 3.1) that different components often follow different trajectories in the same jet due to a number of reasons. A more thorough treatment of the problem would require a more elaborate model, where a number of components can be ejected into the jet with different starting parameters ( $\psi$ ,  $\theta$ ,  $u$ , etc.). In addition, although the underlying physics and structure of AGN jets is expected to be, in principle, the same for every source, different jets are expected to be characterized by slightly different parameters. Therefore, in order to really reproduce these statistical findings, a Monte Carlo simulation of a population of jets, covering a wide range of the parameter space would be required. This is however outside the scope of this work, although should certainly be pursued in the future.

In conclusion, I find very strong evidence of a universal helical structure of AGN jets. The three (at least two independent) different measures describing the AGN jet kinematics can be very well explained by a helically moving jet component, if one also takes into account projection effects, i.e., that BL Lacs are objects observed at the smallest viewing

angles, QSOs are at slightly larger viewing angles, and RGs are at intermediate and large viewing angles. As already described in Sect. 3.1, helical component paths can be induced by a number of different processes, among which jet precession and K-H instabilities. **In this context, the different kinematic scenario recently proposed for a number of BL Lac objects (1803+784, Britzen et al. 2010a; 0735+178, Britzen et al. 2010b; etc.) can be explained as a purely geometrical effect, at least at first order.** Viewing BL Lacs at small angles to their jet axis allows us to uncover their peculiar kinematic behavior that would otherwise be inaccessible at larger viewing angles. Finally, it should be noted that the above results underline the fact that the, until recently usually employed, notion of linear, ballistic trajectories for AGN jet components is a very crude approximation and, more often than not, deviates grossly from the reality. It is of great interest to uncover the exact process that leads to a helical, non-ballistic movement of components in AGN jets. In-depth studies of individual objects (as in the case of 1803+784) can shed more light in respect to that.

## 4 $\gamma$ -ray properties of the CJF sample

With the advent of the Fermi  $\gamma$ -ray satellite and in particular its LAT instrument,  $\gamma$ -ray astronomy has entered a new epoch. The surveying capability of the Fermi-LAT instrument and its all sky coverage have allowed the detection of an unprecedented number of previously unknown  $\gamma$ -ray emitters, most of which have been identified as active galaxies. One of the standing questions for  $\gamma$ -ray astronomy, with respect to AGN, has been the identification of the site (and process) of  $\gamma$ -ray emission. One of the most commonly accepted scenarios for the creation of  $\gamma$ -rays in active galaxies is that of the inverse Compton scattering of the jet synchrotron emission from the *in situ* population of electrons in the AGN jet. This of course inadvertently couples the kinematics of AGN jets to the  $\gamma$ -ray properties of active galaxies. The CJF sample offers a unique possibility to study this putative connection between the two. This chapter is structured as follows: in Sect. 4.1 a short introduction to  $\gamma$ -ray AGN astronomy is presented, in Sect. 4.2 the driver of this work will be discussed, in Sect. 4.3 the available  $\gamma$ -ray data for the CJF sources is discussed, in Sect. 4.4 the data is analyzed and the results are presented. Finally the chapter closes with a discussion and conclusions (Sect. 4.5).

### 4.1 Introduction

Active galaxies are known for their energy output over a broad range of frequencies, reaching up to energy scales of  $10^{12}$ eV. This higher end of the AGN spectrum is most probably created by inverse Compton scattering (either of the incident synchrotron photon field, self-scattering (SSC), of photons arising from the accretion disk, or of cosmic ray radiation) from a population of relativistic electrons in the AGN jets (e.g., [Sikora et al. 1994](#)). Relativistic electrons in AGN jets are not sufficient to explain the  $\gamma$ -ray emission. Acceleration mechanisms, including acceleration from electric fields and acceleration in shocks, can boost the energy of the electron population enough so that  $\gamma$ -ray emission can be efficiently produced through inverse Compton scattering (for a detailed treatment of the inverse Compton mechanism, [Rybicki and Lightman 1979](#); also see [Georganopoulos et al. 2001](#); [Pelletier 2009](#); and references therein).

Most  $\gamma$ -ray radiation is shielded away from us by the Earth's atmosphere, apart from the very high energy (TeV) photons that produce atmospheric particle showers that can be detected and analyzed by Cherenkov telescopes. Therefore, the launch of the Compton  $\gamma$ -ray Observatory satellite ([Gehrels et al. 1993](#)) marked the beginning of the  $\gamma$ -ray astronomy. Carrying four instruments, BATSE, OSSE, COMPTEL, and EGRET, it provided the first study of the  $\gamma$ -ray sky. EGRET, the Energetic Gamma Ray Experiment Telescope ([Kanbach et al. 1988](#)), was designed to detect high energy photons in the range

of 30 MeV to 20 GeV, exploiting the pair production mechanism occurring when the high energy photons interact inside the detector. Following the trajectories of the produced particle pairs allowed the instrument to constrain the direction (to an angular resolution of 0.2-0.4 degrees) from which the photon entered the detector. A calorimeter attached to the back of the instrument enabled the deduction of the energy of the incoming photons. In this way, both energy flux and position on the plane of the sky could be determined. There were 271 sources included in the third EGRET catalog (Hartman et al. 1999), more than 90 of them associated with active galaxies, essentially for the first time linking active galaxies to such energetic emission. With the intermittent space mission of AGILE (Tavani et al. 2008), the Fermi  $\gamma$ -ray Space Telescope (Atwood et al. 2009) offered the possibility of an all-sky survey (using the Large Area Telescope, LAT) at much higher resolution and sensitivity than those offered by the previous instruments (0.1 degrees,  $7.5 \cdot 10^{-9} \text{ ph/cm}^2/\text{s}$ )<sup>1</sup>. There are 1451 sources included in the first source catalog of the Fermi-LAT (Abdo et al. 2010b), 687 of which are identified/associated with active galaxies (see Fig. 4.1 for an 11-month Fermi-LAT map of the sky). Of these, 671 Fermi-LAT detected sources at higher galactic latitudes ( $|b| > 10^\circ$ ) are included in the first catalog of active galactic nuclei (Abdo et al. 2010a), associated with 709 AGN (multiple associations for some sources), comprising 300 BL Lac objects, 296 flat-spectrum radio quasars, 41 AGN of other type, and 72 of unknown class.

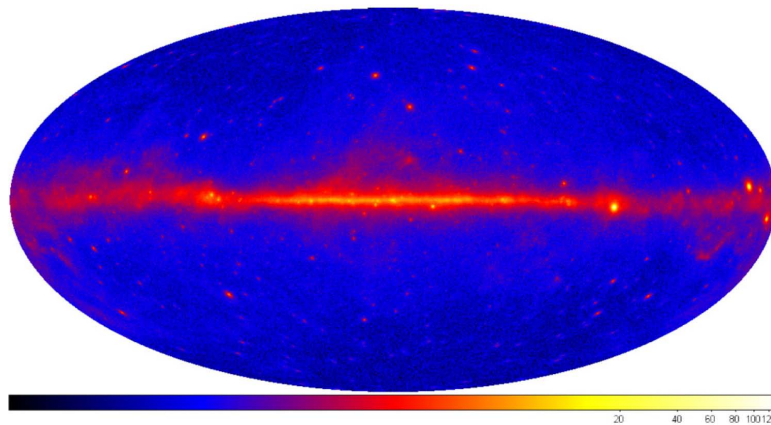


Figure 4.1: A map of the  $\gamma$ -ray sky after 11 months of observations from the Fermi Large Area Telescope. Aitoff projection in Galactic coordinates. The image shows  $\gamma$ -ray intensity for energies  $> 300$  MeV, in units of photons  $m^{-2} s^{-1} sr^{-1}$ . Diffuse galactic emission and a few very bright extragalactic sources can be seen. Figure reproduced from Abdo et al. 2010b.

#### 4.1.1 $\gamma$ -ray emission production

It is generally accepted that AGN  $\gamma$ -ray emission is produced in the relativistic jets of active galaxies (e.g., Blandford and Icke 1978; Ghisellini et al. 1985; Maraschi et al.

<sup>1</sup>Sensitivity for assumed high latitude source, photon index of  $\alpha = 2.2$ , and after 11 months of operation

1992). In particular, [Maraschi et al. \(1992\)](#) proposed that the same electrons producing the low-energy, synchrotron radiation, that is observed in the radio wavebands, are also responsible for the high-energy  $\gamma$ -ray emission, through the inverse Compton scattering process.  $\gamma$ -rays are therefore a high-energy extension of the inverse Compton radiation, responsible for the X-ray emission. For the production of  $\gamma$ -rays, it is essential that the source (in this case the jet) is transparent to photon-photon interactions, so that the  $\gamma$ -ray emission is not absorbed. Together with the observed variability in the  $\gamma$ -rays (i.e., the existence of a minimum length scale), these imply that the  $\gamma$ -ray emission is relativistically beamed. For certain objects, the self-Compton model would however require extremely high radiation fields, leading to rapid radiative losses. This phenomenon has been dubbed as "Compton catastrophe" and provides a constraint to this model (e.g., [Hoyle 1966](#)). One alternative would be that  $\gamma$ -rays are produced directly from the synchrotron mechanism. This however would require an extremely energetic initial population of electrons, essentially transposing the problem to how one can efficiently accelerate these electrons at such high energies. Finally, multiple-zone models have also been introduced to accommodate problems of the standard one-zone models (e.g.,  $\gamma$ -ray emission originating in a very thin spine of ultra-relativistic plasma, embedded in a larger, slower moving jet, [Georganopoulos et al. 2005](#); or even the opposite configuration, [Tavecchio and Ghisellini 2008](#)).

Alternatively, hadronic models have also been employed to explain the high-energy tail of the AGN spectral energy distributions (SEDs). In these models, protons are accelerated to relativistic energies, reaching the threshold of pion production and producing synchrotron-supported pair cascades, creating "hard" Doppler boosted protons that emit in the  $\gamma$ -rays (e.g., [Mannheim and Biermann 1992](#); [Mannheim 1993](#)). Feasibility of this mechanism requires the presence of very powerful magnetic fields. The time-dependence of these models has been difficult to deduce, mainly due to the complexity and resource-heavy nature of the Monte-Carlo simulations necessary to study the pair cascades. These models have been applied to the SEDs of sources like 3C66A and BL Lacertae with different levels of success (for some examples and further references, see [Mannheim 1993](#)). Even in the best case, the exact mechanism of acceleration and the energy budget required are not clear.

Finally, one of the standing problems is identifying the part of the jet in which  $\gamma$ -ray emission originates. Variability arguments for very high energy (VHE)  $\gamma$ -rays imply regions smaller than the Schwarzschild radius of the SMBH in the center of the AGN ([Begelman et al. 2008](#)) and therefore pointing toward the production of this emission either in the base of the jet (probably anchored to the SMBH's ergosphere, [Beskin et al. 1992](#); [Neronov and Aharonian 2007](#)), or by instabilities in an ultra-relativistic jet (with bulk Lorentz factors  $\sim > 50$ ). The latter introduces further complexity, since TeV-emitting sources have been observed to show predominantly sub-luminal or mildly superluminal motions for their jet components ([Lister 2006](#); [Piner et al. 2008](#); [Britzen et al. 2009](#)). A possible explanation is offered by the spine in sheath models (e.g., [Pelletier and Roland 1989](#); [Tavecchio and Ghisellini 2008](#)) that can essentially decouple the synchrotron and inverse Compton emitting regions and thus reduce the Doppler factor required in one-zone models. [Jorstad et al. \(2001b\)](#) find an association (at a more than 99.999% level significance) between  $\gamma$ -ray flares, as detected by EGRET, and the ejection of superluminal components in AGN pc-scale jets. This strongly argues for the emission of  $\gamma$ -ray photons through inverse Compton scattering from the relativistic electrons in the pc-scale

jet of an AGN, rather than in the close vicinity of the SMBH. In support of this scenario, [Lähteenmäki and Valtaoja \(2003\)](#) find that  $\gamma$ -ray emission is connected to the high-frequency radio state of the source, associating  $\gamma$ -ray flares to the rising or peak period of radio flares, in turn causally connected with the ejection of new jet components.

### 4.1.2 $\gamma$ -rays and AGN phenomenology

I have already mentioned the statistics of the AGN detection of the Fermi-LAT first catalog. BL Lac objects dominate the catalog, probably due to their harder  $\gamma$ -ray spectra, making them easier to detect with the Fermi-LAT. It is interesting to note here that apart from all the radio-loud AGN included in the first Fermi-LAT catalog, there exist also 10 sources associated with radio-quiet objects (Seyfert 1 and radio-quiet QSOs). However, 7 of these have multiple possible identifications associated with them, with one of these associations being a radio-loud object. The resolution of the instrument is the limiting factor in pinpointing the exact location of the  $\gamma$ -ray photons origin. Interestingly, there also seems to be a clear separation between different AGN classes on the spectral index/ $\gamma$ -ray luminosity plane. In particular, BL Lacs and flat-spectrum QSOs are found in different parts of that diagram (see Fig. 24 in [Abdo et al. 2010a](#)), with a clear division at a spectral index of  $\alpha=2.2$ . This has been explained in terms of different accretion modes for the two different classes of AGN, with the spectral index threshold corresponding to the transition from an optically thick accretion disk to an advection dominated, radiatively inefficient accretion flow ([Ghisellini et al. 2009](#)).

Of particular interest to the work here is the connection between the  $\gamma$ -ray and radio properties of AGN. As seen in Fig. 28 of [Abdo et al. \(2010a\)](#), the distribution of radio spectral indices of the Fermi-LAT detected AGN is consistent with a flat spectrum, although a tail of steeper spectrum sources exists. This indicates the dominance of core-dominated sources as  $\gamma$ -ray emitters and reflects the importance of the beaming effect for the production of this high-energy emission. There exists however a population of steeper spectrum sources also detected by the Fermi-LAT, that implies a more complex link between the  $\gamma$  and radio properties of AGN. [Lister et al. \(2009c\)](#) study the kinematic properties of the Fermi-LAT detected sources of the MOJAVE sample. The authors find that  $\gamma$ -detected AGN show on average faster jets than their non-detected counterparts, in agreement with previous studies of EGRET-detected sources showing  $\gamma$ -detected sources to have preferentially higher Doppler beaming factors (e.g., [Jorstad et al. 2001b](#); [Kellermann et al. 2004](#)). They also note that BL Lac sources show on average lower apparent speeds but are nevertheless preferentially detected by Fermi-LAT. They attribute this behavior to the spectral shape of BL Lacs and the possibility that BL Lacs are intrinsically more luminous in the  $\gamma$ -rays than flat-spectrum QSOs, concluding that these results merit further investigation.

## 4.2 Motivation

The CJF offers an excellent tool to study anything related to AGN jet kinematics, given its large number of sources and the detailed investigation of the jet kinematics of all these sources. In light of the findings of [Lister et al. \(2009c\)](#), I am interested in investigating the

putative connection between the  $\gamma$ -ray properties of the AGN in the CJF sample and their jet kinematics, utilizing the extensive database of information already available (Britzen et al. 2007b, 2008; this work). I want to disentangle the different effects that might contribute in defining the  $\gamma$ -ray properties of an AGN and identify their relative importance. Based on the analysis and the new information made available in Chap. 3, I also want to investigate whether and how this new kinematic scenario, as revealed by the kinematics of BL Lac jets, might be relevant to the AGN  $\gamma$ -ray emission. In particular, I want to test whether  $\gamma$ -detected AGN indeed show faster jets than their non-detected counterparts. I will also investigate the jet ridge line properties of the  $\gamma$ -detected sources, in relation to those of the non-detected ones.

## 4.3 Data

EGRET has detected 14 CJF sources and has provided an upper limit for 50 more (Fichtel et al. 1994; Hartman et al. 1999). Unlike at the radio and the X-rays, the  $\gamma$ -ray study of this sample is not complete since EGRET only did targeted observations of some of the CJF sources. Fermi-LAT (the renamed GLAST; Atwood et al. 2009) will provide a complete study of these sources through its all-sky survey. 61 CJF sources are included in the first catalog of AGN by the Fermi-LAT, after eleven months of observation (Abdo et al. 2010a). Three additional sources are included in the third EGRET catalog (Hartman et al. 1999) but have not, as of yet, been detected by Fermi.

In total, I find 64 CJF sources (21.8% of the sample) being detected in the  $\gamma$ -rays, while for 40 (13.6% of the sample) only an upper limit is reported. BL Lac objects appear to have a higher detectability than quasars (24 BL Lacs and 34 QSOs) given their relative abundance in the CJF sample, while only 5 CJF radio galaxies have been detected. One  $\gamma$ -detected sources remains unclassified. Five CJF sources belong to the group of few sources that have been detected in the TeV regime (3C66A, Acciari et al. 2009; 0716+714, Teshima and The MAGIC Collaboration 2008; Mrk 421, Punch et al. 1992; Mrk 501, Quinn et al. 1996; BL Lac, Albert et al. 2007) (Table D.1 in the Appendices).

Mkn 501 (Neshpor 2000a) shows quasi-periodic variability in the  $\gamma$ -ray regime on a timescale of a few days. Of the 61 CJF sources already detected by Fermi-LAT (Table D.1 in the Appendices) I note that half of them are found to be  $\gamma$ -variable. In total, 31 sources (10.6%) have been detected to be  $\gamma$ -variable (see Table A.6 in the Appendices). It should be noted that for the following analysis only real detections are used, excluding upper limits information.

### 4.3.1 $\gamma$ -ray luminosities

$\gamma$ -ray observations are based on photon counts per energy bin, surface, and time for each source. In Fig. 4.2 I give a histogram of the photon fluxes for the  $\gamma$ -detected CJF sources. It can be seen that variable  $\gamma$ -ray emitters show higher fluxes, with BL Lacs extending out to higher values compared to QSOs. It appears that variability is closely connected to  $\gamma$ -ray emission. The superposition of stronger beaming due to smaller viewing angles makes BL Lacs appear brighter. A K-S test gives a probability of less than 0.01% that the variable and non-variable  $\gamma$ -ray emitters are drawn from the same parent population. A

K-S test between non-variable  $\gamma$ -ray detected BL Lacs and QSOs gives a probability of 45% that the distributions have the same parent distribution.

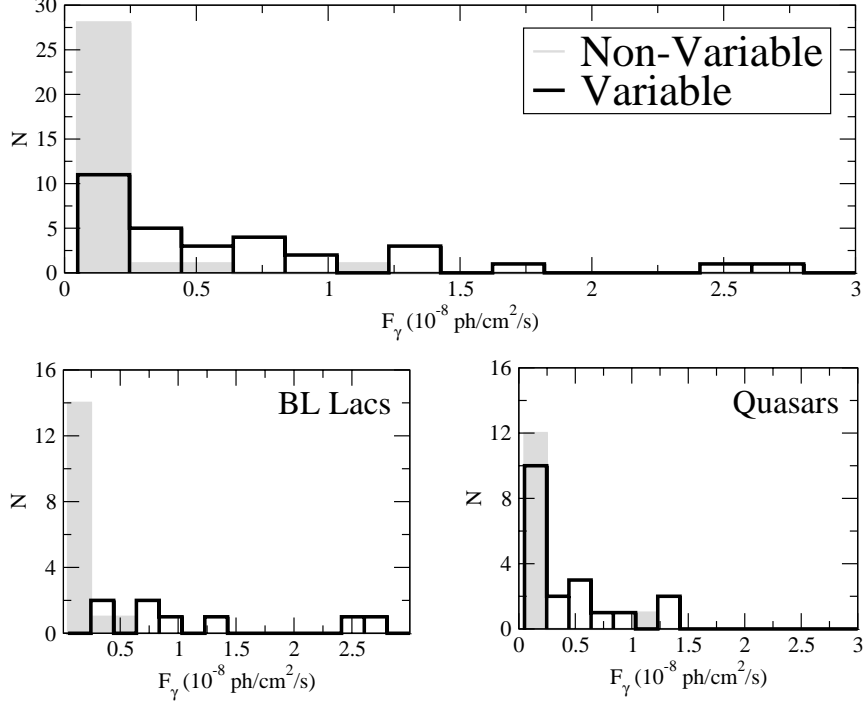


Figure 4.2:  $\gamma$ -ray flux distribution of Fermi-LAT detected (1st Catalog; [Abdo et al. 2010a](#)) CJF sources. The grey shaded bars denote non-variable  $\gamma$ -ray emitters, while the black empty blocks represent variable sources. The distributions are shown for all  $\gamma$ -ray detected CJF sources (upper panel), for BL Lacs (lower left), and for QSOs (lower right).

I am now interested in translating the photon fluxes to luminosities, in order to account for the distance dependence. I follow [Thompson et al. \(1996\)](#) to calculate  $\gamma$ -ray luminosities as follows: assuming an energy range  $(E_1, E_2)$ , then the photon flux translates to an energy flux,

$$F(\Delta E) = \int_{E_1}^{E_2} A E^{-\alpha} dE,$$

where  $A$  is a normalization constant that can be expressed in terms of the integral flux  $F$ . For the Fermi-LAT instrument, a nominal value of 0.1-100 GeV is used for the energy range probed. Then, the energy flux is calculated from the following formula:

$$S(\Delta E) = \frac{1 - \alpha}{2 - \alpha} \cdot \frac{E_2^{2-\alpha} - E_1^{2-\alpha}}{E_2^{1-\alpha} - E_1^{1-\alpha}} F,$$

where  $F$  is the photon flux, the directly observed quantity (measured in photon counts per unit surface and time), and  $S$  is the energy flux (measured in ergs per unit surface and time).



## 4.4 Analysis and Results

As was described in previous sections, I am interested in investigating a possible link between jet kinematics and  $\gamma$ -ray properties in the CJF sample. Before that, there are a couple of points that should be addressed first. As discussed in Sec. 3.7, the CJF sample contains predominantly quasars, with only a few percent of the sample being BL Lac objects and radio galaxies. This is of course a result of the selection criteria of the sample (see Sect. 1.6). 75% of the CJF BL Lacs have been detected by Fermi-LAT, while only 17% of the QSOs and 9.6% of the RGs are included in the first year AGN catalog of the telescope (Abdo et al. 2010a)<sup>2</sup>. The much higher detectability for BL Lacs implies a direct link between production of  $\gamma$ -rays and the viewing angle under which the source is observed. A second effect concerns the redshift distribution of the CJF sources. Quasars show a redshift distribution peaking around  $z=1.3$ , while BL Lacs maximum is around  $z=0.2$ . In Fig. 4.3 I show the redshift distribution of the CJF sources detected in  $\gamma$ -rays. The distribution follows that of the parent sample (see Fig. 1.6), with the highest  $\gamma$ -detected source at redshift  $z = 3.044$ . Taking into account the number of QSOs at  $z < 1$  (56 sources), I derive a  $\gamma$ -ray detectability of 16% for the CJF quasars, as expected, significantly lower than BL Lacs.

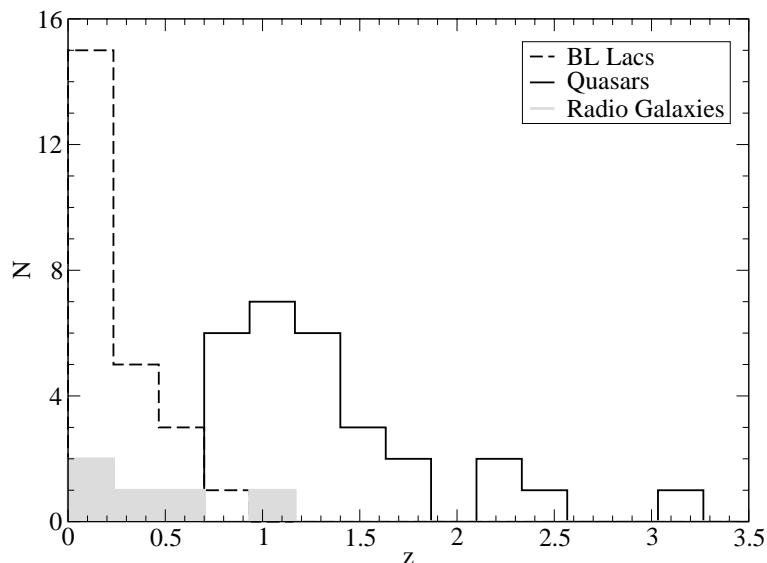


Figure 4.3: Redshift distribution of the Fermi-LAT detected (1st Catalog; Abdo et al. 2010a) CJF sources. The three different classes of AGN are shown: BL Lacs (dashed black line), quasars (continuous black line), and radio galaxies (grey blocks).

It is interesting to see whether there exists a redshift dependency of the  $\gamma$ -ray luminosity of the CJF sources. In Fig. 4.4 I show the  $\gamma$ -ray luminosity of the CJF sources as a function of their redshift. A broad correlation between the two quantities is seen,

<sup>2</sup>These numbers include the three additional sources included in the EGRET catalogs but not yet detected by Fermi-LAT. These sources are: 0804+499, 2346+385, and 2351+456.

with more distant sources being more luminous. This is expected and reflects the flux-limited selection of the CJF sample. Given the large redshift span of the CJF sample, it is important to take into account this redshift bias, especially when investigating possible correlations between  $\gamma$ -ray luminosity and other source properties.

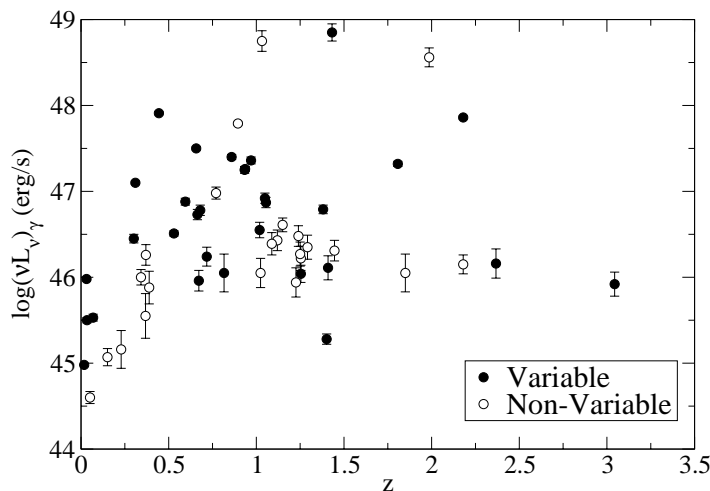


Figure 4.4:  $\gamma$ -ray luminosity of the CJF sources as a function of their redshift.  $\gamma$ -variable (filled) and non-variable sources (empty circles) are separated.

Having calculated the source luminosities, the average and median<sup>3</sup> values for the CJF sample can be calculated. This is shown in Table 4.1. Quasars are consistently more luminous than the BL Lacs. Taking into account only QSOs at redshifts smaller than  $z=1$ , I calculate again the average and median values for this sub-sample ( $45.81 \pm 0.21$  and  $46.27 \pm 0.27$  erg, respectively; the values are given in the  $\log(\nu L_\nu)$  form). Interestingly, it appears that QSOs are genuinely more luminous than BL Lacs, rather than this being a selection effect of the flux-limited CJF sample. A two-sample K-S test gives an 8.2% probability that the two sub-samples are drawn from the same parent distribution.  $\gamma$ -variable and non-variable sources appear distinctively different in their luminosities.  $\gamma$ -variable sources appear more luminous than their non-variable counterparts (both in average and median values). A K-S test gives a 98.4% probability that these are two different samples. This is in agreement with the previous analysis for the fluxes (see previous section).

The intrinsic luminosity of a source might play a role in deciding its  $\gamma$ -ray properties. To that end, I compare the luminosities of the  $\gamma$ -detected and non-detected QSOs at  $z < 1$ , at 5 and 30 GHz (single dish), at optical, and in the X-rays. The  $\gamma$ -detected sources are consistently more luminous in the radio and optical regime, but are fainter in the X-rays. As was described previously, up to soft X-rays the emission is thought to be produced by the synchrotron mechanism and therefore  $\gamma$ -detected sources show a

<sup>3</sup>The uncertainty for the median values is calculated as the median value of the absolute deviation of the median from the measurements, divided by the square root of the number of measurements.

Table 4.1: Characteristic statistic values concerning the  $\gamma$ -ray luminosity (in logarithmic scale) of the sources detected in the  $\gamma$ -rays by Fermi-LAT and EGRET. Average and median values with errors are given for the whole sub-sample, QSOs, BL Lacs, variable, and non-variable sources. Given the small number of RGs (5 sources) detected, separate statistics for that sub-sample are not calculated.

$\log(\nu L_\nu)_\gamma$ (erg)	All	QSO	BL	Var	Non-Var
#	54	34	14	30	21
<b>Average</b>	45.60	46.18	44.60	47.81	47.42
<b>Error</b>	0.12	0.11	0.24	0.11	0.09
<b>Median</b>	45.72	46.01	44.6	47.91	47.53
<b>Error</b>	0.15	0.14	0.3	0.14	0.11
<b>Max</b>	48.53	48.53	46.36	49.06	48.79
<b>Min</b>	42.69	44.39	42.69	46.07	45.98

stronger synchrotron component than their non-detected counterparts. This might in turn be linked to the putative synchrotron self-Compton process often employed to explain the production of  $\gamma$ -ray emission in AGN jets. Conversely,  $\gamma$ -ray detection of a source implies that the inverse Compton hump of its SED is shifted towards higher energies. It is therefore to be expected that  $\gamma$ -detected sources are actually weaker in the soft X-rays than their non-detected counterparts. A larger sample of  $\gamma$ -detected sources, along with a closely matched (in terms of luminosity and redshift) control sample is required to test this scenario.

Concerning the relative importance of the synchrotron and inverse Compton components, I calculate the  $\gamma$ -to-radio luminosity ratio for the  $\gamma$ -detected CJF sources (see Fig. 4.5).

In the left panel of Fig. 4.5 I show the distribution of this ratio for QSOs and BL Lacs (including both variable and non-variable sources). It can be seen that BL Lacs show higher  $\gamma$ -to-radio ratios than QSOs, with the BL Lac distribution peaking around 1.08 compared to the QSO one peaking around 1.05. The fact that I include both variable and non-variable sources might influence my results. In the right panel of Fig. 4.5, I show the  $\gamma$ -to-radio ratio distribution of  $\gamma$ -variable and non-variable QSOs. The distribution of  $\gamma$ -variable QSOs appears shifted towards higher values compared to that of the non-variable QSOs. Given that there are more variable BL Lacs than non-variable ones, the effect observed in the left panel of Fig. 4.5 might in part be due to that. A two sample K-S test for BL Lacs and QSOs gives a probability of 99.7% that their  $\gamma$ -to-radio ratio distributions are drawn from different parent distributions. The same test for variable and non-variable QSOs gives a 91.9% probability that their distributions are significantly different. As was shown above,  $\gamma$ -variable sources are more luminous in the  $\gamma$ -rays than non-variable ones. The radio luminosities (5GHz) of the  $\gamma$ -variable and non-variable sources can also be compared. Within the statistical errors, both sub-samples are, on average, found to be similarly luminous in the radio.

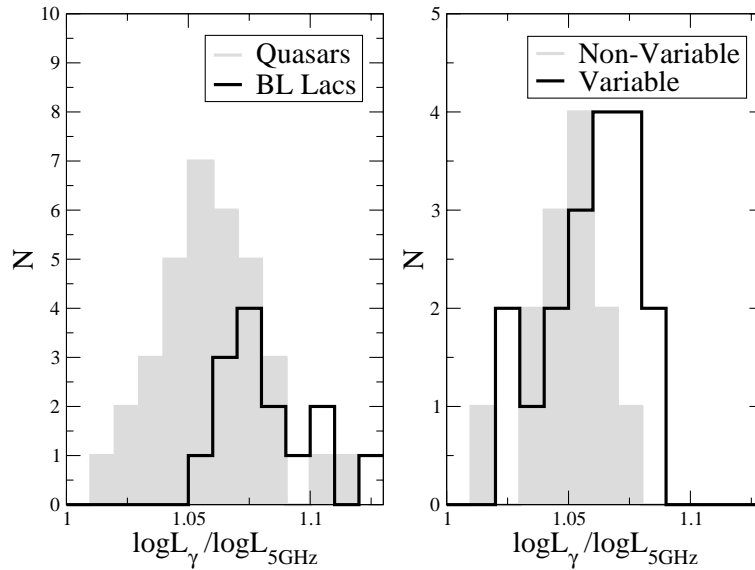


Figure 4.5: Histograms comparing the distributions of  $\gamma$ -to-radio luminosity ratios for different populations of objects: (left panel) BL Lacs and QSOs; (right panel)  $\gamma$ -variable and non-variable QSOs. I use  $\gamma$ -ray luminosities derived from the Fermi-LAT photon fluxes given in the first Fermi-LAT source catalog (Abdo et al. 2010b) and radio luminosities at 5 GHz derived from energy fluxes from Taylor et al. (1996).

Combined with the results of Fig. 4.5, the above imply that the regions producing the radio and  $\gamma$  radiation are not co-spatial. Were that the case, both  $\gamma$  and radio luminosities would be shifted towards higher values, assuming that beaming effects are what make variable sources more luminous. An obvious caveat of this investigation is that  $\gamma$  and radio observations are not contemporaneous, and therefore might not be directly comparable.

#### 4.4.1 Apparent VLBI Jet Component Velocities and $\gamma$ -ray emission

I characterize the kinematics of the CJF sources by the maximum observed component velocity,  $\beta_{app,max}$ , of each source. This maximum component velocity reflects both the orientation of the source (viewing angle) and the intrinsic properties of the jet itself. I investigate whether the distribution of maximum apparent component speeds differs between  $\gamma$ -detected and non-detected sources. For all CJF sources with available redshift, Britzen et al. (2008) have calculated the apparent total component velocities for all the identified components in their VLBI jets. I identify the component with the maximum apparent speed in each source and plot the distribution of these maximum apparent speeds in Fig. 4.6, for  $\gamma$ -detected sources (black empty line) and non-detected ones (grey filled line).

In the upper panel of Fig. 4.6 the distribution of the maximum apparent velocities is plotted for the 191 CJF sources that have not been detected in the  $\gamma$ -rays (grey blocks)

and the 45 sources that have<sup>4</sup> (black line). The maximum of the distribution for the non-detections is found in the [3.5,7] bin. For the detections the maximum lies in the [0,3.5] bin. As can be seen in the inlay of the upper panel<sup>5</sup>, assuming smaller bins, the maximum of the  $\gamma$ -detected sources breaks down to two maxima in the [0,2] and [4,6] bins. The non-detected sources distribution peaks in the [4,6] bin.  $\gamma$ -detected sources appear to have a more extended distribution, towards higher velocities, showing a secondary peak in the [10,12] and [12,14] bin. A K-S test between  $\gamma$ -detected and non-detected sources  $\beta_{app,max}$  distributions gives a 93.7% confidence that these two sub-samples are drawn from different parent distributions.

In the middle panel of Fig. 4.6 I show the same plots as before but only for those sources classified as QSOs. The distribution here seems markedly different from before. Both populations ( $\gamma$ -detected and non-detected) have their distribution shifted towards higher velocities, both of them peaking in the [4,6] bin. The  $\gamma$ -detected QSOs show a prominent secondary peak in the [10,12] bin (secondary to primary ratio of 0.71) and again appear to show a larger fraction of the total number of sources at higher velocities. Non-detected QSOs have a secondary peak in the [8,10] bin (secondary to primary ratio of 0.8). Interestingly enough, the highest velocities for QSOs are found in sources that have not been detected in the  $\gamma$ -rays, implying the presence of a further mechanism at play with regard to  $\gamma$ -ray production. Similarly, in the lower panel of Fig. 4.6 I show the distributions for BL Lac objects. Both  $\gamma$ -detected and non-detected BL Lacs have their distribution maxima in the [0,2] bin, with  $\gamma$ -detected BL Lacs having a considerably more extended distribution, reaching to higher velocities, compared to their non-detected counterparts. Compared to QSOs, the BL Lac velocity distribution is shifted towards lower values. **This reflects what was found in Chap. 3, namely that BL Lacs show slower evolving jets, compared to QSOs. It also provides further evidence that the viewing angle is tightly coupled to  $\gamma$ -ray emission.** A K-S test for the distribution of  $\beta_{app,max}$  for  $\gamma$ -detected QSOs and BL Lacs gives a 97.7% confidence that they are drawn from different parent samples. It should be noted however that the number of  $\gamma$ -detected BL Lacs with available redshift and kinematic information is small and therefore the analysis for BL Lacs is probably affected by low number statistics.

I also calculate average and median values of the maximum apparent velocity for  $\gamma$ -ray detected CJF sources and for those not detected. I find the  $\gamma$ -detected sub-sample of CJF sources to show higher average and median apparent speed values ( $9.0 \pm 0.8$  and  $8.8 \pm 0.7$ , respectively) compared to the non-detected one ( $8.1 \pm 0.4$  and  $6.4 \pm 0.2$ , respectively). A further note concerns the redshift distribution of the two sub-samples. The  $\gamma$ -detected sources have a lower average redshift (0.967) compared to their non-detected counterparts (1.175). As already noted in Sects. 3.5 and 3.7, there appears to be a dependence between apparent velocity and redshift (as noted by Cohen et al. 2007; Britzen et al. 2008; Lister et al. 2009a; and this work), it is therefore expected that the effect observed here might be partially due to the difference of the redshift distribution of the two samples.

Finally, for the  $\gamma$ -ray detected sources, I distinguish between quasars and BL Lac

<sup>4</sup>Previously, it was mentioned that 64 sources have been detected in the  $\gamma$ -rays. The considerably reduced number of both  $\gamma$ -detected and non-detected sources is due to the fact that several sources do not have redshift and/or kinematic information and therefore are excluded from this analysis.

<sup>5</sup>Inlay plots are normalized to surface area one, as I am interested in the relative distributions of the two sub-samples.

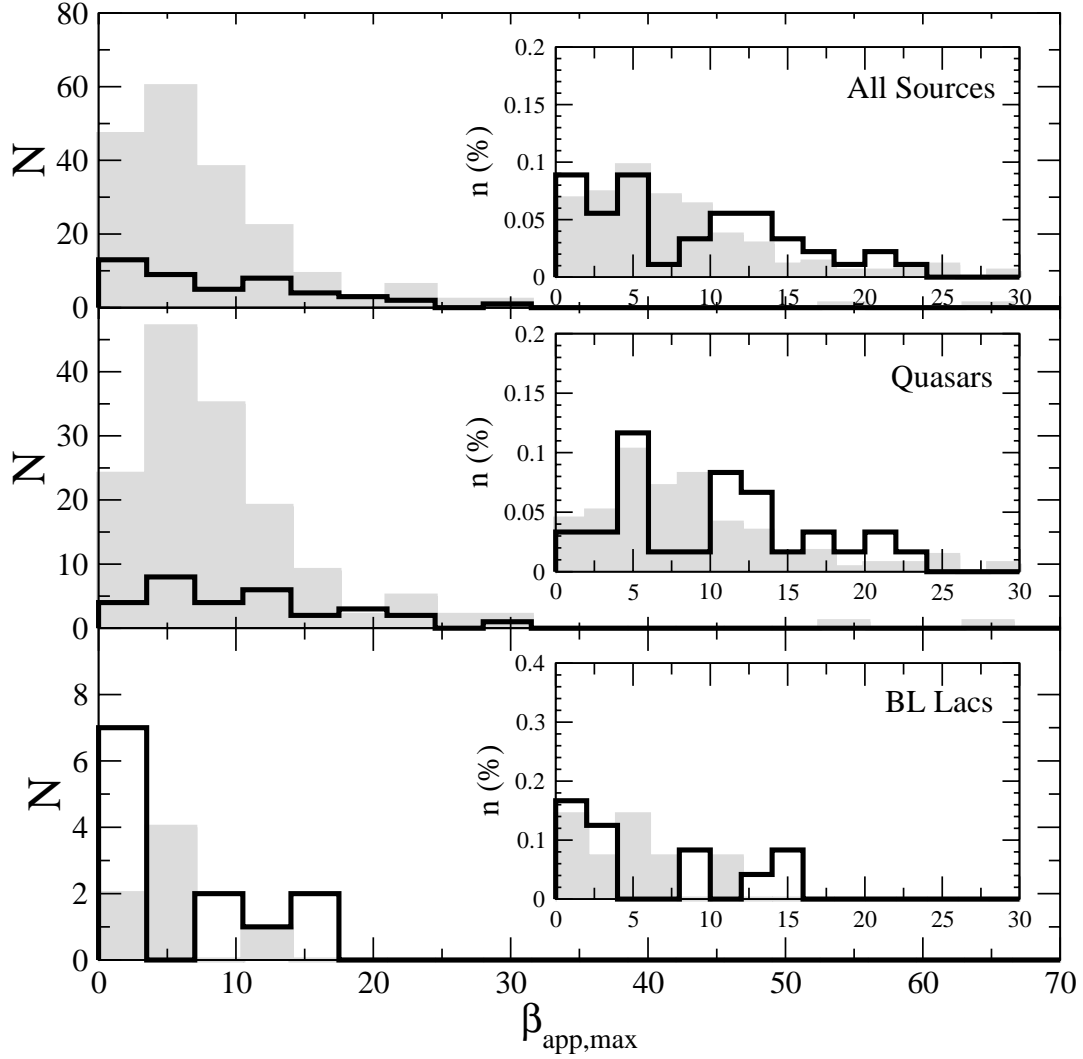


Figure 4.6: The distribution of the maximum apparent velocities  $\beta_{app,max}$  for sources that have been detected in the  $\gamma$ -rays (black line) and for those that have not (grey blocks). The distributions for all sources (upper panel), quasars (middle panel), and BL Lacs (lower panel) are shown. The inlay plots show the normalized to surface area unity distributions for each case and for apparent speeds up to  $30c$ . The kinematic data from [Britzen et al. \(2008\)](#) are used.

objects. It is found that quasars exhibit, on average, considerably higher average and median maximum apparent velocities ( $10.8 \pm 1.0$  and  $10.20 \pm 1.05$ , respectively, compared to  $6.1 \pm 1.5$  and  $2.94 \pm 0.76$ ). Redshift effects might again be influencing these results. I select those QSOs at redshifts lower than 1 and calculate  $\beta_{app,max}$  average and median values. The sub-sample of local QSOs shows, within the statistical errors, the same average values as the BL Lacs ( $\beta_{app,max}^{\gamma,Q} = 6.9 \pm 1.2$ ) but considerably higher median value ( $\beta_{app,max}^{\gamma,Q} = 6.1 \pm 0.9$ ).

In Fig. 4.7 the  $\beta_{app,max}$  distribution of  $\gamma$ -variable (27 sources with available data; average redshift  $z_{avg} = 0.94 \pm 0.09$ ) and non-variable (19 sources with available data; average redshift  $z_{avg} = 0.94 \pm 0.10$ )  $\gamma$ -detected CJF sources are compared. Non-variable  $\gamma$ -detected sources show a more extended distribution than the variable ones, reaching the highest velocities ( $\sim 30c$ ). Both distributions show their main maximum in the [0,3.5] bin.  $\gamma$ -variable sources show a prominent secondary maximum in the [10.5,14] bin (with a secondary to primary ratio of 0.86). Non-variable sources show a weak secondary maximum in the [17.5,21] and [21,24.5] bins (secondary to primary ratio of 0.33). A K-S test for the two distributions does not provide a conclusive result (47.4% probability that the sub-samples are drawn from the same parent distribution). A Student's t-test gives a 23% probability that the two sub-samples are the same.

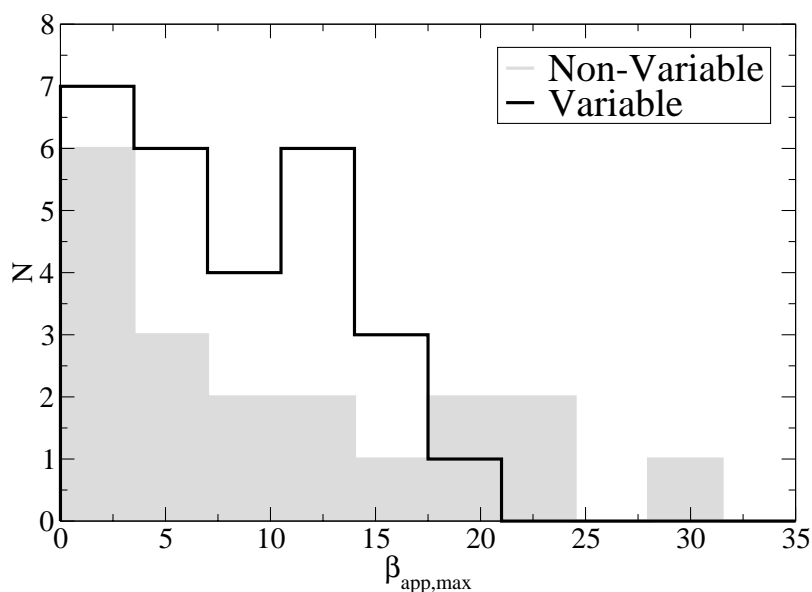


Figure 4.7: The distribution of the maximum apparent velocities  $\beta_{app,max}$  for  $\gamma$ -detected sources that are  $\gamma$ -variable (black line) and for those that are not (grey blocks). The kinematic data from Britzen et al. (2008) are used.

I calculate the statistical properties of the two sub-samples.  $\gamma$ -variable sources show similar  $\beta_{app,max}$  average value to their non-variable counterparts, within the statistical errors ( $7.9 \pm 0.8$  and  $8.9 \pm 1.7$ , respectively). When checking the median values however, the variable sub-sample shows substantially higher value than the non-variable one ( $8.65 \pm 0.84$ , compared to  $4.57 \pm 0.96$ ). Both sub-samples show similar redshift distributions, therefore I do not expect any redshift effect influencing this result.

Unfortunately, as it becomes obvious from the above analysis, there are two effects, possibly dependent, influencing the appearance of a source in the  $\gamma$ -rays regime, (1) variability and (2) viewing angle. For the number of sources available here, I can not robustly decouple these two effects. In Fig. 4.8 I compare the  $\beta_{app,max}$  distributions of  $\gamma$ -variable

QSOs and BL Lacs (left panel) and  $\gamma$ -detected variable and non-variable QSOs (right panel). These two sub-samples (variable sources and QSOs sources) are the largest of the different  $\gamma$ -detected sub-samples (e.g., non-variable sources, BL Lac sources, etc.) and therefore are chosen to check the individual effects of viewing angle and variability.

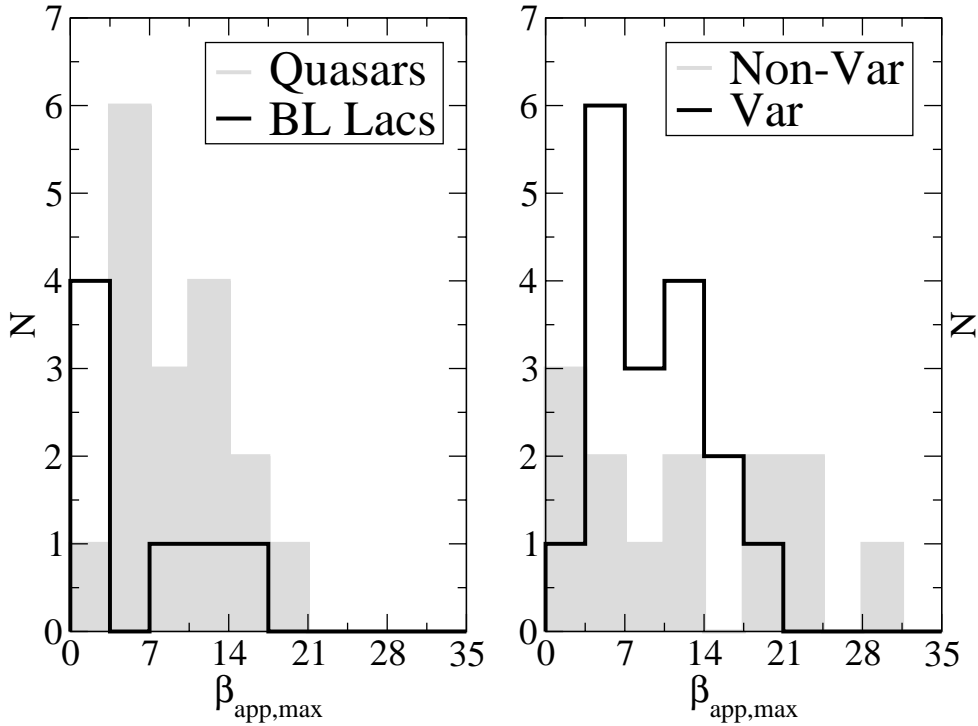


Figure 4.8: Left panel: distributions of the maximum apparent velocities  $\beta_{app,max}$  for  $\gamma$ -detected sources,  $\gamma$ -variable BL Lacs (empty line) and  $\gamma$ -variable QSOs (filled line). Right panel:  $\gamma$ -variable (empty line) and non-variable (filled line) QSOs. I use the kinematic data from Britzen et al. (2008).

Quasars (left panel of Fig. 4.8) show the maximum of their distribution at higher values than BL Lacs ([3.5,7] bin compared to [0,3.5]), with a second peak in the [10.5,14] bin (secondary to primary ratio of 0.67). A Student's t-test<sup>6</sup> gives a 20% probability that these two sub-samples are drawn from the same parent distribution. For variable and non-variable sources the comparison is not so straightforward (right panel of Fig. 4.8). Non-variable  $\gamma$ -detected QSOs show a main maximum in the [0,3.5] bin, lower than their variable counterparts. However, they also show a more extended distribution, with secondary maxima in the [10.5,14], [17.5,21], and [21,24.5] bins (secondary to primary ratio of 0.67). Both Student's t-test and a K-S test give inconclusive results (21% and 23% probability, respectively, that the sub-samples are the same). Small number statistics

<sup>6</sup>We employ Student's t-test due to the small number of sources contained in each sub-sample. The K-S test is not as accurate in such a case.



affect these results and therefore a definitive answer can not be offered concerning the relative importance of the two effects. There is evidence that  $\gamma$ -ray emitting,  $\gamma$ -variable quasars show statistically higher apparent velocities. **Given the available data, I do not find any robust connection between  $\gamma$ -ray emission and fast moving jet components, as has been argued by other authors (see Sect. 4.5 for a discussion on this).**

#### 4.4.2 $\gamma$ -ray Luminosities and Apparent Jet Component Velocities

In the previous section I probed the putative connection between the production of  $\gamma$ -rays and the jet kinematics -i.e., the beaming mechanism-, as reflected in the differences between the  $\beta_{app,max}$  distribution of QSOs and BL Lacs. Another way to approach this is by looking for a possible direct correlation between the apparent velocities measured in the AGN jets and their  $\gamma$ -ray luminosity. This is shown in Fig. 4.9.

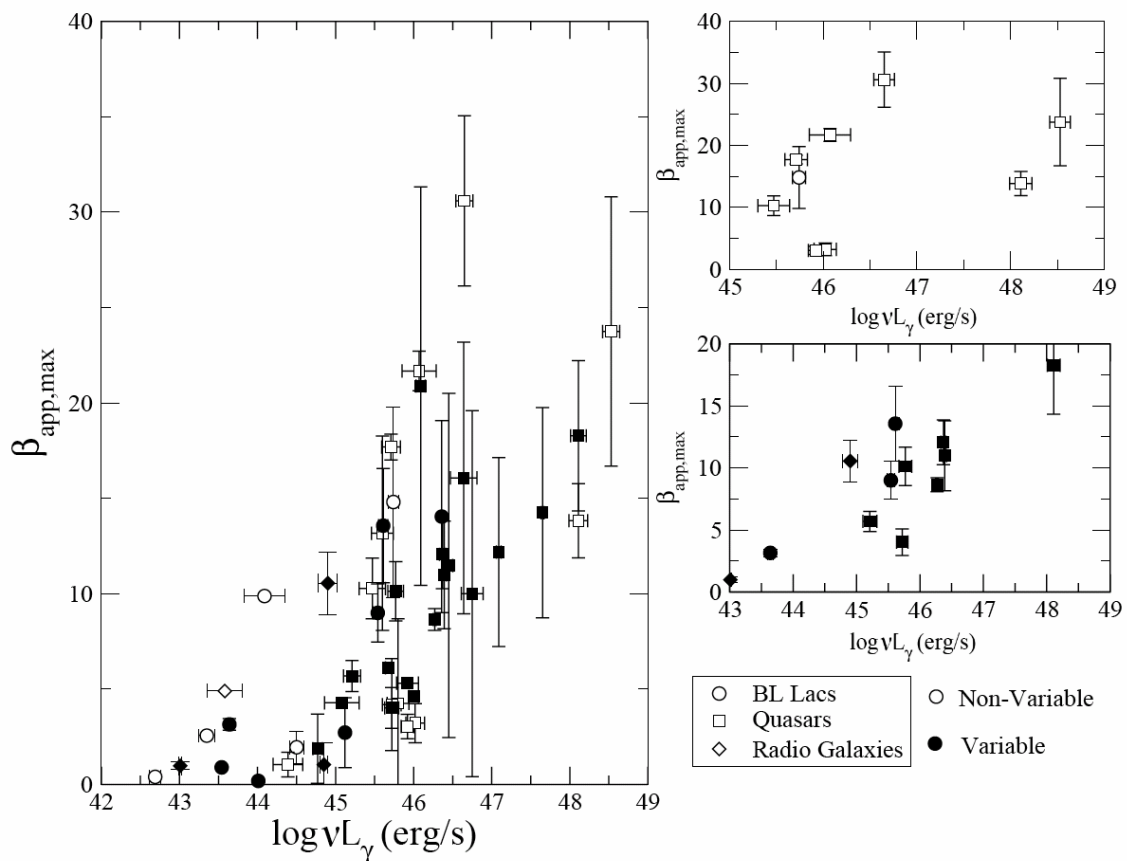


Figure 4.9: The maximum apparent component velocities for all  $\gamma$ -ray detected CJF sources as a function of their  $\gamma$ -ray luminosity, for all sources (left panel) and for high significance values of  $\beta_{app,max}$  (right panels; see text for details). I differentiate between variable (filled symbols) and non-variable sources (open symbols), and between the different AGN classes, i.e., BL Lacs (circles), QSOs (squares), and RGs (diamonds). The kinematic data from Britzen et al. (2008) are used.

As can be seen in Fig. 4.9, there appears to exist a correlation between the  $\beta_{app,max}$

of a source and its  $\gamma$ -ray luminosity. Variable sources appear to cluster closer to the implied trend, with non-variable QSOs deviating the most. We find Spearman correlation coefficients of 0.68 and 0.77 (both at a significance of  $> 99.999\%$ ), respectively. Given the mutual dependence of luminosity and jet component apparent velocity to the redshift of a source, we also calculate the Pearson product moment partial correlation coefficients  $r(L_\gamma, \beta_{app,max}, z)$ <sup>7</sup>. While for the whole sample we get a relatively low partial correlation coefficient (0.43 at a significance of 99.8%), the correlation for variable sources persists (0.68 at a significance of  $> 99.9\%$ ). Given the expected degree of scatter in the data, the correlation coefficients combined with the calculated significance imply that the trend seen in Fig. 4.9 is indeed true. We note that some of the apparent velocities show relatively large errors, therefore, in the right panels of Fig. 4.9, we plot only sources for which  $\beta_{app,max} \geq 3\sigma$ . We also separate variable sources from non-variable ones. It becomes clear that the non-variable sources show the most scatter. For the variable sources, we calculate a Spearman correlation coefficient of 0.69 (at a 99.1% significance level), lower than the coefficient we got when fitting all the sources. Calculating the partial correlation coefficient for the same sub-sample gives a smaller correlation coefficient (0.61 at a 98.1% significance). We also investigate the same correlation for individual classes of objects. The strongest correlations are seen for both  $\gamma$ -variable BL Lacs (partial correlation coefficient of 0.68 at 95.1% significance) and quasars (partial correlation coefficient of 0.69 at 99.9% significance). The differences seen between the different classes of AGN, as well as between variable and non-variable sources reveal a complicated picture. We shall discuss the robustness and implications of our results more extensively in Sect. 4.5.

### 4.4.3 $\gamma$ -ray and jet ridge line properties

The above analysis reveals a rather complex picture of how  $\gamma$ -ray properties may be connected to the properties of the CJF sample in the radio. I therefore now turn to the results of Chap. 3, to see whether there is a connection between the  $\gamma$ -rays and the evolution of the jet ridge lines. I shall again divide this analysis into three parts, concerning the three different main measures used: (1) jet ridge line width, (2) width evolution, and (3) linear evolution (for more information see Sect. 3.4).

#### Jet ridge line width, dP, and $\gamma$ -rays

I compare the jet ridge line width of the  $\gamma$ -detected and non-detected sources. No constraints concerning the width are used, given the relatively small number of sources detected in the  $\gamma$ -rays (but for the different effects and possible constraints, see Sects: 3.5 and 3.7). As a first step, I calculate average and median values for the two sub-samples.  **$\gamma$ -detected sources show significantly wider jet ridge lines, both in average and median values ( $16.9 \pm 1.0^\circ$  and  $11.15 \pm 0.58^\circ$ , respectively), compared to the non-detected ones ( $13.6 \pm 0.4^\circ$  and  $9.35 \pm 0.29^\circ$ ).** This can be seen clearly in the upper panel of Fig. 4.10: the maximum of the jet ridge line width distribution of the  $\gamma$ -detected (non-variable) sources

---

<sup>7</sup>For this we use the Web tool: Wessa P., (2008), Partial Correlation (v1.0.4) in Free Statistics Software (v1.1.23-r6), Office for Research Development and Education, URL [http://www.wessa.net/rwasp\\_partialcorrelation.wasp/](http://www.wessa.net/rwasp_partialcorrelation.wasp/).

is shifted to higher values (in the [5,10] bin), compared to their non-detected counterparts (which have their maximum in the [0,5] bin).

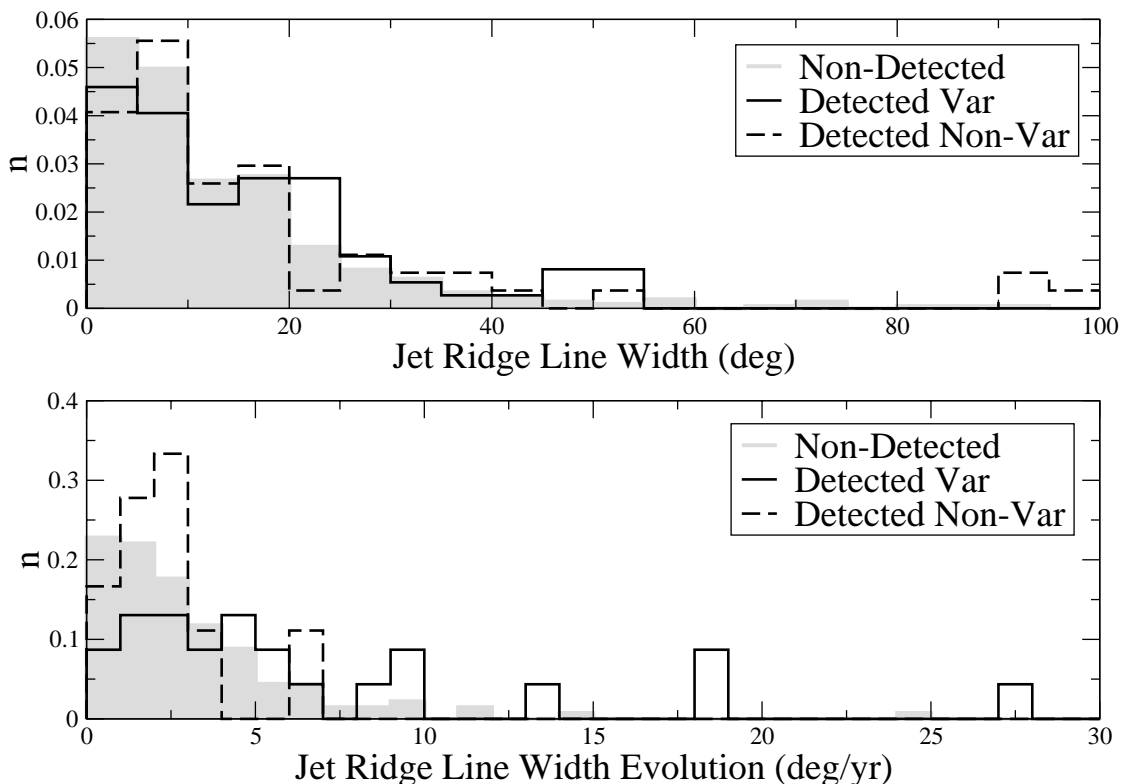


Figure 4.10: Histograms of jet ridge line width,  $dP$ , and width evolution,  $\Delta P$ , for  $\gamma$ -detected variable sources (solid line),  $\gamma$ -detected non-variable sources (dashed line), and  $\gamma$ -ray non-detected sources (grey blocks). Given the large difference in absolute numbers, histograms normalized to surface area unity are plotted. The data from Chap. 3 are used.

Furthermore, I can also distinguish between  $\gamma$ -ray variable and non-variable sources. Going back to the analysis in Sect. 3.5, it is expected that variable sources exhibit wider jets. This is not as clear in this case. Within statistical errors, both  $\gamma$ -variable and non-variable sources have on average the same width ( $16.1 \pm 1.2^\circ$  and  $18.3 \pm 1.9^\circ$ , respectively), with non-variable sources having marginally wider jets. If median values are taken into account, variable sources show wider jets ( $11.5 \pm 0.8^\circ$  compared to  $10.5 \pm 0.8^\circ$ ). Checking the distributions of the two sub-samples, I find that non-variable sources have their peak at higher widths compared to the variable ones. **The clear distinction of the widths of  $\gamma$ -detected and non-detected sources reflects the importance of the transverse, non-radial, motion of components in AGN jets, rather than of the outward one.**

### Jet ridge line width evolution, $\Delta P$ , and $\gamma$ -rays

Similarly, the jet ridge line width evolution of  $\gamma$ -detected and non-detected sources is compared. Given the small number of sources, the sample is not narrowed down as it was done for some cases in Sect. 3.5. If my previous assumption is indeed true, namely that the transverse motion of AGN jet components is relevant for  $\gamma$ -ray emission, then a clear division in this measure is expected too.  $\gamma$ -detected sources are found to show stronger evolution of their widths, both in average and median values ( $4.7 \pm 0.5$  deg/yr and  $2.50 \pm 0.16$  deg/yr, respectively), compared to their non-detected counterparts ( $3.13 \pm 0.18$  deg/yr and  $2.26 \pm 0.12$  deg/yr). In the lower panel of Fig. 4.10 I show the distribution of the width evolution values for  $\gamma$ -detected and non-detected sources. The  $\gamma$ -detected distribution is peaked in the [2,3] bin, compared to the non-detected one, peaking in the [0,1] bin.

As before, I distinguish between variable and non-variable  $\gamma$ -detected CJF sources and investigate their jet ridge line width evolution in this context. Variable sources are found to have significantly stronger evolving jet ridge line widths, at a  $4\sigma$  significance level, both in average and median values ( $6.7 \pm 1.0$  and  $4.4 \pm 0.6$  deg/yr, compared to  $2.4 \pm 0.3$  and  $2.17 \pm 0.16$  deg/yr). In Fig. 4.10 (lower panel) I plot the distribution of  $\gamma$ -variable and non-variable sources. I see that both sub-samples have the peaks of their distributions in the [2,3] bin, however the non-variable sources distribution is fairly confined to lower values, whereas variable sources extend up to the highest values of width evolution. **This is in agreement with what is expected, assuming that variability originates in the pc-scale jet and is due to changes of the viewing angle (and therefore of the Doppler factor).**

### Jet ridge line linear evolution, $\Delta \ell$ , and $\gamma$ -rays

I finally compare how the jet ridge line evolves, in linear terms, in  $\gamma$ -loud and  $\gamma$ -quiet sources. As already discussed previously, the redshift distributions of the two sub-samples are fairly similar, therefore no redshift-induced effects, related to linear distances, are expected to influence the results. As I showed above, no robust connection is found between fast moving jet components and  $\gamma$ -ray detectability of a source. In this context, it is not expected to find important differences in terms of the linear evolution of the jet ridge line between  $\gamma$ -detected and non-detected sources. Indeed, I find that both in average and median values, the two sub-samples show similar values of linear evolution ( $0.47 \pm 0.03$  and  $0.400 \pm 0.028$  pc/yr/comp, respectively, for the  $\gamma$ -detected sources, compared to  $0.44 \pm 0.02$  and  $0.38 \pm 0.011$  pc/yr/comp for the non-detected ones).

The same behavior is seen when comparing between  $\gamma$ -variable and non-variable sources. It should be noted however, that the median value for  $\gamma$ -variable sources is considerably higher than the one for non-variable sources ( $0.43 \pm 0.03$  pc/yr/comp compared to  $0.291 \pm 0.019$  pc/yr/comp, respectively). This discrepancy between average and median values implies a large scattering within this data that might be posing some limitations to the robustness of my results. Aside from that, I confirm my finding from before, i.e., that the link between fast apparent jet speeds and the  $\gamma$ -ray detectability of a source is questionable. **It appears that, although there are certainly indications that higher speed sources are preferentially  $\gamma$ -ray emitters, some other effect might play a more important role in defining the  $\gamma$ -ray properties of a source.**

#### 4.4.4 TeV sources

39 extragalactic sources have been identified to be emitters in the TeV regime (for an updated list of these sources and references, see [www.mppmu.mpg.de/rwagner/sources/](http://www.mppmu.mpg.de/rwagner/sources/)). Five CJF sources, all BL Lac objects, are detected in TeV. All are variable in  $\gamma$ -rays, optical, and infrared, while four of them are variable in radio and three in the X-rays.

The mechanism that produces such energetic photons in AGN is still unclear (e.g., [Mannheim and Biermann 1992](#); [Maraschi et al. 1992](#); [Georganopoulos et al. 2005](#)), one of the main problems being the variability also observed in this regime (for a discussion and a proposed solution see, e.g., [Tavecchio and Ghisellini 2008](#)).

Extremely high energetic photons coming from AGN (TeV sources, see [Table D.1](#)) can be a result of acceleration taking place in sharp bends of the AGN jets (for a discussion on high energy  $\gamma$ -ray emission from AGN see e.g., [von Montigny et al. 1995](#)). I therefore check the kinematics of the TeV sources in the CJF ([Table 4.2](#)). The misalignment angle between the parsec and the kiloparsec scale (as calculated by [Britzen et al. 2007a](#)) is given. The bending of the parsec scale jet (as calculated by [Britzen et al. 2008](#)) is also listed for all identified components. Finally, the maximum apparent jet component velocity is given. No apparent link is found between the bending of the jet and the  $\gamma$ -ray flux. 2 out of 4 sources exhibit superluminal motion in their VLBI jets. Former studies find that TeV sources exhibit slow jet speeds (e.g., [Piner et al. 2008](#); [Britzen et al. 2010b](#)). Unfortunately, the relatively small number of objects known as TeV emitters does not allow for a robust statistical analysis. Given the relatively low observing frequency of the CJF sample (compared, e.g., to the MOJAVE sample, or mm-VLBI samples), it can be argued that the mechanisms or conditions responsible for this very high energy emission are closer to the jet base (or the SMBH itself) and therefore at scales that can not be probed by these observations.

## 4.5 Discussion and Conclusions

In this section, I first present a short summary of the results presented previously. I shall then discuss the implication of these results.

### 4.5.1 Summary

In this chapter, I have investigated the  $\gamma$ -ray properties of the CJF sources detected by Fermi-LAT and by EGRET, in terms of their jet properties and jet kinematics, as were described and analyzed in [Chap. 3](#) and [Britzen et al. \(2008\)](#). I find that:

- 21.8% of the CJF sample is detected in the  $\gamma$ -rays (either from EGRET or the Fermi-LAT; three EGRET associations not included in the 11 month catalog)
- BL Lacs appear to be preferentially detected in the  $\gamma$ -rays. Taking into account the difference of the redshift distributions of QSOs and BL Lacs in our sample, we still get fairly different detection ratios between the two classes (16% and 75%, respectively).

Table 4.2: TeV detected CJF sources. Columns (1)-(3) as in Table A.1, Col. (4) gives the misalignment angle between the pc and kpc-scale jet (from Britzen et al. 2007a), Col. (5) gives the bending of the identified components of the pc-scale jet (for details see Britzen et al. 2008), Col. (6) gives the maximum apparent total Doppler factor for the VLBI jet of the source, and Col. (7) gives the source’s  $\gamma$ -ray flux (Tabel D.1).

Source	Type	$z$	$\Delta PA$ (deg)	Bend (deg)	$\beta_{tot,max}$	$\gamma$ -rays ( $10^{-8} ph cm^{-2} s^{-1}$ )
0219+428	BL	0.444	8	24 4 1	$14 \pm 5$	$2.49 \pm 0.10$
0716+714	BL		75	3 7 3		$1.31 \pm 0.07$
1101+384	BL	0.031	13	2	$0.19 \pm 0.07$	$2.61 \pm 0.10$
1652+398	BL	0.034	83	10 40 10 3	0.90	$0.83 \pm 0.06$
2200+420	BL	0.069	30	25 16 47	$3.2 \pm 0.3$	$0.71 \pm 0.06$

- $\gamma$ -variable sources appear significantly brighter in the  $\gamma$ -rays than non-variable ones. A two-sample K-S test gives a 99.999% significance result that the two samples are drawn from different parent distributions.
- after calculating the  $\gamma$ -ray luminosities of both QSOs and BL Lacs, and taking into account the redshift effects of the flux-limited sample used here, QSOs appear intrinsically more luminous in the  $\gamma$ -rays than BL Lacs.
- $\gamma$ -detected sources show the peak of their  $\beta_{app,max}$  distribution at similar values as their non-detected counterparts but show a more extended distribution towards higher jet component speeds. A K-S give a 97.7% confidence that the two sub-samples are significantly different.
- breaking down the sources to QSOs and BL Lacs, for both  $\gamma$ -detected and non-detected sources of each class, the  $\beta_{app,max}$  distributions between objects of the same class are fairly similar, with  $\gamma$ -detected sources showing more extended distributions towards higher values.
- comparing between  $\gamma$ -detected QSOs and BL Lacs, after accounting for redshift effects, both sub-samples show on average and within statistical errors the same apparent speeds.
- trying to distinguish between the effects of (1) variability and (2) viewing angle, variable QSOs show the highest apparent component speeds.

- a correlation between  $\beta_{app,max}$  and  $\gamma$ -ray luminosity. The correlation is stronger for BL Lac objects and for  $\gamma$ -variable sources, with non-variable QSOs deviating the most from the implied trend.
- $\gamma$ -detected sources have significantly wider jet ridge lines than their non-detected counterparts. I also find that  $\gamma$ -detected sources show stronger jet ridge line width evolution than non-detected ones.
- no significant difference in terms of linear evolution of the jet ridge lines between  $\gamma$ -detected and non-detected sources.
- no direct link between highly bent jets and TeV emission. Furthermore, I note that 2 out of 4 TeV CJF sources with  $\beta_{app,max}$  information show superluminal speeds, opposite to previous studies.

## 4.5.2 Discussion

It is interesting to compare these results with similar studies using different samples of AGN. As was already mentioned in Sect. 4.1, a number of authors have claimed a tight connection between  $\gamma$ -ray bright AGN and large Doppler factors (e.g., [Jorstad et al. 2001b](#); [Kellermann et al. 2004](#); [Lister et al. 2009c](#)). [Lister et al. \(2009c\)](#), in particular, examine the kinematic properties of the MOJAVE sources ([Lister et al. 2009a](#)) in light of the, then recently, published 3-month bright AGN Fermi-LAT list. In short, they find that (1) the  $\gamma$ -detected MOJAVE sources have the peak of their  $\beta_{app,max}$  distribution around 10-15c, quite a higher value compared to the non-detected ones ( $\sim 5c$ ). They also find that (2)  $\gamma$ -detected variable sources show higher apparent speeds. Finally, although BL Lacs in their sample have lower redshifts and slow median jet speeds (6c), (3) they are preferentially detected by Fermi-LAT. Similarly to [Lister et al. \(2009c\)](#), [Jorstad et al. \(2001b\)](#) and [Kellermann et al. \(2004\)](#) also conclude that  $\gamma$ -detected AGN have significantly higher apparent speeds than their non-detected counterparts.

The results presented in this chapter are somewhat different. Although a secondary maximum is found around 10-15c for the  $\gamma$ -detected sources, the primary maximum of both distributions appears to be around 5c, with  $\gamma$ -detected sources actually showing a double maximum in the [0,2] and [4,6] bins. **It appears that the  $\beta_{app,max}$  distribution of the sources is more strongly dependent on the viewing angle (as reflected in the classification of the source as a QSO or a BL Lac) and whether the source appears variable, rather than it being detected in the  $\gamma$ -rays.** In particular, as I showed in the previous section, QSOs show higher apparent jet speeds than BL Lacs, irrespectively of their  $\gamma$ -ray properties. A common feature for  $\gamma$ -detected sources is that their  $\beta_{app,max}$  distribution appears more extended, with larger percentage of the sources at higher speeds, compared to those of non-detected sources. Coming to point (2) -i.e., that  $\gamma$ -variable sources show higher apparent jet speeds- my results agree, as I showed for the case of  $\gamma$ -variable and non-variable  $\gamma$ -detected QSOs. However this should not come as a surprise in light of the findings from Chap. 3. In Sect. 3.5 it was shown that variable sources (throughout the electromagnetic spectrum) show stronger linear evolution of their jet ridge lines, a measure essentially reflecting their apparent jet speeds. **Therefore, the higher**

**apparent speeds of  $\gamma$ -detected variable sources can probably be attributed to the variability (possibly linked to beaming effects), rather than the  $\gamma$ -ray emission itself.**

Finally, concerning point (3), I showed that, at least for the CJF sample, BL Lac objects are not preferentially detected by Fermi-LAT if I correct for the different redshift distribution of QSOs and BL Lacs. Although the percentage of detected BL Lacs is indeed higher (75%, compared to 60% for QSOs), it is not as high as originally implied. It is interesting that  $\gamma$ -detected QSOs in the CJF sample show higher  $\gamma$ -ray luminosities. [Lister et al. \(2009c\)](#) argue that BL Lacs might be preferentially detected by Fermi-LAT because of their flatter spectrum, i.e., their higher  $\gamma$ -to-radio ratio, compared to QSOs. As was shown in previous sections, this is indeed true, although the relative importance of the viewing angle and the variability is still not clear.

Although my results are in general agreement with previous studies, there are some differences that merit further interpretation, in particular, the fact that I do not find a strong connection between fast moving components and  $\gamma$ -detected sources, as opposed to previous works. As was already discussed in Sect. 4.1, one of the models proposed for the origin of  $\gamma$ -ray emission in AGN involves a spine-sheath geometry, where a high Doppler spine is embedded in a slower moving sheath. According to these models, the ultra-relativistic spine gives rise to the  $\gamma$ -ray emission that is observed. Assuming that the jet as a whole becomes gradually more opaque at lower observing frequencies, I could then argue that, given the lower frequency that the CJF sample has been observed in, only the (transversely) outer regions of the jet are probed and therefore only the slower motions linked to the sheath of the jet are recovered. Conversely, the MOJAVE sample (15 GHz) as well as the samples used by both [Jorstad et al. \(2001b\)](#) (42, 22, and occasionally 15 and 8.4 GHz) and [Kellermann et al. \(2004\)](#) (15 GHz) are all at higher observing frequencies and thus more sensitive to the inner layers of the jet, compared to the CJF. It is therefore plausible that these studies have recovered the faster speeds linked to the ultra-relativistic spine and the production of the  $\gamma$ -ray emission observed.

An alternative scenario would be that indeed  $\gamma$ -ray emission is not directly linked to fast jet components speeds. Given that [Lister et al. \(2009c\)](#) use the three month bright source list for their study, it is possible that only the most strongly beamed sources are detected by that time and therefore there is a strong bias towards sources with higher Doppler factor jets. Including sources from the first, 11-month, Fermi-LAT catalog allows us to probe lower-luminosity sources (given the higher sensitivity achieved after 11-months of observations) and therefore the bias towards the most highly beamed sources is lifted. This scenario however is probably not true since (1) by using only the sources included in the 3-month bright sources Fermi-LAT list and the CJF apparent speed data, a low-velocity component is still found in the  $\beta_{app,max}$  distribution of the  $\gamma$ -detected sources and (2) [Savolainen et al. \(2010\)](#), after calculating Doppler and Lorentz factors of Fermi-LAT detected AGN (3-month list), find a notable absence of sources at the smallest (and therefore most highly beamed) co-moving viewing angles, essentially showing that  $\gamma$ -detected sources are not necessarily associated to the fast moving jets. Distinguishing between either scenarios will require a larger sample of  $\gamma$ -detected AGN with uniform, multi-frequency kinematic data available.

A last point that needs to be discussed concerns the connection between the jet ridge line width to the  $\gamma$ -ray properties of a source. [Pushkarev et al. \(2009\)](#) study the jet opening angles of the MOJAVE sample again in the context of the 3-month bright source list



of the Fermi-LAT. The authors find that  $\gamma$ -bright sources have larger apparent opening angles, but in their co-moving frame both  $\gamma$ -bright and faint sources show similar opening angle distributions. This is in turn interpreted as evidence that  $\gamma$ -detected sources are seen at smaller viewing angles than the non-detected ones. My results agree with these findings, as I find that  $\gamma$ -detected sources exhibit wider jet ridge lines compared to their non-detected counterparts. It should however be noted that preferential detection of BL Lacs in the  $\gamma$ -rays combined with my results from Chap. 3 -i.e., that BL Lacs have apparently wider jet ridge lines- might introduce an additional effect in such an analysis. It is also interesting to note that, according to my findings from Sect. 4.4,  $\gamma$ -detected sources also exhibit large changes in their jet ridge line widths, larger than the non-detected ones. That would introduce a noise factor when comparing the width distributions of  $\gamma$ -detected and non-detected sources. **This in turn implies that  $\gamma$ -detected sources might in reality be even wider than implied by the distribution shown in Fig. 4.10.** Given the still small number of available CJF sources detected by Fermi-LAT, it is, for the time being, not possible to decouple these effects.

### 4.5.3 Conclusions

In the previous sections I have investigated the connection of the  $\gamma$ -ray properties of the CJF sources to the morphological and kinematic properties of their jets. From my analysis it becomes clear that there is a number of factors influencing whether a source is luminous in the  $\gamma$ -rays or not. Although it is tempting to think in terms of  $\gamma$ -loud and quiet objects, the picture is surely more complicated. As has recently been demonstrated for the radio divide (radio-loud and radio-quiet objects) there is a number of sources that actually seem to populate an intermediate space, implying a rather continuous distribution. It is possible that with more sensitive  $\gamma$ -ray telescopes a greater number of  $\gamma$ -ray emitting sources will be recovered. Of course the question still remains as to what it is that differentiates those  $\gamma$ -quite (or -faint) sources from those already detected by the Fermi-LAT and EGRET missions. This analysis, combined with previous studies on this question, indicates that the viewing angle is what makes some sources to be  $\gamma$ -ray luminous and others not. However, as was indicated by Savolainen et al. (2010), the picture is more complicated than that. Given the relatively weak link between jet apparent speeds and  $\gamma$ -detected sources that I find in this work, as well as the different picture arising at higher observing frequencies, a spine-sheath configuration scenario is supported, where the most energetic emission - coming from an ultra-relativistic flow- originates from the spine of the AGN outflow and is therefore partly or fully obscured at lower observing frequencies. In addition, the comparison of the  $\gamma$ -to-radio luminosity ratio of  $\gamma$ -variable and non-variable sources implies that the  $\gamma$  and radio-emitting regions are not co-spatial, offering further support to such a two-zone model. Finally, the link between the width and width evolution of the jet ridge lines of the CJF sources to their  $\gamma$ -ray properties implies that transverse, non-radial, motions in the jet are important in this context, probably also related to the variability detected for almost half of the  $\gamma$ -detected AGN in the CJF sample. It is obvious that a larger sample of  $\gamma$ -detected AGN with complete, multi-frequency kinematic data will allow us to investigate the above effects in a more robust manner. Furthermore, the investigation of individual objects, with detailed modeling of their SEDs will surely shed light to the actual processes producing the  $\gamma$ -ray emission. As a final note, one can

also investigate intra-galactic  $\gamma$ -ray emitting jets. Their much closer vicinity will allow a more in depth investigation of the relevant processes. Results from such a study can then be scaled-up and applied to active galaxies, providing further insight into the underlying physics that drive both classes of objects.

## 5 Epilogue

In this work, I have presented results pertaining to the characteristic properties of active galaxies in different wavelengths. The work presented here was multi-aimed and reflects the complexity and breadth of topics related to activity at the centers of galaxies. As I described in Chap. 1, active galaxies comprise many different components, including a supermassive black hole at their centers, an accretion disk, an obscuring molecular torus, broad and narrow-line emission regions, as well as a radio jet for some of them. On top of that, one also needs to account for the host galaxy that harbors the active nucleus, also being a very complex system on its own. The scales involved in this kind of research, including size, energy, and time, cover many orders of magnitude differences, starting from the really small (event horizon of the SMBH, radio emission, intra-day variability) and going up to the extremely big (dark-matter halo of the galaxy,  $\gamma$ -ray emission, relaxation time of host galaxy). It is therefore imperative that one breaks down this field into smaller, more manageable pieces of science, focusing on the tree while not losing the forest. The content of this work reflects exactly this effort to bridge phenomenologically different AGN scales and properties, trying to make a further step towards a true unification of this field of research. There is a number of reasons why the objects observed are different. It is therefore the unification of our understanding of these objects that motivated this work, rather than a belief that all AGN in the Universe are intrinsically and fundamentally the same.

A second axis of my work has been an effort to utilize information and knowledge that was already available, rather than basing this work on new observations. In an epoch of information overflow, it sometimes appears that one does not really fully exploit the available data but rather focuses on the race for the next newer, bigger, more sensitive telescope that will provide new, better, more accurate, more "rich" datasets. It is a fact that one of the challenges that the next generation of big telescopes, like SKA, ALMA, and even current generation instruments like LOFAR, face is the huge volume of produced data, still lacking an effective and cost-efficient way of managing their deliverables. This reflects the philosophy of pluralism and sometimes even the "quantity over quality" principle often encountered in both scientific and non-scientific settings. Aside from that, it also implies that there might be a wealth of information still to be extracted from already existing datasets. Moreover, given the fragmentation of the AGN field, or any research field for that matter, just creating links between already existing results often leads to new and exciting aspects for all fields involved. This philosophy threads the work presented here, as I strived to make connections between different fields of research, i.e., galaxy evolution and infrared astronomy to AGN and radio astronomy,  $\gamma$ -ray astronomy to radio astronomy, etc. The results presented in the previous chapters gratify these motives and illustrate that astronomy needn't be an expensive, or isolated, science.

## 5.1 Summary

In this section, I shall summarize the main results of the previous chapters. For further details I refer the reader to the individual chapters and the numerous references therein.

### 5.1.1 Active galaxies in the context of galaxy evolution

In Chap. 2 I investigated the role of active galaxies in the context of galaxy formation and evolution. The discovery of ultra-luminous infrared and sub-millimeter galaxies, combined with the fact that active galaxies (both starburst and AGN) show the peak of their density distribution at redshifts  $z \sim 2-3$ , gave rise to a host of models, both qualitative and quantitative. These integrated vigorous accretion onto a supermassive black hole (AGN) and intense bursts of star-formation (starburst) in the evolution of galaxies in the context of a hierarchically assembling,  $\Lambda$ CDM Universe, as separate, inter-dependent phases that each galaxy may experience under certain circumstances, i.e., mergers.

This merger-driven evolution scheme has gained momentum in the last couple of decades, with both observational and numerical evidence supporting it. The current paradigm includes the formation of elliptical galaxies through major mergers between spiral galaxies. When the two spirals interact and eventually merge, assuming a gas-rich ("wet") merger, a huge amount of gas and dust is funneled towards the center of the merging system. As a result of the morphological (and thus dynamical) asymmetries created during such a phase, induced star-formation at increased rates occurs. At later stages, given a sufficient amount of matter amassed in the center of the system, efficient accretion upon the central black hole occurs, giving rise to an, initially obscured, AGN. As the core becomes more luminous, the obscuring material either gets blown away, or settles into a disk and/or torus, and powerful radio jets are ejected from the nucleus. This results to the traditional picture of a radio-loud AGN, as was described in Chap. 1. After sufficient time and some feedback mechanisms, the star-formation in the host galaxy gets quenched and in turn the AGN itself fades away. What remains is an elliptical, non-active, galaxy. An individual stage of this evolution track is of particular interest: the putative binary black hole stage. If one assumes that each galaxy hosts a SMBH at its center, then it is to be expected that any major merger event will eventually lead to the formation of a bound binary black hole system. These systems would exhibit certain morphological and emission properties and are important both in the context of galaxy evolution as well as for the search for gravitational waves. The identification of BBH systems in the CJF sample has been an aim of this work.

However, despite the fact that more than 30 years have passed since the discovery of ULIRGs by the IRAS observatory and the first link between these systems and AGN, the quantitatively specific transition between the different phases of evolution still remains unknown. In addition, the exact conditions that lead to the triggering of an AGN and the relevance of mergers to that is still under investigation. A small part of that problem concerns the relevance of radio-loud AGN to this merger-driven evolution scheme. Most studies of this kind have traditionally focused on radio-faint sources, presumably associated to younger sources at earlier stages of their evolution. Moreover, most samples used in the past to study the link between merger events and active galaxies have been selected either in the optical or in the infrared and have therefore suffered from bi-

ases towards "transitory" systems, giving us a somewhat distorted view of how important mergers really are for AGN. To lift this bias, I decided to use the CJF, a radio-selected sample, comprising 293 radio-loud, flat-spectrum active galaxies. By undertaking an extensive bibliographic search, I gathered all relevant information about the CJF sources, concerning their morphological and emission properties.

My most important result in the above context therefore pertains to the percentage of CJF sources associated with merger events. I find that 4.4% of the CJF sources are associated with present or recently past merger events. Translated to the local Universe ( $z < 0.4$ ) the percent amounts to 28.6% of the sample. Other studies of similar scope but with optically or infrared selected AGN samples find a similar percentage ( $\sim 30\%$ ). The convergence of the two percentages together with the selection criteria of the CJF sample imply that mergers are tightly connected to activity in galaxies, probably more so than previously believed. In fact, I showed that given the incompleteness of the available information at different wavelengths, this percentage only reflects a lower limit rather than a hard value. Apart from that, I note a broken correlation found between NIR and radio luminosity for the CJF sample. In particular, low luminosity sources are found to show an excess of NIR radiation, compared to the correlation implied by higher luminosity sources. This is interpreted in terms of a star-formation or dust component that contributes significantly to the total NIR luminosity of these sources. In addition, I find a possible link between evolutionary transitory systems (as defined by their NIR colors) and multi-wavelength variability, possibly related to BBH systems. Finally, using a set of criteria I classify a sub-sample of the CJF in different evolutionary stages, among which current merging systems and BBH systems.

### 5.1.2 Properties and evolution of AGN jet ridge lines

In Chap. 3 I studied the properties and evolution of the jet ridge lines of the CJF sources, in light of the new kinematic scenario proposed for BL Lac objects, based on the sources 1803+784 and 0735+178. According to this, BL Lac components are predominantly stationary with respect to the core but change their position angle significantly, essentially reflecting an important transverse component in their movement. The paradigm for AGN jet kinematics usually entails distinct components (usually interpreted as either moving "blobs" of matter or shocks propagating down the jet) that move outwards, away from the assumed core. For flat-spectrum sources (i.e., core-dominated AGN) in particular, apparent superluminal speeds are observed, usually interpreted in the context of a specific projected geometry combined with relativistic effects, due to the intrinsically high (but of course subluminal) speeds of the moving components. Such motions have so far been observed in flat-spectrum QSOs and BL Lacs, both of them together usually labeled as blazars. Large effort has been given to investigate in detail the jet kinematics of both individual objects as well as samples of AGN, as these studies provide indirect information on the structure and underlying physics of AGN jets.

For most cases, the often used scheme for jet kinematics entails ballistic, outward linear motions for the components. Treated as blobs, the component positions at different epochs would be described by linear fits whose slope would indicate the apparent velocity of that component. Most components are found to move outward with a few showing inward motion, usually interpreted as due to variations of the flux of the component that

lead to an inward displacement of the center of the Gaussian fit representing the component. The actual situation is rarely that simple. Detailed investigations of individual objects have shown that components not only do not follow linear paths, but they neither have constant expansion velocities nor do all components in one jet follow the same path. These apparent accelerations or decelerations, as well as bent, varying trajectories, are extremely difficult to explain in the context of a linear ballistic scenario. Three sources in particular have shown indications of a radically different kinematic scenario and have also been the motivation of this chapter's investigation: 1803+784, 0716+714, and 0735+178. All of these objects are classified as BL Lacs and exhibit quasi-stationary components in their jets. In addition, for the interesting case of 0735+178, its jet appears to undergo mode transitions from all components moving outwardly to all components being stationary. The large number of epochs investigated for these objects has allowed the detailed study of their kinematics and the decomposition of the different motion components, showing that transverse, non-radial motions are of relevance to these sources.

In particular, and specially for the cases of 1803+784 and 0716+714, it has been shown that the study of their jet ridge lines<sup>1</sup> can provide important information concerning the kinematics of the sources and, more importantly, it is a measure that describes the jet as a whole rather than a topically focused probe, as is the case for individual components. For the case of 1803+784 the jet ridge line of the source was followed for more than 90 epochs. It was observed that the jet ridge line of that object evolves periodically, changing its width and curvature, at moments resembling a sinusoid-like curve and exhibiting a very wide flow. In light of this discovery, it would be extremely important to investigate whether such behavior is common among other objects, objects of a certain class, or is just characteristic of individual objects. To do this I developed a number of measures that characterize both the transverse and the radial evolution of the jet ridge line. I applied these tools for the case of the CJF sample, a sample selected specifically to identify and study active galaxies with jets showing superluminal motions.

If the essence of this chapter were to be condensed in one sentence, that would be that component motions in AGN jets are not linear. They are not linear not in a second order approach, but in first order approximation too. By statistically analyzing the CJF sample, I provide compelling arguments concerning the morphology and evolution of the jet ridge lines of AGN. In particular, BL Lac objects show significantly wider jets, compared to both QSOs and RGs, in agreement to findings from 1803+784. Moreover BL Lacs are found to change their jet ridge line widths more strongly than QSOs and RGs, again following the implied behavior shown for 1803+784. On the contrary, BL Lacs appear to linearly evolve their jet ridge lines less than the other classes. This implies that the individual jet components of BL Lac objects move less than their QSO or RG counterparts, again something already witnessed as stationary components in the jets of 1803+784, 0716+714, and 0735+178. However, once again the picture does not remain "simple". By studying a sub-sample of CJF sources identified as variable, I find that these sources actually show wider, more strongly evolving jet ridge lines, both linearly and in width. Finally, I note the existence of a correlation, in the form of an upper envelope, between radio luminosity and the total linear displacement of the jet ridge line of a source. This points towards an intrinsic link between the energy output of an AGN and the

---

<sup>1</sup>I remind that a jet ridge line of a source at a certain epoch is defined as a line linearly connecting the sky positions of all identified components at this epoch.

kinematics of its jet.

I employ a simple helical jet model to investigate a possible interpretation of the results above. I find that strongly helical jets of changing viewing angle can reproduce the behavior seen from this statistical analysis. In fact, given that BL Lacs are seen at the smallest viewing angles, QSOs at intermediate angles, and RGs at the largest viewing angles from the jet, then assuming a strongly or mildly helical jet (and therefore strongly non-linear, non-constant velocity) reproduces very well both the difference in widths, width evolution, and linear evolution of the jet ridge lines.

### 5.1.3 $\gamma$ -rays and AGN kinematic properties

In Chap. 4 I focused on a possible connection between the jet properties and kinematics of an AGN to its  $\gamma$ -ray properties. The Compton  $\gamma$ -ray Space Observatory, carrying among others the EGRET instrument, allowed the first thorough investigation of the  $\gamma$ -ray sky and discovered that most extragalactic  $\gamma$ -ray radiation can be associated with active galaxies and in particular radio-loud, flat-spectrum sources, blazars. The launch of the Fermi  $\gamma$ -ray space telescope and in particular its Large Area Telescope (LAT) revolutionized  $\gamma$ -ray astronomy by providing unprecedented resolution and sensitivity. Combined with its all-sky survey capability, the Fermi telescope allowed the discovery of numerous new sources, with its first year (11 months) catalog containing more than 1400 sources. Of these, 671 sources were associated with active galaxies, again mostly blazars (with some notable exceptions that merit further investigation). The availability of such a big sample of  $\gamma$ -detected AGN allows an in depth investigation of the  $\gamma$ -ray properties of these objects and the possible links and correlations to properties of the  $\gamma$ -emitting sources at other wavelengths.

One of the main questions concerning AGN  $\gamma$ -ray astronomy is how can such energetic radiation be produced. There are obviously different answers to this question, depending on the model that one looks at. Although the lower energy radiation coming from AGN is widely accepted to be a product of the synchrotron mechanism from charged particles (presumably leptons, i.e., electrons and positrons) gyrating in the magnetic field of AGN jets, the origin of its higher energy counterpart is still under debate. One of the most widely accepted scenarios is that partly X-rays and surely  $\gamma$ -rays are produced through the inverse Compton scattering mechanism, where photons are up-scattered, gaining energy, from relativistic particles. A tightly related question is of course then the where, i.e., which part of an active galaxy can provide the right conditions for this mechanism to take place. Both the near vicinity of the black hole (ergosphere) as well as the jet itself (either at its base or even at parsec scales) have been proposed as possible sites for  $\gamma$ -ray creation. Taking that scenario a step further, one needs to identify both the source of the photon field that gets up-scattered, as well as the population of relativistic particles doing the scattering. In that context, the synchrotron self-Compton (SSC) model indicates that low-energy photons produced through the synchrotron mechanism provide the incident photon field to be up-scattered by the same population of relativistic particles producing the synchrotron radiation. Other alternatives include the cosmic ray background, light from the broad line region, and/or the accretion disk emission providing the seed photons (e.g., [Maraschi et al. 1992](#); [Dermer and Schlickeiser 1993](#); [Sikora et al. 1994](#); [Ghisellini and Madau 1996](#)). One final debate concerns the variability observed at these wavelengths

(even at energies as high as TeV scales). From light-travel time arguments, one can see that the  $\gamma$ -ray emitting regions should be fairly small, for some cases smaller than the event horizon of a typical SMBH found at the centers of AGN.

There is a particular area of the above questions that one can readily attack with an AGN sample like the CJF. If  $\gamma$ -ray emission is indeed generated in the jets of active galaxies and in particular in the pc-scale jets, then one expects a certain imprint of the one onto the other. It is to be expected that the macroscopic properties related to the synchrotron emission in AGN jets -i.e., jet components- might to some degree be correlated to the  $\gamma$ -ray properties of a source. Even before the advent of the Fermi telescope, extensive work had been done, combining  $\gamma$ -ray information from the EGRET instrument and kinematic information acquired through extensive VLBI surveys. The general consensus has been that, on average,  $\gamma$ -detected AGN have jet components with higher apparent speeds than those for the non-detected ones. This is in turn interpreted as an effect of the viewing angle, namely that  $\gamma$ -ray emission becomes relevant for sources that have their jets oriented very close to our line of sight. After the first three months of the Fermi-LAT operation, this result was reinforced, both from the point of view of apparent velocities, as well as from direct Doppler factors measured through photometry and from a study of the opening angles of  $\gamma$ -bright AGN. In this context and given the interesting results of Chap. 3 implying a somewhat different kinematic scenario for most sources, I was interested in investigating whether these correlations found between  $\gamma$ -ray detectability and fast jet components and wide jet opening angles would hold for the CJF sample as well.

**The most important result of this chapter would be that I do not find any significant difference between the apparent speed distribution of  $\gamma$ -detected and non-detected sources.** I find a tentative correlation between the  $\gamma$ -ray luminosity of a source and its maximum apparent jet speed that becomes more significant for BL Lac objects and variable sources. I observe a clear differentiation between QSOs and BL Lacs in what pertains to their apparent velocity distributions, regardless of their  $\gamma$ -ray properties, result that is essentially reflecting the findings discussed in Chap. 3. I do conclude that the  $\gamma$ -detected sources tend to have a more extended distribution of apparent speeds, extending to higher values than their non-detected counterparts. I confirm that the BL Lacs in the CJF sample have higher  $\gamma$ -to-radio luminosity ratio that is translated to higher detectability over QSOs. It should however be noted that when taking the redshift distribution of the two classes in account, the difference in detectability becomes considerably smaller. Interestingly, it is found that  $\gamma$ -detected sources have significantly wider jet ridge lines and they evolve their widths more strongly than non-detected ones. On the contrary,  $\gamma$ -detected sources show similar linear evolution of their jet ridge lines compared to their non-detected counterparts. This is interpreted as evidence for the importance of non-radial motion in AGN jets, transverse to the symmetry axis of the outflow.

This apparent discrepancy between my results and previous studies is qualitatively explained in the context of a two-zone model proposed to explain several features of  $\gamma$ -ray emission from AGN. In this model, the jet is assumed to comprise two components, a slow, massive, outer one, called a sheath, and a fast, ultra-relativistic, light, inner component, called a spine.  $\gamma$ -ray emission is in this scheme is created from the spine of the jet. Given the low frequency of observations used for the CJF sample, I postulate that the sheath is seen, rather than the spine, which should be oblique at these observing frequencies. All previous investigation connecting fast moving jet components were made at



higher observing frequencies and therefore could, at least partially, probe the fast spine.

## 5.2 Concluding Remarks

It is neither trivial nor straightforward to summarize and present conclusions for a work spanning three years and such a breadth of topics. As was already mentioned, the spine of this work has been a sort of unification of our understanding of different aspects of active galaxies. In the following I give a personal assessment of the results presented in this work and their implications for our understanding of activity in galaxies.

The work presented in Chap. 2 first of all exhibits the importance of mergers for AGN and links them to radio-loud AGN. I show that even for radio-loud (mature) AGN, there is a signature of additional components (e.g., as seen in the NIR-radio correlation for low luminosity sources) influencing the properties of the galaxy. My results underline the need of expanding in a statistically significant manner the study of galaxy evolution towards systems that have been traditionally seen as "unrelated" to transitory stages. The results in this chapter point towards a temporal unification of AGN, in addition to a time-independent, static unification of the different flavors of active galaxies.

My results from Chap. 3 show quite clearly that the ballistic, linear motions most often assumed for components in AGN jets grossly oversimplify the true nature of the trajectories followed by the components. I present strong evidence supporting a helical nature of all AGN jets, as this could explain the significant transverse motion signatures uncovered from my analysis. It is a tempting thought that all components, at least in the scales investigated here, follow helical trajectories and that the opening angle of the helix, as well as the intrinsic power of the jet and the viewing angle are the factors that regulate our view of a jet. Then of course the question arises as to which mechanism leads to such a helical motion pattern. Several explanations exist, with some more probable than others. If one thing is certain however, it is that the (VLBI) observations in the radio have reached a certain level of maturity and sophistication that requires a re-evaluation of the way that data are interpreted.

Finally, the work included in Chap. 4 is of particular interest given that we are now entering a new era of  $\gamma$ -ray astronomy. These results point towards a rather complicated picture concerning the site and mechanism that produces the  $\gamma$ -ray emission coming from active galaxies. This work is tightly coupled with the findings of Chap. 3. A multi-zone model seems a natural way to explain the different properties characterizing  $\gamma$ -ray emission. The stratification of any kind of flow is not a new concept and it is in principle readily applicable to AGN jets. Once again the quality and sophistication of the available data allow us to shed some of the basic assumptions made about AGN jets in the past and introduce further degrees of complexity to the problem. It is of course interesting how one can combine an intrinsically helical jet geometry with a spine-sheath configuration. This however is outside the scope of this work.

## 5.3 Into the future...

It is the nature of science such that every piece of scientific work is based on its predecessors and becomes a footing for further progress. In this context, I would like to shortly

describe an outlook for the topics that have been included in this work. Both observational and theoretical work are necessary for furthering our understanding of activity in galaxies. Given the somewhat more observationally oriented work presented here, my outlook will be colored accordingly.

Acquiring a better understanding of the role of AGN in the context of formation and evolution of galaxies is, to my eyes, one of the most fundamental areas of AGN research, rivaled only by the unification efforts started by [Antonucci \(1993\)](#) and [Urry and Padovani \(1995\)](#). Given the long list of different phenomena and effects taking place throughout the billions of years comprising the evolutionary track of a galaxy, the temporal unification of these systems is not straightforward. A number of additional observations could however potentially offer some key information and further our understanding of the subject. More in depth optical and infrared observations are needed in order to unambiguously distinguish between the different phenomena (as they were described in Chap. 2). High quality infrared data (mid and far) of these objects would provide us with the means to pinpoint the actual position of each object on the presumed evolution track of galaxies. Something that I have not investigated in this work concerns the nuclear activity itself in AGN, as this is reflected in the accretion rate of mass onto the central SMBH. There is a number of models connecting the appearance and apparent age of an AGN to its accretion mode and accretion rate. It seems that the investigation of both the accretion rate and the star-formation rate of a carefully selected sample of AGN might provide further insight in their relative importance at different evolutionary stages. A good proxy for accretion is the X-ray flux, which is readily available for many AGN. It is therefore crucial to fill the apparent gap of infrared information on active galaxies in order to study the effects described here. The recently launched Herschel telescope, as well as the future James Webb space telescope, will identify and study a large number of active galaxies in the near to far infrared and even into the sub-millimeter range. First results from the Herschel mission have already offered perhaps surprising results, concerning star-formation in radio-loud galaxies ([Hardcastle et al. 2010](#), private communication).

Alternatively, on the front of binary black hole system studies, high resolution observations of those sources that present multi-wavelength variability would help us to model the possible existence of a binary black hole in these AGN. However, given the, both time and resource-wise, quite costly process of acquiring a large number of epochs to model such systems, more efficient ways of identifying BBH candidates are needed. Apart from the criteria presented in this work (i.e., variability), statistical investigation of other signatures in this context, like double emission lines or X-shaped radio galaxies (e.g., [Mezcua et al. 2009](#)), could also offer alternatives for this search. The definitive answer should come with the advent of gravitational interferometers like L.I.S.A., or the pulsar timing array. These efforts, once online, should detect a large number of BBH candidates and then a reverse procedure will have to be followed, to identify the actual sources of the detected gravitational waves. In this context, studies like the one presented here are of great relevance.

Concerning the AGN jet kinematics, the next steps seem to be more straightforward. There already exist samples, like the MOJAVE sample, that have a similar number of sources as the CJF, but a larger number of epochs. Applying the above described method for such a bigger and temporally more sensitive sample would provide us with a more in depth understanding of the mechanics of AGN jets. It would be extremely interesting

to see whether transverse motions are equally relevant at higher frequencies, or if for example the putative spine of the jet is actually a linear flow, embedded in a helical sheath. It would also be of interest to study a sample that contains a larger number of BL Lacs and RGs. Due to the selection criteria applied in the CJF (and the MOJAVE) to find the most compact sources plus the stringent flux limit, QSOs dominate these samples and therefore any comparison between the different AGN classes is limited by the small number of available sources to compare with. Polarization measurements offer a further way of approaching the same problem. Polarization allows one to directly study the properties of the synchrotron emission and therefore recover information concerning the magnetic fields that thread the AGN jets. It is of great importance to make a direct link between magnetic fields and the jet kinematics, as these two should be closely correlated. It is not trivial whether magnetic fields, an essentially microscopic measure of AGN jets, directly affect the macroscopic aspects of the flow, i.e., the jet component motions.

The possibility also exists of studying individual objects and therefore diving into the details, trying to uncover the exact mechanisms relevant for that objects. As in the case of BBH systems, the effects that I are looking for are usually of second order importance and therefore need a sufficiently large number of observations to be studied. It seems however that, especially for the case jet kinematics, studies of individual objects are unavoidable, given the many different factors that come into play. It should also be noted that modeling, either analytical or numerical, is highly complimentary to the observational work. Such studies can essentially provide us with the kind of signatures that one should look for and that would help distinguish between different scenarios.

AGN  $\gamma$ -ray astronomy is, as was seen, tightly coupled with the above. Given time, more sources will be detected by Fermi-LAT. That will allow a more significant statistical analysis of the correlation between kinematic and emission properties. Photometry and the compilation of detailed SEDs will also provide key elements to our understanding of the processes that come into play when talking about  $\gamma$ -rays. The recently started effort to compile and model the SEDs of all the MOJAVE sources (Chang et al. 2010; Chang et al., in prep.) will surely provide important information on possible correlations between  $\gamma$ -ray emission and other wavelengths.

In any case it is rewarding to not be able to offer a final answer. Science by definition and in essence is the opposite of finality and that is why it is only fitting to finish this work with a promise and an outlook for the next steps to follow. It has been a long time since people turned their gazes towards the stars for the first time and wondered about the unknown. Now is a time when the stars seem a bit closer than before. Be it that our gazes have become more sensitive, or that our minds, much like the Universe itself, have become more open, slowly and steadily we have pushed our way into the unknown, mapping out the Universe by the shear force of our will, self-perceived importance, and stubbornness. If anything, this is an exciting time for astronomy. Each day we come closer to answering the ultimate questions of Life, The Universe, and Everything. And let's hope it is not 42...



# Bibliography

- Abdo, A. A., 2009, Bright AGN Source List from the First Three Months of the Fermi Large Area Telescope All-Sky Survey, ArXiv e-prints, [0902.1559](#)
- Abdo, A. A., Ackermann, M., Ajello, M., et al., 2010a, The First Catalog of Active Galactic Nuclei Detected by the Fermi Large Area Telescope, *ApJ*, 715, 429–457, [1002.0150](#)
- Abdo, A. A., Ackermann, M., Ajello, M., et al., 2010b, The First Catalog of Active Galactic Nuclei Detected by the Fermi Large Area Telescope, *ApJ*, 715, 429–457, [1002.0150](#)
- Abraham, Z., Carrara, E. A., Zensus, J. A., Unwin, S. C., 1996, Velocities and life-times in the VLBI jet of 3C 273., *A&AS*, 115, 543–549
- Acciari, V. A., Aliu, E., Arlen, T., et al., 2009, Veritas Observations of a Very High Energy  $\gamma$ -Ray Flare From the Blazar 3C66A, *ApJ*, 693, L104–L108, [0901.4527](#)
- Agudo, I., Gómez, J., Martí, J., Ibáñez, J., Marscher, A. P., Alberdi, A., Aloy, M., Hardee, P. E., 2001, Jet Stability and the Generation of Superluminal and Stationary Components, *ApJ*, 549, L183–L186, [arXiv:astro-ph/0101188](#)
- Alberdi, A., Krichbaum, T. P., Graham, D. A., Greve, A., Grewing, M., Marcaide, J. M., Witzel, A., Booth, R. S., Baath, L. B., Colomer, F., Doeleman, S., Marscher, A. P., Rogers, A. E. E., Schalinski, C. J., Standke, K., 1997, The high-frequency compact radio structure of the peculiar quasar 4C 39.25., *A&A*, 327, 513–521
- Alberdi, A., Gómez, J. L., Marcaide, J. M., Marscher, A. P., Pérez-Torres, M. A., 2000, 4C 39.25: Witnessing the interaction between a moving and a stationary component, *A&A*, 361, 529–534
- Albert, J., Aliu, E., Anderhub, H., et al., 2007, Discovery of Very High Energy  $\gamma$ -Ray Emission from the Low-Frequency-peaked BL Lacertae Object BL Lacertae, *ApJ*, 666, L17–L20, [arXiv:astro-ph/0703084](#)
- Alfvén, H., Herlofson, N., 1950, Cosmic Radiation and Radio Stars, *Physical Review*, 78, 616–616
- Andernach, H., Han Tie, Sievers, A., Reuter, H.-P., Junkes, N., Wielebinski, R., 1988, A radio survey of clusters of galaxies. VI - More observations of 34 Abell cluster areas at 11.1, 6.3 and 2.8 CM and a preliminary statistical review of data in papers I-VI, *A&AS*, 73, 265–324

- Antonucci, R., 1993, Unified models for active galactic nuclei and quasars, *ARA&A*, 31, 473–521
- Antonucci, R. R. J., Miller, J. S., 1985, Spectropolarimetry and the nature of NGC 1068, *ApJ*, 297, 621–632
- Antonucci, R. R. J., Hickson, P., Olszewski, E. W., Miller, J. S., 1986, Deep radio maps of high-frequency selected BL Lac objects, *AJ*, 92, 1–5
- Atwood, W. B., Abdo, A. A., Ackermann, M., et al., 2009, The Large Area Telescope on the Fermi Gamma-Ray Space Telescope Mission, *ApJ*, 697, 1071–1102, [0902.1089](#)
- Babadzhanyants, M. K., Belokon', E. T., Gamm, N. G., 1995, Optical monitoring of the superluminal quasar 3C345 from 1984 to 1991, *Astronomy Reports*, 39, 393–401
- Barkhouse, W. A., Hall, P. B., 2001, Quasars in the 2MASS Second Incremental Data Release, *AJ*, 121, 2843–2850, [arXiv:astro-ph/0101270](#)
- Barnes, J. E., Hernquist, L. E., 1991, Fueling starburst galaxies with gas-rich mergers, *ApJ*, 370, L65–L68
- Baty, H., Keppens, R., Comte, P., 2003, The two-dimensional magnetohydrodynamic Kelvin-Helmholtz instability: Compressibility and large-scale coalescence effects, *Physics of Plasmas*, 10, 4661–4674, [arXiv:astro-ph/0403125](#)
- Begelman, M. C., Blandford, R. D., Rees, M. J., 1980, Massive black hole binaries in active galactic nuclei, *Nature*, 287, 307–309
- Begelman, M. C., Blandford, R. D., Rees, M. J., 1984, Theory of extragalactic radio sources, *Reviews of Modern Physics*, 56, 255–351
- Begelman, M. C., Fabian, A. C., Rees, M. J., 2008, Implications of very rapid TeV variability in blazars, *MNRAS*, 384, L19–L23, [0709.0540](#)
- Bekki, K., Shioya, Y., Whiting, M., 2006, Numerical simulations on the relative importance of starbursts and AGN in ultraluminous infrared galaxies, *MNRAS*, 371, 805–820, [arXiv:astro-ph/0607349](#)
- Belokon, E. T., Babadzhanyants, M. K., 2003, The 2.5-year Period in the Optical Variability of 3C 66A (Poster), in *High Energy Blazar Astronomy*, ASP Conference Proceedings, Vol. 299, held 17-21 June 2002 at Tuorla Observatory, Piikkio, Finland. Edited by Leo O. Takalo and Esko Valtaoja. ISBN: 1-58381-146-X. San Francisco: Astronomical Society of the Pacific, 2003, p.205., (Eds.) L. O. Takalo, E. Valtaoja, pp. 205–+
- Bennert, N., Canalizo, G., Jungwiert, B., Stockton, A., Schweizer, F., Peng, C. Y., Lacy, M., 2008, Evidence for Merger Remnants in Early-Type Host Galaxies of Low-Redshift QSOs, *ApJ*, 677, 846–857, [arXiv:0801.0832](#)
- Beskin, V. S., Istomin, Y. N., Parev, V. I., 1992, Filling the Magnetosphere of a Supermassive Black-Hole with Plasma, *Soviet Astronomy*, 36, 642–+

- Bian, W., Zhao, Y., 2003, Timescales of Soft X-Ray Variability and Physical Constraints in Active Galactic Nuclei, *ApJ*, 591, 733–740, [arXiv:astro-ph/0303548](#)
- Bird, J., Martini, P., Kaiser, C., 2008, The Lifetime of FR II Sources in Groups and Clusters: Implications for Radio-Mode Feedback, *ApJ*, 676, 147–162, [0709.2167](#)
- Birkinshaw, M., 1991, The Kelvin-Helmholtz instability for relativistic particle beams. II - Flows bounded by a simple shear layer, *MNRAS*, 252, 505–527
- Blakeslee, J. P., Franx, M., Postman, M., et al., 2003, Advanced Camera for Surveys Photometry of the Cluster RDCS 1252.9-2927: The Color-Magnitude Relation at  $z = 1.24$ , *ApJ*, 596, L143–L146, [arXiv:astro-ph/0309036](#)
- Blandford, R., 2008, Extragalactic Jets: Some Unanswered Questions and the Prospects for GLAST, in *Extragalactic Jets: Theory and Observation from Radio to Gamma Ray*, (Ed.) T. A. Rector & D. S. De Young, vol. 386 of *Astronomical Society of the Pacific Conference Series*, pp. 3–+
- Blandford, R. D., 1986, Black hole models of quasars, in *Quasars*, (Eds.) G. Swarup, V. K. Kapahi, vol. 119 of *IAU Symposium*, pp. 359–368
- Blandford, R. D., Begelman, M. C., 1999, On the fate of gas accreting at a low rate on to a black hole, *MNRAS*, 303, L1–L5, [arXiv:astro-ph/9809083](#)
- Blandford, R. D., Icke, V., 1978, A dynamical interpretation of the radio jet in 3C 31, *MNRAS*, 185, 527–538
- Blandford, R. D., Konigl, A., 1979, Relativistic jets as compact radio sources, *ApJ*, 232, 34–48
- Blandford, R. D., Payne, D. G., 1982, Hydromagnetic flows from accretion discs and the production of radio jets, *MNRAS*, 199, 883–903
- Blandford, R. D., Rees, M. J., 1974, A 'twin-exhaust' model for double radio sources, *MNRAS*, 169, 395–415
- Blandford, R. D., Znajek, R. L., 1977, Electromagnetic extraction of energy from Kerr black holes, *MNRAS*, 179, 433–456
- Bloom, S. D., Marscher, A. P., Gear, W. K., Terasranta, H., Valtaoja, E., Aller, H. D., Aller, M. F., 1994, Radio, millimeter-submillimeter, and infrared spectra of flat-spectrum extragalactic radio sources, *AJ*, 108, 398–404
- Boller, T., Gallo, L. C., Lutz, D., Sturm, E., 2002, Mrk 1014: an AGN-dominated ultra-luminous infrared galaxy, *MNRAS*, 336, 1143–1146, [arXiv:astro-ph/0207378](#)
- Bondi, H., 1952, On spherically symmetrical accretion, *MNRAS*, 112, 195–+
- Bozayan, E. P., Hemenway, P. D., Argue, A. N., 1990, Optical variability of extragalactic objects used to tie the HIPPARCOS reference frame to an extragalactic system using Hubble space telescope observations, *AJ*, 99, 1421–1434

- Braito, V., Reeves, J. N., Della Ceca, R., Ptak, A., Risaliti, G., Yaqoob, T., 2009, A Suzaku observation of the ULIRG IRAS19254-7245: discerning the AGN component, *A&A*, 504, 53–59, [0905.1041](#)
- Britzen, S., Krichbaum, T. P., 1997, Geodetic VLBI observations of the gamma-bright blazar PKS 0528 + 134, *Vistas in Astronomy*, 41, 275–279
- Britzen, S., Vermeulen, R. C., Taylor, G. B., Pearson, T. J., Readhead, A. C. S., Wilkinson, P. N., Browne, I. W., 1999a, The CJF Survey - First Results on Superluminal Motion, in *BL Lac Phenomenon*, (Eds.) L. O. Takalo, A. Sillanpää, vol. 159 of *Astronomical Society of the Pacific Conference Series*, pp. 431–+
- Britzen, S., Witzel, A., Krichbaum, T. P., Qian, S. J., Campbell, R. M., 1999b, 8.4 GHz VLBI monitoring of the gamma-bright blazar PKS 0528+134, *A&A*, 341, 418–426
- Britzen, S., Witzel, A., Krichbaum, T. P., Campbell, R. M., Wagner, S. J., Qian, S. J., 2000, Three-year VLBI monitoring of PKS 0420-014, *A&A*, 360, 65–75
- Britzen, S., Roland, J., Laskar, J., Kokkotas, K., Campbell, R. M., Witzel, A., 2001, On the origin of compact radio sources. The binary black hole model applied to the gamma-bright quasar PKS 0420-014, *A&A*, 374, 784–799
- Britzen, S., Krichbaum, T. P., Strom, R. G., Witzel, A., Muxlow, T. W. B., Matveenko, L. I., Campbell, R. M., Alef, W., Hummel, C. A., Zensus, A., 2005a, Large-scale motion, oscillations and a possible halo on the counter-jet side in 1803+784, *A&A*, 444, 443–454
- Britzen, S., Witzel, A., Krichbaum, T. P., Beckert, T., Campbell, R. M., Schalinski, C., Campbell, J., 2005b, The radio structure of S5 1803+784, *MNRAS*, 362, 966–974
- Britzen, S., Meyer, V., Witzel, A., Agudo, I., Aller, M. F., Aller, H. D., Eckart, A., Zensus, J. A., 2006, "Oscillating" components in the BL Lac object 0716+714, in *Proceedings of the 8th European VLBI Network Symposium*
- Britzen, S., Brinkmann, W., Campbell, R. M., Gliozzi, M., Readhead, A. C. S., Browne, I. W. A., Wilkinson, P., 2007a, The soft X-ray properties of AGN from the CJF sample. A correlation analysis between soft X-ray and VLBI properties, *A&A*, 476, 759–777, [arXiv:0802.4347](#)
- Britzen, S., Vermeulen, R. C., Taylor, G. B., Campbell, R. M., Pearson, T. J., Readhead, A. C. S., Xu, W., Browne, I. W. A., Henstock, D. R., Wilkinson, P., 2007b, A multi-epoch VLBI survey of the kinematics of CJF sources. I. Model-fit parameters and maps, *A&A*, 472, 763–771, [arXiv:0802.4182](#)
- Britzen, S., Vermeulen, R. C., Campbell, R. M., Taylor, G. B., Pearson, T. J., Readhead, A. C. S., Xu, W., Browne, I. W., Henstock, D. R., Wilkinson, P., 2008, A multi-epoch VLBI survey of the kinematics of CFJ sources. II. Analysis of the kinematics, *A&A*, 484, 119–142



- Britzen, S., Kam, V. A., Witzel, A., Agudo, I., Aller, M. F., Aller, H. D., Karouzos, M., Eckart, A., Zensus, J. A., 2009, Non-radial motion in the TeV blazar S5 0716+714. The pc-scale kinematics of a BL Lacertae object, *A&A*, 508, 1205–1215, [1001.2126](#)
- Britzen, S., Kudryavtseva, N. A., Witzel, A., Campbell, R. M., Ros, E., Karouzos, M., Mehta, A., Aller, M. F., Aller, H. D., Beckert, T., Zensus, J. A., 2010a, The kinematics in the pc-scale jets of AGN. The case of S5 1803+784, *A&A*, 511, A57+, [1001.1973](#)
- Britzen, S., Witzel, A., Gong, B. P., Zhang, J. W., Gopal-Krishna, Goyal, A., Aller, M. F., Aller, H. D., Zensus, J. A., 2010b, Understanding BL Lac objects Structural & kinematic mode changes in the BL Lac object PKS 0735+178, *ArXiv e-prints*, [1002.3531](#)
- Brodwin, M., Eisenhardt, P. R., Gonzalez, A. H., Stanford, S. A., Stern, D., Moustakas, L. A., Brown, M. J. I., Chary, R.-R., Galametz, A., 2008, A Large Population of High Redshift Galaxy Clusters in the IRAC Shallow Cluster Survey, in *Astronomical Society of the Pacific Conference Series*, (Eds.) T. Kodama, T. Yamada, K. Aoki, vol. 399 of *Astronomical Society of the Pacific Conference Series*, pp. 322–+
- Browne, I. W. A., Murphy, D. W., 1987, Beaming and the X-ray, optical and radio properties of quasars, *MNRAS*, 226, 601–627
- Bryant, P. M., Scoville, N. Z., 1996, High-Resolution CO Observations of the Ultraluminous Infrared Galaxy Markarian 231, *ApJ*, 457, 678–+
- Bychkova, V. S., Kardashev, N. S., Vlasyuk, V. V., Spiridonova, O. I., 2003, Optical Variability of the Blazar 2007 + 777, *Astronomy Reports*, 47, 1–5
- Camenzind, M., Krockenberger, M., 1992, The lighthouse effect of relativistic jets in blazars - A geometric origin of intraday variability, *A&A*, 255, 59–62
- Canalizo, G., Stockton, A., 2001, Quasi-Stellar Objects, Ultraluminous Infrared Galaxies, and Mergers, *ApJ*, 555, 719–743, [arXiv:astro-ph/0103332](#)
- Cao, C., Xia, X. Y., Wu, H., Mao, S., Hao, C. N., Deng, Z. G., 2008, Mid-Infrared spectroscopic properties of ultra-luminous infrared quasars, *MNRAS*, pp. 983–+
- Cao, X., Jiang, D. R., 2002, Relation between radio core length and black hole mass for active galactic nuclei, *MNRAS*, 331, 111–116, [arXiv:astro-ph/0110541](#)
- Caproni, A., Abraham, Z., 2004, Can long-term periodic variability and jet helicity in 3C 120 be explained by jet precession?, *MNRAS*, 349, 1218–1226, [arXiv:astro-ph/0312407](#)
- Caproni, A., Livio, M., Abraham, Z., Mosquera Cuesta, H. J., 2006, Warping and Precession in Galactic and Extragalactic Accretion Disks, *ApJ*, 653, 112–126, [arXiv:astro-ph/0608398](#)
- Carballo, R., Sánchez, S. F., González-Serrano, J. I., Benn, C. R., Vigotti, M., 1998, K-Band Imaging of 52 B3-VLA Quasars: Nucleus and Host Properties, *AJ*, 115, 1234–1252, [arXiv:astro-ph/9712220](#)

- Carilli, C. L., Wrobel, J. M., Ulvestad, J. S., 1998, A Subkiloparsec Disk in Markarian 231, *AJ*, 115, 928–937
- Cattaneo, A., Combes, F., Colombi, S., Bertin, E., Melchior, A., 2005, Spectral and morphological properties of quasar hosts in smoothed particle hydrodynamics simulations of active galactic nucleus feeding by mergers, *MNRAS*, 359, 1237–1249, [arXiv:astro-ph/0504394](https://arxiv.org/abs/astro-ph/0504394)
- Celotti, A., Blandford, R. D., 2001, On the Formation of Jets, in *Black Holes in Binaries and Galactic Nuclei*, (Ed.) L. Kaper, E. P. J. van den Heuvel, & P. A. Woudt, pp. 206–+, [arXiv:astro-ph/0001056](https://arxiv.org/abs/astro-ph/0001056)
- Chang, C. S., Ros, E., Kadler, M., Aller, M. F., Aller, H. D., Angelakis, E., Fuhrmann, L., Nestoras, I., Ungerechts, H., 2010, The Broadband Spectral Energy Distribution of the MOJAVE Sample, *ArXiv e-prints*, [1006.4777](https://arxiv.org/abs/1006.4777)
- Chen, A. W., D’Ammando, F., Villata, M., et al., 2008, AGILE detection of variable gamma-ray activity from the blazar S5 0716+714 in September-October 2007, *ArXiv e-prints*, [0808.4053](https://arxiv.org/abs/0808.4053)
- Chernomordik, V. V., 1995, Evidence for Small-Scale Clustering in a Column-Density-limited Sample of the Lyman-Alpha Forest, *ApJ*, 440, 431–+
- Ciaramella, A., Bongardo, C., Aller, H. D., Aller, M. F., De Zotti, G., Lähteenmaki, A., Longo, G., Milano, L., Tagliaferri, R., Teräsanta, H., Tornikoski, M., Urpo, S., 2004, A multifrequency analysis of radio variability of blazars, *A&A*, 419, 485–500, [arXiv:astro-ph/0401501](https://arxiv.org/abs/astro-ph/0401501)
- Clegg, P. E., 1980, The Infrared Astronomical Satellite - IRAS., *Phys. Scr*, 21, 678–683
- Cohen, M. H., Lister, M. L., Homan, D. C., Kadler, M., Kellermann, K. I., Kovalev, Y. Y., Vermeulen, R. C., 2007, Relativistic Beaming and the Intrinsic Properties of Extragalactic Radio Jets, *ApJ*, 658, 232–244, [arXiv:astro-ph/0611642](https://arxiv.org/abs/astro-ph/0611642)
- Colina, L., Perez-Fournon, I., 1990, Interaction versus radio source generation - The properties of radio jet parent galaxies, *ApJ*, 349, 45–56
- Condon, J. J., Mitchell, K. J., 1984, 4C 29.47 - Quasi-periodic outbursts recorded by precessing jets?, *ApJ*, 276, 472–475
- Condon, J. J., Dickey, J. M., Salpeter, E. E., 1990, A 1.4 GHz source survey in an area without nearby rich galaxy clusters, *AJ*, 99, 1071–1078
- Condon, J. J., Cotton, W. D., Broderick, J. J., 2002, Radio Sources and Star Formation in the Local Universe, *AJ*, 124, 675–689
- Conselice, C. J., Rajgor, S., Myers, R., 2008, The structures of distant galaxies - I. Galaxy structures and the merger rate to  $z \sim 3$  in the Hubble Ultra-Deep Field, *MNRAS*, 386, 909–927, [0711.2333](https://arxiv.org/abs/0711.2333)

- Conway, J. E., Murphy, D. W., 1993, Helical jets and the misalignment distribution for core-dominated radio sources, *ApJ*, 411, 89–102
- Cotton, W. D., 1995, Fringe Fitting, in *Very Long Baseline Interferometry and the VLBA*, (Ed.) J. A. Zensus, P. J. Diamond, & P. J. Napier, vol. 82 of *Astronomical Society of the Pacific Conference Series*, pp. 189–+
- Cristiani, S., D’Odorico, S., D’Odorico, V., Fontana, A., Giallongo, E., Savaglio, S., 1997, The clustering properties of the Lyman  $\alpha$  clouds, *MNRAS*, 285, 209–217, [arXiv:astro-ph/9610006](#)
- Curtis, H. D., 1918, *The planetary nebulae.*, Publications of Lick Observatory, 13, 55–74
- Davies, R. I., Tacconi, L. J., Genzel, R., 2004, The Nuclear Gas Dynamics and Star Formation of Markarian 231, *ApJ*, 613, 781–793, [arXiv:astro-ph/0406342](#)
- De Paolis, F., Ingrosso, G., Nucita, A. A., Zakharov, A. F., 2003, Binary black holes in Mkns as sources of gravitational radiation for space based interferometers, *A&A*, 410, 741–747, [arXiv:astro-ph/0310213](#)
- de Vaucouleurs, G., 1991, Book-Review - Third Reference Catalogue of Bright Galaxies, *Science*, 254, 1667–+
- de Vries, W. H., O’Dea, C. P., Perlman, E., Baum, S. A., Lehnert, M. D., Stocke, J., Rector, T., Elston, R., 1998, Near-Infrared Imaging of Gigahertz Peaked Spectrum, Compact Steep Spectrum, and Large-Scale FR II Radio Galaxies, *ApJ*, 503, 138–+
- Dekel, A., Birnboim, Y., Engel, G., Freundlich, J., Goerdt, T., Mumcuoglu, M., Neistein, E., Pichon, C., Teyssier, R., Zinger, E., 2009, Cold streams in early massive hot haloes as the main mode of galaxy formation, *Nature*, 457, 451–454, [0808.0553](#)
- Denn, G., Mutel, R., 1996, VLBA Studies of BL Lac, in *Extragalactic Radio Sources*, (Ed.) R. D. Ekers, C. Fanti, & L. Padrielli, vol. 175 of *IAU Symposium*, pp. 41–+
- Dermer, C. D., Schlickeiser, R., 1993, Model for the High-Energy Emission from Blazars, *ApJ*, 416, 458–+
- Disney, M. J., 1974, Parkes 0548-322: a BL Lacertae Object in a Cluster of Galaxies, *ApJ*, 193, L103+
- Dobrzycki, A., Bechtold, J., Scott, J., Morita, M., 2002, A Uniform Analysis of the Ly $\alpha$  Forest at  $z = 0-5$ . IV. The Clustering and Evolution of Clouds at  $z \leq 1.7$ , *ApJ*, 571, 654–664, [arXiv:astro-ph/0111487](#)
- Donato, D., Sambruna, R. M., Gliozzi, M., 2005, Six years of BeppoSAX observations of blazars: A spectral catalog, *A&A*, 433, 1163–1169, [arXiv:physics/0412114](#)
- Dotti, M., Ruzsowski, M., Paredi, L., Colpi, M., Volonteri, M., Haardt, F., 2009, Dual black holes in merger remnants - I. Linking accretion to dynamics, *MNRAS*, 396, 1640–1646, [0902.1525](#)

- Dotti, M., Volonteri, M., Perego, A., Colpi, M., Ruszkowski, M., Haardt, F., 2010, Dual black holes in merger remnants - II. Spin evolution and gravitational recoil, *MNRAS*, 402, 682–690, [0910.5729](#)
- Dudik, R. P., Satyapal, S., Gliozzi, M., Sambruna, R. M., 2005, A Chandra Snapshot Survey of Infrared-bright LINERs: A Possible Link Between Star Formation, Active Galactic Nucleus Fueling, and Mass Accretion, *ApJ*, 620, 113–125, [arXiv:astro-ph/0410305](#)
- Dunn, R. J. H., Fabian, A. C., Taylor, G. B., 2005, Radio bubbles in clusters of galaxies, *MNRAS*, 364, 1343–1353, [arXiv:astro-ph/0510191](#)
- Eddington, A. S., 1925, A limiting case in the theory of radiative equilibrium, *MNRAS*, 85, 408–+
- Edelson, R. A., Malkan, M. A., 1987, Far-infrared variability in active galactic nuclei, *ApJ*, 323, 516–535
- Edge, A. C., Rottgering, H., 1995, X-ray properties of head-tail radio sources in clusters of galaxies, *MNRAS*, 277, 1580–1586
- Eggum, G. E., Coroniti, F. V., Katz, J. I., 1985, Jet production in super-Eddington accretion disks, *ApJ*, 298, L41–L45
- Eisenhauer, F., Genzel, R., Alexander, T., Abuter, R., Paumard, T., Ott, T., Gilbert, A., Gillessen, S., Horrobin, M., Trippe, S., Bonnet, H., Dumas, C., Hubin, N., Kaufer, A., Kissler-Patig, M., Monnet, G., Ströbele, S., Szeifert, T., Eckart, A., Schödel, R., Zucker, S., 2005, SINFONI in the Galactic Center: Young Stars and Infrared Flares in the Central Light-Month, *ApJ*, 628, 246–259, [arXiv:astro-ph/0502129](#)
- Elbaz, D., Jahnke, K., Pantin, E., Le Borgne, D., Letawe, G., 2009, Quasar induced galaxy formation: a new paradigm?, *A&A*, 507, 1359–1374, [0907.2923](#)
- Fabian, A. C., Miniutti, G., Iwasawa, K., Ross, R. R., 2005, X-ray reflection in the Seyfert galaxy 1H 0419-577 revealing strong relativistic effects in the vicinity of a Kerr black hole, *MNRAS*, 361, 795–802, [arXiv:astro-ph/0504472](#)
- Falomo, R., Carangelo, N., Treves, A., 2003, Host galaxies and black hole masses of low- and high-luminosity radio-loud active nuclei, *MNRAS*, 343, 505–511, [arXiv:astro-ph/0304190](#)
- Fan, J. H., Lin, R. G., 1999, Infrared Variation of Radio-selected BL Lacertae Objects, *ApJS*, 121, 131–157, [arXiv:astro-ph/9908104](#)
- Fan, J. H., Adam, G., Xie, G. Z., Cao, S. L., Lin, R. G., Qin, Y. P., Copin, Y., Bai, J. M., Zhang, X., Li, K. H., 1998, The infrared and optical variability of OJ 287, *A&AS*, 133, 163–169, [arXiv:astro-ph/9809007](#)
- Fan, J.-H., Cheng, K. S., Zhang, L., 2002, Multi-Wavelength Variation Properties of  $\gamma$ -Ray-Loud Blazars, *PASJ*, 54, 533–539

- Fan, J. H., Liu, Y., Yuan, Y. H., Hua, T. X., Wang, H. G., Wang, Y. X., Yang, J. H., Gupta, A. C., Li, J., Zhou, J. L., Xu, S. X., Chen, J. L., 2007, Radio variability properties for radio sources, *A&A*, 462, 547–552, [arXiv:astro-ph/0701540](https://arxiv.org/abs/astro-ph/0701540)
- Fanaroff, B. L., Riley, J. M., 1974, The morphology of extragalactic radio sources of high and low luminosity, *MNRAS*, 167, 31P–36P
- Fanti, C., Fanti, R., Dallacasa, D., Schilizzi, R. T., Spencer, R. E., Stanghellini, C., 1995, Are compact steep-spectrum sources young?, *A&A*, 302, 317–+
- Fath, E. A., 1908, The northern limit of the zodiacal light, *Lick Observatory Bulletin*, 5, 45–49
- Ferreira, J., Pelletier, G., 1993, Magnetized accretion-ejection structures. 1. General statements, *A&A*, 276, 625–+
- Fichtel, C. E., Bertsch, D. L., Chiang, J., et al., 1994, The first energetic gamma-ray experiment telescope (EGRET) source catalog, *ApJS*, 94, 551–581
- Franceschini, A., Braitto, V., Persic, M., Della Ceca, R., Bassani, L., Cappi, M., Malaguti, P., Palumbo, G. G. C., Risaliti, G., Salvati, M., Severgnini, P., 2003, An XMM-Newton hard X-ray survey of ultraluminous infrared galaxies, *MNRAS*, 343, 1181–1194, [arXiv:astro-ph/0304529](https://arxiv.org/abs/astro-ph/0304529)
- Frenk, C. S., White, S. D. M., Davis, M., Efstathiou, G., 1988, The formation of dark halos in a universe dominated by cold dark matter, *ApJ*, 327, 507–525
- Frieden, B. R., 1972, Restoring with Maximum Likelihood and Maximum Entropy, *Journal of the Optical Society of America (1917-1983)*, 62, 511–+
- Gabuzda, D. C., 1995, Possible Links between BL Lacertae Objects and Quasars from Very Long Baseline Interferometry Radio Data, *Proceedings of the National Academy of Science*, 92, 11 393–11 398
- Gabuzda, D. C., 2005, Evidence for Helical B Fields in AGN Jets from Faraday-Rotation Gradients, in *Astronomical Society of the Pacific Conference Series*, (Ed.) N. Kassim, M. Perez, W. Junor, & P. Henning, vol. 345 of *Astronomical Society of the Pacific Conference Series*, pp. 264–+
- Gabuzda, D. C., Pushkarev, A. B., Cawthorne, T. V., 2000, Analysis of  $\lambda=6\text{cm}$  VLBI polarization observations of a complete sample of northern BL Lacertae objects, *MNRAS*, 319, 1109–1124, [arXiv:astro-ph/0307192](https://arxiv.org/abs/astro-ph/0307192)
- Gabuzda, D. C., Vitrishchak, V. M., Mahmud, M., O’Sullivan, S. P., 2008, Radio circular polarization produced in helical magnetic fields in eight active galactic nuclei, *MNRAS*, 384, 1003–1014, [0711.4572](https://arxiv.org/abs/0711.4572)
- Gallagher, S. C., Brandt, W. N., Chartas, G., Garmire, G. P., Sambruna, R. M., 2002, X-Raying the Ultraluminous Infrared Starburst Galaxy and Broad Absorption Line QSO Markarian 231 with Chandra, *ApJ*, 569, 655–670, [arXiv:astro-ph/0112257](https://arxiv.org/abs/astro-ph/0112257)

- Gehrels, N., Chipman, E., Kniffen, D. A., 1993, The Compton Gamma Ray Observatory, *A&AS*, 97, 5–12
- Gehren, T., Fried, J., Wehinger, P. A., Wyckoff, S., 1984, Host galaxies of quasars and their association with galaxy clusters, *ApJ*, 278, 11–27
- Geller, M. J., Beers, T. C., Bothun, G. D., Huchra, J. P., 1984, A redshift survey of the poor cluster A1142, *AJ*, 89, 319–322
- Genzel, R., Lutz, D., Sturm, E., Egami, E., Kunze, D., Moorwood, A. F. M., Rigopoulou, D., Spoon, H. W. W., Sternberg, A., Tacconi-Garman, L. E., Tacconi, L., Thatte, N., 1998, What Powers Ultraluminous IRAS Galaxies?, *ApJ*, 498, 579–+, [arXiv:astro-ph/9711255](https://arxiv.org/abs/astro-ph/9711255)
- Genzel, R., Pichon, C., Eckart, A., Gerhard, O. E., Ott, T., 2000, Stellar dynamics in the Galactic Centre: proper motions and anisotropy, *MNRAS*, 317, 348–374, [arXiv:astro-ph/0001428](https://arxiv.org/abs/astro-ph/0001428)
- Genzel, R., Schödel, R., Ott, T., Eisenhauer, F., Hofmann, R., Lehnert, M., Eckart, A., Alexander, T., Sternberg, A., Lenzen, R., Clénet, Y., Lacombe, F., Rouan, D., Renzini, A., Tacconi-Garman, L. E., 2003, The Stellar Cusp around the Supermassive Black Hole in the Galactic Center, *ApJ*, 594, 812–832, [arXiv:astro-ph/0305423](https://arxiv.org/abs/astro-ph/0305423)
- Georganopoulos, M., Kirk, J. G., Mastichiadis, A., 2001, The Beaming Pattern and Spectrum of Radiation from Inverse Compton Scattering in Blazars, *ApJ*, 561, 111–117, [arXiv:astro-ph/0107152](https://arxiv.org/abs/astro-ph/0107152)
- Georganopoulos, M., Perlman, E. S., Kazanas, D., 2005, Is the Core of M87 the Source of Its TeV Emission? Implications for Unified Schemes, *ApJ*, 634, L33–L36, [arXiv:astro-ph/0510783](https://arxiv.org/abs/astro-ph/0510783)
- Ghisellini, G., 1993, High energy emission from AGN, *Advances in Space Research*, 13, 587–
- Ghisellini, G., Madau, P., 1996, On the origin of the gamma-ray emission in blazars, *MNRAS*, 280, 67–76
- Ghisellini, G., Maraschi, L., Treves, A., 1985, Inhomogeneous synchrotron-self-Compton models and the problem of relativistic beaming of BL Lac objects, *A&A*, 146, 204–212
- Ghisellini, G., Padovani, P., Celotti, A., Maraschi, L., 1993, Relativistic bulk motion in active galactic nuclei, *ApJ*, 407, 65–82
- Ghisellini, G., Maraschi, L., Tavecchio, F., 2009, The Fermi blazars’ divide, *MNRAS*, 396, L105–L109, [0903.2043](https://arxiv.org/abs/0903.2043)
- Golev, V., Prugniel, P., 1998, A catalogue of Mg<sub>2</sub> indices of galaxies and globular clusters, *A&AS*, 132, 255–260
- Golombek, D., Miley, G. K., Neugebauer, G., 1988, IRAS observations of radio galaxies, *AJ*, 95, 26–36

- Gómez, J. L., Guirado, J. C., Agudo, I., Marscher, A. P., Alberdi, A., Marcaide, J. M., Gabuzda, D. C., 2001, Changes in the trajectory of the radio jet in 0735+178?, MNRAS, 328, 873–881, [arXiv:astro-ph/0109179](#)
- Gong, B., 2008, The non-ballistic superluminal motion in the plane of the sky, MNRAS, 389, 315–320, [arXiv:0806.2708](#)
- González-Pérez, J. N., Kidger, M. R., Martín-Luis, F., 2001, Optical and Near-Infrared Calibration of AGN Field Stars: An All-Sky Network of Faint Stars Calibrated on the Landolt System, AJ, 122, 2055–2098
- Gregory, P. C., Condon, J. J., 1991, The 87GB catalog of radio sources covering delta between 0 and + 75 deg at 4.85 GHz, ApJS, 75, 1011–1291
- Gupta, A. C., Banerjee, D. P. K., Ashok, N. M., Joshi, U. C., 2004, Near infrared intraday variability of Mrk 421, A&A, 422, 505–508, [arXiv:astro-ph/0405186](#)
- Haardt, F., Maraschi, L., Ghisellini, G., 1997, X-Ray Variability and Correlations in the Two-Phase Disk-Corona Model for Seyfert Galaxies, ApJ, 476, 620–+, [arXiv:astro-ph/9609050](#)
- Haehnelt, M. G., Kauffmann, G., 2002, Multiple supermassive black holes in galactic bulges, MNRAS, 336, L61–L64, [arXiv:astro-ph/0208215](#)
- Hagen-Thorn, V. A., Marchenko, S. G., Mikolaichuk, O. V., Yakovleva, V. A., 1997, Searches for periodicity in the light curves of active extragalactic objects: Results for BL Lac and OJ287, Astronomy Reports, 41, 154–159
- Hagen-Thorn, V. A., Larionov, V. M., Efimova, N. V., Hagen-Thorn, E. I., Arkharov, A. A., di Paola, A., Dolci, M., Takalo, L. O., Sillanpää, A., Ostorero, L., 2006, Optical and IR monitoring of the BL Lac object S5 0716+714 from 2001 2004, Astronomy Reports, 50, 458–467
- Hardee, P. E., Norman, M. L., 1988, Spatial stability of the slab jet. I - Linearized stability analysis. II - Numerical simulations, ApJ, 334, 70–94
- Hardee, P. E., Stone, J. M., 1997, The Stability of Radiatively Cooling Jets I. Linear Analysis, ApJ, 483, 121–+
- Hardee, P. E., Cooper, M. A., Clarke, D. A., 1994, On jet response to a driving frequency and the jets in 3C 449, ApJ, 424, 126–137
- Hartman, R. C., Bertsch, D. L., Bloom, S. D., et al., 1999, The Third EGRET Catalog of High-Energy Gamma-Ray Sources, ApJS, 123, 79–202
- Hasinger, G., 1998, The X-ray background and the AGN X-ray luminosity function, Astronomische Nachrichten, 319, 37–+, [arXiv:astro-ph/9712342](#)
- Heckman, T. M., 1980, An optical and radio survey of the nuclei of bright galaxies - Activity in normal galactic nuclei, A&A, 87, 152–164

- Heckman, T. M., Lebofsky, M. J., Rieke, G. H., van Breugel, W., 1983, An infrared and optical investigation of galactic nuclei with compact radio sources, *ApJ*, 272, 400–410
- Heidt, J., Wagner, S. J., 1996, Statistics of optical intraday variability in a complete sample of radio-selected BL Lacertae objects., *A&A*, 305, 42–+, [arXiv:astro-ph/9506032](#)
- Hewitt, A., Burbidge, G., 1989, A new optical catalog of Quasi-Stellar Objects., in *A new optical catalog of QSO (1989)*, pp. 0–+
- Hickox, R. C., Jones, C., Forman, W. R., et al., 2009, Host galaxies, clustering, Eddington ratios, and evolution of radio, X-ray, and infrared-selected AGNs, *ArXiv e-prints*, [0901.4121](#)
- Hill, G. J., Lilly, S. J., 1991, A change in the cluster environments of radio galaxies with cosmic epoch, *ApJ*, 367, 1–18
- Hintzen, P., 1984, Wide-angle radio tail QSOs as members of clusters of galaxies. II - Direct optical observations and spectroscopy of QSO fields, *ApJS*, 55, 533–550
- Hintzen, P., Ulvestad, J., Owen, F., 1983, Are wide-angle radio-tail QSOs members of clusters of galaxies? I - VLA maps at 20 CM of 117 radio quasars, *AJ*, 88, 709–758
- Ho, L. C., Filippenko, A. V., Sargent, W. L. W., 1993, A Reevaluation of the Excitation Mechanism of LINERs, *ApJ*, 417, 63–+
- Ho, L. C., Filippenko, A. V., Sargent, W. L. W., 1997, A Search for “Dwarf” Seyfert Nuclei. V. Demographics of Nuclear Activity in Nearby Galaxies, *ApJ*, 487, 568–+, [arXiv:astro-ph/9704108](#)
- Hoffmeister, C., 1929, Relative Koordinaten, Oerter und Karten neuer Veraenderlicher, *Mitteilungen der Sternwarte zu Sonneberg*, 16, 1–15
- Högbom, J. A., 1974, Aperture Synthesis with a Non-Regular Distribution of Interferometer Baselines, *A&AS*, 15, 417–+
- Hook, I. M., McMahon, R. G., Patnaik, A. R., Browne, I. W. A., Wilkinson, P. N., Irwin, M. J., Hazard, C., 1995, GB:1508+5714 - a Radio Loud Quasar with  $Z=4.30$  and the Space Density of High Redshift Radio Loud Quasars, *MNRAS*, 273, L63+, [arXiv:astro-ph/9502071](#)
- Hopkins, P. F., Hernquist, L., Cox, T. J., Di Matteo, T., Robertson, B., Springel, V., 2006, A Unified, Merger-driven Model of the Origin of Starbursts, Quasars, the Cosmic X-Ray Background, Supermassive Black Holes, and Galaxy Spheroids, *ApJS*, 163, 1–49, [arXiv:astro-ph/0506398](#)
- Hopkins, P. F., Bundy, K., Hernquist, L., Ellis, R. S., 2007, Observational Evidence for the Coevolution of Galaxy Mergers, Quasars, and the Blue/Red Galaxy Transition, *ApJ*, 659, 976–996, [arXiv:astro-ph/0601621](#)



- Hough, D. H., Vermeulen, R. C., Readhead, A. C. S., Cross, L. L., Barth, E. L., Yu, L. H., Beyer, P. J., Phifer, E. M., 2002, Parsec-Scale Radio Structure and Broad Optical Emission Lines in a Complete Sample of 3CR Lobe-dominated Quasars, *AJ*, 123, 1258–1287
- Hoyle, F., 1966, On the Nature of the Quasi-stellar Sources, *Nature*, 209, 751–753
- Hudson, D. S., Reiprich, T. H., Clarke, T. E., Sarazin, C. L., 2006, X-ray detection of the proto supermassive binary black hole at the centre of Abell 400, *A&A*, 453, 433–446, [arXiv:astro-ph/0603272](https://arxiv.org/abs/astro-ph/0603272)
- Huo, Z. Y., Xia, X. Y., Xue, S. J., Mao, S., Deng, Z. G., 2004, Chandra Observations of Ultraluminous Infrared Galaxies: Extended Hot Gaseous Halos in Merging Galaxies, *ApJ*, 611, 208–219, [arXiv:astro-ph/0312185](https://arxiv.org/abs/astro-ph/0312185)
- Hutchings, J. B., Campbell, B., 1983, Are QSOs activated by interactions between galaxies?, *Nature*, 303, 584–588
- Hutchings, J. B., Johnson, I., Pyke, R., 1988, Optical images of quasars and radio galaxies, *ApJS*, 66, 361–385
- Hutchings, J. B., Dewey, A., Chaytor, D., Ryneveld, S., Gower, A. C., Ellingson, E., 1998, Radio Maps of QSOs in Clusters, *PASP*, 110, 111–124
- Hutchings, J. B., Crampton, D., Morris, S. L., Durand, D., Steinbring, E., 1999, QSO Hosts and Environments at  $Z=0.9-4.2$ : JHK Images with Adaptive Optics, *AJ*, 117, 1109–1121, [arXiv:astro-ph/9812159](https://arxiv.org/abs/astro-ph/9812159)
- Imanishi, M., Ueno, S., 1999, Hard X-Ray Luminosities of Multinuclei Infrared Luminous Galaxies Showing a Radio/Far-Infrared Excess, *ApJ*, 527, 709–718, [arXiv:astro-ph/9908122](https://arxiv.org/abs/astro-ph/9908122)
- Iwasawa, K., Fabian, A. C., Brandt, W. N., Kunieda, H., Misaki, K., Terashima, Y., Reynolds, C. S., 1998, Detection of an X-ray periodicity in the Seyfert galaxy IRAS 18325-5926, *MNRAS*, 295, L20–L24, [arXiv:astro-ph/9801226](https://arxiv.org/abs/astro-ph/9801226)
- Jaegers, W. J., de Grijp, M. H. K., 1985, The radio structure of 3C130 interpreted with a dynamical model, *A&A*, 143, 176–181
- James, P., Bate, C., Wells, M., Wright, G., Doyon, R., 1999, Do galaxy mergers form elliptical galaxies? A comparison of kinematic and photometric properties, *MNRAS*, 309, 585–592, [arXiv:astro-ph/9906276](https://arxiv.org/abs/astro-ph/9906276)
- Jarrett, T. H., Chester, T., Cutri, R., Schneider, S. E., Huchra, J. P., 2003, The 2MASS Large Galaxy Atlas, *AJ*, 125, 525–554
- Jiang, L., Fan, X., Ivezić, Ž., Richards, G. T., Schneider, D. P., Strauss, M. A., Kelly, B. C., 2007, The Radio-Loud Fraction of Quasars is a Strong Function of Redshift and Optical Luminosity, *ApJ*, 656, 680–690, [arXiv:astro-ph/0611453](https://arxiv.org/abs/astro-ph/0611453)

- Jorstad, S. G., Marscher, A. P., Mattox, J. R., Aller, M. F., Aller, H. D., Wehrle, A. E., Bloom, S. D., 2001a, Multiepoch Very Long Baseline Array Observations of EGRET-detected Quasars and BL Lacertae Objects: Connection between Superluminal Ejections and Gamma-Ray Flares in Blazars, *ApJ*, 556, 738–748, [arXiv:astro-ph/0102012](#)
- Jorstad, S. G., Marscher, A. P., Mattox, J. R., Aller, M. F., Aller, H. D., Wehrle, A. E., Bloom, S. D., 2001b, Multiepoch Very Long Baseline Array Observations of EGRET-detected Quasars and BL Lacertae Objects: Connection between Superluminal Ejections and Gamma-Ray Flares in Blazars, *ApJ*, 556, 738–748, [arXiv:astro-ph/0102012](#)
- Jorstad, S. G., Marscher, A. P., Lister, M. L., Stirling, A. M., Cawthorne, T. V., Gear, W. K., Gómez, J. L., Stevens, J. A., Smith, P. S., Forster, J. R., Robson, E. I., 2005, Polarimetric Observations of 15 Active Galactic Nuclei at High Frequencies: Jet Kinematics from Bimonthly Monitoring with the Very Long Baseline Array, *AJ*, 130, 1418–1465, [arXiv:astro-ph/0502501](#)
- Kaastra, J. S., Roos, N., 1992, Massive Binary Black-Holes and Wiggling Jets, *A&A*, 254, 96–+
- Kanbach, G., Bertsch, D. L., Fichtel, C. E., Hartman, R. C., Hunter, S. D., Kniffen, D. A., Hughlock, B. W., Favale, A., Hofstadter, R., Hughes, E. B., 1988, The project EGRET (Energetic Gamma-Ray Experiment Telescope) on NASA’s Gamma-Ray Observatory (GRO), *Space Science Reviews*, 49, 69–84
- Kaspi, S., Brandt, W. N., Maoz, D., Netzer, H., Schneider, D. P., Shemmer, O., 2007, Reverberation Mapping of High-Luminosity Quasars: First Results, *ApJ*, 659, 997–1007, [arXiv:astro-ph/0612722](#)
- Katz, J. I., 1997, A Precessing Disk in OJ 287?, *ApJ*, 478, 527–+
- Kawakatu, N., Imanishi, M., Nagao, T., 2007, Anticorrelation between the Mass of a Supermassive Black Hole and the Mass Accretion Rate in Type 1 Ultraluminous Infrared Galaxies and Nearby QSOs, *ApJ*, 661, 660–671, [arXiv:astro-ph/0702552](#)
- Kellermann, K. I., Sramek, R., Schmidt, M., Shaffer, D. B., Green, R., 1989, VLA observations of objects in the Palomar Bright Quasar Survey, *AJ*, 98, 1195–1207
- Kellermann, K. I., Lister, M. L., Homan, D. C., Ros, E., Zensus, J. A., Cohen, M. H., Russo, M., Vermeulen, R. C., 2003, Superluminal Motion and Relativistic Beaming in Blazar Jets, in *High Energy Blazar Astronomy*, (Eds.) L. O. Takalo, E. Valtaoja, vol. 299 of *Astronomical Society of the Pacific Conference Series*, pp. 117–+
- Kellermann, K. I., Lister, M. L., Homan, D. C., Vermeulen, R. C., Cohen, M. H., Ros, E., Kadler, M., Zensus, J. A., Kovalev, Y. Y., 2004, Sub-Milliarcsecond Imaging of Quasars and Active Galactic Nuclei. III. Kinematics of Parsec-scale Radio Jets, *ApJ*, 609, 539–563, [arXiv:astro-ph/0403320](#)

- Kelly, B. C., Bechtold, J., 2007, Virial Masses of Black Holes from Single Epoch Spectra of Active Galactic Nuclei, *ApJS*, 168, 1–18, [arXiv:astro-ph/0609303](#)
- Kelly, B. C., Hughes, P. A., Aller, H. D., Aller, M. F., 2003, The Cross-Wavelet Transform and Analysis of Quasi-periodic Behavior in the Pearson-Readhead VLBI Survey Sources, *ApJ*, 591, 695–713, [arXiv:astro-ph/0301002](#)
- Kim, D.-C., Veilleux, S., Sanders, D. B., 2002, Optical and Near-Infrared Imaging of the IRAS 1 Jy Sample of Ultraluminous Infrared Galaxies. I. The Atlas, *ApJS*, 143, 277–314, [arXiv:astro-ph/0207373](#)
- Kim, K.-T., Kronberg, P. P., Tribble, P. C., 1991, Detection of excess rotation measure due to intracluster magnetic fields in clusters of galaxies, *ApJ*, 379, 80–88
- Kirhakos, S., Bahcall, J. N., Schneider, D. P., Kristian, J., 1999, The Host Galaxies of Three Radio-loud Quasars: 3C 48, 3C 345, and B2 1425+267, *ApJ*, 520, 67–77, [arXiv:astro-ph/9902175](#)
- Kleinmann, S. G., 1992, 2MASS - The 2 Micron All Sky Survey, in *Robotic Telescopes in the 1990s*, (Ed.) A. V. Filippenko, vol. 34 of *Astronomical Society of the Pacific Conference Series*, pp. 203–212
- Knapp, G. R., Bies, W. E., van Gorkom, J. H., 1990, Infrared properties of nearby radio galaxies, *AJ*, 99, 476–496
- Kollatschny, W., Dietrich, M., Hagen, H., 1992, Absorption line variability in Markarian 231, *A&A*, 264, L5–L8
- Komossa, S., 2006, Observational evidence for binary black holes and active double nuclei, *Memorie della Societa Astronomica Italiana*, 77, 733–+
- Komossa, S., Burwitz, V., Hasinger, G., Predehl, P., Kaastra, J. S., Ikebe, Y., 2003, Discovery of a Binary Active Galactic Nucleus in the Ultraluminous Infrared Galaxy NGC 6240 Using Chandra, *ApJ*, 582, L15–L19, [arXiv:astro-ph/0212099](#)
- Königl, A., 1989, Self-similar models of magnetized accretion disks, *ApJ*, 342, 208–223
- Königl, A., 2006, AGN winds and jets: a theoretical perspective, *Memorie della Societa Astronomica Italiana*, 77, 598–+
- Kormendy, J., Gebhardt, K., 2001, Supermassive Black Holes in Galactic Nuclei (Plenary Talk), in *20th Texas Symposium on relativistic astrophysics*, (Eds.) J. C. Wheeler, H. Martel, vol. 586 of *American Institute of Physics Conference Series*, pp. 363–+
- Kotilainen, J. K., Hyvönen, T., Falomo, R., 2005, The luminous host galaxies of high redshift BL Lac objects, *A&A*, 440, 831–843, [arXiv:astro-ph/0505443](#)
- Krichbaum, T. P., 1990, Images of Parsec-Scale Jets from 7 mm VLBI, in *Parsec-scale radio jets*, (Ed.) J. A. Zensus & T. J. Pearson, pp. 83–+

- Krichbaum, T. P., Witzel, A., Standke, K. J., Graham, D. A., Schalinski, C. J., Zensus, J. A., 1994, MM-VLBI: Bending of Jets in the Vicinity of AGN, in Compact Extragalactic Radio Sources, (Ed.) J. A. Zensus & K. I. Kellermann, pp. 39–+
- Krichbaum, T. P., Britzen, S., Standke, K. J., Witzel, A., Schalinski, C. J., Zensus, J. A., 1995, Very-Long-Baseline Radio Interferometry (VLBI) Observations of  $\gamma$ -Ray Blazars: Results from Millimeter-VLBI Observations, Proceedings of the National Academy of Science, 92, 11 377–11 380
- Krichbaum, T. P., Bach, U., Graham, D. A., Alef, W., Roy, A. L., Witzel, A., Zensus, A. J., Bremer, M., Sanchez, S., 2008, Towards mm-VLBI, in The role of VLBI in the Golden Age for Radio Astronomy
- Krolik, J. H., 1999, Active galactic nuclei : from the central black hole to the galactic environment, Active galactic nuclei : from the central black hole to the galactic environment /Julian H. Krolik. Princeton, N. J. : Princeton University Press, c1999.
- Kudryavtseva, N. A., Britzen, S., Witzel, A., Ros, E., Karouzos, M., Aller, M. F., Aller, H. D., Teräsanta, H., Eckart, A., Zensus, A. J., 2010, A possible jet precession in the periodic quasar B0605-085
- Kuehr, H., Witzel, A., Pauliny-Toth, I. I. K., Nauber, U., 1981, A catalogue of extragalactic radio sources having flux densities greater than 1 Jy at 5 GHz, A&AS, 45, 367–430
- Kundt, W., Gopal-Krishna, 1980, Extremely relativistic electron-positron twin-jets form extragalactic radio sources, Nature, 288, 149–+
- Lähteenmäki, A., Valtaoja, E., 2003, Testing of Inverse Compton Models for Active Galactic Nuclei with Gamma-Ray and Radio Observations, ApJ, 590, 95–108
- Lai, D., 2003, Warping of Accretion Disks with Magnetically Driven Outflows: A Possible Origin for Jet Precession, ApJ, 591, L119–L122, [arXiv:astro-ph/0306012](https://arxiv.org/abs/astro-ph/0306012)
- Lainela, M., Takalo, L. O., Sillanpää, A., Pursimo, T., Nilsson, K., Katajainen, S., Tosti, G., Fiorucci, M., Luciani, M., Villata, M., Raiteri, C. M., de Francesco, G., Sobrito, G., Benítez, E., Dultzin-Hacyan, D., de Diego, J. A., Turner, G. W., Robertson, J. W., Honeycutt, R. K., 1999, The 65 Day Period in 3C 66A during Bright State, ApJ, 521, 561–564
- Lara, L., Alberdi, A., Marcaide, J. M., Muxlow, T. W. B., 1994, The quasar 3C395 revisited: new VLBI observations and numerical simulations, A&A, 285, 393–403
- Lara, L., Alberdi, A., Marcaide, J. M., Muxlow, T. W. B., 1999, Space-VLBI observations of the twisted jet in 3C 395, A&A, 352, 443–446, [arXiv:astro-ph/9911084](https://arxiv.org/abs/astro-ph/9911084)
- Ledlow, M. J., Owen, F. N., 1995, A 20 CM VLA Survey of Abell clusters of galaxies. 4: The radio sample and cluster properties, AJ, 109, 853–873
- Lehto, H. J., Valtonen, M. J., 1996, OJ 287 Outburst Structure and a Binary Black Hole Model, ApJ, 460, 207–+

- Li, C., Kauffmann, G., Heckman, T. M., White, S. D. M., Jing, Y. P., 2008, Interactions, star formation and AGN activity, *MNRAS*, 385, 1915–1922, [0712.0383](#)
- Lilly, S. J., Longair, M. S., Allington-Smith, J. R., 1985, Infrared Observations of 1-JANSKY Radio Source Identifications and Empty Fields, *MNRAS*, 215, 37–+
- Lind, K. R., Blandford, R. D., 1985, Semidynamical models of radio jets - Relativistic beaming and source counts, *ApJ*, 295, 358–367
- Lípari, S. L., Terlevich, R. J., 2006, Evolutionary unification in composite active galactic nuclei, *MNRAS*, 368, 1001–1015, [arXiv:astro-ph/0602090](#)
- Lipovka, A. A., Lipovka, N. M., 2002, The Nature of Active Radio Galaxies in the Cluster A569, *Astronomy Reports*, 46, 867–870
- Lister, M. L., 2001, Parsec-Scale Jet Polarization Properties of a Complete Sample of Active Galactic Nuclei at 43 GHz, *ApJ*, 562, 208–232, [arXiv:astro-ph/0107594](#)
- Lister, M. L., 2006, Structure and Evolution of Blazar Jets: Recent Results from VLBI Surveys, in *Blazar Variability Workshop II: Entering the GLAST Era*, (Ed.) H. R. Miller, K. Marshall, J. R. Webb, & M. F. Aller, vol. 350 of *Astronomical Society of the Pacific Conference Series*, pp. 139–+
- Lister, M. L., Homan, D. C., 2005, MOJAVE: Monitoring of Jets in Active Galactic Nuclei with VLBA Experiments. I. First-Epoch 15 GHz Linear Polarization Images, *AJ*, 130, 1389–1417, [arXiv:astro-ph/0503152](#)
- Lister, M. L., Kellermann, K. I., Vermeulen, R. C., Cohen, M. H., Zensus, J. A., Ros, E., 2003, 4C +12.50: A Superluminal Precessing Jet in the Recent Merger System IRAS 13451+1232, *ApJ*, 584, 135–146, [arXiv:astro-ph/0210372](#)
- Lister, M. L., Aller, H. D., Aller, M. F., Cohen, M. H., Homan, D. C., Kadler, M., Kellermann, K. I., Kovalev, Y. Y., Ros, E., Savolainen, T., Zensus, J. A., Vermeulen, R. C., 2009a, MOJAVE: Monitoring of Jets in Active Galactic Nuclei with VLBA Experiments. V. Multi-Epoch VLBA Images, *AJ*, 137, 3718–3729, [0812.3947](#)
- Lister, M. L., Cohen, M. H., Homan, D. C., Kadler, M., Kellermann, K. I., Kovalev, Y. Y., Ros, E., Savolainen, T., Zensus, J. A., 2009b, MOJAVE: Monitoring of Jets in Active Galactic Nuclei with VLBA Experiments. VI. Kinematics Analysis of a Complete Sample of Blazar Jets, *AJ*, 138, 1874–1892, [0909.5100](#)
- Lister, M. L., Homan, D. C., Kadler, M., Kellermann, K. I., Kovalev, Y. Y., Ros, E., Savolainen, T., Zensus, J. A., 2009c, A Connection Between Apparent VLBA Jet Speeds and Initial Active Galactic Nucleus Detections Made by the Fermi Gamma-Ray Observatory, *ApJ*, 696, L22–L26, [0902.2087](#)
- Liu, F. K., Wu, X.-B., 2002, Black hole mass and binary model for BL Lac object OJ 287, *A&A*, 388, L48–L52, [arXiv:astro-ph/0212475](#)

- Liu, Y., Jiang, D. R., Gu, M. F., 2006, The Jet Power, Radio Loudness, and Black Hole Mass in Radio-loud Active Galactic Nuclei, *ApJ*, 637, 669–681, [arXiv:astro-ph/0510241](#)
- Liu, Y., Jiang, D. R., Shen, Z., 2010, A kinematic study of the compact jet in quasar B3 1633+382, *ArXiv e-prints*, [1006.4002](#)
- Lobanov, A., 2007, Compact radio jets and nuclear regions in active galaxies, *ArXiv e-prints*, [0708.4280](#)
- Lobanov, A. P., Roland, J., 2005, A supermassive binary black hole in the quasar 3C 345, *A&A*, 431, 831–846, [arXiv:astro-ph/0411417](#)
- Lobanov, A. P., Zensus, J. A., 1999, Spectral Evolution of the Parsec-Scale Jet in the Quasar 3C 345, *ApJ*, 521, 509–525, [arXiv:astro-ph/9903318](#)
- Lobanov, A. P., Zensus, J. A., 2001, A Cosmic Double Helix in the Archetypical Quasar 3C273, *Science*, 294, 128–131
- Lobanov, A. P., Krichbaum, T. P., Witzel, A., Zensus, J. A., 2006, Dual-Frequency VSOP Imaging of the Jet in S5 0836+710, *PASJ*, 58, 253–259, [arXiv:astro-ph/0507667](#)
- Lodato, G., Nayakshin, S., King, A. R., Pringle, J. E., 2009, Black hole mergers: can gas discs solve the ‘final parsec’ problem?, *MNRAS*, 398, 1392–1402, [0906.0737](#)
- Lotz, J. M., Jonsson, P., Cox, T. J., Primack, J. R., 2008, Galaxy Merger Morphologies and Time-Scales from Simulations of Equal-Mass Gas-Rich Disc Mergers, *ArXiv e-prints*, [0805.1246](#)
- Lovelace, R. V. E., 1976, Dynamo model of double radio sources, *Nature*, 262, 649–652
- Lowe, S. R., Gawroński, M. P., Wilkinson, P. N., Kus, A. J., Browne, I. W. A., Pazderski, E., Feiler, R., Kettle, D., 2007, 30 GHz flux density measurements of the Caltech-Jodrell flat-spectrum sources with OCRA-p, *A&A*, 474, 1093–1100, [arXiv:0707.3368](#)
- Lu, J.-F., Zhou, B.-Y., 2005, Observational Evidence of Jet Precession in Galactic Nuclei Caused by Accretion Disks, *ApJ*, 635, L17–L20, [arXiv:astro-ph/0511212](#)
- Lupton, R. H., Gott, III, J. R., 1982, A new double jet model for 3C 449, *ApJ*, 255, 408–412
- Machalski, J., Brandt, W. N., 1996, The radio, optical and X-ray properties of the radio source 0927+352, *MNRAS*, 282, 1305–1312
- Madau, P., Ferguson, H. C., Dickinson, M. E., Giavalisco, M., Steidel, C. C., Fruchter, A., 1996, High-redshift galaxies in the Hubble Deep Field: colour selection and star formation history to  $z \sim 4$ , *MNRAS*, 283, 1388–1404, [arXiv:astro-ph/9607172](#)
- Maia, M. A. G., Machado, R. S., Willmer, C. N. A., 2003, The Seyfert Population in the Local Universe, *AJ*, 126, 1750–1762, [arXiv:astro-ph/0307180](#)

- Maiolino, R., Rieke, G. H., 1995, Low-Luminosity and Obscured Seyfert Nuclei in Nearby Galaxies, *ApJ*, 454, 95–+
- Maness, H. L., Taylor, G. B., Zavala, R. T., Peck, A. B., Pollack, L. K., 2004, Breaking All the Rules: The Compact Symmetric Object 0402+379, *ApJ*, 602, 123–134, [arXiv:astro-ph/0310663](#)
- Mannheim, K., 1993, The proton blazar, *A&A*, 269, 67–76, [arXiv:astro-ph/9302006](#)
- Mannheim, K., Biermann, P. L., 1992, Gamma-ray flaring of 3C 279 - A proton-initiated cascade in the jet?, *A&A*, 253, L21–L24
- Mannheim, K., Biermann, P. L., Kruells, W. M., 1991, A novel mechanism for nonthermal X-ray emission, *A&A*, 251, 723–731
- Maoz, D., 1995, Limits on Dust in Rich Clusters of Galaxies from the Color of Background Quasars, *ApJ*, 455, L115+, [arXiv:astro-ph/9508093](#)
- Maraschi, L., Ghisellini, G., Celotti, A., 1992, A jet model for the gamma-ray emitting blazar 3C 279, *ApJ*, 397, L5–L9
- Marscher, A. P., 2005, The Relationship between Radio and Higher-Frequency Emission in Active Galactic Nuclei, *Memorie della Societa Astronomica Italiana*, 76, 13–+
- Marscher, A. P., Gear, W. K., 1985, Models for high-frequency radio outbursts in extragalactic sources, with application to the early 1983 millimeter-to-infrared flare of 3C 273, *ApJ*, 298, 114–127
- Martí, J. M., Müller, E., 2003, Numerical Hydrodynamics in Special Relativity, *Living Reviews in Relativity*, 6, 7–+
- Mayer, L., Kazantzidis, S., Madau, P., Colpi, M., Quinn, T., Wadsley, J., 2007, Rapid Formation of Supermassive Black Hole Binaries in Galaxy Mergers with Gas, *Science*, 316, 1874–, [arXiv:0706.1562](#)
- McKinney, J. C., Blandford, R. D., 2009, Stability of relativistic jets from rotating, accreting black holes via fully three-dimensional magnetohydrodynamic simulations, *MNRAS*, 394, L126–L130, [0812.1060](#)
- McLure, R. J., Willott, C. J., Jarvis, M. J., Rawlings, S., Hill, G. J., Mitchell, E., Dunlop, J. S., Wold, M., 2004, A sample of radio galaxies spanning three decades in radio luminosity - I. The host galaxy properties and black hole masses, *MNRAS*, 351, 347–361, [arXiv:astro-ph/0403106](#)
- Meier, D. L., Nakamura, M., 2006, Magnetically-Dominated Jets and Accretion Flows, in *Blazar Variability Workshop II: Entering the GLAST Era*, (Eds.) H. R. Miller, K. Marshall, J. R. Webb, M. F. Aller, vol. 350 of *Astronomical Society of the Pacific Conference Series*, pp. 195–+

- Melrose, D. B., 1994, Low Frequency Variability of Extragalactic Radio Sources, in *The Physics of Active Galaxies*, (Eds.) G. V. Bicknell, M. A. Dopita, P. J. Quinn, vol. 54 of *Astronomical Society of the Pacific Conference Series*, pp. 91–+
- Merritt, D., Ekers, R. D., 2002, Tracing Black Hole Mergers Through Radio Lobe Morphology, *Science*, 297, 1310–1313, [arXiv:astro-ph/0208001](https://arxiv.org/abs/astro-ph/0208001)
- Merritt, D., Ferrarese, L., 2001, The  $M$ - $\sigma$  Relation for Supermassive Black Holes, *ApJ*, 547, 140–145, [arXiv:astro-ph/0008310](https://arxiv.org/abs/astro-ph/0008310)
- Merritt, D., Milosavljević, M., 2005, Massive Black Hole Binary Evolution, *Living Reviews in Relativity*, 8, 8–+, [arXiv:astro-ph/0410364](https://arxiv.org/abs/astro-ph/0410364)
- Mezcua, M., Lobanov, A. P., Chavushyan, V. H., León-Tavares, J., 2009, Black Hole Masses in X-shaped radio sources, in *Physics of Galactic Nuclei*
- Miller, C. J., Nichol, R. C., Gómez, P. L., Hopkins, A. M., Bernardi, M., 2003, The Environment of Active Galactic Nuclei in the Sloan Digital Sky Survey, *ApJ*, 597, 142–156, [arXiv:astro-ph/0307124](https://arxiv.org/abs/astro-ph/0307124)
- Miller, N. A., Ledlow, M. J., Owen, F. N., Hill, J. M., 2002, Redshifts for a Sample of Radio-selected Poor Clusters, *AJ*, 123, 3018–3040, [arXiv:astro-ph/0203281](https://arxiv.org/abs/astro-ph/0203281)
- Milosavljević, M., Merritt, D., 2001, Formation of Galactic Nuclei, *ApJ*, 563, 34–62, [arXiv:astro-ph/0103350](https://arxiv.org/abs/astro-ph/0103350)
- Mimica, P., Aloy, M., Agudo, I., Martí, J. M., Gómez, J. L., Miralles, J. A., 2009, Spectral Evolution of Superluminal Components in Parsec-Scale Jets, *ApJ*, 696, 1142–1163, [0811.1143](https://arxiv.org/abs/0811.1143)
- Moshir, M., Kopan, G., Conrow, T., McCallon, H., Hacking, P., Gregorich, D., Rohrbach, G., Melnyk, M., Rice, W., Fullmer, L., White, J., Chester, T., 1990, The IRAS Faint Source Catalog, Version 2, in *Bulletin of the American Astronomical Society*, vol. 22 of *Bulletin of the American Astronomical Society*, pp. 1325–+
- Murphy, Jr., T. W., Soifer, B. T., Matthews, K., Armus, L., 2001, Age Dating Ultraluminous Infrared Galaxies along the Merger Sequence, *ApJ*, 559, 201–224, [arXiv:astro-ph/0103425](https://arxiv.org/abs/astro-ph/0103425)
- Nagar, N. M., Wilson, A. S., Falcke, H., Veilleux, S., Maiolino, R., 2003, The AGN content of ultraluminous IR galaxies: High resolution VLA imaging of the IRAS 1 Jy ULIRG sample, *A&A*, 409, 115–121, [arXiv:astro-ph/0309298](https://arxiv.org/abs/astro-ph/0309298)
- Nair, A. D., 1997, Investigating properties of a set of variable AGN with cluster analysis, *MNRAS*, 287, 641–650
- Narayan, R., Nityananda, R., 1984, Maximum Entropy - Flexibility Versus Fundamentalism, in *Indirect Imaging. Measurement and Processing for Indirect Imaging*, (Ed.) J. A. Roberts, pp. 281–+



- Neronov, A., Aharonian, F. A., 2007, Production of TeV Gamma Radiation in the Vicinity of the Supermassive Black Hole in the Giant Radio Galaxy M87, *ApJ*, 671, 85–96, [0704.3282](#)
- Nesci, R., Massaro, E., Maesano, M., Montagni, F., Sclavi, S., Venturi, T., Dallacasa, D., D’Alessio, F., 2002, Optical and Radio Monitoring of S5 1803+784, *AJ*, 124, 53–64, [arXiv:astro-ph/0204365](#)
- Nesci, R., Massaro, E., Rossi, C., Sclavi, S., Maesano, M., Montagni, F., 2005, The Long-Term Optical Variability of the BL Lacertae Object S5 0716+714: Evidence for a Precessing Jet, *AJ*, 130, 1466–1471, [arXiv:astro-ph/0506172](#)
- Neshpor, Y. I., 2000a, A 23.2-Days Period in the Ultrahigh-Energy Gamma-Ray Flux from the Mk 501 Active Galactic Nucleus, *Astronomy Letters*, 26, 763–764
- Neshpor, Y. I., 2000b, A 23.2-Days Period in the Ultrahigh-Energy Gamma-Ray Flux from the Mk 501 Active Galactic Nucleus, *Astronomy Letters*, 26, 763–764
- Neufeld, D. A., Lepp, S., Melnick, G. J., 1995, Thermal Balance in Dense Molecular Clouds: Radiative Cooling Rates and Emission-Line Luminosities, *ApJS*, 100, 132–+
- Neugebauer, G., Miley, G. K., Soifer, B. T., Clegg, P. E., 1986, Quasars measured by the Infrared Astronomical Satellite, *ApJ*, 308, 815–828
- Ochsenbein, F., Bauer, P., Marcout, J., 2000, The VizieR database of astronomical catalogues, *A&AS*, 143, 23–32, [arXiv:astro-ph/0002122](#)
- O’Dea, C. P., Stanghellini, C., Baum, S. A., Charlot, S., 1996, On the Host Galaxies of the Gigahertz Peaked-Spectrum Radio Sources, *ApJ*, 470, 806–+
- Osonne, S., 2006, Study of 23 day periodicity of Blazar Mkn501 in 1997, *Astroparticle Physics*, 26, 209–218, [arXiv:astro-ph/0506328](#)
- Osonne, S., Teshima, M., 2001, Long periodicity of Blaser with RXTE ASM, in *International Cosmic Ray Conference*, vol. 7 of *International Cosmic Ray Conference*, pp. 2695–+
- Padovani, P., 1993, The Radio Loud Fraction of QSOS and its Dependence on Magnitude and Redshift, *MNRAS*, 263, 461–+
- Padovani, P., Giommi, P., Ábrahám, P., Csizmadia, S., Moór, A., 2006, Filling the infrared gap: ISO observations of 1 Jy BL Lacertae objects, *A&A*, 456, 131–139, [arXiv:astro-ph/0606219](#)
- Panessa, F., Bassani, L., Cappi, M., Dadina, M., Barcons, X., Carrera, F. J., Ho, L. C., Iwasawa, K., 2006, On the X-ray, optical emission line and black hole mass properties of local Seyfert galaxies, *A&A*, 455, 173–185, [arXiv:astro-ph/0605236](#)
- Papadopoulos, P. P., Isaak, K. G., van der Werf, P. P., 2007, First CO J = 6-5 and J = 4-3 Detections in Local ULIRGs: The Dense Gas in Markarian 231 and Its Cooling Budget, *ApJ*, 668, 815–825, [0706.0811](#)

- Pearson, T. J., Readhead, A. C. S., 1981, The milli-arcsecond structure of a complete sample of radio sources. I - VLBI maps of seven sources, *ApJ*, 248, 61–81
- Pearson, T. J., Browne, I. W. A., Henstock, D. R., Polatidis, A. G., Readhead, A. C. S., Taylor, G. B., Thakkar, D. D., Vermeulen, R. C., Wilkinson, P. N., Xu, W., 1998, The Caltech-Jodrell Bank VLBI Surveys, in *IAU Colloq. 164: Radio Emission from Galactic and Extragalactic Compact Sources*, (Eds.) J. A. Zensus, G. B. Taylor, J. M. Wrobel, vol. 144 of *Astronomical Society of the Pacific Conference Series*, pp. 17–+
- Peck, A. B., Taylor, G. B., 1998, Kinematics of the Neutral Hydrogen Toward the Core of NGC 3894, *ApJ*, 502, L23+
- Pelletier, G., 2009, Synchrotron and Inverse Compton radiation from relativistic plasma. Effects of coherence and turbulence., in *Proceedings of the Quantum of Quasars workshop. December 2-4, 2009. Grenoble, France*. Published online at <http://pos.sissa.it/cgi-bin/reader/conf.cgi?confid=101>; <http://pos.sissa.it/cgi-bin/reader/conf.cgi?confid=101/A>, p.10
- Pelletier, G., Roland, J., 1989, Two-fluid model of superluminal radio sources - Application to cosmology, *A&A*, 224, 24–30
- Peng, B., Kraus, A., Krichbaum, T. P., Müller, S. A. H., Qian, S. J., Quirrenbach, A., Wagner, S. J., Witzel, A., Zensus, J. A., Jin, C., Bock, H., 2000, Infrared, radio and optical variability of the BL Lacertae object 2007+777, *A&A*, 353, 937–943
- Perlman, E. S., Stocke, J. T., Conway, J., Reynolds, C., 2001, Host Galaxies, Obscuration, and Nuclear Structure of Three Nearby Compact Symmetric Objects, *AJ*, 122, 536–548, [arXiv:astro-ph/0104439](https://arxiv.org/abs/astro-ph/0104439)
- Perucho, M., Lobanov, A. P., Martí, J.-M., Hardee, P. E., 2006, The role of Kelvin-Helmholtz instability in the internal structure of relativistic outflows. The case of the jet in 3C 273, *A&A*, 456, 493–504, [arXiv:astro-ph/0606109](https://arxiv.org/abs/astro-ph/0606109)
- Perucho, M., Lobanov, A. P., Kovalev, Y. Y., 2009, Physical Information Derived from the Internal Structure in Jets, in *Astronomical Society of the Pacific Conference Series*, (Ed.) Y. Hagiwara, E. Fomalont, M. Tsuboi, & M. Yasuhiro, vol. 402 of *Astronomical Society of the Pacific Conference Series*, pp. 349–+
- Petrosian, A., McLean, B., Allen, R. J., Leitherer, C., MacKenty, J., Panagia, N., 2002, Studies of the Second Byurakan Survey Galaxies. I. Mergers, Interacting Systems, and Close Pairs, *AJ*, 123, 2280–2301
- Pica, A. J., Smith, A. G., 1983, Optical variability, absolute luminosity, and the Hubble diagram for QSOs, *ApJ*, 272, 11–25
- Pietilä, H., 1998, Possibilities and Predictions of the OJ 287 Binary Black Hole Model, *ApJ*, 508, 669–675
- Piner, B. G., Pant, N., Edwards, P. G., 2008, The Parsec-Scale Jets of the TeV Blazars H1426+428, 1ES 1959+650, and PKS 2155-304: 2001-2004, *ApJ*, 678, 64–77, [0801.2749](https://arxiv.org/abs/0801.2749)

- Pollack, L. K., Taylor, G. B., Zavala, R. T., 2003, VLBI Polarimetry of 177 Sources from the Caltech-Jodrell Bank Flat-Spectrum Survey, *ApJ*, 589, 733–751, [arXiv:astro-ph/0302211](#)
- Porcas, R., 1983, Superluminal motions - Astronomers still puzzled, *Nature*, 302, 753–+
- Pringle, J. E., 1996, Self-induced warping of accretion discs, *MNRAS*, 281, 357–361
- Pronik, I. I., 1988, The variability of emission lines and Seyfert galaxy NGC 1275 nucleus duplicity., *Izvestiya Ordena Trudovogo Krasnogo Znameni Krymskoj Astrofizicheskoj Observatorii*, 79, 122–133
- Ptak, A., Heckman, T., Levenson, N. A., Weaver, K., Strickland, D., 2003, A Chandra Survey of the Nearest Ultraluminous Infrared Galaxies: Obscured Active Galactic Nuclei or Superstarbursts?, *ApJ*, 592, 782–803, [arXiv:astro-ph/0304222](#)
- Punch, M., Akerlof, C. W., Cawley, M. F., Chantell, M., Fegan, D. J., Fennell, S., Gaidos, J. A., Hagan, J., Hillas, A. M., Jiang, Y., Kerrick, A. D., Lamb, R. C., Lawrence, M. A., Lewis, D. A., Meyer, D. I., Mohanty, G., O’Flaherty, K. S., Reynolds, P. T., Rovero, A. C., Schubnell, M. S., Sembroski, G., Weekes, T. C., Wilson, C., 1992, Detection of TeV photons from the active galaxy Markarian 421, *Nature*, 358, 477–+
- Punsly, B., Igumenshchev, I. V., Hirose, S., 2009, Three-Dimensional Simulations of Vertical Magnetic Flux in the Immediate Vicinity of Black Holes, *ApJ*, 704, 1065–1085, [0908.3697](#)
- Pursimo, T., Nilsson, K., Takalo, L. O., Sillanpää, A., Heidt, J., Pietilä, H., 2002, Deep optical imaging of radio selected BL Lacertae objects, *A&A*, 381, 810–824
- Puschell, J. J., Owen, F. N., Laing, R. A., 1982, Near-infrared photometry of distant radio galaxies - Spectral flux distributions and redshift estimates, *ApJ*, 257, L57–L61
- Pushkarev, A. B., Kovalev, Y. Y., Lister, M. L., Savolainen, T., 2009, Jet opening angles and gamma-ray brightness of AGN, *A&A*, 507, L33–L36, [0910.1813](#)
- Pustilnik, S. A., Kniazev, A. Y., Lipovetsky, V. A., Ugryumov, A. V., 2001, Environment status of blue compact galaxies and trigger of star formation, *A&A*, 373, 24–37, [arXiv:astro-ph/0104334](#)
- Qian, S.-J., Kudryavtseva, N. A., Britzen, S., Krichbaum, T. P., Gao, L., Witzel, A., Zensus, J. A., Aller, M. F., Aller, H. D., Zhang, X.-Z., 2007, A Possible Periodicity in the Radio Light Curves of 3C 454.3, *Chinese Journal of Astronomy and Astrophysics*, 7, 364–374, [arXiv:0710.1876](#)
- Quinn, J., Akerlof, C. W., Biller, S., et al., 1996, Detection of Gamma Rays with  $E > 300$  GeV from Markarian 501, *ApJ*, 456, L83+
- Quirrenbach, A., Witzel, A., Wagner, S., Sanchez-Pons, F., Krichbaum, T. P., Wegner, R., Anton, K., Erkens, U., Haehnelt, M., Zensus, J. A., Johnston, K. J., 1991, Correlated radio and optical variability in the BL Lacertae object 0716 + 714, *ApJ*, 372, L71–L74

- Rafferty, D. A., McNamara, B. R., Nulsen, P. E. J., Wise, M. W., 2006, The Feedback-regulated Growth of Black Holes and Bulges through Gas Accretion and Starbursts in Cluster Central Dominant Galaxies, *ApJ*, 652, 216–231, [arXiv:astro-ph/0605323](#)
- Raiteri, C. M., Villata, M., Tosti, G., et al., 2003, Optical and radio behaviour of the BL Lacertae object J0716+714, *A&A*, 402, 151–169, [arXiv:astro-ph/0302518](#)
- Rajagopal, M., Romani, R. W., 1995, Ultra-Low-Frequency Gravitational Radiation from Massive Black Hole Binaries, *ApJ*, 446, 543–+, [arXiv:astro-ph/9412038](#)
- Rees, M. J., 1966, Appearance of Relativistically Expanding Radio Sources, *Nature*, 211, 468–470
- Rees, M. J., 1978, Accretion and the quasar phenomenon, *Phys. Scr*, 17, 193–200
- Rees, M. J., 1989, The radio/optical alignment of high-z radio galaxies - Triggering of star formation in radio lobes, *MNRAS*, 239, 1P–4P
- Richards, A. M. S., Knapen, J. H., Yates, J. A., Cohen, R. J., Collett, J. L., Wright, M. M., Gray, M. D., Field, D., 2005, OH megamasers, starburst and AGN activity in Markarian 231, *MNRAS*, 364, 353–366, [arXiv:astro-ph/0509327](#)
- Richards, G. T., Strauss, M. A., Fan, X., et al., 2006, The Sloan Digital Sky Survey Quasar Survey: Quasar Luminosity Function from Data Release 3, *AJ*, 131, 2766–2787, [arXiv:astro-ph/0601434](#)
- Richer, H. B., Crabtree, D. R., Fabian, A. C., Lin, D. N. C., 1993, Star and cluster formation in NGC 1275, *AJ*, 105, 877–885
- Rickett, B. J., 1990, Radio propagation through the turbulent interstellar plasma, *ARA&A*, 28, 561–605
- Riechers, D. A., Walter, F., Carilli, C. L., Bertoldi, F., Momjian, E., 2008, Formation of a Quasar Host Galaxy through a Wet Merger 1.4 Billion Years after the Big Bang, *ArXiv e-prints*, 808, [0808.3774](#)
- Rieger, F. M., 2004, On the Geometrical Origin of Periodicity in Blazar-type Sources, *ApJ*, 615, L5–L8, [arXiv:astro-ph/0410188](#)
- Rieke, G. H., 1978, The infrared emission of Seyfert galaxies, *ApJ*, 226, 550–558
- Rodriguez, C., Taylor, G. B., Zavala, R. T., Peck, A. B., Pollack, L. K., Romani, R. W., 2006, A Compact Supermassive Binary Black Hole System, *ApJ*, 646, 49–60, [arXiv:astro-ph/0604042](#)
- Rogers, A. E. E., Cappallo, R. J., Hinteregger, H. F., Levine, J. I., Nesman, E. F., Webber, J. C., Whitney, A. R., Clark, T. A., Ma, C., Ryan, J., Corey, B. E., Counselman, C. C., Herring, T. A., Shapiro, I. I., Knight, C. A., Shaffer, D. B., Vandenberg, N. R., Lacasse, R., Mauzy, R., Rayhrer, B., Schupler, B. R., Pigg, J. C., 1983, Very-long-baseline radio interferometry - The Mark III system for geodesy, astrometry, and aperture synthesis, *Science*, 219, 51–54

- Roland, J., Teyssier, R., Roos, N., 1994, On the origin of the variability of superluminal radio sources similar to 3C 273, *A&A*, 290, 357–363
- Roland, J., Britzen, S., Kudryavtseva, N. A., Witzel, A., Karouzos, M., 2008, Modeling nuclei of radio galaxies from VLBI radio observations. Application to the BL Lac Object S5 1803+784, *A&A*, 483, 125–135, [arXiv:0805.2832](#)
- Roland, J., Britzen, S., Witzel, A., Zensus, J. A., 2009, The origin of intrinsic variability of intraday variable sources, *A&A*, 496, 645–651
- Romero, G. E., Chajet, L., Abraham, Z., Fan, J. H., 2000, Beaming and precession in the inner jet of 3C 273 — II. The central engine, *A&A*, 360, 57–64
- Romero, G. E., Fan, J.-H., Nuza, S. E., 2003, The Binary Black Hole Scenario for the BL Lacertae Object AO<sup>2</sup>0235+16, *Chinese Journal of Astronomy and Astrophysics*, 3, 513–525, [arXiv:astro-ph/0312197](#)
- Roos, N., Kaastra, J. S., Hummel, C. A., 1993, A massive binary black hole in 1928 + 738?, *ApJ*, 409, 130–133
- Ross, R. R., Fabian, A. C., Young, A. J., 1999, X-ray reflection spectra from ionized slabs, *MNRAS*, 306, 461–466, [arXiv:astro-ph/9902325](#)
- Rowan-Robinson, M., Clegg, P. E., Beichman, C. A., Neugebauer, G., Soifer, B. T., Aumann, H. H., Beintema, D. A., Boggess, N., Emerson, J. P., Gautier, T. N., Gillett, F. C., Hauser, M. G., Houck, J. R., Low, F. J., Walker, R. G., 1984, The IRAS minisurvey, *ApJ*, 278, L7–L10
- Rybicki, G. B., Lightman, A. P., 1979, *Radiative processes in astrophysics*, New York, Wiley-Interscience, 1979. 393 p.
- Rybicki, G. B., Lightman, A. P., 1986, *Radiative Processes in Astrophysics*
- Ryle, M., Windram, M. D., 1968, The radio emission from galaxies in the Perseus cluster, *MNRAS*, 138, 1–+
- Salpeter, E. E., 1964, Accretion of Interstellar Matter by Massive Objects., *ApJ*, 140, 796–800
- Sánchez, S. F., González-Serrano, J. I., 2003, The near-infrared properties of the host galaxies of radio quasars, *A&A*, 406, 435–451, [arXiv:astro-ph/0305293](#)
- Sanders, D. B., Mirabel, I. F., 1996, Luminous Infrared Galaxies, *ARA&A*, 34, 749–+
- Sanders, D. B., Soifer, B. T., Elias, J. H., Neugebauer, G., Matthews, K., 1988, Warm ultraluminous galaxies in the IRAS survey - The transition from galaxy to quasar?, *ApJ*, 328, L35–L39
- Savolainen, T., Homan, D. C., Hovatta, T., Kadler, M., Kovalev, Y. Y., Lister, M. L., Ros, E., Zensus, J. A., 2010, Relativistic beaming and gamma-ray brightness of blazars, *A&A*, 512, A24+, [0911.4924](#)

- Schlegel, D. J., Finkbeiner, D. P., Davis, M., 1998, Maps of Dust Infrared Emission for Use in Estimation of Reddening and Cosmic Microwave Background Radiation Foregrounds, *ApJ*, 500, 525–+, [arXiv:astro-ph/9710327](https://arxiv.org/abs/astro-ph/9710327)
- Schmidt, M., 1963, 3C 273 : A Star-Like Object with Large Red-Shift, *Nature*, 197, 1040–+
- Schmitt, H. R., 2001, The Frequency of Active and Quiescent Galaxies with Companions: Implications for the Feeding of the Nucleus, *AJ*, 122, 2243–2256, [arXiv:astro-ph/0110235](https://arxiv.org/abs/astro-ph/0110235)
- Schödel, R., Ott, T., Genzel, R., et al., 2002, A star in a 15.2-year orbit around the supermassive black hole at the centre of the Milky Way, *Nature*, 419, 694–696, [arXiv:astro-ph/0210426](https://arxiv.org/abs/astro-ph/0210426)
- Schramm, K.-J., Borgeest, U., Camenzind, M., et al., 1993, Recent activity in the optical and radio lightcurves of the blazar 3C 345: indications for a 'lighthouse effect' due to jet rotation, *A&A*, 278, 391–405
- Searle, L., Zinn, R., 1978, Compositions of halo clusters and the formation of the galactic halo, *ApJ*, 225, 357–379
- Sesana, A., Haardt, F., Madau, P., Volonteri, M., 2005, The Gravitational Wave Signal from Massive Black Hole Binaries and Its Contribution to the LISA Data Stream, *ApJ*, 623, 23–30, [arXiv:astro-ph/0409255](https://arxiv.org/abs/astro-ph/0409255)
- Seyfert, C. K., 1943, Nuclear Emission in Spiral Nebulae., *ApJ*, 97, 28–+
- Shakura, N. I., Sunyaev, R. A., 1973, Black holes in binary systems. Observational appearance., *A&A*, 24, 337–355
- Shields, J. C., 1992, Normal O stars in dense media generate LINERs, *ApJ*, 399, L27–L30
- Shklovsky, I. S., 1953, *Radioastronomiia*.
- Sikora, M., Madejski, G., 2000, On Pair Content and Variability of Subparsec Jets in Quasars, *ApJ*, 534, 109–113, [arXiv:astro-ph/9912335](https://arxiv.org/abs/astro-ph/9912335)
- Sikora, M., Begelman, M. C., Rees, M. J., 1994, Comptonization of diffuse ambient radiation by a relativistic jet: The source of gamma rays from blazars?, *ApJ*, 421, 153–162
- Sikora, M., Begelman, M. C., Madejski, G. M., Lasota, J., 2005, Are Quasar Jets Dominated by Poynting Flux?, *ApJ*, 625, 72–77, [arXiv:astro-ph/0502115](https://arxiv.org/abs/astro-ph/0502115)
- Silk, J., Rees, M. J., 1998, Quasars and galaxy formation, *A&A*, 331, L1–L4, [arXiv:astro-ph/9801013](https://arxiv.org/abs/astro-ph/9801013)
- Sillanpaa, A., Haarala, S., Valtonen, M. J., Sundelius, B., Byrd, G. G., 1988, OJ 287 - Binary pair of supermassive black holes, *ApJ*, 325, 628–634

- Simon, R. S., Hall, J., Johnston, K. J., Spencer, J. H., Waak, J. A., Mutel, R. L., 1988, Superluminal motion toward a stationary knot in the radio core of the quasar 3C 395, *ApJ*, 326, L5–L8
- Skrutskie, M. F., Cutri, R. M., Stiening, R., et al., 2003, The 2MASS Extended sources (IPAC/UMass, 2003-2006), *VizieR Online Data Catalog*, 7233, 0–+
- Skrutskie, M. F., Cutri, R. M., Stiening, R., et al., 2006, The Two Micron All Sky Survey (2MASS), *AJ*, 131, 1163–1183
- Smail, I., Ivison, R. J., Gilbank, D. G., Dunlop, J. S., Keel, W. C., Motohara, K., Stevens, J. A., 2003, A SCUBA Galaxy in the Protocluster around 53W002 at  $z=2.4$ , *ApJ*, 583, 551–558, [arXiv:astro-ph/0210183](https://arxiv.org/abs/astro-ph/0210183)
- Smith, A. G., Nair, A. D., 1995, Timescales of Long-Term Optical Base-Level Fluctuations in Three Classes of AGN, *PASP*, 107, 863–+
- Smith, A. G., Nair, A. D., Leacock, R. J., Clements, S. D., 1993, The longer optical time scales of a large sample of quasars, *AJ*, 105, 437–455
- Snellen, I. A. G., Bremer, M. N., Schilizzi, R. T., Miley, G. K., 1996, Near-infrared imaging of gigahertz-peaked-spectrum radio galaxies: tracing the evolution of giant ellipticals?, *MNRAS*, 283, L123–L126
- Snellen, I. A. G., Lehnert, M. D., Bremer, M. N., Schilizzi, R. T., 2003, Fundamental galaxy parameters for radio-loud active galactic nuclei and the black hole-radio power connection, *MNRAS*, 342, 889–900, [arXiv:astro-ph/0209380](https://arxiv.org/abs/astro-ph/0209380)
- Sol, H., Pelletier, G., Asseo, E., 1989, Two-flow model for extragalactic radio jets, *MNRAS*, 237, 411–429
- Springel, V., White, S. D. M., Jenkins, A., Frenk, C. S., Yoshida, N., Gao, L., Navarro, J., Thacker, R., Croton, D., Helly, J., Peacock, J. A., Cole, S., Thomas, P., Couchman, H., Evrard, A., Colberg, J., Pearce, F., 2005, Simulations of the formation, evolution and clustering of galaxies and quasars, *Nature*, 435, 629–636, [arXiv:astro-ph/0504097](https://arxiv.org/abs/astro-ph/0504097)
- Stanghellini, C., O’Dea, C. P., Baum, S. A., Laurikainen, E., 1993, Optical CCD imaging of GHz-peaked-spectrum radio sources, *ApJS*, 88, 1–21
- Steffen, W., 1997, Signatures of helical jets, *Vistas in Astronomy*, 41, 71–78, [arXiv:astro-ph/9611133](https://arxiv.org/abs/astro-ph/9611133)
- Steffen, W., Krichbaum, T. P., Britzen, S., Witzel, A., 1995a, 1803+78: A Helical Core Jet, in *The XXVIIth Young European Radio Astronomers Conference*, (Ed.) D. A. Green & W. Steffen, pp. 29–+
- Steffen, W., Zensus, J. A., Krichbaum, T. P., Witzel, A., Qian, S. J., 1995b, A helical model for the compact jet in 3C345., *A&A*, 302, 335–+, [arXiv:astro-ph/9505075](https://arxiv.org/abs/astro-ph/9505075)
- Stickel, M., Fried, J. W., Kuehr, H., 1993, The complete sample of 1 Jy BL Lac objects. II - Observational data, *A&AS*, 98, 393–442

- Stickel, M., Rieke, G. H., Kuehr, H., Rieke, M. J., 1996, Flat-Spectrum Radio Sources with Faint Optical Counterparts, *ApJ*, 468, 556–+
- Stone, J. M., Pringle, J. E., 2001, Magnetohydrodynamical non-radiative accretion flows in two dimensions, *MNRAS*, 322, 461–472, [arXiv:astro-ph/0009233](https://arxiv.org/abs/astro-ph/0009233)
- Surace, J. A., 1998, A High-Resolution Near-Infrared Study of the Evolutionary Link Between Ultraluminous Infrared Galaxies and Optical QSOS, Ph.D. thesis, Institute for Astronomy University of Hawaii 2680 Woodlawn Dr. Honolulu, HI 96822
- Takalo, L. O., Kidger, M. R., de Diego, J. A., Sillanpaa, A., Nilsson, K., 1992, Near infrared monitoring of a sample of blazars with the Carlos Sanchez Telescope., *AJ*, 104, 40–52
- Tavani, M., Barbiellini, G., Argan, A., et al., 2008, The AGILE space mission, *Nuclear Instruments and Methods in Physics Research A*, 588, 52–62, [0807.4254](https://arxiv.org/abs/0807.4254)
- Tavecchio, F., Ghisellini, G., 2008, Structured jets and VHE emission of blazars and radiogalaxies, *ArXiv e-prints*, [0810.0134](https://arxiv.org/abs/0810.0134)
- Taylor, G. B., Vermeulen, R. C., Readhead, A. C. S., Pearson, T. J., Henstock, D. R., Wilkinson, P. N., 1996, A Complete Flux-Density-limited VLBI Survey of 293 Flat-Spectrum Radio Sources, *ApJS*, 107, 37–+
- Taylor, G. B., Silver, C. S., Ulvestad, J. S., Carilli, C. L., 1999, The Starburst in the Central Kiloparsec of Markarian 231, *ApJ*, 519, 185–190, [arXiv:astro-ph/9902082](https://arxiv.org/abs/astro-ph/9902082)
- Terlevich, R., Melnick, J., 1985, Warmers - The missing link between Starburst and Seyfert galaxies, *MNRAS*, 213, 841–856
- Teshima, M., The MAGIC Collaboration, 2008, MAGIC discovers VHE gamma ray emission from the blazar S50716+714, *The Astronomer's Telegram*, 1500, 1–+
- Thompson, D., Mannucci, F., Beckwith, S. V. W., 1996, A Narrowband Imaging Survey for High Redshift Galaxies in the Near Infrared, *AJ*, 112, 1794–+, [arXiv:astro-ph/9610135](https://arxiv.org/abs/astro-ph/9610135)
- Tran, H. D., 2001, Hidden Broad-Line Seyfert 2 Galaxies in the CFA and 12  $\mu$ M Samples, *ApJ*, 554, L19–L23, [arXiv:astro-ph/0105462](https://arxiv.org/abs/astro-ph/0105462)
- Tsuboi, M., 2008, VSOP2/ASTRO-G project, *Journal of Physics Conference Series*, 131, 012048–+, [0809.3350](https://arxiv.org/abs/0809.3350)
- Turner, T. J., 1999, X-Ray Observations of Markarian 231, *ApJ*, 511, 142–148, [arXiv:astro-ph/9808090](https://arxiv.org/abs/astro-ph/9808090)
- Tyson, J. A., 1986, Galaxy clustering in QSO fields at  $Z = 1-1.5$  - Evidence for galaxy luminosity evolution, *AJ*, 92, 691–699
- Ulvestad, J. S., Wrobel, J. M., Carilli, C. L., 1999a, Radio Continuum Evidence for Outflow and Absorption in the Seyfert 1 Galaxy Markarian 231, *ApJ*, 516, 127–140, [arXiv:astro-ph/9901190](https://arxiv.org/abs/astro-ph/9901190)



- Ulvestad, J. S., Wrobel, J. M., Roy, A. L., Wilson, A. S., Falcke, H., Krichbaum, T. P., 1999b, Subrelativistic Radio Jets and Parsec-Scale Absorption in Two Seyfert Galaxies, *ApJ*, 517, L81–L84, [arXiv:astro-ph/9903378](#)
- Urrutia, T., Lacy, M., Becker, R. H., 2008, Evidence for Quasar Activity Triggered by Galaxy Mergers in HST Observations of Dust-reddened Quasars, *ApJ*, 674, 80–96, [arXiv:0709.2805](#)
- Urry, C. M., Padovani, P., 1995, Unified Schemes for Radio-Loud Active Galactic Nuclei, *PASP*, 107, 803–+, [arXiv:astro-ph/9506063](#)
- Urry, C. M., Scarpa, R., O’Dowd, M., Falomo, R., Pesce, J. E., Treves, A., 2000, The Hubble Space Telescope Survey of BL Lacertae Objects. II. Host Galaxies, *ApJ*, 532, 816–829, [arXiv:astro-ph/9911109](#)
- Valtonen, M. J., 2007, New Orbit Solutions for the Precessing Binary Black Hole Model of OJ 287, *ApJ*, 659, 1074–1081
- Valtonen, M. J., Lehto, H. J., Pietilä, H., 1999, Probing the jet in the binary black hole model of the quasar OJ287, *A&A*, 342, L29–L31
- Veilleux, S., Kim, D., Sanders, D. B., Mazzarella, J. M., Soifer, B. T., 1995, Optical Spectroscopy of Luminous Infrared Galaxies. II. Analysis of the Nuclear and Long-Slit Data, *ApJS*, 98, 171–+
- Veilleux, S., Kim, D., Sanders, D. B., 1999, Optical Spectroscopy of the IRAS 1 JY Sample of Ultraluminous Infrared Galaxies, *ApJ*, 522, 113–138, [arXiv:astro-ph/9904149](#)
- Vermeulen, R. C., 1995, Superluminal Sources, *Proceedings of the National Academy of Science*, 92, 11 385–11 389
- Vermeulen, R. C., Cohen, M. H., 1994, Superluminal motion statistics and cosmology, *ApJ*, 430, 467–494
- Vermeulen, R. C., Britzen, S., Taylor, G. B., Pearson, T. J., Readhead, A. C. S., Wilkinson, P. N., Browne, I. W. A., 2003, Motion Statistics in the CJ Survey - The Status in October 2002, in *Radio Astronomy at the Fringe*, (Eds.) J. A. Zensus, M. H. Cohen, E. Ros, vol. 300 of *Astronomical Society of the Pacific Conference Series*, pp. 43–+
- Villani, D., di Serego Alighieri, S., 1999, Infrared imaging of WENSS radio sources, *A&AS*, 135, 299–317, [arXiv:astro-ph/9812126](#)
- Virani, S. N., De Robertis, M. M., VanDalsen, M. L., 2000, A CCD Study of the Environment of Seyfert Galaxies. III. Host Galaxies and the Nearby Environments, *AJ*, 120, 1739–1749, [arXiv:astro-ph/0007030](#)
- von Montigny, C., Bertsch, D. L., Chiang, J., et al., 1995, High-Energy Gamma-Ray Emission from Active Galaxies: EGRET Observations and Their Implications, *ApJ*, 440, 525–+

- Wagner, S. J., Witzel, A., 1995, Intraday Variability In Quasars and BL Lac Objects, *ARA&A*, 33, 163–198
- Wagner, S. J., Camenzind, M., Dreissigacker, O., Borgeest, U., Britzen, S., Brinkmann, W., Hopp, U., Schramm, K., von Linde, J., 1995, Simultaneous optical and gamma-ray flaring in PKS 0420-014. Implications for emission processes and rotating jet models., *A&A*, 298, 688–+
- Wagner, S. J., Witzel, A., Heidt, J., Krichbaum, T. P., Qian, S. J., Quirrenbach, A., Wegner, R., Aller, H., Aller, M., Anton, K., Appenzeller, I., Eckart, A., Kraus, A., Naundorf, C., Kneer, R., Steffen, W., Zensus, J. A., 1996, Rapid Variability in S5 0716+714 Across the Electromagnetic Spectrum, *AJ*, 111, 2187–+
- Walker, R. C., 1986, Very long baseline interferometry., in *Synthesis Imaging*, (Ed.) R. A. Perley, F. R. Schwab, & A. H. Bridle, pp. 189–213
- Walker, R. C., Benson, J. M., Unwin, S. C., Lystrup, M. B., Hunter, T. R., Pilbratt, G., Hardee, P. E., 2001, The Structure and Motions of the 3C 120 Radio Jet on Scales of 0.6-300 Parsecs, *ApJ*, 556, 756–772, [arXiv:astro-ph/0103379](https://arxiv.org/abs/astro-ph/0103379)
- Wardle, J. F. C., Homan, D. C., Ojha, R., Roberts, D. H., 1998, Electron-positron jets associated with the quasar 3C279, *Nature*, 395, 457–461
- Webb, J. R., Smith, A. G., Leacock, R. J., Fitzgibbons, G. L., Gombola, P. P., Shepherd, D. W., 1988, Optical observations of 22 violently variable extragalactic sources - 1968-1986, *AJ*, 95, 374–397
- West, M. J., 1991, Superclustering at high redshifts, *ApJ*, 379, 19–36
- White, R. A., Bliton, M., Bhavsar, S. P., Bornmann, P., Burns, J. O., Ledlow, M. J., Loken, C., 1999, A Catalog of Nearby Poor Clusters of Galaxies, *AJ*, 118, 2014–2037, [arXiv:astro-ph/9907283](https://arxiv.org/abs/astro-ph/9907283)
- White, R. L., Becker, R. H., 1992, A new catalog of 30,239 1.4 GHz sources, *ApJS*, 79, 331–467
- Whitney, A. R., Shapiro, I. I., Rogers, A. E. E., Robertson, D. S., Knight, C. A., Clark, T. A., Goldstein, R. M., Marandino, G. E., Vandenberg, N. R., 1971, Quasars Revisited: Rapid Time Variations Observed Via Very-Long-Baseline Interferometry, *Science*, 173, 225–230
- Witzel, A., 1987, Superluminal motion and other indications of bulk relativistic motion in a complete sample of radio sources from the S5 survey, in *Superluminal Radio Sources*, (Ed.) J. A. Zensus & T. J. Pearson, pp. 83–93
- Woo, J.-H., Urry, C. M., 2002, Active Galactic Nucleus Black Hole Masses and Bolometric Luminosities, *ApJ*, 579, 530–544, [arXiv:astro-ph/0207249](https://arxiv.org/abs/astro-ph/0207249)
- Wright, S. C., McHardy, I. M., Abraham, R. G., Crawford, C. S., 1998, Near-infrared imaging of the host galaxies of BLLacertae objects, *MNRAS*, 296, 961–976

- Wu, X.-B., Liu, F. K., Zhang, T. Z., 2002, Supermassive black hole masses of AGNs with elliptical hosts, *A&A*, 389, 742–751, [arXiv:astro-ph/0203158](#)
- Wu, X.-P., Han, J., 1995, A search for associations of distant radio-bright quasars with Abell clusters: an effect of gravitational amplification bias?, *MNRAS*, 272, 705–709, [arXiv:astro-ph/9408087](#)
- Xie, G. Z., Zhang, X., Bai, J. M., Xie, Z. H., 1998, Gamma-Ray and Near-Infrared Emission from Gamma-Ray-loud Blazars, *ApJ*, 508, 180–185
- Xie, G. Z., Zhou, S. B., Dai, B. Z., Liang, E. W., Li, K. H., Bai, J. M., Xing, S. Y., Liu, W. W., 2002, Photometric monitoring of 12 BL Lacertae objects, *MNRAS*, 329, 689–699
- Xie, G. Z., Zhou, S. B., Liang, E. W., 2004, The Mass-Luminosity Relation, Accretion Rate-Luminosity Relation, and Evolutionary Sequence of Blazars, *AJ*, 127, 53–57
- Xie, G.-Z., Chen, L.-E., Xie, Z.-H., Ma, L., Zhou, S.-B., 2005, AGN Black Hole Masses and Methods to Estimate the Mass, *PASJ*, 57, 183–186
- Yokosawa, M., Inoue, M., 1985, Binary galaxy model for wiggling radio jets and its application to 3C 75, *PASJ*, 37, 655–667
- Yuan, T., Kewley, L. J., Sanders, D. B., 2010, The Role of Starburst-Active Galactic Nucleus Composites in Luminous Infrared Galaxy Mergers: Insights from the New Optical Classification Scheme, *ApJ*, 709, 884–911, [0911.3728](#)
- Zamorani, G., Maccacaro, T., Giommi, P., Tananbaum, H., 1984, X-ray variability of quasars, *ApJ*, 278, 28–36
- Zel'Dovich, Y. B., 1964, The Fate of a Star and the Evolution of Gravitational Energy Upon Accretion, *Soviet Physics Doklady*, 9, 195–+
- Zensus, J. A., Pearson, T. J., 1990, Book-Review - Parsec-Scale Radio Jets, *Journal of the British Astronomical Association*, 100, 316–+
- Zensus, J. A., Cohen, M. H., Unwin, S. C., 1995, The Parsec-scale jet in quasar 3C 345, *ApJ*, 443, 35–53
- Zensus, J. A., Ros, E., Kadler, M., Kellermann, K. I., Lister, M. L., Homan, D. C., Cohen, M. H., Vermeulen, R. C., 2003, The 2 cm VLBA Survey, in *Radio Astronomy at the Fringe*, (Ed.) J. A. Zensus, M. H. Cohen, & E. Ros, vol. 300 of *Astronomical Society of the Pacific Conference Series*, pp. 27–+
- Zhang, X., Xie, G. Z., Bai, J. M., 1998, A historical light curve of 3C 345 and its periodic analysis, *A&A*, 330, 469–473
- Zhao, J., Burns, J. O., Norman, M. L., Sulkanen, M. E., 1992, Instabilities in astrophysical jets. II - Numerical simulations of slab jets, *ApJ*, 387, 83–94

## Bibliography

---

Zier, C., 2007, Merging of a massive binary due to ejection of bound stars - II, MNRAS, 378, 1309–1327

Zwicky, F., Herzog, E., Wild, P., 1966, Catalogue of galaxies and of clusters of galaxies, Vol. 3

Zwicky, F., Herzog, E., Wild, P., 1968, Catalogue of galaxies and of clusters of galaxies, Pasadena: California Institute of Technology (CIT), 1961-1968

# Acknowledgements

Given that an Oscar<sup>TM</sup> acceptance speech is not in my foreseeable future, this is probably the next best thing<sup>2</sup>. I always thought my acceptance speech would start with something like "Oh my, this is so unexpected!" but this does not quite fit the current context. This PhD work has been the result of 3 years of, occasionally hard, work, almost constant stress, intermittent hope, and relentless questioning of one's motives, progress, and future prospects. Then I thought I would go on to thank God, some higher power, or an otherwise supernatural entity. However, since I firmly believe in self-disposition and one's power over one's life, I think I will skip that part too. Then would come the part of me thanking a list of people that in one way or another have contributed to my "success". This part I want to keep and expand. When I started this PhD I was not at all sure what to expect, from the PhD itself, from my colleagues, from science, from the future. I guess I had a notion of how things would turn out, but I can safely say that that notion I had was...how can I put this politely...well, it was a bit (or a lot) off. I guess it sounds cliché to say, but this PhD could not have come to fruition without the contribution of a host of people. In the following I would like to mention a few of them.

When I first came to Germany, I heard of the concept of a Doktorvater. I always wondered, given my supervisor, Silke Britzen, whether she would be called my Doktormutter. It is a very interesting, and quite true, concept, that of an almost familial connection between a senior<sup>3</sup> scientist and a doctorate student. Aside from that however, I wouldn't be here today without Silke. Silke believed in me when I myself did not and supported my dream to become an astronomer when I thought that there was no support to be found. Back in 2006, when for the first time I marched into her AGN seminar and, although there were only master students there, I decided to stay, she welcomed me. It was she who for the first time introduced me to the, back then, wild concept of binary black holes and was the one that nurtured my interest in science by offering a way to pursue it. This work has benefited from her input, her ideas, her scientific insight and knowledge. I need to thank Silke for three years of scientific exchange, of long lectures on why my introductions should not take up 20 slides of a 30-slide talk, of lengthy discussions on how to focus on the smaller, individual questions than swamping one's self by the big whys and hows, of ups and downs, of self-doubting, of happy, sad, angry, funny, frustrating moments, of...well, I need to thank her for three years of life, nothing more, nothing less<sup>4</sup>. I can only hope that after these three years she feels that her trust, energy, and effort were well placed on me. It was certainly a pleasure being her student and I can only hope that this

---

<sup>2</sup>A Nobel<sup>TM</sup> prize excluded, of course!

<sup>3</sup>Meant here in the most complimenting way possible!

<sup>4</sup>...and all of this in German!!! Thank you Silke for putting up with my some times challenged German.

PhD work is just the basis for a fruitful collaboration for many years to come!

I guess the next thank you goes to my family. I dedicated this PhD to them, because without them, my mother, my father, and my siblings, I just wouldn't be here. I would need 200 pages more to thank them properly, but given the current costs of printing and the alarmingly fast rate of deforestation I will try to be brief. First of all I have to thank my mother, Beky, because she has always told me that I can be anything I want to be. She has been my number 1. fan since my birth and has always supported me in any way she could. Her path in life, her accomplishments, and her attitude towards things has been an inspiration to me and has shown me the infinite reservoirs of strength and determination hidden in each of us. I can only hope that I'm made of the same "Stoff" that she is made of. She is my inspiration, my supporter, and a deep well of curiosity and natural inquisitiveness<sup>5</sup> that has been partially instilled in me. I need to thank my father too, because he has always been my anchor to reality. He is the balancing force that prevents me from floating away into the horizon. His quiet strength and good will have taught me that there are more than one ways of making one's point, of bridging gaps, and of going through life with your head up. His love and unflinching support have always been some of the constants in my life (pretty much like  $c$ ). Of course, I have also been blessed with having two wonderful siblings, without whom my life would simply be incomplete and downright boring! My sister, Katerina, has always been the pioneer in this family (when it comes to academia), paving the way and making it so much easier to follow in her steps. Her sensitivity, her intelligence, her devotion to her science, and her sense of being have all been both an inspiration and ultimately an aim for me, both as a scientist and as a person. I have to thank her for all the long discussions on life, science, love, friendship, Edith Piaf, Elli Kokkinou, and everything in between. I also have to thank her for my first contact with Germany, the wonderful breakfasts, that one fateful night in Wuppertal many many years ago, the amazing summer vacations, and everything that has partly made me into who I am today. Finally, a big thank you goes out to my brother, Nikos, and his family, Pinelopi, Paulina, and Apollonas. They have been a second family for me. A model for what I would like to have one day and a promise of an achievable happiness. I want to thank my brother in particular for infecting me with the computer-worm, without which I would have faced huge difficulties with my work. I also want to thank him for being a living example of the constant struggle and victory over life's hardships. Finally I want to thank him for all the weekends spent at his place watching movies and eating like pigs...<sup>6</sup>. Although not a perfect family by any measure, I wouldn't change it for anything in the world! I love you all.

Next in line would be my "extended family". In particular three very special people that have made my stay in Bonn what it has been. First and foremost Mar Mezcuca. Mar, I really do not think I can find the proper words to thank you for everything. You have offered me so much, asking so little in return. From the first, obviously in hindsight fateful, moment that I approached you as the PhD student representative to now, we have shared so many things that is impossible to include here<sup>7</sup>. Your constant support and

---

<sup>5</sup>Thank you for the relentless questioning concerning all the different aspects of my work and for insisting that I explain to you even the most complicated notions of astronomy! You have helped me to "keep it simple".

<sup>6</sup>It's your fault I'm on a constant diet! I'll send you the bill for the gym.

<sup>7</sup>Well, I could share some: salsa dancing, swimming, climbing, hiking, clubbing, cooking, watching

persevering wave of happiness have helped me stay sane throughout many different trials. Your unquenchable thirst for activities has motivated me to "keep walking" and your constant nagging about me not eating pop corn has helped me fit in my pants for all these years. Aside from all the time lost in idle chit-chat and dance improv outside my door as a result of you moving next to my office (shhhh...don't tell anyone), you have been a reason for starting every morning in the office with a smile. Particular thanks is due for accepting the daunting task of reading this manuscript (along with any other proposal, application, paper, poster, or post-it note that I've written while here in Bonn) and giving me several corrections, comments, insights, and ideas. Apart from a best friend, you have also been a scientific companion in this journey of knowledge. OK, that's enough compliments. You know I like you...My only complaint would be that you haven't been here since my first year!

Chin Shin Chang. What should I say about you? Xie xie I guess. You have been by my side since day one (well almost day one...more like day 70 something) and (almost) never left. I have to thank you for being a soul match in so many ways. I have also to thank you for all those evenings and dinners<sup>8</sup> either at my place or yours, with Billie Holiday playing in the background and us discussing about anything and everything. I need also mention our common musical career and the many extremely amusing hours spent trying to coordinate our four hands on the same piano. You have been an inspiration for your dedication to your duties, your sense of rhythm, and your attitude towards life. Finally, I want to also thank you for the last few months of our PhD, which we spent in the same office, writing our thesis together. It made the long hours seem a bit shorter. It was a pleasure knowing you, and I'll be sure to send you some post-cards in the future...

Finally, Filomena Volino, you have earned your place in this acknowledgments. I have you to thank for always being a voice of conscience, a strict but fair judge, and a funny person (especially that...!). Our discussions about democracy have been thoroughly inspiring and have always made me feel like a small dictator. The time that we shared as student representatives has left me with many fond memories! So, grazie mille for being who you are, for teaching me some Italian, and for showing me how carbonara is supposed to be made. You have always been a telephone or an email away and I hope that you will stay that way in the future too. Oh...and sorry for always having some problems with your birthdays. I assure you, it was not intentional!

Since this acknowledgements are starting to become dangerously long, I will have to try and compress my thank yous to many people. I want to sincerely thank all my office mates throughout these three years: Violeta (thanks for pushing me to go to all the "group events" and making me socialize with people), Elena (thanks for all the sweets and thanks for introducing me to Giovanni Allevi), Giannis (thanks for a bit of Greek in an ocean of English), Liu Yi (xie xie for a wonderful moon-cake), Christian (danke für unsere wissenschaftliche Diskussionen und für Deine Fragen!), Chin Shin (see above). Then there is a large number of people whose company has been indispensable throughout these three years: Yoon, Luciano, Laura, Nadia, Seungkyung, Kazi, Herbie, Luis, Amir, Michelle, Leuteris, Gayoung, Sophia, Despina, Simone, Felipe, Fatemeh, Manolo, John,

---

movies, German course buddy, test-talk audience, morning gossiper, afternoon gossiper (!), procrastination buddy, travel buddy (London rules!), PhD representative, conference co-organizer, OC co-member, etc.

<sup>8</sup>You and your appetite have consistently sabotaged Mar's efforts to keep me away from pop corn or other not so healthy food. Two words: sushi buffet...

Brenda, Xiu, Rusen, Kosmas, Simone, Veronika, Manolis, Kiril, Frank, Arturo, Nicola, John, Devaky, Mohammad, Gunther, Peng, Esteban, Sibylle, and many others that I'm sure I'm forgetting now. I want to especially thank Simone Bernhardt for helping me out with writing the German summary of this thesis and for so skillfully accompanying my piano with her accordion!

Slowly coming closer to the end, I want to take this chance to sincerely thank my director Prof. Anton Zensus and Prof. Eduardo Ros, the IMPRS Coordinator at the time of my arrival in the MPIfR, for trusting me and for offering their support throughout these years. I would also like to thank Dr. Manolis Angelakis for always having an open ear for the troubles of PhD students and for an excellent collaboration during our overlap as an IMPRS Coordinator (him) and PhD student representative (me). I would especially like to thank Prof. Zensus, as well as Prof. Andreas Eckart for being the official supervisors of my PhD. In addition I would like to thank Prof. Claus Kiefer for kindly accepting to be the chair of my PhD defense and one of the referees of my PhD thesis. I want to sincerely thank Profs. Nektarios Vlahakis and Apostolos Mastichiadis, who supported and encouraged me during my first baby steps in astrophysics as an undergrad student in the Department of Physics at the National and Kapodistrian University of Athens. I would also like to thank a number of colleagues inside and outside the MPIfR for our direct and indirect interactions inside our working environment, in particular: Prof. Wagner Steffen, Dr. Richard Porcas, Dr. Arno Witzel, Dr. Thomas Krichbaum, Dr. Eduardo Ros, Dr. Jens Zuther, Prof. Jacques Roland, Prof. Biping Gong, Dr. Andrei Lobanov, and Dr. James Anderson. I would finally like to note my thank you for the secretaries that have made my stay in the MPIfR as smooth as possible: Frau Gabi Breuer, Frau Beate Naunheim, Frau Astrid Lebehl, as well as the IMPRS Assistant, Frau Simone Pott.

Last but not least, I want to thank one of my best friends, whom I have known since high school, Iliana. Special thanks are due not only because of the beautiful friendship between us for the last almost 10 years, but also because she is probably the reason why I'm here today. I thank you Iliana for urging me to apply for the Erasmus scholarship that eventually brought me to Bonn and to the MPIfR. Thank you for promising that we would undertake the step of going abroad together, so that I found the inner strength to defy my insecurities and leave Athens for Bonn, although in the end you didn't follow, as originally planned. I moreover thank you for being a phone call away (sorry I haven't called as often as I should have) whenever I needed someone to vent, to complain, to relate my happiness or my sorrow, to gossip, or just to speak Greek with. Thanks for being one of the reasons to look forward to visiting Greece every time! More importantly thank you for showing me what true friendship means and for preparing me for all the wonderful friendships that I developed during these three years. I couldn't have done it without you...

Although these past three years in Bonn have not always been easy, they have by far surpassed my wildest dreams of what my PhD would be like. In the end, all the ups and downs aside, it has been so much fun! Thank you.

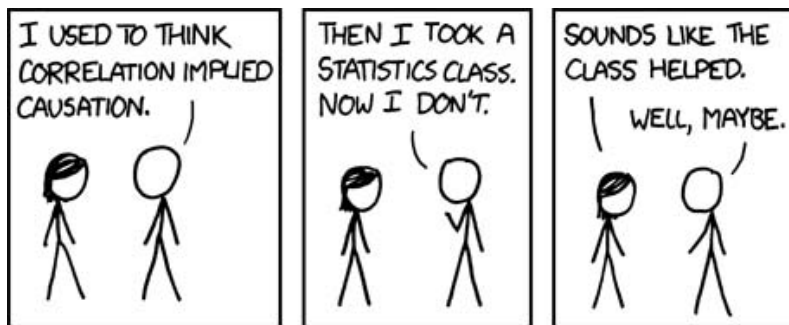
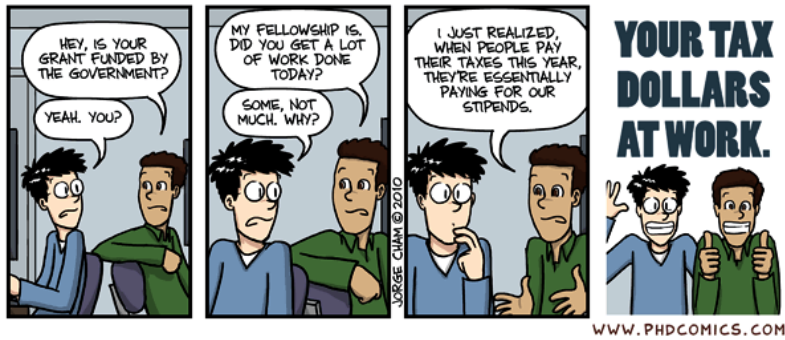
And now some scientific acknowledgements...I was supported for this research through a stipend from the International Max Planck Research School (IMPRS) for Astronomy and Astrophysics. I also want to acknowledge the very helpful comments from an anonymous



A&A referee that substantially improved part of Chap. 2. This research has made use of the NASA/IPAC Extragalactic Database (NED) which is operated by the Jet Propulsion Laboratory, California Institute of Technology, under contract with the National Aeronautics and Space Administration. This research has made use of NASA's Astrophysics Data System Bibliographic Services. This research has also made use of the VizieR service (Ochsenbein et al. 2000). The Very Long Baseline Array is operated by the USA National Radio Astronomy Observatory, which is a facility of the USA National Science Foundation operated under cooperative agreement by Associated Universities, Inc. This research has made use of the United States Naval Observatory (USNO) Radio Reference Frame Image Database (RRFID).

## PhD-adjacent...

Three years is a long time without some procrastination...I couldn't have done it without xkcd.com and phdcomics.com! Two examples<sup>9</sup>:



---

<sup>9</sup>PhD-related commentary intended!

# A AGN Evolution Tables

Table A.1: CJF sources observed and detected in the near infrared. Column (1) gives the IAU name of the source, Col. (2) the type of source (Q=Quasar, BL=BL Lac object, G=Radio Galaxy), Col. (3) the redshift  $z$ , Columns (4)-(6) fluxes in three different NIR bands, Col. (7) the relevant references (Table A.2), and Col. (8) gives the calculated spectral index in the NIR.

Source	Type	$z$	Near-IR			Reference	$\alpha_{NIR}$
			1.25 $\mu m$ (mJy)	1.65 $\mu m$ (mJy)	2.20 $\mu m$ (mJy)		
0022+390	Q	1.946			0.06 (0.03)	1	
0035+413	Q	1.353	0.64 (0.06)	0.75 (0.13)	1.37 (0.24)	2	-1.29
0108+388	G	0.669			0.14 (0.06)	3	
0133+476	Q	0.859	0.479 (0.02)	0.813 (0.04)	1.32 (0.04)	4	-1.74
0145+386	Q	1.442	0.40 (0.04)	0.68 (0.11)	0.30 (0.17)	2	0.55
0153+744	Q	2.388	0.93 (0.07)	1.29 (0.15)	1.96 (0.23)	2	-0.89
0219+428	BL	0.444	9.22 (0.25)	12.5 (0.4)	15.4 (1.1)	5, 9	-0.83
0249+383	Q	1.122			0.12 (0.03)	1	
0251+393	Q	0.289	0.70 (0.05)	0.79 (0.11)	1.21 (0.19)	2	-0.89
0316+413	G	0.018	46.5 (0.7)	57.8 (0.9)	55.70 (0.8)	6	-0.10
0344+405	G	0.039	17.8 (0.6)	26.0 (1.0)	20.0 (1.0)	7	0.26
0402+379	G	0.055	19.1 (1.8)	39.8 (2.6)	40 (3)	2	-0.38
0546+726	Q	1.555	0.84 (0.02)	1.24 (0.03)	0.91 (0.02)	2	0.03
0650+453	Q	0.933	0.33 (0.02)	0.49 (0.02)	0.84 (0.02)	2	-1.58
0651+410	G	0.022	46.6 (1.1)	57.0 (1.9)	48.0 (1.5)	7	0.03
0707+476	Q	1.292	13.2 (0.3)	10.9 (0.5)	7.4 (0.6)	2	1.08
0710+439	G	0.518			0.84 (0.19)	8	
0731+479	Q	0.782	0.58 (0.02)	0.52 (0.03)	0.67 (0.02)	2	-0.17
0733+597	G	0.041	43.2 (1.3)	52.3 (1.9)	45.1 (1.8)	7	-0.01
0814+425	BL	0.245	1.42 (0.04)	2.21 (0.06)	3.14 (0.07)	9	-1.34
0821+394	Q	1.216	0.77 (0.02)	1.15 (0.02)	1.45 (0.02)	2	-1.07
0824+355	Q	2.249			0.10 (0.06)	10	
0831+557	G	0.240	0.80	1.03	1.23	11	-0.72
0833+416	Q	1.298	0.36 (0.02)	0.43	0.35 (0.02)	2	0.09
0836+710	Q	2.180	1.00 (0.02)	1.30 (0.03)	1.50 (0.02)	2	-0.68
0847+379	G	0.407			0.63 (0.04)	10	
0923+392	Q	0.699	1.22 (0.06)	1.20 (0.12)	1.66 (0.22)	2	-0.53
0927+352	BL				0.81 (0.09)	10	
0945+664	G	0.850	0.030 (0.001)	0.005 (0.001)	0.08 (0.01)	12	-1.89

Continued on Next Page...

## A AGN Evolution Tables

Table A.1 – Continued

Source	Type	z	Near-IR			Reference	$\alpha_{NIR}$
			1.25 $\mu$ m (mJy)	1.65 $\mu$ m (mJy)	2.20 $\mu$ m (mJy)		
0954+658	BL	0.368		3.17		13	
1003+830	G	0.322	0.86 (0.13)	2.0 (0.4)	2.3 (0.4)	7	-1.67
1020+400	Q	1.254	0.74 (0.04)	1.00 (0.07)	1.53 (0.07)	2	-1.27
1030+415	Q	1.120	0.07	0.12	0.30	14	-2.56
1031+567	G	0.460			0.19 (0.13)	8	
1038+528	Q	0.677	0.65 (0.05)	0.42 (0.10)	0.84 (0.16)	2	-0.45
1058+726	Q	1.460	0.42 (0.02)	0.44 (0.02)	0.48 (0.03)	2	-0.20
1101+384	BL	0.031	71 (5)	81 (8)	83 (15)	9	-0.25
1124+455	Q	1.811	0.57 (0.01)	0.54 (0.02)	0.66 (0.02)	2	-0.25
1128+385	Q	1.733			0.32	14	
1144+402	Q	1.088	1.17 (0.06)	1.69 (0.15)	2.53 (0.25)	2	-1.35
1144+352	G	0.063	20.0 (0.8)	34.0 (1.3)	23.3 (1.5)	3	-0.24
1146+596	G	0.011	247 (2)	311 (5)	248 (8)	2	0.03
1226+373	Q	1.515	0.33 (0.02)	0.48 (0.02)	0.41 (0.03)	2	-0.36
1254+571	Q	0.042	62.0 (1.2)	113 (2)	199 (3)	15	-2.04
1306+360	Q	1.055	0.23 (0.02)	0.41 (0.02)	0.54 (0.02)	2	-1.49
1309+555	Q	0.926	0.65 (0.02)	0.93 (0.03)	1.36 (0.03)	2	-1.28
1333+459	Q	2.449	0.34 (0.05)	0.40 (0.11)	0.66 (0.20)	2	-1.15
1347+539	Q	0.980	0.47 (0.02)	0.53 (0.03)	0.65 (0.04)	2	-0.56
1413+373	Q	2.360	0.36 (0.02)	0.36 (0.02)	0.84 (0.03)	2	-1.50
1418+546	BL	0.151	6.68 (0.31)	9.2 (0.4)	11.8 (0.5)	9, 16	-0.99
1417+385	Q	1.832	0.41 (0.02)	0.52 (0.02)	0.66 (0.02)	2	-0.83
1432+422	Q	1.240	0.02		0.05	17	
1435+638	Q	2.068	1.10 (0.02)	1.00 (0.03)	1.40 (0.03)	2	-0.42
1442+637	Q	1.38	0.51 (0.02)	0.88 (0.02)	0.71 (0.02)	2	-0.56
1504+377	G	0.671	0.06 (0.01)	0.12 (0.01)	0.25 (0.02)	12	-2.62
1531+722	Q	0.899	1.25 (0.12)	2.0 (0.4)	1.7 (0.4)	7	-0.53
1622+665	G	0.201			3.3 (0.3)	18	
1633+382	Q	1.807			1.95 (0.07)	8, 19	
1637+574	Q	0.749	1.70 (0.02)	1.90 (0.02)	2.50 (0.03)	20	-0.67
1641+399	Q	0.595	3.23 (0.10)	5.08 (0.25)	7.5 (0.4)	2	-1.46
1652+398	BL	0.034	86.0 (2.0)	115.0 (2.0)	99.0 (2.0)	21, 9	-0.22
1656+477	Q	1.622	0.53 (0.02)	0.60 (0.03)	0.53	2	0.02
1700+685	G	0.301	0.64 (0.02)	1.00 (0.03)	1.60 (0.04)	2	-1.57
1716+686	Q	0.339	1.30	1.70	2.00	2	-0.73
1719+357	Q	0.263	0.83 (0.21)	1.6 (0.3)	2.8 (0.4)	7	-2.10
1726+455	Q	0.717	0.61 (0.02)	0.84 (0.03)	1.01 (0.03)	2	-0.86
1732+389	Q	0.970	0.26 (0.02)	0.49 (0.02)	0.77 (0.02)	2	-1.87
1744+557	G	0.031	66 (1)	80 (2)	66 (2)	22	0.05
1749+701	BL	0.770			2.2 (1.7)	16	
1755+578	Q	2.110	0.33 (0.02)	0.50 (0.02)	0.67 (0.03)	2	-1.20
1758+388	Q	2.092	0.43 (0.02)	0.38 (0.02)	0.49 (0.02)	2	-0.21
1803+784	BL	0.680	5.50 (0.25)	5.9 (0.4)	7.1 (0.8)	16, 9	-0.39
1800+440	Q	0.663	1.00	1.20	0.84 (0.02)	2	0.37
1807+698	BL	0.051	20.2 (0.9)	25.4 (1.1)	29.7 (2.7)	21, 9	-0.65
1826+796	G	0.224	1.10 (0.20)	1.3 (0.3)	1.9 (0.4)	7	-0.89
1823+568	BL	0.664			4.98	9, 23	

Continued on Next Page. . .

Table A.1 – Continued

Source	Type	z	<u>Near-IR</u>			Reference	$\alpha_{NIR}$
			1.25 $\mu m$ (mJy)	1.65 $\mu m$ (mJy)	2.20 $\mu m$ (mJy)		
1843+356	G	0.764			0.13 (0.09)	3	
1946+708	G	0.101	2.8 (0.3)	2.4 (0.5)	3.0 (0.5)	18	0.07
2116+818	Q	0.084	8.5 (0.4)	12.5 (0.6)	15.7 (0.7)	7	-0.95
2200+420	BL	0.069	38.4 (2.8)	53 (4)	71 (14)	2, 9	-0.80
2351+456	Q	1.986			0.63	8	
2352+495	G	0.237			0.9 (0.4)	8	

Table A.2: References for Table A.1.

Number	Reference	Number	Reference
1	Sánchez and González-Serrano (2003)	13	Wright et al. (1998)
2	Barkhouse and Hall (2001)	14	Carballo et al. (1998)
3	Snellen et al. (1996)	15	Sanders et al. (1988)
4	Bloom et al. (1994)	16	Padovani et al. (2006)
5	González-Pérez et al. (2001)	17	Puschell et al. (1982)
6	Jarrett et al. (2003)	18	Villani and di Serego Alighieri (1999)
7	Skrutskie et al. (2003)	19	Xie et al. (1998)
8	de Vries et al. (1998)	20	Neugebauer et al. (1986)
9	Fan and Lin (1999)	21	Golombek et al. (1988)
10	Lilly et al. (1985)	22	Knapp et al. (1990)
11	Heckman et al. (1983)	23	Kotilainen et al. (2005)
12	Stickel et al. (1996)		

Table A.3: CJF sources observed and detected in the optical regime as group or cluster members. Columns (1)-(3) as in Table A.1, Column (4) gives the reference for clustering (Table A.4).

Source	Type	z	Reference	Source	Type	z	Reference
0010+405	G	0.255	24	1038+528	Q	0.677	43
0014+813	Q	3.366	25	1101+384	BL	0.031	44
0153+744	Q	2.388	26	1144+352	G	0.063	45
0212+735	Q	2.367	26	1146+596	G	0.011	46
0219+428	BL	0.444	27	1150+812	Q	1.250	26
0309+411	Q	0.134	28	1213+350	Q	0.857	24
0316+413	G	0.018	29	1216+487	Q	1.076	26
0636+680	Q	3.174	30	1254+571	G	0.422	47
0651+410	G	0.022	31	1415+463	Q	1.552	38
0700+470	G		32	1435+638	Q	2.068	27
0710+439	G	0.518	24	1624+416	Q	2.550	39
0727+409	Q	2.500	33	1633+382	Q	1.807	38
0733+597	G	0.041	34	1636+473	Q	0.740	38
0821+394	Q	1.216	35	1637+574	Q	0.749	48
0831+557	G	0.240	36	1638+540	Q	1.977	49
0836+710	Q	2.180	24	1638+398	Q	1.660	41
0847+379	G	0.407	37	1642+690	Q	0.751	26
0850+581	Q	1.322	35	1641+399	Q	0.595	50
0859+470	Q	1.462	38	1652+398	BL	0.034	51
0923+392	Q	0.699	24	1716+686	Q	0.339	26
0945+408	Q	1.252	27	1744+557	G	0.031	31
0954+556	Q	0.909	39	1751+441	Q	0.871	26
0955+476	Q	1.873	40	1803+784	BL	0.680	27
1010+350	Q	1.414	41	1807+698	BL	0.051	44
1020+400	Q	1.254	38	2214+350	Q	0.510	52
1031+567	G	0.460	42				

Table A.4: References for Table A.3.

<b>Symbol</b>	<b>Reference</b>	<b>Symbol</b>	<b>Reference</b>
24	<a href="#">Geller et al. (1984)</a>	39	<a href="#">Wu and Han (1995)</a>
25	<a href="#">Chernomordik (1995)</a>	40	<a href="#">Condon et al. (1990)</a>
26	<a href="#">West (1991)</a>	41	<a href="#">Kim et al. (1991)</a>
27	<a href="#">Dobrzycki et al. (2002)</a>	42	<a href="#">O’Dea et al. (1996)</a>
28	<a href="#">Edge and Rottgering (1995)</a>	43	<a href="#">Hintzen (1984)</a>
29	<a href="#">Ryle and Windram (1968)</a>	44	<a href="#">Nair (1997)</a>
30	<a href="#">Cristiani et al. (1997)</a>	45	<a href="#">White et al. (1999)</a>
31	<a href="#">Zwicky et al. (1966)</a>	46	<a href="#">Golev and Prugniel (1998)</a>
32	<a href="#">Lipovka and Lipovka (2002)</a>	47	<a href="#">Smail et al. (2003)</a>
33	<a href="#">Ledlow and Owen (1995)</a>	48	<a href="#">Hintzen et al. (1983)</a>
34	<a href="#">Zwicky et al. (1968)</a>	49	<a href="#">Andernach et al. (1988)</a>
35	<a href="#">Tyson (1986)</a>	50	<a href="#">Hutchings et al. (1998)</a>
36	<a href="#">Dunn et al. (2005)</a>	51	<a href="#">Miller et al. (2002)</a>
37	<a href="#">Hill and Lilly (1991)</a>	52	<a href="#">Gehren et al. (1984)</a>
38	<a href="#">Maoz (1995)</a>		



Table A.5: CJF sources observed to have a companion and sources showing evidence for ongoing interaction with another system. Columns (1)-(4) as previously. Col. (5) gives the optical magnitude, Col. (6) gives cluster information for comparison (Table A.3), Col. (7) and (8) give references in regard to companion galaxies and their separation respectively, and Col. (9) gives the references with regard to interacting systems. With a star I mark ambiguous evidence.

Source	Other Name	Type	z	m [mag]	Reference (Cluster)	Reference (Companion)	Separation [kpc]	Reference (Interaction)
0018+729		G	0.821					58
0108+388	OC 314	G	0.669	22				58
0316+413	3C 84	G	0.018	11.9	29	53	~ 600	53
0402+379	4C 37.11	G	0.055	18.5		54	29	54
0710+439		G	0.518	20.4	24	55*	53	55
0804+499	OJ508	Q	1.432	17.5				56
0831+557	4C 55.16	G	0.240	17.5	36	55*	81	55*
0954+658		BL	0.368	16.7		57	474	
1031+567	COINS J1035+5628	G	0.460	20.2	58	42	65	8
1146+596	NGC3894	G	0.011	13	46			59
1254+571	Mrk 231	G	0.042	13.6	47	60	361	60
1418+546	OQ530	BL	0.151	15.5	44			61
1641+399	3C345	Q	0.595	16	50	62,63	47	
1652+398	Mkn 501	BL	0.034	13.8	51			61
1807+698	3C 371.0	BL	0.051	14.8	44	57	81	61
1823+568	4C 56.27	BL	0.664	18.4		23	46	23
1843+356	COINS J1845+3541	G	0.764	21.9		42*	129	58
1946+708		G	0.101	16.1		64	67	64
2021+614	OW 637	Q	0.227	19	42*	42*	36	
2352+495	OZ 488	G	0.237	19	42	42*	47	
53. Colina and Perez-Fournon (1990)					54. Rodriguez et al. (2006)	55. Hutchings et al. (1988)		
56. Hutchings et al. (1999)					57. Stickel et al. (1993)	58. Stanghellini et al. (1993)		
59. Pustilnik et al. (2001)					60. Gallagher et al. (2002)	61. Pursimo et al. (2002)		
62. Bozayan et al. (1990)					63. Kirhakos et al. (1999)	64. Perlman et al. (2001)		

Table A.6: CJF sources studied for variability across the spectrum. If available, I give the respective timescales. Columns (1)-(4) as in previous tables, Col. (5) gives the variability in the radio, Col. (6) the infrared, Col. (7) the optical, Col. (8) the X-Rays, and Col. (9) the  $\gamma$ -rays. For references see Table A.7.

Source	Other Names	Type	z	Var <sup>65</sup> <sub>Radio</sub> [yr]	Var <sub>IR</sub> [yr]	Var <sub>Opt</sub> [yr]	Var <sub>X-ray</sub> [d]	Var <sub><math>\gamma</math></sub> [d]
0016+731		Q	1.781	6.6				
0035+367	4C 36.01	Q	0.366			6.8 <sup>78</sup>		
0133+476	OC 457	Q	0.859	5.8-10.9				
0212+735		Q	2.367	15				
0219+428	3C 66A	BL	0.444		yes <sup>72</sup>			yes <sup>97</sup>
0316+413	3C 84	G	0.018	9.7		4.25 <sup>73</sup> , 2.5 <sup>79</sup> , 63 <sup>80,**</sup> , 65 <sup>81,**</sup>	800 <sup>93,*</sup>	
0402+379	4C 37.11	G	0.055	yes <sup>54</sup>		3.06, 65-68 <sup>62</sup>		
0454+844		BL	0.112			3.1 <sup>82,**</sup>		
0642+449	OH+471	Q	3.396			yes <sup>83</sup>	yes <sup>94</sup>	
0711+356	OI 318	Q	1.620	0.7 <sup>66</sup>		11.2 <sup>84</sup>		
0716+714		BL		5.4-15.5-5-6 <sup>67</sup>	yes <sup>73</sup>	3.3 <sup>67</sup>	1470 <sup>93,*</sup>	yes <sup>98</sup>
0804+499	OJ508	Q	1.432	1.1, 1.8, 2.7 <sup>66</sup>				yes <sup>95</sup>
0814+425	OJ425	BL	0.245	19.2-20.7	yes <sup>9</sup>	2.4 <sup>82,**</sup>		
0836+710	4C 71.07	Q	2.180	5.7-9.0				yes <sup>97</sup>
0917+449	VIPS 0214	Q	2.180					yes <sup>97</sup>
0923+392	4C 39.25	Q	0.699	22.5-22.4	(?) <sup>20</sup>	yes <sup>62</sup>		
0927+352		BL		6 <sup>68</sup>				
0945+408		Q	1.252	3.6-7.3 <sup>69</sup>				yes <sup>97</sup>
0954+556	4C 55.17	Q	0.909					yes <sup>97</sup>
0954+658		BL	0.368			2.6 <sup>82,**</sup>		
1038+528	OL 564	Q	0.677	9.3				
1101+384	Mrk 421	BL	0.031	3.7-8.0	yes <sup>74,75</sup>	6.2 <sup>78</sup>	62 <sup>95</sup>	yes <sup>97</sup>
1254+571	Mrk 231	G	0.042	yes <sup>70</sup>		yes <sup>85</sup>	yes <sup>60</sup>	

Continued on Next Page...

Table A.6 – Continued

Source	Other Names	Type	z	Var <sup>65</sup> <sub>Radio</sub> [yr]	Var <sub>IR</sub> [yr]	Var <sub>Opt</sub> [yr]	Var <sub>Xray</sub> [d]	Var <sub>γ</sub> [d]
1418+546	OQ530	BL	0.151	2.5-11.3	yes <sup>74</sup>	yes <sup>86</sup>		
1504+377		G	0.671		yes <sup>12</sup>			
1624+416	4C 41.32	Q	2.550	16.7-37.1				yes <sup>97</sup>
1633+382	4C 38.41	Q	1.807	14.3		yes <sup>62</sup>		
1638+398	NRAO 512	Q	1.660			0.5-31 <sup>62</sup>		
1642+690		Q	0.751	6.6-7.0				
1641+399	3C345	Q	0.595	5.1 <sup>66</sup> , 3.5-4 <sup>71</sup>	yes <sup>74</sup>	5.6, 11.4 <sup>87</sup> , 10.1 <sup>88</sup> , 1.9 <sup>89</sup>	0.72 <sup>93</sup>	
1652+398	Mrk 501	BL	0.034	6.8-12.3	yes <sup>71</sup>	yes <sup>86</sup>	23 <sup>96</sup>	23.2 <sup>99</sup>
1739+522	4C 51.37	Q	1.381	1.4 <sup>66</sup>				yes <sup>97</sup>
1749+701		BL	0.769	12.3		yes <sup>62</sup>		
1803+784		BL	0.679	7.0-11.3		1.1 <sup>82,**</sup>		
1807+698	3C 371.0	BL	0.051		yes <sup>76</sup>	2.7 <sup>73</sup> , 2.4 <sup>78</sup>		
1823+568		BL	0.664	8.8-14.9				
1928+738	4C 73.18	Q	0.302	7.7-8.2		yes <sup>62</sup>		
2007+777		BL	0.342		yes <sup>77</sup>	0.6 <sup>82,**</sup> , 10-40 <sup>90,**</sup>		
2200+420	BL Lac	BL	0.069	3.9-7.8	yes <sup>74</sup>	7.8 <sup>91</sup> , 0.6, 0.88, 14 <sup>92</sup> , 7.7 <sup>8</sup>		yes <sup>97</sup>
2351+456	4C 45.51	Q	1.986	11.8				

\*\* in days

Table A.7: References for Table A.6.

Symbol	Reference	Symbol	Reference
65	<a href="#">Fan et al. (2007)</a>	83	<a href="#">Pica and Smith (1983)</a>
66	<a href="#">Kelly et al. (2003)</a>	84	<a href="#">Smith et al. (1993)</a>
67	<a href="#">Raiteri et al. (2003)</a>	85	<a href="#">Kollatschny et al. (1992)</a>
68	<a href="#">Machalski and Brandt (1996)</a>	86	<a href="#">Iwasawa et al. (1998)</a>
69	<a href="#">Ciaramella et al. (2004)</a>	87	<a href="#">Webb et al. (1988)</a>
70	<a href="#">Ulvestad et al. (1999a)</a>	88	<a href="#">Zhang et al. (1998)</a>
71	<a href="#">Lobanov and Zensus (1999)</a>	89	<a href="#">Babadzhanyants et al. (1995)</a>
72	<a href="#">Abdo (2009)</a>	90	<a href="#">Bychkova et al. (2003)</a>
73	<a href="#">Hagen-Thorn et al. (2006)</a>	91	<a href="#">Hagen-Thorn et al. (1997)</a>
74	<a href="#">Takalo et al. (1992)</a>	92	<a href="#">Fan et al. (1998)</a>
75	<a href="#">Gupta et al. (2004)</a>	93	<a href="#">Bian and Zhao (2003)</a>
76	<a href="#">Edelson and Malkan (1987)</a>	94	<a href="#">Zamorani et al. (1984)</a>
77	<a href="#">Peng et al. (2000)</a>	95	<a href="#">Osone and Teshima (2001)</a>
78	<a href="#">Smith and Nair (1995)</a>	96	<a href="#">Osone (2006)</a>
79	<a href="#">Belokon and Babadzhanyants (2003)</a>	97	<a href="#">Fan et al. (2002)</a>
80	<a href="#">Xie et al. (2002)</a>	98	<a href="#">Chen et al. (2008)</a>
81	<a href="#">Lainela et al. (1999)</a>	99	<a href="#">Neshpor (2000b)</a>
82	<a href="#">Heidt and Wagner (1996)</a>	**	in days

## B CJF Black Hole Masses

Table B.1: CJF sources with calculated SMBH masses. Columns (1)-(3) as in Table A.1, Col. (4) gives the mass of the BH in logarithmic scale and measured in solar masses, Col. (5) shows the technic used (BLR: broad line region size, BoL: bolometric luminosity, VeD: velocity dispersion, BBH: BBH model, OptL: optical luminosity, BuL: bulge luminosity, VeD\*:velocity dispersion calculated from the fundamental plane, and  $\gamma$ L: gamma-ray luminosity), and Col. (6) gives the reference (Table B.2).

Source	Type	Redshift	BH Mass ( $M_{\odot}$ )	Technic	Reference
0110+495	Q	0.389	9.004	BLR	100
0133+476	Q	0.859	9.309	BLR	100
0153+744	Q	2.388	9.150	BLR	101
0212+735	Q	2.367	6.960	BLR	102
0219+428	BL	0.444	8.000	BoL	103
0227+403	Q	1.019	9.239	BLR	100
0248+430	Q	1.310	8.490	BLR	102
0251+393	Q	0.289	8.626	BLR	100
0316+413	G	0.018	8.510	VeD	104
0402+379	G	0.055	8.176	BBH	54
0444+634	Q	0.781	9.261	BLR	100
0554+580	Q	0.904	9.656	BLR	100
0646+600	Q	0.455	8.740	OptL	105
0711+356	Q	1.620	8.140	BLR	102
0716+714	BL		8.100	BoL	103
0724+571	Q	0.426	9.073	BLR	100
0730+504	Q	0.720	8.908	BLR	100
0804+499	Q	1.432	9.390	BLR	102
0806+573	Q	0.611	9.576	BLR	100
0831+557	G	0.240	8.699	BuL	106
0836+710	Q	2.180	9.415	ReV	107
0847+379	G	0.407	8.930	BuL	108
0850+581	Q	1.322	8.490	BLR	102
0859+470	Q	1.462	7.670	BLR	102
0923+392	Q	0.699	9.956	BLR	100
0945+408	Q	1.252	8.600	BLR	102
0954+556	Q	0.909	8.070	OptL	105
1058+629	Q	0.663	9.056	BLR	100
1101+384	BL	0.031	7.900	OptL	109

Continued on Next Page...

Table B.1 – Continued

Source	Type	Redshift	BH Mass ( $M_{\odot}$ )	Technic	Reference
1151+408	Q	0.916	8.455	BLR	100
1254+571	Q	0.043	7.940	BLR	110
1309+555	Q	0.926	7.718	BLR	100
1418+546	BL	0.151	9.030	VeD*	105
1531+722	Q	0.899	9.562	BLR	100
1622+665	G	0.201	9.588	BLR	100
1624+416	Q	2.550	6.350	BLR	102
1633+382	Q	1.807	8.670	BLR	102
1637+574	Q	0.749	9.800	BLR	100
1642+690	Q	0.751	8.425	BLR	100
1641+399	Q	0.595	9.841	BLR	100
1652+398	BL	0.034	8.300	OptL	109
1726+455	Q	0.717	8.848	BLR	100
1739+522	Q	1.381	9.320	BLR	102
1803+784	BL	0.680	7.920	BLR	102
1807+698	BL	0.051	10.100	VeD*	105
1826+796	G	0.224	7.994	BLR	100
1823+568	BL	0.664	9.600	VeD*	111
1849+670	Q	0.657	9.140	OptL	105
1856+737	Q	0.461	9.144	BLR	100
1928+738	Q	0.302	9.386	BLR	100
1946+708	G	0.101	7.826	VeD	112
1954+513	Q	1.223	9.180	BLR	102
2007+777	BL	0.342	8.800	BuL	113
2200+420	BL	0.069	8.230	VeD*	105
2351+456	Q	1.986	9.700	$\gamma$ L	71

Table B.2: References for Table B.1.

Symbol	Reference	Symbol	Reference
100	<a href="#">Cao and Jiang (2002)</a>	117	<a href="#">Kaspi et al. (2007)</a>
101	<a href="#">Kelly and Bechtold (2007)</a>	118	<a href="#">McLure et al. (2004)</a>
102	<a href="#">Liu et al. (2006)</a>	119	<a href="#">Xie et al. (2005)</a>
103	<a href="#">Xie et al. (2004)</a>	110	<a href="#">Kawakatu et al. (2007)</a>
114	<a href="#">Panessa et al. (2006)</a>	111	<a href="#">Wu et al. (2002)</a>
115	<a href="#">Woo and Urry (2002)</a>	112	<a href="#">Snellen et al. (2003)</a>
116	<a href="#">Rafferty et al. (2006)</a>	113	<a href="#">Falomo et al. (2003)</a>

## C CJF Jet Ridge Lines

Table C.1: CJF Jet ridge line lengths. Columns (1)-(3) as in previous tables, Cols. (4)-(5) give the values and uncertainty of the jet ridge line length in milliarcseconds, and Cols. (6)-(7) give the values of the jet ridge line length in parsecs (zero value for sources of unknown redshift).

Source	Type	Redshift	Jet Length (mas)	Error	Jet Length (pc)	Uncertainty
0003+380	G	0.229	5.23	0.15	18.98	0.54
0010+405	G	0.255	2.64	0.20	10.38	0.79
0014+813	Q	3.366	9.16	0.04	69.19	0.30
0016+731	Q	1.781	1.06		9.06	
0018+729	G	0.821	6.64	0.05	50.37	0.38
0022+390	Q	1.946	4.66	0.14	39.59	1.19
0035+367	Q	0.366	10.73	0.13	54.21	0.66
0035+413	Q	1.353	12.93	0.05	109.59	0.42
0102+480	G		1.85	0.04		
0108+388	G	0.669	5.62		39.39	
0109+351	Q	0.45	2.60	0.02	14.91	0.11
0110+495	Q	0.389	9.87	0.05	51.83	0.26
0133+476	Q	0.859	2.53	0.04	19.48	0.31
0145+386	Q	1.442	1.28	0.02	10.91	0.17
0151+474	Q	1.026	2.43	0.03	19.66	0.24
0153+744	Q	2.388	11.45	0.05	94.64	0.41
0205+722	G	0.895	3.78	0.08	29.48	0.62
0212+735	Q	2.367	14.26	0.01	118.05	0.08
0218+357	G	0.936				
0219+428	BL	0.444	16.21	0.28	92.21	1.59
0227+403	Q	1.019	4.20	0.08	33.93	0.65
0248+430	Q	1.31	13.13	0.02	110.90	0.17
0249+383	Q	1.122	7.65	0.03	63.10	0.25
0251+393	Q	0.289	1.61	0.03	6.93	0.13
0307+380	Q	0.816	1.28	0.10	9.69	0.76
0309+411	Q	0.134	7.06	0.05	16.6	0.12
0316+413	G	0.018	12.5	0.01	4.51	
0340+362	Q	1.485	1.67	0.04	14.25	0.34
0346+800	Q		3.83	0.25		
0402+379	G	0.055	21.4	0.06	22.58	0.06
0444+634	Q	0.781	5.82	0.03	43.38	0.22
0454+844	BL	0.112	2.24	0.03	4.51	0.06
0537+531	Q	1.275	11.34	0.09	95.47	0.76
0546+726	Q	1.555	6.23	0.01	53.27	0.09

Continued on Next Page...

## C CJK Jet Ridge Lines

Table C.1 – Continued

Source	Type	Redshift	Jet Length (mas)	Error	Jet Length (pc)	Uncertainty
0554+580	Q	0.904	3.78	0.04	29.57	0.31
0600+442	G	1.136	6.44	0.07	53.24	0.58
0602+673	Q	1.95	0.69	0.01	5.86	0.08
0604+728	Q	0.986	21.57	0.03	172.83	0.24
0609+607	Q	2.702	5.44	0.02	43.79	0.16
0615+820	Q	0.71				
0620+389	Q	3.469	6.89	0.03	51.50	0.22
0621+446	BL					
0627+532	Q	2.204	12.63	0.06	105.78	0.50
0633+596	na		1.67	0.02		
0633+734	Q	1.85	12.16	0.11	103.69	0.94
0636+680	Q	3.174				
0641+393	Q	1.266	4.35	0.01	36.59	0.08
0642+449	Q	3.396	3.41	0.02	25.68	0.15
0646+600	Q	0.455	3.08		17.77	
0650+371	Q	1.982	1.97	0.07	16.71	0.59
0650+453	Q	0.933				
0651+410	G	0.022	4.35	0.06	1.91	0.03
0700+470	G		9.76	0.04		
0702+612	Q		3.83	0.04		
0707+476	Q	1.292	6.08	0.06	51.27	0.51
0710+439	G	0.518	14.16	0.01	87.77	0.06
0711+356	Q	1.62	5.85	0.01	50.06	0.09
0714+457	Q	0.94	5.33	0.03	42.17	0.24
0716+714	BL	0.31	5.55	0.07	24.16	0.30
0718+793	na					
0724+571	Q	0.426	14.57	0.07	80.88	0.39
0727+409	Q	2.5	6.15	0.12	50.38	0.98
0730+504	Q	0.72	3.24	0.01	23.41	0.07
0731+479	Q	0.782	3.55	0.04	26.47	0.30
0733+597	G	0.041	21.08	0.12	16.85	0.10
0738+491	Q	2.32	1.32	0.05	10.97	0.42
0740+768	G		3.41	0.02		
0743+744	Q	1.629	5.42	0.08	46.38	0.68
0746+483	Q	1.951	2.94	0.02	24.97	0.17
0749+426	Q	3.59	10.64	0.16	78.57	1.18
0749+540	BL		1.65	0.05		
0800+618	Q	3.044	5.21	0.04	40.62	0.31
0803+452	Q	2.102	1.27		10.7	
0804+499	Q	1.432	4.08	0.04	34.75	0.34
0805+410	Q	1.42	7.42	0.06	63.15	0.51
0806+573	Q	0.611	32.37	0.68	217.86	4.58
0812+367	Q	1.025	12.29	0.03	99.42	0.24
0814+425	BL	0.53	4.96	0.08	12.54	0.20
0820+560	Q	1.409	2.97	0.03	25.26	0.26
0821+394	Q	1.216	5.42	0.10	45.33	0.84
0821+621	Q	0.542	32.97	0.04	209.24	0.25
0824+355	Q	2.249	11.40	0.08	95.19	0.67
0831+557	G	0.24	18.54	0.06	69.71	0.23

Continued on Next Page...



Table C.1 – Continued

Source	Type	Redshift	Jet Length (mas)	Error	Jet Length (pc)	Uncertainty
0833+416	Q	1.298	3.31	0.06	27.93	0.51
0833+585	Q	2.101	1.86		15.68	
0836+710	Q	2.18	34.96	0.06	293.25	0.50
0843+575	G		6.40	0.02		
0847+379	G	0.407	5.47	0.15	29.54	0.81
0850+581	Q	1.322	7.76	0.02	65.61	0.17
0859+470	Q	1.462	4.19	0.01	35.73	0.09
0859+681	Q	1.499	5.22	0.04	44.57	0.34
0900+520	Q	1.537	2.26	0.06	19.32	0.51
0902+490	Q	2.69	1.25	0.01	10.07	0.08
0917+449	Q	2.18	19.10	0.15	160.22	1.26
0917+624	Q	1.446	6.03	0.01	51.39	0.09
0923+392	Q	0.699	2.83	0.06	20.21	0.43
0925+504	BL	0.37	5.98	0.06	30.42	0.31
0927+352	BL		5.98	0.01		
0929+533	Q	0.595	1.52	0.03	10.10	0.20
0930+493	Q	2.582	3.26	0.01	26.52	0.08
0942+468	G	0.639	4.08	0.07	28.03	0.48
0945+408	Q	1.252	11.62	0.03	97.59	0.25
0949+354	Q	1.875	7.56	0.02	64.41	0.17
0950+748	G	0.695	21.87	0.02	155.79	0.14
0954+556	Q	0.895				
0954+658	BL	0.368	9.79	0.13	49.63	0.66
0955+476	Q	1.873	0.76	0.03	6.48	0.26
1003+830	G	0.322	7.23	0.02	33.56	0.09
1010+350	Q	1.414	9.05	0.13	77.00	1.11
1014+615	Q	2.8	0.91	0.01	7.26	0.08
1015+359	Q	1.226	4.51	0.06	37.76	0.50
1020+400	Q	1.254	13.47	0.04	113.15	0.34
1030+398	G	1.095	2.37	0.01	19.45	0.08
1030+415	Q	1.12	12.97	0.15	106.94	1.24
1030+611	Q	1.401	3.44	0.09	5.09	0.13
1031+567	G	0.46	33.71		195.71	
1038+528	Q	0.677	1.16	0.02	8.17	0.14
1039+811	Q	1.254	7.36	0.05	61.83	0.42
1041+536	Q	1.897	4.11	0.02	34.99	0.17
1044+719	Q	1.15	0.55	0.02	4.56	0.17
1053+704	Q	2.492	2.55	0.10	20.90	0.82
1053+815	G	0.706	1.31	0.08	9.39	0.57
1058+629	Q	0.663	1.20	0.05	8.38	0.35
1058+726	Q	1.46	4.06	0.01	34.62	0.09
1101+384	BL	0.031	5.95	0.11	3.62	0.07
1105+437	Q	1.226	8.95	0.10	74.94	0.84
1106+380	G	2.29	7.11	0.01	59.20	0.08
1107+607	na		2.43	0.14		
1124+455	Q	1.811	3.81	0.01	32.53	0.09
1124+571	Q	2.89	2.27	0.03	17.96	0.24
1125+596	Q	1.779	0.56	0.02	4.78	0.17
1128+385	Q	1.733	0.82	0.01	7.01	0.09

Continued on Next Page...

## C CJK Jet Ridge Lines

Table C.1 – Continued

Source	Type	Redshift	Jet Length (mas)	Error	Jet Length (pc)	Uncertainty
1143+590	Q	1.982	1.22	0.03	10.35	0.25
1144+352	G	0.063	24.98	0.17	29.91	0.20
1144+402	Q	1.088				
1144+542	Q	2.201	2.63	0.02	22.03	0.17
1146+596	G	0.011	7.73	0.06	1.69	0.01
1150+812	Q	1.25	4.75	0.05	39.88	0.42
1151+408	Q	0.916	2.90	0.01	22.77	0.08
1155+486	Q	2.028	2.92	0.07	24.71	0.59
1205+544	na		5.32	0.02		
1206+415	BL					
1213+350	Q	0.857	37.00	0.04	284.70	0.31
1216+487	Q	1.076	2.54	0.02	20.77	0.16
1218+444	Q	1.345	8.80	0.12	74.54	1.02
1221+809	BL		9.13	0.05		
1223+395	Q	0.623	15.52	0.07	105.40	0.48
1226+373	Q	1.515	1.23	0.06	10.51	0.51
1239+376	Q	3.818	1.79		12.92	
1240+381	Q	1.316	1.23	0.01	10.39	0.08
1246+586	BL		2.25	0.07		
1250+532	BL		8.92	0.06		
1254+571	Q	0.042				
1258+507	Q	1.561	2.80	0.05	23.95	0.43
1300+580	G	1.088	2.90	0.05	23.77	0.41
1305+804	Q	1.183	14.57	0.03	121.32	0.25
1306+360	Q	1.055	1.11	0.01	9.04	0.08
1307+562	Q	1.629	1.99	0.03	17.03	0.26
1308+471	na	1.113				
1309+555	Q	0.926	1.00	0.06	7.88	0.47
1312+533	na		1.63	0.02		
1321+410	G	0.496	5.42		32.82	
1322+835	na	1.024	3.91	0.15	31.62	1.21
1323+800	G	1.97	3.88	0.07	32.93	0.59
1325+436	Q	2.073	1.80	0.02	15.20	0.17
1333+459	Q	2.449	2.50	0.05	20.56	0.41
1333+589	G		12.81	0.01		
1335+552	Q	1.096	3.61	0.06	29.64	0.49
1337+637	Q	2.558	6.83	0.04	55.68	0.33
1342+663	Q	1.351				
1347+539	Q	0.98	18.66	0.06	149.28	0.48
1355+441	G	0.646	13.53	0.04	93.40	0.28
1356+478	G	0.23	6.08		22.14	
1357+769	BL		1.14	6		
1413+373	Q	2.36	5.18	0.02	42.90	0.17
1415+463	Q	1.552	12.10	0.01	103.46	0.09
1417+385	Q	1.832				
1418+546	BL	0.151	4.77	0.02	12.41	0.05
1421+482	Q	2.22	3.03	0.04	25.35	0.33
1424+366	BL	1.091	1.33	0.02	10.91	0.16
1427+543	Q	2.991	1.57	0.01	12.30	0.08

Continued on Next Page...

Table C.1 – Continued

Source	Type	Redshift	Jet Length (mas)	Error	Jet Length (pc)	Uncertainty
1432+422	Q	1.24	1.82	0.07	15.26	0.59
1435+638	Q	2.068	9.96	0.04	84.11	0.34
1438+385	Q	1.775	6.56	0.13	56.05	1.11
1442+637	Q	1.38	9.23	0.03	78.38	0.25
1448+762	Q	0.899	2.39	0.20	18.67	1.56
1456+375	G	0.333	1.69	0.01	8.02	0.05
1459+480	BL	1.059	7.19	0.08	58.60	0.65
1504+377	G	0.672	11.56	0.03	81.16	0.21
1505+428	G	0.587	7.65	0.05	50.52	0.33
1526+670	Q	3.02	2.31	0.11	18.05	0.86
1531+722	Q	0.899				
1534+501	Q	1.121	1.26	0.02	10.39	0.16
1543+480	Q	1.277	63.12	0.12	531.51	1.01
1543+517	Q	1.924	24.89	0.11	211.67	0.94
1547+507	Q	2.169	7.24	0.01	60.77	0.08
1550+582	Q	1.324	2.20	0.09	18.6	0.76
1619+491	Q	1.513	10.97	0.21	93.71	1.79
1622+665	G	0.201	0.67	0.04	2.20	0.13
1623+578	G	0.789	6.52	0.06	48.78	0.45
1624+416	Q	2.55	3.51	0.02	28.63	0.16
1629+495	Q	0.52	5.64	0.10	35.03	0.62
1633+382	Q	1.807	5.38	0.03	45.94	0.26
1636+473	Q	0.74	10.40	0.07	75.97	0.51
1637+574	Q	0.749	3.78	0.07	27.74	0.51
1638+398	Q	1.66				
1638+540	Q	1.977	1.31	0.02	11.11	0.17
1641+399	Q	0.595	7.98	0.02	53.04	0.13
1642+690	Q	0.751	10.61	0.15	77.94	1.10
1645+410	Q	0.835	2.73	0.32	20.83	2.44
1645+635	Q	2.379	3.72	0.07	30.77	0.58
1652+398	BL	0.034	10.51	0.02	6.96	0.01
1656+477	Q	1.622	7.19	0.05	61.53	0.43
1656+482	G		2.08	0.03		
1656+571	Q	1.281	4.91	0.09	41.36	0.76
1700+685	G	0.301	2.06	0.25	9.13	1.11
1716+686	Q	0.339	5.09	0.02	24.46	0.10
1719+357	Q	0.263	6.30	0.04	25.35	0.16
1722+401	Q	1.049	6.29	0.03	51.15	0.24
1726+455	Q	0.717	1.57	0.01	11.33	0.07
1732+389	Q	0.97	4.05	0.06	32.31	0.48
1734+508	G	0.835	3.66	0.01	27.92	0.08
1738+476	BL	0.95	2.18	0.03	17.30	0.24
1738+499	Q	1.545	1.57	0.08	13.42	0.68
1739+522	Q	1.381	2.73	0.03	23.18	0.25
1744+557	G	0.031	14.12	0.06	8.53	0.04
1745+624	Q	3.889	2.43	0.12	17.41	0.86
1746+470	na		1.46	0.06		
1747+433	BL		13.35	0.01		
1749+701	BL	0.77	3.84	0.03	28.47	0.22

Continued on Next Page...

## C CJF Jet Ridge Lines

Table C.1 – Continued

Source	Type	Redshift	Jet Length (mas)	Error	Jet Length (pc)	Uncertainty
1751+441	Q	0.871	1.51	0.01	11.68	0.08
1755+578	Q	2.11	13.39	0.04	112.81	0.34
1758+388	Q	2.092	1.91	0.03	16.11	0.25
1800+440	Q	0.663				
1803+784	BL	0.68	28.84	0.06	203.53	0.42
1807+698	BL	0.051	6.46	0.02	6.35	0.02
1809+568	Q		5.94	0.01		
1812+412	Q	1.564	14.48	0.34	123.84	2.91
1818+356	Q	0.971	1.95	0.04	15.56	0.32
1823+568	BL	0.664	7.87	0.03	54.99	0.21
1826+796	G	0.224	15.89	0.01	56.70	0.04
1828+399	na		1.28	0.01		
1834+612	Q	2.274	3.46	0.01	28.84	0.08
1839+389	Q	3.095	1.87	0.15	14.51	1.16
1842+681	Q	0.472	11.68	0.05	68.81	0.29
1843+356	G	0.764	11.09	0.03	81.99	0.22
1849+670	Q	0.657	6.01	0.08	41.80	0.56
1850+402	Q	2.12	2.31	0.01	19.45	0.08
1851+488	Q	1.25				
1856+737	Q	0.461	7.86	0.04	45.69	0.23
1908+484	Q	0.513	1.38	0.01	8.51	0.06
1910+375	Q	1.104	8.47	0.06	69.64	0.49
1924+507	Q	1.098	3.65	0.47	29.98	3.86
1926+611	BL		2.90	0.04		
1928+738	Q	0.302	21.39	0.03	95.00	0.13
1936+714	Q	1.864	1.69	0.08	14.40	0.68
1943+546	G	0.263	25.80	0.01	103.81	0.04
1946+708	G	0.101	22.14	0.05	40.71	0.09
1950+573	G	0.652	14.91	0.08	103.35	0.55
1954+513	Q	1.223	13.75	0.02	115.09	0.17
2005+642	Q	1.574				
2007+659	Q	1.325	6.01	0.13	50.83	1.10
2007+777	BL	0.342	3.25	0.04	15.71	0.19
2010+723	BL		6.00	0.06		
2017+745	Q	2.187	5.59	0.13	46.87	1.09
2021+614	Q	0.227	9.62		34.68	
2023+760	BL		7.95	0.40		
2054+611	Q	0.864	7.19	0.03	55.47	0.23
2116+818	Q	0.084	7.14	0.05	11.13	0.08
2136+824	Q	2.357	3.36	0.05	27.84	0.41
2138+389	na	1.306	6.38	0.07	53.87	0.59
2200+420	BL	0.069	6.35	0.02	8.23	0.03
2214+350	Q	0.51	0.76	0.02	4.67	0.12
2229+695	BL	1.413	1.35	0.02	11.49	0.17
2235+731	Q	1.345	5.23	0.12	44.30	1.02
2238+410	BL	0.726	4.48	0.11	32.48	0.80
2253+417	Q	1.476	7.80	0.02	66.55	0.17
2255+416	Q	2.15	42.21	0.08	354.74	0.67
2259+371	Q	2.179	4.75	0.05	39.85	0.42

Continued on Next Page...

Table C.1 – Continued

Source	Type	Redshift	Jet Length (mas)	Error	Jet Length (pc)	Uncertainty
2309+454	Q	1.447	2.09	0.02	17.81	0.17
2310+385	Q	2.181	6.42	0.01	53.85	0.08
2319+444	G	1.251	2.62	0.01	22.00	0.08
2346+385	Q	1.032	2.92	0.06	23.66	0.49
2351+456	Q	1.986	9.05	0.07	76.75	0.59
2352+495	G	0.237	49.36	0.03	183.85	0.11
2353+816	BL	1.344	1.42	0.07	12.03	0.59
2356+385	Q	2.704	2.27	0.08	18.27	0.64
2356+390	Q	1.198	1.79	0.01	14.94	0.08

Table C.2: CJF Jet ridge line widths. Columns (1)-(3) as in previous tables, Col. (4) gives the epoch of observation, Cols. (5)-(7) give the name, position angle, and position angle uncertainty of the component with the maximum values of position angle for that epoch, Cols. (8)-(10) give the same for the component with the minimum value of position angle in the same epoch, Col. (11) gives the absolute distance between the two components, and Cols. (12)-(13) give the value and uncertainty of the jet ridge line width at that epoch.

Source	Type	Redshift	Epoch	Component		P.A. (deg)	Error (deg)	Component	P.A. (deg)	Error (deg)	Distance (pc)	Width (deg)	Error
				Max	Min								
0003+380	G	0.229	1993.52	C2	C4	127.9	0.9	C4	114.2	1.1	12.4	13.70	1.42
0003+380	G	0.229	1995.73	C2	C1	124.2	0.2	C1	111.2	0.4	3.9	13.00	0.45
0003+380	G	0.229	1996.72	C2	C3	127.5	0.6	C3	116.9	1.1	6.3	10.60	1.25
0010+405	G	0.255	1990.27	C2	C1	332.7	0.6	C1	327.1	0.3	7.7	5.60	0.67
0010+405	G	0.255	1993.53	C2	C1	330.9	0.7	C1	329.8	0.4	6.5	1.10	0.81
0010+405	G	0.255	1996.72	C1	C2	330.7	0.4	C2	327.8	1.7	6.6	2.90	1.75
0014+813	Q	3.366	1992.81	C2	C1	196.5	0.3	C1	184.1	0.1	31.9	12.40	0.32
0014+813	Q	3.366	1994.78	C2	C1	195.2	0.6	C1	183.1	0.3	33.9	12.10	0.67
0014+813	Q	3.366	1996.71	C2	C1	194.1	0.2	C1	183.7	0.2	33.9	10.40	0.28
0016+731	Q	1.781	1996.72	n/a	n/a								
0016+731	Q	1.781	1999.96	C1	C1	305.1	0.2	C1	305.1	0.2			
0016+731	Q	1.781	2001.03	C1	C1	311.0	0.1	C1	311.0	0.1			
0018+729	G	0.821	1994.78	C1	C2	292.6	2.9	C2	273.5	1.2	17.2	19.10	3.14
0018+729	G	0.821	1996.72	C1	C2	289.4	1.0	C2	262.3	0.5	17.3	27.10	1.12
0018+729	G	0.821	1999.98	C1	C2	284.1	0.5	C2	261.6	0.2	18.1	22.50	0.54
0022+390	Q	1.946	1990.27	C2	C1	173.8	0.4	C1	159.3	0.3	23.0	14.50	0.50
0022+390	Q	1.946	1993.53	C2	C1	173.2	0.3	C1	142.9	0.5	28.0	30.30	0.58
0022+390	Q	1.946	1996.72	C2	C1	172.4	0.2	C1	157.7	0.2	22.2	14.70	0.28
0035+367	Q	0.366	1995.73	n/a	n/a								
0035+367	Q	0.366	1996.70	n/a	n/a								
0035+367	Q	0.366	1999.96	n/a	n/a								
0035+367	Q	0.366	2001.03	n/a	n/a								
0035+413	Q	1.353	1995.73	C1	C1	104.4	0.4	C1	104.4	0.4			
0035+413	Q	1.353	1998.19	C2	C1	111.9	1.7	C1	104.9	0.5	9.2	7.00	1.77

Continued on Next Page...

Table C.2 – Continued

Source	Type	Redshift	Epoch	Component		P.A.		Component	P.A.		Distance	Width	Error
				Max	Min	(deg)	(deg)		(deg)	(deg)			
0035+413	Q	1.353	1999.96	C1	C2	111.0	106.2	C2	0.1	0.7	9.8	4.80	0.71
0102+480	G		1990.27	C1	C1	193.4	193.4	C1	0.3	0.3			
0102+480	G		1993.53	C1	C1	195.5	195.5	C1	0.3	0.3			
0102+480	G		1996.72	C1	C1	191.9	191.9	C1	0.2	0.2			
0108+388	G	0.669	1996.72	C1	C2	253.4	240.4	C2	0.1		31.1	13.00	0.10
0108+388	G	0.669	1999.96	C1	C2	260.7	240.9	C2	0.1		30.4	19.80	0.10
0108+388	G	0.669	2001.03	C1	C2	256.4	240.8	C2	0.1		30.8	15.60	0.10
0109+351	Q	0.450	1993.53	C1	C1	203.6	203.6	C1	1.1	1.1			
0109+351	Q	0.450	1995.73	C2	C2	204.3	204.3	C2	1.4	1.4			
0109+351	Q	0.450	1998.19	C2	C1	205.2	203.7	C1	0.3	0.4	10.4	1.50	0.50
0110+495	Q	0.389	1993.53	C1	C2	328.6	324.6	C2	0.2	0.2	9.8	4.00	0.28
0110+495	Q	0.389	1995.73	C1	C2	329.0	326.7	C2	0.2	0.2	7.9	2.30	0.28
0110+495	Q	0.389	1998.19	C1	C2	336.9	326.0	C2	0.2	0.1	10.9	10.90	0.22
0133+476	Q	0.859	1996.72	C1	C1	343.0	320.0	C2	4.6	0.1	11.3	23.00	4.60
0133+476	Q	0.859	1999.96	C1	C1	328.9	325.0	C2	0.3	0.5	11.0	3.90	0.58
0133+476	Q	0.859	2001.03	C2	C1	326.7	324.8	C1	0.2	0.5	8.9	1.90	0.54
0145+386	Q	1.442	1993.53	C1	C1	304.5	304.5	C1	0.4	0.4			
0145+386	Q	1.442	1995.73	C1	C1	319.5	319.5	C1	0.3	0.3			
0145+386	Q	1.442	1998.19	C1	C1	326.9	326.9	C1	0.6	0.6			
0151+474	Q	1.026	1993.53	C1	C2	189.1	179.6	C2	0.7	0.4	10.0	9.50	0.81
0151+474	Q	1.026	1995.73	C1	C1	193.3	180.7	C2	0.8	0.4	13.5	12.60	0.89
0151+474	Q	1.026	1998.19	C1	C2	182.9	180.2	C2	0.2	0.3	15.0	2.70	0.36
0153+744	Q	2.388	1996.72	n/a	n/a			n/a					
0153+744	Q	2.388	1999.96	n/a	n/a			n/a					
0153+744	Q	2.388	2001.03	n/a	n/a			n/a					
0205+722	G	0.895	1992.81	C2	C1	262.0	249.7	C1	1.1	1.7	4.8	12.30	2.02
0205+722	G	0.895	1994.78	C2	C1	254.5	244.3	C1	1.2	2.4	7.8	10.20	2.68
0205+722	G	0.895	1996.72	C2	C3	248.2	243.9	C3	1.1	2.1	9.7	4.30	2.37
0212+735	Q	2.367	1996.72	C1	C2	124.7	101.4	C2	0.3	0.2	12.8	23.30	0.36

Continued on Next Page...

Table C.2 – Continued

Source	Type	Redshift	Epoch	Component		P.A. (deg)	Error (deg)	Component	P.A. (deg)	Error (deg)	Distance (pc)	Width (deg)	Error (deg)
				Max	Min								
0212+735	Q	2.367	1999.96	C3	C2	111.4	0.4	C2	85.7	0.5	13.4	25.70	0.64
0212+735	Q	2.367	2001.03	C1	C3	114.9	0.1	C3	103.7	0.1	19.1	11.20	0.14
0218+357	G	0.936	1992.32	n/a	n/a			n/a					
0218+357	G	0.936	1996.70	n/a	n/a			n/a					
0218+357	G	0.936	1999.96	n/a	n/a			n/a					
0219+428	BL	0.444	1995.73	C1	C3	192.2	0.2	C3	170.3	0.3	28.2	21.90	0.36
0219+428	BL	0.444	1996.71	C1	C3	190.9	0.2	C3	167.9	0.5	29.2	23.00	0.54
0219+428	BL	0.444	1998.19	C1	C3	189.2	0.1	C3	168.7	0.2	28.0	20.50	0.22
0227+403	Q	1.019	1993.54	C1	C2	159.7	0.8	C2	132.1	1.3	8.6	27.60	1.53
0227+403	Q	1.019	1995.73	C1	C3	165.6	0.5	C3	133.1	0.5	24.2	32.50	0.71
0227+403	Q	1.019	1998.19	C1	C3	151.2	0.4	C3	134.1	0.4	28.0	17.10	0.57
0227+403	Q	1.019	1999.98	C1	C2	155.3	0.6	C2	133.0	2.5	14.1	22.30	2.57
0248+430	Q	1.310	1992.81	C2	C1	146.2	0.1	C1	146.0	0.2	9.8	0.20	0.22
0248+430	Q	1.310	1994.78	C1	C2	147.5	0.4	C2	145.9	0.1	9.2	1.60	0.41
0248+430	Q	1.310	1996.71	C1	C2	147.3	0.1	C2	144.9	0.1	9.5	2.40	0.14
0249+383	Q	1.122	1993.53	n/a	n/a			n/a					
0249+383	Q	1.122	1995.73	C2	C1	344.0	0.2	C1	336.2	0.7	18.0	7.80	0.73
0249+383	Q	1.122	1998.19	C2	C1	343.8	0.1	C1	337.9	0.2	18.5	5.90	0.22
0251+393	Q	0.289	1993.54	C1	C1	89.6	0.9	C1	89.6	0.9			
0251+393	Q	0.289	1995.73	C2	C1	90.3	0.4	C1	86.4	0.9	3.7	3.90	0.98
0251+393	Q	0.289	1996.70	C2	C1	87.4	0.4	C1	81.6	1.0	3.7	5.80	1.08
0251+393	Q	0.289	1998.19	C2	C1	87.5	0.3	C1	87.4	0.4	3.4	0.10	0.50
0307+380	Q	0.816	1993.52	C1	C1	43.3	3.2	C1	43.3	3.2			
0307+380	Q	0.816	1995.73	C1	C1	34.2	2.8	C1	34.2	2.8			
0307+380	Q	0.816	1998.19	n/a	n/a			n/a					
0309+411	Q	0.134	1993.53	C1	C3	307.3	0.5	C3	301.9	3.4	5.0	5.40	3.44
0309+411	Q	0.134	1995.73	C3	C2	305.3	22.7	C2	300.8	1.2	2.0	4.50	22.73
0309+411	Q	0.134	1996.71	C5	C2	306.0	0.6	C2	301.3	0.7	9.1	4.70	0.92
0309+411	Q	0.134	1998.19	C1	C4	305.5	0.5	C4	300.1	0.6	7.6	5.40	0.78

Continued on Next Page...



Table C.2 – Continued

Source	Type	Redshift	Epoch	Component		P.A.		Error (deg)	Distance (pc)	Width (deg)	Error (deg)
				Max	Min	(deg)	(deg)				
0316+413	G	0.018	1996.71	C2	C3	192.3	175.1	0.1	0.8	17.20	0.14
0316+413	G	0.018	1999.96	C2	C1	191.7	163.6	0.1	1.2	28.10	0.32
0316+413	G	0.018	2001.03	C4	C3	190.9	171.9	0.2	0.1	19.00	0.54
0340+362	Q	1.485	1993.53	C1	C1	32.5	32.5	0.4			
0340+362	Q	1.485	1995.73	C1	C1	29.1	29.1	0.4			
0340+362	Q	1.485	1998.19	C1	C1	32.4	32.4	0.7			
0346+800	Q		1992.81	C1	C2	149.6	140.3	0.2		9.30	0.54
0346+800	Q		1994.79	C1	C2	144.4	138.3	1.2		6.10	1.63
0346+800	Q		1996.71	C1	C2	152.3	142.3	0.8		10.00	1.34
0402+379	G	0.055	1990.27	C2	C6	358.8	9.1	0.6	7.6	10.30	0.67
0402+379	G	0.055	1994.79	C2	C6	357.1	10.5	0.5	7.5	13.40	0.51
0402+379	G	0.055	1996.70	C2	C6	355.5	10.8	0.5	8.3	15.30	0.51
0444+634	Q	0.781	1992.81	C2	C4	182.5	163.0	0.3	26.6	19.50	0.36
0444+634	Q	0.781	1994.79	C2	C1	180.5	174.0	0.8	11.6	6.50	1.00
0444+634	Q	0.781	1996.71	C2	C1	179.0	172.9	0.4	10.1	6.10	0.72
0454+844	BL	0.112	1996.71	C2	C1	167.2	150.7	0.7	2.3	16.50	1.48
0454+844	BL	0.112	1999.96	C2	C1	172.8	153.9	0.5	2.4	18.90	0.78
0454+844	BL	0.112	2001.03	C2	C1	169.7	150.9	0.6	1.9	18.80	1.25
0537+531	Q	1.275	1993.25	C1	C1	317.9	317.9	0.1			
0537+531	Q	1.275	1995.73	C1	C1	318.5	318.5	0.1			
0537+531	Q	1.275	1998.19	C1	C1	318.5	318.5	0.2			
0537+531	Q	1.275	1999.98	C1	C1	319.2	319.2	0.2			
0546+726	Q	1.555	1994.79	C1	C2	300.9	300.5	0.5	25.6	0.40	0.78
0546+726	Q	1.555	1996.70	C1	C2	300.5	297.1	0.3	24.5	3.40	0.50
0546+726	Q	1.555	1999.98	C1	C2	299.4	296.8	0.3	26.2	2.60	0.32
0554+580	Q	0.904	1993.25	C1	C2	283.9	283.7	0.8	19.0	0.20	0.85
0554+580	Q	0.904	1995.73	C2	C1	285.6	283.7	0.4	18.9	1.90	0.45
0554+580	Q	0.904	1996.71	C2	C1	285.1	282.9	0.6	17.3	2.20	0.67
0554+580	Q	0.904	1998.19	C2	C1	287.7	280.9	0.5	19.2	6.80	0.54

Continued on Next Page...

Table C.2 – Continued

Source	Type	Redshift	Epoch	Component		P.A. (deg)	Error (deg)	Component	P.A. (deg)	Error (deg)	Distance (pc)	Width (deg)	Error (deg)
				Max	Min								
0600+442	G	1.136	1995.73	C2	C1	312.3	0.2	n/a	284.3	0.6	14.1	28.00	0.63
0600+442	G	1.136	1998.19	C2	C1	305.9	0.1	n/a	287.4	0.3	12.2	18.50	0.32
0600+442	G	1.136	1999.96	C2	C1	305.1	0.2	n/a	289.2	0.7	14.1	15.90	0.73
0602+673	Q	1.950	1990.27	C1	C1	160.7	0.4	n/a	160.7	0.4			
0602+673	Q	1.950	1993.53	C1	C1	175.4	0.5	n/a	175.4	0.5			
0602+673	Q	1.950	1996.71	C1	C1	171.0	0.6	n/a	171.0	0.6			
0604+728	Q	0.986	1992.81	n/a	n/a			n/a					
0604+728	Q	0.986	1994.79	n/a	n/a			n/a					
0604+728	Q	0.986	1996.70	n/a	n/a			n/a					
0604+728	Q	0.986	1999.98	n/a	n/a			n/a					
0609+607	Q	2.702	1993.25	C2	C3	162.8	0.2	n/a	142.1	0.4	29.4	20.70	0.44
0609+607	Q	2.702	1995.73	C2	C3	163.4	0.2	n/a	138.5	0.4	28.2	24.90	0.45
0609+607	Q	2.702	1998.19	C2	C3	164.1	0.1	n/a	142.3	0.1	24.3	21.80	0.14
0615+820	Q	0.710	1990.27	n/a	n/a			n/a					
0615+820	Q	0.710	1993.53	n/a	n/a			n/a					
0615+820	Q	0.710	1996.71	n/a	n/a			n/a					
0620+389	Q	3.469	1991.52	C1	C1	148.4	0.5	n/a	148.4	0.5			
0620+389	Q	3.469	1993.53	C1	C1	141.5	0.8	n/a	141.5	0.8			
0620+389	Q	3.469	1996.71	C1	C1	140.1	1.7	n/a	140.1	1.7			
0620+389	Q	3.469	1999.98	C1	C1	130.5	0.3	n/a	130.5	0.3			
0621+446	BL		1995.75	n/a	n/a			n/a					
0621+446	BL		1998.19	n/a	n/a			n/a					
0621+446	BL		1999.96	n/a	n/a			n/a					
0627+532	Q	2.204	1993.52	C3	C2	50.3	0.2	n/a	46.1	0.2	6.9	4.20	0.28
0627+532	Q	2.204	1995.73	C3	C2	52.5	0.2	n/a	46.2	0.2	7.8	6.30	0.28
0627+532	Q	2.204	1998.19	C3	C1	51.8	0.1	n/a	39.5	1.0	23.4	12.30	1.00
0633+596	na		1993.25	C1	C2	243.3	0.4	n/a	237.5	0.2		5.80	0.45
0633+596	na		1995.73	C1	C2	244.5	0.4	n/a	238.7	0.2		5.80	0.45
0633+596	na		1998.19	C1	C2	244.0	0.3	n/a	237.3	0.2		6.70	0.36

Continued on Next Page...

Table C.2 – Continued

Source	Type	Redshift	Epoch	Component		P.A. (deg)	Error (deg)	Component	P.A. (deg)	Error (deg)	Distance (pc)	Width (deg)	Error (deg)
				Max	Min								
0633+734	Q	1.850	1992.81	C1	C3	358.3	0.1	351.4	0.3	18.7	6.90	0.32	
0633+734	Q	1.850	1994.79	C2	C0	357.3	1.3	1.3	1.2	16.2	4.00	1.77	
0633+734	Q	1.850	1996.71	C1	C3	356.4	0.4	349.5	0.7	17.9	6.90	0.81	
0636+680	Q	3.174	1992.51	n/a	n/a								
0636+680	Q	3.174	1994.79	n/a	n/a								
0636+680	Q	3.174	1996.70	n/a	n/a								
0641+393	Q	1.266	1993.52	C2	C1	357.0	0.2	5.0	0.4	25.1	8.00	0.45	
0641+393	Q	1.266	1995.75	C2	C1	359.6	0.2	2.2	0.5	26.8	2.60	0.54	
0641+393	Q	1.266	1998.19	C2	C1	358.4	0.1	352.9	0.3	30.7	5.50	0.32	
0641+393	Q	1.266	1999.96	C2	C1	359.2	0.1	341.8	0.5	28.9	17.40	0.51	
0642+449	Q	3.396	1991.52	C1	C1	92.6	0.4	92.6	0.4				
0642+449	Q	3.396	1992.51	C1	C1	90.6	0.4	90.6	0.4				
0642+449	Q	3.396	1996.70	C1	C1	91.5	0.3	91.5	0.3				
0646+600	Q	0.455	1991.52	C1	C2	216.2	0.2	215.4		9.1	0.80	0.20	
0646+600	Q	0.455	1994.79	C2	C2	216.4	0.1	216.4	0.1				
0646+600	Q	0.455	1998.19	C1	C2	219.6	0.1	216.1		8.9	3.50	0.10	
0650+371	Q	1.982	1990.27	C1	C2	46.2	0.3	34.6	2.6	5.0	11.60	2.62	
0650+371	Q	1.982	1993.53	C1	C2	51.5	1.3	41.8	0.6	3.4	9.70	1.43	
0650+371	Q	1.982	1996.70	C1	C2	49.2	0.4	44.1	0.7	9.6	5.10	0.81	
0650+453	Q	0.933	1993.52	n/a	n/a								
0650+453	Q	0.933	1998.19	n/a	n/a								
0650+453	Q	0.933	1999.98	n/a	n/a								
0651+410	G	0.022	1993.52	C1	C2	167.0	0.4	160.1	0.6	0.4	6.90	0.72	
0651+410	G	0.022	1995.75	C1	C3	167.8	0.7	144.2	1.3	1.3	23.60	1.48	
0651+410	G	0.022	1996.71	C1	C3	168.1	1.3	139.0	2.1	1.2	29.10	2.47	
0651+410	G	0.022	1998.19	C1	C3	162.0	0.4	136.7	0.8	1.4	25.30	0.89	
0700+470	G		1993.53	C1	C2	154.8	0.3	126.9	0.2		27.90	0.36	
0700+470	G		1995.75	C1	C5	153.8	0.4	96.2	0.2		57.60	0.43	
0700+470	G		1998.19	C1	C5	151.8	0.2	94.6	0.2		57.20	0.27	

Continued on Next Page...

Table C.2 – Continued

Source	Type	Redshift	Epoch	Component		P.A. (deg)	Error (deg)	Component	P.A. (deg)	Error (deg)	Distance (pc)	Width (deg)	Error (deg)
				Max	Min								
0702+612	Q		1993.25	C2	C1	74.7	0.2		68.3	1.7		6.40	1.71
0702+612	Q		1995.73	C2	C1	72.4	0.2		66.2	0.6		6.20	0.63
0702+612	Q		1998.19	C1	C2	74.6	0.5		69.9	0.6		4.70	0.77
0702+612	Q		1999.98	C2	C1	73.5	0.2		64.3	1.1		9.20	1.12
0707+476	Q	1.292	1990.27	C1	C2	346.4	0.4		3.3	1.9	14.0	16.90	1.94
0707+476	Q	1.292	1993.52	C1	C3	327.4	6.7		2.8	0.4	22.9	35.40	6.71
0707+476	Q	1.292	1996.70	C2	C3	356.1	0.5		11.3	0.4	15.3	15.20	0.64
0707+476	Q	1.292	1999.98	C1	C2	340.7	0.3		1.8	0.4	11.6	21.10	0.50
0710+439	G	0.518	1996.71	C1	C1	7.4	0.2		7.4	0.2			
0710+439	G	0.518	1999.96	C1	C1	4.4	0.2		4.4	0.2			
0710+439	G	0.518	2001.03	C1	C1	5.6	0.2		5.6	0.2			
0711+356	Q	1.620	1996.71	C1	C2	339.5	0.3		338.2	0.1	27.4	1.30	0.32
0711+356	Q	1.620	1999.96	C1	C1	336.3	0.1		336.3	0.1			
0711+356	Q	1.620	2001.03	C1	C2	338.8	0.2		336.4	0.1	25.6	2.40	0.22
0714+457	Q	0.940	1993.52	C1	C3	142.0	0.7		125.3	0.6	23.3	16.70	0.92
0714+457	Q	0.940	1995.75	C1	C2	142.7	0.4		124.5	0.4	17.2	18.20	0.57
0714+457	Q	0.940	1998.19	C1	C2	144.1	0.3		125.5	0.6	19.0	18.60	0.67
0716+714	BL	0.310	1992.81	C1	C4	23.1	0.4		14.1	1.1	17.8	9.00	1.17
0716+714	BL	0.310	1994.78	C2	C1	21.2	1.5		10.9	2.1	6.0	10.30	2.58
0716+714	BL	0.310	1996.70	C3	C1	17.6	1.6		15.8	4.3	13.0	1.80	4.59
0716+714	BL	0.310	1999.97	C4	C1	15.1	0.5		7.5	0.3	17.6	7.60	0.58
0716+714	BL	0.310	2001.03	C2	C4	16.5	1.8		12.2	0.3	14.8	4.30	1.82
0718+793	na		1992.81	n/a	n/a								
0718+793	na		1994.78	n/a	n/a								
0718+793	na		1996.71	n/a	n/a								
0724+571	Q	0.426	1993.25	C2	C1	154.4	0.7		152.2	0.3	7.4	2.20	0.76
0724+571	Q	0.426	1995.75	C3	C0	154.2	0.4		150.5	0.6	26.6	3.70	0.72
0724+571	Q	0.426	1998.19	C2	C0	153.2	0.8		148.8	0.3	12.8	4.40	0.85
0727+409	Q	2.500	1995.73	C2	C1	304.6	0.3		299.3	0.7	5.8	5.30	0.76

Continued on Next Page...

Table C.2 – Continued

Source	Type	Redshift	Epoch	Component		P.A.		Error (deg)	Distance (pc)	Width (deg)	Error (deg)
				Max	Min	(deg)	(deg)				
0727+409	Q	2.500	1998.19	C2	C1	305.2	300.6	0.1	6.7	4.60	0.32
0727+409	Q	2.500	1999.96	C2	C1	305.3	299.7	0.4	8.0	5.60	0.98
0730+504	Q	0.720	1992.51	C2	C3	216.2	207.5	0.3	7.2	8.70	0.36
0730+504	Q	0.720	1994.79	C2	C1	213.2	199.6	1.7	7.9	13.60	1.84
0730+504	Q	0.720	1996.71	C1	C3	211.8	208.2	0.1	16.3	3.60	0.14
0731+479	Q	0.782	1993.52	C3	C1	271.7	255.4	0.5	14.5	16.30	0.64
0731+479	Q	0.782	1995.75	C3	C1	270.9	255.5	0.3	18.7	15.40	0.42
0731+479	Q	0.782	1998.19	C3	C1	270.3	253.0	0.1	16.1	17.30	0.22
0733+597	G	0.041	1996.71	C2	C4	357.6	347.8	0.5	2.9	9.80	0.64
0733+597	G	0.041	1998.19	C2	C1	358.9	341.6	0.3	1.7	17.30	0.76
0733+597	G	0.041	1999.96	C2	C1	354.3	340.0	0.3	2.1	14.30	0.85
0738+491	Q	2.320	1993.52	C1	C1	9.1	9.1	1.7			
0738+491	Q	2.320	1995.75	C1	C1	0.4	0.4	1.0			
0738+491	Q	2.320	1998.19	C1	C1	4.1	4.1	0.5			
0740+768	G		1992.81	C2	C1	248.4	243.3	0.1		5.10	0.41
0740+768	G		1994.78	C2	C1	248.4	242.8	0.2		5.60	0.82
0740+768	G		1996.71	C2	C1	248.8	246.7	0.1		2.10	0.61
0743+744	Q	1.629	1993.53	C1	C2	27.3	23.2	0.2	9.2	4.10	0.36
0743+744	Q	1.629	1995.73	C1	C2	28.9	23.0	0.2	7.6	5.90	0.36
0743+744	Q	1.629	1998.20	C1	C2	25.5	22.1	0.2	7.4	3.40	0.54
0746+483	Q	1.951	1991.52	C1	C2	284.3	268.0	0.2	13.8	16.30	0.55
0746+483	Q	1.951	1993.52	C1	C2	281.8	266.0	0.3	16.0	15.80	0.61
0746+483	Q	1.951	1996.71	C1	C2	271.5	267.3	1.1	16.3	4.20	1.15
0749+426	Q	3.590	1992.51	n/a	n/a						
0749+426	Q	3.590	1994.78	n/a	n/a						
0749+426	Q	3.590	1996.73	n/a	n/a						
0749+540	BL		1993.25	C1	C2	46.6	7.5	0.3		39.10	0.42
0749+540	BL		1995.75	C1	C2	38.0	7.9	0.8		30.10	1.00
0749+540	BL		1998.19	n/a	n/a						

Continued on Next Page...

Table C.2 – Continued

Source	Type	Redshift	Epoch	Component		P.A. (deg)	Error (deg)	Component	P.A. (deg)	Error (deg)	Distance (pc)	Width (deg)	Error (deg)
				Max	Min								
0800+618	Q	3.044	1995.75	C1	C3	176.1	0.9		129.3	0.5	30.1	46.80	1.03
0800+618	Q	3.044	1998.68	C1	C2	177.4	0.2		160.4	0.3	9.7	17.00	0.36
0800+618	Q	3.044	1999.96	C1	C3	175.7	0.6		124.0	0.3	30.1	51.70	0.67
0803+452	Q	2.102	1993.52	C1	C1	232.2	0.8		232.2	0.8			
0803+452	Q	2.102	1995.73	C1	C1	232.7	0.2		232.7	0.2			
0803+452	Q	2.102	1998.19	C1	C1	233.7	0.1		233.7	0.1			
0804+499	Q	1.432	1996.73	C2	C1	151.6	0.5		127.7	0.3	17.5	23.90	0.58
0804+499	Q	1.432	1999.96	C2	C1	154.5	0.5		137.5	0.1	23.0	17.00	0.51
0804+499	Q	1.432	2001.03	C2	C1	159.3	0.6		136.1	0.1	23.2	23.20	0.61
0805+410	Q	1.420	1991.52	C2	C1	28.3	0.3		12.3	0.5	14.0	16.00	0.58
0805+410	Q	1.420	1993.52	C2	C1	38.1	0.5		20.1	0.3	15.2	18.00	0.58
0805+410	Q	1.420	1996.73	C2	C1	38.3	0.6		25.7	0.5	14.9	12.60	0.78
0806+573	Q	0.611	1992.51	C1	C1	276.7	0.6		276.7	0.6			
0806+573	Q	0.611	1994.78	C1	C1	263.4	0.7		263.4	0.7			
0806+573	Q	0.611	1996.73	C2	C2	262.4	1.8		262.4	1.8			
0812+367	Q	1.025	1990.27	C1	C1	349.4	0.1		349.4	0.1			
0812+367	Q	1.025	1992.51	C1	C1	351.2	0.1		351.2	0.1			
0812+367	Q	1.025	1996.73	C1	C1	353.4	0.2		353.4	0.2			
0814+425	BL	0.530	1996.73	C2	C1	139.8	0.3		91.5	0.2	2.8	48.30	0.36
0814+425	BL	0.530	1999.96	C3	C1	118.9	0.4		87.3	0.1	8.0	31.60	0.41
0814+425	BL	0.530	2001.03	C2	C1	139.8	0.6		88.6	0.1	1.5	51.20	0.61
0820+560	Q	1.409	1990.28	C1	C2	100.9	1.5		85.5	2.1	6.3	15.40	2.58
0820+560	Q	1.409	1992.51	C2	C2	93.0	0.6		93.0	0.6			
0820+560	Q	1.409	1996.73	C1	C3	101.1	0.5		88.3	0.3	20.3	12.80	0.58
0821+394	Q	1.216	1990.27	n/a	n/a								
0821+394	Q	1.216	1992.51	C2	C1	315.6	2.3		309.7	2.0	18.1	5.90	3.05
0821+394	Q	1.216	1996.73	C1	C2	317.3	0.7		313.3	0.8	13.5	4.00	1.06
0821+621	Q	0.542	1992.51	n/a	n/a								
0821+621	Q	0.542	1994.78	n/a	n/a								

Continued on Next Page...

Table C.2 – Continued

Source	Type	Redshift	Epoch	Component		P.A. (deg)	Error (deg)	Component	P.A. (deg)	Error (deg)	Distance (pc)	Width (deg)	Error (deg)
				Max	Min								
0821+621	Q	0.542	1996.73	n/a				n/a					
0824+355	Q	2.249	1995.73	n/a				n/a					
0824+355	Q	2.249	1998.19	n/a				n/a					
0831+557	G	0.240	1996.73	C4		333.3	0.3	C5	13.0	0.2	3.7	39.70	0.36
0831+557	G	0.240	1999.96	C4		348.1	0.2	C5	17.1	0.3	1.2	29.00	0.36
0831+557	G	0.240	2001.03	C4		336.2	0.2	C5	9.1	0.3	0.2	32.90	0.36
0833+416	Q	1.298	1996.73	C1		9.4	0.1	C2	7.3	0.2	8.8	2.10	0.22
0833+416	Q	1.298	1998.19	C1		8.4	0.1	C2	7.5	0.1	10.9	0.90	0.14
0833+416	Q	1.298	1999.96	C2		7.3	0.1	C1	5.9	0.4	10.0	1.40	0.41
0833+585	Q	2.101	1990.28	C1		81.4	0.2	C1	81.4	0.2			
0833+585	Q	2.101	1992.51	C1		79.3	0.2	C1	79.3	0.2			
0833+585	Q	2.101	1995.75	C1		83.1	0.1	C1	83.1	0.1			
0836+710	Q	2.180	1996.73	C1		221.9	0.2	C2	215.3	0.1	15.8	6.60	0.21
0836+710	Q	2.180	1999.96	C1		223.8	0.6	C2	215.2	0.1	18.0	8.60	0.61
0836+710	Q	2.180	2001.03	C1		219.6	0.1	C2	213.1	0.1	19.2	6.50	0.13
0843+575	G		1993.25	C3		239.7	0.7	C1	215.8	0.4		23.90	0.81
0843+575	G		1995.73	C3		243.3	0.4	C1	216.9	0.3		26.40	0.50
0843+575	G		1996.70	C3		242.5	0.9	C1	216.8	0.3		25.70	0.95
0843+575	G		1998.19	C3		246.3	0.2	C1	216.9	0.1		29.40	0.22
0847+379	G	0.407	1995.73	C1		9.5	0.6	C3	4.2	1.8	23.4	5.30	1.90
0847+379	G	0.407	1996.70	C1		8.9	1.1	C2	8.2	0.9	5.1	0.70	1.42
0847+379	G	0.407	1998.19	C2		8.3	0.6	C3	2.6	0.9	15.0	5.70	1.08
0850+581	Q	1.322	1996.70	C1		166.1	0.2	C2	153.6	0.1	12.8	12.50	0.22
0850+581	Q	1.322	1999.96	C1		171.7	0.3	C2	154.4	0.1	14.0	17.30	0.32
0850+581	Q	1.322	2001.03	C1		165.4	0.1	C2	154.7	0.1	15.0	10.70	0.14
0859+470	Q	1.462	1996.70	C1		352.4	0.1	C2	2.1	0.1	21.1	9.70	0.14
0859+470	Q	1.462	1999.96	C1		345.3	0.1	C2	2.1	0.1	20.7	16.80	0.14
0859+470	Q	1.462	2001.03	C1		346.1	0.1	C2	0.3		22.9	14.20	0.10
0859+681	Q	1.499	1992.51	C1		14.6	0.3	C2	14.5	0.2	13.1	0.10	0.36

Continued on Next Page...

Table C.2 – Continued

Source	Type	Redshift	Epoch	Component		P.A. (deg)	Error (deg)	Component	P.A. (deg)	Error (deg)	Distance (pc)	Width (deg)	Error
				Max	Min								
0859+681	Q	1.499	1994.78	C2	C1	13.8	0.4	C1	9.6	0.7	14.8	4.20	0.81
0859+681	Q	1.499	1996.73	C1	C2	14.5	0.3	C2	13.8	0.2	14.2	0.70	0.36
0900+520	Q	1.537	1993.25	C2	C1	268.9	2.0	C1	227.2	0.8	8.5	41.70	2.15
0900+520	Q	1.537	1995.73	C2	C1	272.1	1.5	C1	228.4	0.8	12.0	43.70	1.70
0900+520	Q	1.537	1998.19	C1	C1	229.7	2.4	C1	229.7	2.4			
0902+490	Q	2.690	1993.52	C1	C1	320.1	0.2	C1	320.1	0.2			
0902+490	Q	2.690	1995.73	C1	C1	322.3	0.2	C1	322.3	0.2			
0902+490	Q	2.690	1998.19	C1	C1	321.6	0.1	C1	321.6	0.1			
0917+449	Q	2.180	1991.52	C1	C1	173.6		C1	173.6				
0917+449	Q	2.180	1993.52	C1	C1	176.8	0.1	C1	176.8	0.1			
0917+449	Q	2.180	1996.70	C1	C1	179.1	0.1	C1	179.1	0.1			
0917+624	Q	1.446	1991.52	C1	C1	341.7	0.1	C1	341.7	0.1			
0917+624	Q	1.446	1993.53	C1	C1	347.6	0.1	C1	347.6	0.1			
0917+624	Q	1.446	1996.70	C1	C1	339.0	0.2	C1	339.0	0.2			
0917+624	Q	1.446	2001.03	C1	C1	343.0	0.1	C1	343.0	0.1			
0923+392	Q	0.699	1996.70	C1	C1	85.6	1.6	C1	85.6	1.6			
0923+392	Q	0.699	1999.96	C1	C1	106.8	2.3	C1	106.8	2.3			
0923+392	Q	0.699	2001.03	C1	C1	59.0	2.3	C1	59.0	2.3			
0925+504	BL	0.370	1993.53	C1	C1	127.0	0.8	C1	127.0	0.8	23.1	7.00	0.92
0925+504	BL	0.370	1995.73	C2	C1	131.1	0.6	C1	124.1	0.7	23.7	12.70	1.30
0925+504	BL	0.370	1998.19	C2	C2	132.0	0.5	C1	119.3	1.2		19.30	2.16
0927+352	BL		1993.52	C1	C1	120.7	2.1	C2	101.4	0.5		18.30	1.48
0927+352	BL		1995.73	C1	C1	120.8	1.3	C2	102.5	0.7		21.60	0.67
0927+352	BL		1998.19	C1	C1	123.0	0.6	C2	101.4	0.3			
0929+533	Q	0.595	1993.25	C1	C1	135.8	0.2	C1	135.8	0.2			
0929+533	Q	0.595	1995.73	C1	C1	132.2	0.6	C1	132.2	0.6			
0929+533	Q	0.595	1998.19	C1	C1	134.3	0.1	C1	134.3	0.1			
0930+493	Q	2.582	1993.52	C2	C3	45.8	0.5	C3	44.1	0.3	6.4	1.70	0.58
0930+493	Q	2.582	1995.75	C3	C2	44.9	0.2	C2	44.1	0.9	6.0	0.80	0.92

Continued on Next Page...



Table C.2 – Continued

Source	Type	Redshift	Epoch	Component		P.A.		Component	P.A.		Distance	Width		Error
				Max	Min	(deg)	(deg)		(deg)	(deg)		(pc)	(deg)	
0930+493	Q	2.582	1998.19	C3	C2	52.0	43.6	C2	43.6	0.1	4.7	8.40	0.22	
0942+468	G	0.639	1993.52	C1	C2	45.4	36.2	C2	36.2	0.7	11.4	9.20	0.81	
0942+468	G	0.639	1995.75	C3	C2	358.8	34.4	C2	34.4	0.4	9.5	35.60	0.64	
0942+468	G	0.639	1996.70	C3	C1	355.4	50.7	C1	50.7	0.5	21.2	55.30	0.94	
0942+468	G	0.639	1998.19	C3	C2	357.2	34.1	C2	34.1	0.3	8.2	36.90	0.58	
0945+408	Q	1.252	1996.72	C1	C1	114.3	114.3	C1	114.3	2.1				
0945+408	Q	1.252	1999.96	C1	C1	118.7	118.7	C1	118.7	0.5				
0945+408	Q	1.252	2001.03	C1	C1	124.8	124.8	C1	124.8	0.4				
0949+354	Q	1.875	1993.52	C1	C2	167.0	166.4	C2	166.4	0.3	10.4	0.60	0.42	
0949+354	Q	1.875	1995.75	C1	C2	167.6	165.4	C2	165.4	0.3	9.9	2.20	0.58	
0949+354	Q	1.875	1998.19	C2	C1	166.6	162.7	C1	162.7	0.2	13.0	3.90	0.22	
0950+748	G	0.695	1992.81	C1	C2	266.9	258.9	C2	258.9	0.4	8.9	8.00	0.50	
0950+748	G	0.695	1994.78	C1	C2	259.9	252.9	C2	252.9	1.6	12.3	7.00	1.89	
0950+748	G	0.695	1996.70	C1	C1	261.1	261.1	C1	261.1	2.0				
0954+556	Q	0.895	1996.70	n/a	n/a									
0954+556	Q	0.895	1999.96	n/a	n/a									
0954+658	BL	0.368	1996.70	C1	C3	339.6	288.8	C3	288.8	0.7	13.5	50.80	0.81	
0954+658	BL	0.368	1999.96	C3	C3	289.0	289.0	C3	289.0	0.4				
0954+658	BL	0.368	2001.03	C1	C3	329.8	288.0	C3	288.0	0.6	13.8	41.80	0.78	
0955+476	Q	1.873	1991.52	C1	C1	127.3	127.3	C1	127.3	1.2				
0955+476	Q	1.873	1993.53	C1	C1	119.1	119.1	C1	119.1	1.0				
0955+476	Q	1.873	1996.70	C1	C1	134.0	134.0	C1	134.0	0.5				
1003+830	G	0.322	1991.52	C4	C1	86.8	75.9	C1	75.9	0.5	26.8	10.90	0.50	
1003+830	G	0.322	1993.52	C4	C1	84.9	72.9	C1	72.9	0.7	29.0	12.00	0.71	
1003+830	G	0.322	1996.71	C4	C1	83.7	78.5	C1	78.5	0.8	31.5	5.20	0.81	
1010+350	Q	1.414	1993.52	C2	C1	99.0	98.6	C1	98.6	0.5	22.0	0.40	1.49	
1010+350	Q	1.414	1995.75	C1	C1	98.4	91.3	C1	91.3	0.5	19.1	7.10	0.54	
1010+350	Q	1.414	1998.19	C1	C1	97.5	97.5	C1	97.5	0.2				
1014+615	Q	2.800	1992.81	C1	C1	249.8	249.8	C1	249.8	0.2				

Continued on Next Page...

Table C.2 – Continued

Source	Type	Redshift	Epoch	Component		P.A.		Component	P.A.		Distance	Width		Error
				Max	Min	(deg)	(deg)		(deg)	(deg)		(pc)	(deg)	
1014+615	Q	2.800	1994.78	C1	C1	252.7	0.4	C1	252.7	0.4				
1014+615	Q	2.800	1996.70	C1	C1	254.5	0.2	C1	254.5	0.2		18.50	3.91	
1015+359	Q	1.226	1991.80	C1	C3	199.8	3.9	C3	181.3	0.2	26.7	7.70	1.04	
1015+359	Q	1.226	1993.52	C1	C3	188.4	1.0	C3	180.7	0.3	25.7	7.90	0.22	
1015+359	Q	1.226	1996.72	C1	C3	188.2	0.1	C3	180.3	0.2	27.7	8.20	0.92	
1020+400	Q	1.254	1991.79	C2	C1	319.7	0.2	C1	311.5	0.9	16.5	7.30	1.61	
1020+400	Q	1.254	1993.53	C2	C1	318.6	0.2	C1	311.3	1.6	26.5	13.00	0.32	
1020+400	Q	1.254	1996.72	C2	C1	319.4	0.1	C1	306.4	0.3	27.6	6.90	0.36	
1030+398	G	1.095	1993.52	C2	C1	42.7	0.2	C1	35.8	0.3	13.3	15.40	0.45	
1030+398	G	1.095	1995.75	C2	C1	44.2	0.2	C1	28.8	0.4	9.1	14.20	0.22	
1030+398	G	1.095	1998.19	C2	C1	44.5	0.1	C1	30.3	0.2	11.6	7.50	0.36	
1030+415	Q	1.120	1991.79	C1	C2	353.0	0.2	C2	0.5	0.3	27.5	9.60	0.99	
1030+415	Q	1.120	1993.52	C2	C1	359.1	0.7	C1	349.5	0.7	28.2	4.80	1.04	
1030+415	Q	1.120	1996.72	C1	C2	357.1	1.0	C2	1.9	0.3	26.1	1.40	1.08	
1030+611	Q	1.401	1992.81	C2	C1	167.1	1.0	C1	165.7	0.3	2.7	9.50	1.10	
1030+611	Q	1.401	1994.78	C2	C1	170.2	0.8	C1	160.7	0.8	3.3	7.90	0.54	
1030+611	Q	1.401	1996.72	C2	C1	168.8	0.2	C1	160.9	0.5	3.1			
1031+567	G	0.460	1996.72	C1	C1	56.7	0.2	C1	56.7	0.2				
1031+567	G	0.460	1999.96	C1	C1	59.0	0.1	C1	59.0	0.1				
1031+567	G	0.460	2001.03	C1	C1	57.2	0.3	C1	57.2	0.3				
1038+528	Q	0.677	1993.52	C1	C1	22.0	0.2	C1	22.0	0.2				
1038+528	Q	0.677	1995.75	C1	C1	18.6	0.2	C1	18.6	0.2				
1038+528	Q	0.677	1998.19	C1	C1	18.5	0.4	C1	18.5	0.4				
1039+811	Q	1.254	1992.81	C1	C3	296.4	0.2	C3	290.8	0.3	17.9	5.60	0.38	
1039+811	Q	1.254	1994.78	C1	C3	296.2	0.5	C3	291.9	0.5	17.1	4.30	0.71	
1039+811	Q	1.254	1996.71	C1	C3	294.1	0.2	C3	289.9	0.3	18.4	4.20	0.36	
1041+536	Q	1.897	1993.52	C3	C2	167.6	0.8	C2	141.3	1.0	19.3	26.30	1.28	
1041+536	Q	1.897	1995.75	C3	C1	174.4	0.4	C1	141.6	0.8	27.2	32.80	0.89	
1041+536	Q	1.897	1998.19	C3	C1	172.1	0.3	C1	139.8	0.6	30.6	32.30	0.67	

Continued on Next Page...

Table C.2 – Continued

Source	Type	Redshift	Epoch	Component		P.A.		Component	P.A.		Distance	Width	Error
				Max	Min	(deg)	(deg)		(deg)	(deg)			
1044+719	Q	1.150	1991.52	C1	C1	118.9	0.4	C1	118.9	0.4			
1044+719	Q	1.150	1993.52	C1	C1	104.4	0.6	C1	104.4	0.6			
1044+719	Q	1.150	1996.71	C1	C1	92.2	0.2	C1	92.2	0.2			
1053+704	Q	2.492	1991.52	C1	C1	196.3	0.5	C1	196.3	0.5			
1053+704	Q	2.492	1993.52	C1	C1	203.2	0.7	C1	203.2	0.7			
1053+704	Q	2.492	1996.71	C1	C1	216.2	0.9	C1	216.2	0.9			
1053+815	G	0.706	1991.52	C1	C1	225.0	0.4	C1	225.0	0.4			
1053+815	G	0.706	1993.53	C1	C1	232.2	0.6	C1	232.2	0.6			
1053+815	G	0.706	1996.71	C1	C1	231.4	1.6	C1	231.4	1.6			
1058+629	Q	0.663	1992.81	C1	C1	26.9	0.4	C1	26.9	0.4			
1058+629	Q	0.663	1994.78	C1	C1	20.1	1.0	C1	20.1	1.0			
1058+629	Q	0.663	1996.72	C1	C1	24.7	0.6	C1	24.7	0.6			
1058+726	Q	1.460	1991.52	C2	C1	358.8	0.1	C1	8.3	0.4	10.1	9.50	0.41
1058+726	Q	1.460	1993.52	C1	C1	349.0	0.6	C2	5.0	0.1	12.0	16.00	0.61
1058+726	Q	1.460	1996.71	C3	C1	12.0	0.1	C1	4.4	2.0	29.3	7.60	2.00
1058+726	Q	1.460	1999.98	C1	C1	11.8	0.3	C2	8.7	0.1	15.1	3.10	0.32
1101+384	BL	0.031	1993.53	C1	C1	331.1	0.5	C2	322.2	1.7	2.3	8.90	1.77
1101+384	BL	0.031	1996.72	C2	C2	324.3	0.6	C1	319.9	0.6	2.2	4.40	0.87
1101+384	BL	0.031	1999.96	C1	C1	319.6	0.3	C2	318.0	0.3	1.9	1.60	0.42
1105+437	Q	1.226	1993.52	n/a	n/a								
1105+437	Q	1.226	1995.75	C3	C3	247.8	1.7	C1	213.1	0.7	31.1	34.70	1.84
1105+437	Q	1.226	1998.19	C3	C3	242.1	1.3	C1	217.9	0.3	34.1	24.20	1.33
1106+380	G	2.290	1995.73	C2	C2	207.7	0.1	C1	206.2	0.3	22.5	1.50	0.32
1106+380	G	2.290	1998.19	C2	C2	208.0	0.1	C1	207.2	0.2	22.2	0.80	0.22
1106+380	G	2.290	1999.96	C2	C2	209.7	0.1	C1	203.5	0.3	19.4	6.20	0.32
1107+607	na		1992.81	C2	C2	24.8	0.3	C3	15.4	0.2		9.40	0.36
1107+607	na		1994.78	C1	C1	51.3	2.7	C3	13.8	1.2		37.50	2.95
1107+607	na		1996.72	C1	C1	41.6	0.9	C2	20.2	0.8		21.40	1.20
1124+455	Q	1.811	1993.52	C2	C2	354.9	0.1	C1	347.3	0.2	18.3	7.60	0.22

Continued on Next Page...

Table C.2 – Continued

Source	Type	Redshift	Epoch	Component		P.A. (deg)	Error (deg)	Component	P.A. (deg)	Error (deg)	Distance (pc)	Width (deg)	Error (deg)
				Max	Min								
1124+455	Q	1.811	1995.73	C2	C1	355.3	0.1	n/a	347.4	0.2	22.5	7.90	0.22
1124+455	Q	1.811	1998.20	C2	C1	355.3	0.1	n/a	348.7	0.1	19.0	6.60	0.10
1124+571	Q	2.890	1992.81	C1	C1	87.7	0.2	n/a	87.7	0.2			
1124+571	Q	2.890	1994.78	C1	C1	88.8	0.8	n/a	88.8	0.8			
1124+571	Q	2.890	1996.72	C1	C1	81.7	0.3	n/a	81.7	0.3			
1125+596	Q	1.779	1992.81	n/a	n/a								
1125+596	Q	1.779	1994.78	C1	C1	265.2	1.5	n/a	265.2	1.5			
1125+596	Q	1.779	1996.72	C1	C1	255.0	1.3	n/a	255.0	1.3			
1128+385	Q	1.733	1992.32	C1	C1	200.4	0.4	n/a	200.4	0.4			
1128+385	Q	1.733	1994.79	C1	C1	201.5	0.4	n/a	201.5	0.4			
1128+385	Q	1.733	1996.72	C1	C1	202.2	0.2	n/a	202.2	0.2			
1143+590	Q	1.982	1992.81	C1	C1	55.3	0.2	n/a	55.3	0.2			
1143+590	Q	1.982	1994.78	C1	C1	58.1	0.4	n/a	58.1	0.4			
1143+590	Q	1.982	1996.72	C1	C1	61.6	0.3	n/a	61.6	0.3			
1144+352	G	0.063	1993.52	C2	C1	339.2	0.6	n/a	280.3	1.8	4.5	58.90	1.90
1144+352	G	0.063	1995.73	C2	C1	341.0	0.5	n/a	268.2	0.8	3.9	72.80	0.94
1144+352	G	0.063	1996.72	C2	C1	351.0	1.4	n/a	283.7	1.6	3.1	67.30	2.13
1144+402	Q	1.088	1992.32	n/a	n/a								
1144+402	Q	1.088	1994.78	n/a	n/a								
1144+402	Q	1.088	1996.72	n/a	n/a								
1144+542	Q	2.201	1991.52	C2	C1	192.7	0.2	n/a	177.6	0.1	13.2	15.10	0.22
1144+542	Q	2.201	1993.52	C2	C1	192.6	0.4	n/a	182.3	0.3	12.2	10.30	0.50
1144+542	Q	2.201	1996.72	C2	C1	187.0	0.2	n/a	180.6	0.7	12.9	6.40	0.73
1146+596	G	0.011	1992.81	C3	C2	139.5	0.5	n/a	132.6	0.4	0.3	6.90	0.64
1146+596	G	0.011	1994.78	C1	C2	142.7	0.5	n/a	139.7	0.5	0.3	3.00	0.71
1146+596	G	0.011	1996.72	C3	C2	145.4	0.2	n/a	139.8	0.2	0.5	5.60	0.28
1150+812	Q	1.250	1992.81	C2	C4	182.3	0.1	n/a	164.1	0.1	22.1	18.20	0.17
1150+812	Q	1.250	1994.78	C1	C4	189.7	0.8	n/a	163.5	0.3	34.5	26.20	0.87
1150+812	Q	1.250	1996.71	C1	C4	187.5	0.3	n/a	160.4	0.1	34.0	27.10	0.32

Continued on Next Page...

Table C.2 – Continued

Source	Type	Redshift	Epoch	Component		P.A. (deg)	Error (deg)	Component	P.A. (deg)	Error (deg)	Distance (pc)	Width (deg)	Error
				Max	Min								
1151+408	Q	0.916	1995.73	C2	C1	72.8	0.2	57.7	0.1	11.1	15.10	0.22	
1151+408	Q	0.916	1996.72	C2	C1	72.2	0.2	54.3	0.2	9.8	17.90	0.28	
1151+408	Q	0.916	1998.19	C2	C1	72.8	0.1	60.9	0.1	10.9	11.90	0.14	
1155+486	Q	2.028	1993.52	C1	C2	284.0	1.1	252.6	1.7	11.5	31.40	2.02	
1155+486	Q	2.028	1995.73	C1	C2	275.8	1.4	246.8	0.9	14.2	29.00	1.66	
1155+486	Q	2.028	1996.72	C1	C2	264.4	1.8	244.1	1.0	15.9	20.30	2.06	
1205+544	na		1993.52	C1	C2	285.5	1.9	258.7	0.8		26.80	2.06	
1205+544	na		1995.73	C1	C4	273.5	1.8	227.7	0.6		45.80	1.90	
1205+544	na		1998.20	C1	C4	262.6	0.5	227.7	0.2		34.90	0.54	
1206+415	BL		1993.52	n/a	n/a								
1206+415	BL		1995.73	n/a	n/a								
1206+415	BL		1998.20	n/a	n/a								
1213+350	Q	0.857	1992.33	n/a	n/a								
1213+350	Q	0.857	1994.79	n/a	n/a								
1213+350	Q	0.857	1996.72	n/a	n/a								
1216+487	Q	1.076	1992.33	C2	C1	99.9	0.3	99.8	0.4	7.3	0.10	0.50	
1216+487	Q	1.076	1994.78	C2	C1	103.6	0.8	101.0	0.8	6.7	2.60	1.13	
1216+487	Q	1.076	1996.72	C1	C2	98.2	0.4	97.2	0.2	11.5	1.00	0.45	
1218+444	Q	1.345	1992.51	C1	C1	329.7	0.4	329.7	0.4				
1218+444	Q	1.345	1994.79	C1	C1	334.8	1.0	334.8	1.0				
1218+444	Q	1.345	1996.72	C1	C1	332.5	0.5	332.5	0.5				
1221+809	BL		1993.53	C1	C4	354.8	0.2	349.8	0.5		5.00	0.54	
1221+809	BL		1995.75	C3	C4	354.9	0.3	349.6	0.3		5.30	0.42	
1221+809	BL		1998.20	C1	C4	359.9	0.5	349.5	0.1		10.40	0.51	
1223+395	Q	0.623	1993.52	n/a	n/a								
1223+395	Q	0.623	1995.73	C1	C1	32.2	1.6	32.2	1.6				
1223+395	Q	0.623	1996.72	C1	C1	30.6	1.5	30.6	1.5				
1223+395	Q	0.623	1998.19	C1	C1	32.8	0.7	32.8	0.7				
1226+373	Q	1.515	1993.52	C1	C1	331.2	1.1	331.2	1.1				

Continued on Next Page...

Table C.2 – Continued

Source	Type	Redshift	Epoch	Component		P.A. (deg)	Error (deg)	Component	P.A. (deg)	Error (deg)	Distance (pc)	Width (deg)	Error (deg)
				Max	Min								
1226+373	Q	1.515	1995.73	C1	326.9	1.2	1.2	C1	326.9	1.2			
1226+373	Q	1.515	1998.20	n/a				n/a					
1239+376	Q	3.818	1993.52	n/a				n/a					
1239+376	Q	3.818	1995.73	C1	16.5	0.1	0.1	C1	16.5	0.1			
1239+376	Q	3.818	1998.20	C1	16.5	0.1	0.1	C1	16.5	0.1			
1240+381	Q	1.316	1993.52	C1	113.2	0.4	0.4	C1	113.2	0.4			
1240+381	Q	1.316	1995.73	C1	112.6	0.6	0.6	C1	112.6	0.6			
1240+381	Q	1.316	1998.20	C1	124.5	0.5	0.5	C1	124.5	0.5			
1246+586	BL		1992.81	C1	0.9	0.7	0.7	C1	0.9	0.7			
1246+586	BL		1994.78	C1	1.3	1.6	1.6	C1	1.3	1.6			
1246+586	BL		1996.72	C1	1.9	0.7	0.7	C1	1.9	0.7			
1250+532	BL		1993.52	C1	240.2	0.7	0.7	C1	240.2	0.7			
1250+532	BL		1995.73	C2	257.7	0.2	0.2	C1	249.8	0.8	7.90	0.82	
1250+532	BL		1998.20	C3	258.1	0.3	0.3	C1	248.5	0.6	9.60	0.67	
1254+571	Q		1992.81	n/a				n/a					
1254+571	Q		1994.78	n/a				n/a					
1254+571	Q		1996.72	n/a				n/a					
1258+507	Q	1.561	1993.53	C1	161.8	0.4	0.4	C1	161.8	0.4			
1258+507	Q	1.561	1995.73	C2	167.2	0.5	0.5	C1	163.7	0.2	10.9	3.50	0.54
1258+507	Q	1.561	1998.20	C2	167.0	0.2	0.2	C1	163.9	0.1	10.6	3.10	0.22
1258+507	Q	1.561	1999.98	C2	165.2	0.3	0.3	C1	163.2	0.1	10.8	2.00	0.32
1300+580	G	1.088	1992.81	C1	12.5	0.2	0.2	C1	12.5	0.2			
1300+580	G	1.088	1994.78	C1	17.5	1.1	1.1	C1	17.5	1.1			
1300+580	G	1.088	1996.72	C1	9.6	0.7	0.7	C1	9.6	0.7			
1305+804	Q	1.183	1995.73	C1	59.3	0.5	0.5	C1	59.3	0.5			
1305+804	Q	1.183	1998.20	C1	58.8	0.3	0.3	C1	58.8	0.3			
1305+804	Q	1.183	1999.96	C1	58.9	0.3	0.3	C1	58.9	0.3			
1306+360	Q	1.055	1995.73	C1	346.0	0.5	0.5	C1	346.0	0.5			
1306+360	Q	1.055	1998.20	C1	344.4	0.2	0.2	C1	344.4	0.2			

Continued on Next Page...

Table C.2 – Continued

Source	Type	Redshift	Epoch	Component		P.A. (deg)	Error (deg)	Component	P.A. (deg)	Error (deg)	Distance (pc)	Width (deg)	Error	
				Max	Min									
1306+360	Q	1.055	1999.96	n/a	n/a			n/a						
1307+562	Q	1.629	1992.81	C2	C1	194.7	0.7	C1	178.3	0.2	9.8	16.40	0.73	
1307+562	Q	1.629	1994.78	C2	C1	191.8	1.9	C1	181.3	0.6	8.0	10.50	1.99	
1307+562	Q	1.629	1996.72	C1	C1	186.7	0.6	C1	186.7	0.6				
1308+471	na	1.113	1993.53	n/a	n/a			n/a						
1308+471	na	1.113	1995.73	n/a	n/a			n/a						
1308+471	na	1.113	1998.20	n/a	n/a			n/a						
1309+555	Q	0.926	1992.81	C1	C1	349.3	0.2	C1	349.3	0.2				
1309+555	Q	0.926	1994.78	C1	C1	341.5	1.5	C1	341.5	1.5				
1309+555	Q	0.926	1996.72	C1	C1	334.5	1.2	C1	334.5	1.2				
1312+533	na		1993.52	C1	C1	241.4	0.2	C1	241.4	0.2				
1312+533	na		1995.73	C1	C1	242.9	0.1	C1	242.9	0.1				
1312+533	na		1998.19	n/a	n/a			n/a						
1321+410	G	0.496	1993.53	C1	C1	97.5		C1	97.5					
1321+410	G	0.496	1995.73	C1	C1	97.4		C1	97.4					
1321+410	G	0.496	1998.19	C1	C1	97.3		C1	97.3					
1322+835	na	1.024	1992.81	C1	C2	295.7	0.4	C2	291.1	0.8	21.6	4.60	0.89	
1322+835	na	1.024	1994.78	C1	C1	299.8	1.2	C1	299.8	1.2				
1322+835	na	1.024	1996.71	C1	C2	304.9	0.6	C2	289.4	1.8	24.7	15.50	1.90	
1323+800	G	1.970	1992.81	C3	C2	97.7	0.8	C2	73.7	0.2	12.4	24.00	0.82	
1323+800	G	1.970	1994.78	C3	C2	100.2	1.5	C2	79.0	0.3	14.7	21.20	1.53	
1323+800	G	1.970	1996.71	C3	C2	104.6	0.7	C2	82.2	0.2	15.4	22.40	0.73	
1325+436	Q	2.073	1993.52	C2	C1	222.3	0.4	C1	220.4	0.4	6.5	1.90	0.57	
1325+436	Q	2.073	1995.73	C2	C1	223.6	0.5	C1	222.3	0.5	5.4	1.30	0.71	
1325+436	Q	2.073	1998.19	C2	C1	228.9	0.3	C1	221.6	0.2	6.9	7.30	0.36	
1333+459	Q	2.449	1992.51	C1	C2	294.7	0.2	C2	294.1	0.2	7.1	0.60	0.28	
1333+459	Q	2.449	1994.79	C2	C1	295.0	0.3	C1	294.6	0.2	7.0	0.40	0.36	
1333+459	Q	2.449	1996.71	C1	C2	295.4	0.1	C2	294.7	0.6	10.0	0.70	0.61	
1333+589	G		1992.51	C1	C2	202.5	0.1	C2	197.5	0.1		5.00	0.14	

Continued on Next Page...

Table C.2 – Continued

Source	Type	Redshift	Epoch	Component		P.A. (deg)	Error (deg)	Component	P.A. (deg)	Error (deg)	Distance (pc)	Width (deg)	Error (deg)
				Max	Min								
1333+589	G		1994.79	C1	C2	201.3	0.2	n/a	197.3	0.2		4.00	0.28
1333+589	G		1996.70	C1	C2	200.8	0.2	n/a	197.1	0.1		3.70	0.22
1335+552	Q	1.096	1992.81	C4	C1	106.7	1.5	n/a	70.3	0.8	22.5	36.40	1.70
1335+552	Q	1.096	1994.78	C3	C1	95.9	1.0	n/a	70.6	1.0	14.9	25.30	1.41
1335+552	Q	1.096	1996.71	C4	C1	105.8	0.7	n/a	79.2	0.6	25.3	26.60	0.92
1337+637	Q	2.558	1992.81	C3	C1	207.4	0.3	n/a	184.1	0.6	28.9	23.30	0.67
1337+637	Q	2.558	1994.78	C2	C1	193.6	1.4	n/a	175.0	8.1	4.5	18.60	8.22
1337+637	Q	2.558	1996.71	C3	C2	208.9	0.7	n/a	201.8	0.2	20.8	7.10	0.73
1342+663	Q	1.351	1991.52	n/a	n/a								
1342+663	Q	1.351	1993.53	n/a	n/a								
1342+663	Q	1.351	1996.71	n/a	n/a								
1347+539	Q	0.980	1990.28	C3	C2	141.0	1.0	n/a	136.7	1.0	12.1	4.30	1.41
1347+539	Q	0.980	1992.51	C1	C2	151.6	1.9	n/a	131.6	1.0	7.7	20.00	2.15
1347+539	Q	0.980	1996.71	C1	C3	146.2	1.2	n/a	136.0	0.9	23.0	10.20	1.50
1355+441	G	0.646	1995.73	C1	C1	277.4	0.2	n/a	277.4	0.2			
1355+441	G	0.646	1996.71	C1	C1	273.3	0.4	n/a	273.3	0.4			
1355+441	G	0.646	1998.19	C1	C1	271.6	0.3	n/a	271.6	0.3			
1355+441	G	0.646	1999.98	C1	C1	279.5	0.3	n/a	279.5	0.3			
1356+478	G	0.230	1995.73	C3	C1	248.1		n/a	238.7	0.6	17.1	9.40	0.60
1356+478	G	0.230	1996.71	C3	C1	248.1		n/a	241.5	0.6	16.6	6.60	0.60
1356+478	G	0.230	1998.19	C3	C1	247.9		n/a	238.7	0.3	16.4	9.20	0.30
1356+478	G	0.230	1999.96	C3	C1	247.8		n/a	234.4	0.5	15.3	13.40	0.50
1357+769	BL		1991.52	C1	C1	247.0	1.1	n/a	247.0	1.1			
1357+769	BL		1993.53	C1	C1	256.9	2.5	n/a	256.9	2.5			
1357+769	BL		1996.71	C1	C1	243.5	1.8	n/a	243.5	1.8			
1413+373	Q	2.360	1993.52	n/a	n/a								
1413+373	Q	2.360	1995.73	n/a	n/a								
1413+373	Q	2.360	1998.19	n/a	n/a								
1415+463	Q	1.552	1993.52	C2	C1	265.1	0.5	n/a	261.8	0.2	22.4	3.30	0.54

Continued on Next Page...



Table C.2 – Continued

Source	Type	Redshift	Epoch	Component		P.A. (deg)	Error (deg)	Component	P.A. (deg)	Error (deg)	Distance (pc)	Width (deg)	Error (deg)
				Max	Min								
1415+463	Q	1.552	1995.73	C1	C2	260.1	0.8	258.3	0.3	19.8	1.80	0.85	
1415+463	Q	1.552	1996.71	C1	C2	260.7	1.1	260.5	0.3	21.3	0.20	1.14	
1415+463	Q	1.552	1998.19	C1	C2	261.0	0.3	259.5	0.2	21.4	1.50	0.36	
1417+385	Q	1.832	1993.52	n/a	n/a								
1417+385	Q	1.832	1995.73	n/a	n/a								
1417+385	Q	1.832	1998.19	n/a	n/a								
1418+546	BL	0.151	1990.28	C2	C3	129.1	0.1	124.4	0.3	6.1	4.70	0.32	
1418+546	BL	0.151	1992.51	C1	C3	129.8	0.1	126.6	0.2	8.5	3.20	0.22	
1418+546	BL	0.151	1996.71	C3	C3	124.8	0.2	124.8	0.2				
1421+482	Q	2.220	1993.52	C2	C1	287.3	0.7	271.3	1.5	21.4	16.00	1.66	
1421+482	Q	2.220	1995.73	C2	C1	283.1	0.3	279.3	0.7	16.6	3.80	0.76	
1421+482	Q	2.220	1998.19	C2	C1	283.9	0.3	273.8	0.4	16.0	10.10	0.50	
1424+366	BL	1.091	1993.52	C1	C1	228.1	0.3	228.1	0.3				
1424+366	BL	1.091	1995.73	C1	C1	222.1	0.3	222.1	0.3				
1424+366	BL	1.091	1998.19	C1	C1	230.4	0.6	230.4	0.6				
1427+543	Q	2.991	1993.52	C1	C1	136.3	0.1	136.3	0.1				
1427+543	Q	2.991	1995.73	C1	C1	138.1	0.4	138.1	0.4				
1427+543	Q	2.991	1998.19	C1	C1	135.0	0.1	135.0	0.1				
1432+422	Q	1.240	1995.73	C1	C1	131.1	2.4	131.1	2.4				
1432+422	Q	1.240	1998.19	C1	C1	147.6	1.4	147.6	1.4				
1432+422	Q	1.240	1999.96	C1	C1	148.2	1.2	148.2	1.2				
1435+638	Q	2.068	1990.27	C2	C3	242.2	0.2	233.5	0.2	9.5	8.70	0.28	
1435+638	Q	2.068	1992.51	C2	C3	240.6	0.3	233.4	0.3	14.6	7.20	0.45	
1435+638	Q	2.068	1996.71	C2	C3	241.3	0.5	232.0	0.1	12.8	9.30	0.51	
1438+385	Q	1.775	1992.51	C2	C1	347.6	0.4	5.2	0.6	13.5	17.60	0.72	
1438+385	Q	1.775	1994.79	C2	C1	348.2	0.6	0.7	1.8	11.8	12.50	1.87	
1438+385	Q	1.775	1996.71	C2	C1	347.4	0.2	3.3	0.5	13.4	15.90	0.54	
1442+637	Q	1.380	1992.51	n/a	n/a								
1442+637	Q	1.380	1994.79	n/a	n/a								

Continued on Next Page...

Table C.2 – Continued

Source	Type	Redshift	Epoch	Component		P.A. (deg)	Error (deg)	Component	P.A. (deg)	Error (deg)	Distance (pc)	Width (deg)	Error (deg)
				Max	Min								
1442+637	Q	1.380	1996.71	n/a	n/a								
1448+762	Q	0.899	1993.52	C2	C1	84.0	0.9	C1	80.9	0.2	9.4	3.10	0.92
1448+762	Q	0.899	1995.75	C1	C2	86.7	0.6	C2	82.3	2.7	10.7	4.40	2.77
1448+762	Q	0.899	1998.19	C2	C1	80.8	0.6	C1	80.4	0.6	9.1	0.40	0.85
1456+375	G	0.333	1993.53	C1	C1	118.9	1.1	C1	118.9	1.1			
1456+375	G	0.333	1995.73	C1	C1	116.6	0.4	C1	116.6	0.4			
1456+375	G	0.333	1996.71	C1	C1	118.5	0.5	C1	118.5	0.5			
1456+375	G	0.333	1998.19	C1	C1	117.3	0.3	C1	117.3	0.3			
1459+480	BL	1.059	1993.52	C2	C1	83.0	0.8	C1	79.1	0.8	20.5	3.90	1.13
1459+480	BL	1.059	1995.73	C1	C2	82.9	0.3	C2	82.2	1.0	21.6	0.70	1.04
1459+480	BL	1.059	1998.20	C2	C1	84.7	0.3	C1	81.3	0.8	20.6	3.40	0.85
1504+377	G	0.672	1992.51	C2	C1	225.3	0.9	C1	218.1	0.3	6.0	7.20	0.95
1504+377	G	0.672	1994.79	C2	C1	223.8	0.7	C1	219.5	0.3	6.1	4.30	0.76
1504+377	G	0.672	1996.71	C1	C2	223.3	1.7	C2	222.1	0.2	9.5	1.20	1.71
1505+428	G	0.587	1993.53	C1	C3	263.1	0.5	C3	255.8	0.7	30.6	7.30	0.86
1505+428	G	0.587	1995.73	C1	C3	265.2	0.4	C3	257.6	0.4	25.8	7.60	0.57
1505+428	G	0.587	1998.20	C1	C3	262.3	0.2	C3	257.5	0.3	27.9	4.80	0.36
1526+670	Q	3.020	1992.81	C2	C1	49.2	0.2	C1	40.5	0.2	7.4	8.70	0.28
1526+670	Q	3.020	1994.78	C2	C1	48.4	0.7	C1	42.2	0.4	7.1	6.20	0.77
1526+670	Q	3.020	1996.71	C2	C1	45.9	0.2	C1	41.1	0.3	6.8	4.80	0.36
1531+722	Q	0.899	1992.81	n/a	n/a								
1531+722	Q	0.899	1994.78	n/a	n/a								
1531+722	Q	0.899	1996.71	n/a	n/a								
1534+501	Q	1.121	1993.53	C1	C1	324.1	0.1	C1	324.1	0.1			
1534+501	Q	1.121	1995.73	C1	C1	324.4	0.1	C1	324.4	0.1			
1534+501	Q	1.121	1998.20	C1	C1	324.9	0.6	C1	324.9	0.6			
1543+480	Q	1.277	1993.52	C2	C1	142.2	0.4	C1	139.9	0.2	10.2	2.30	0.45
1543+480	Q	1.277	1995.73	C1	C3	140.6	0.2	C3	119.6	1.0	24.3	21.00	1.02
1543+480	Q	1.277	1998.20	C1	C3	140.8	0.1	C3	118.9	0.5	24.4	21.90	0.51

Continued on Next Page...

Table C.2 – Continued

Source	Type	Redshift	Epoch	Component		P.A.		Component	P.A.		Distance	Width		Error
				Max	Min	(deg)	(deg)		(deg)	(deg)				
1543+480	Q	1.277	1999.96	C2	C1	141.7	139.2	C1	139.2	0.4	12.3	2.50	0.50	
1543+517	Q	1.924	1993.52	C2	C1	192.4	177.0	C1	177.0	0.2	13.3	15.40	0.36	
1543+517	Q	1.924	1995.73	C2	C1	188.3	181.4	C1	181.4	0.3	16.2	6.90	0.36	
1543+517	Q	1.924	1999.01	C2	C1	190.8	181.5	C1	181.5	0.2	12.3	9.30	0.22	
1547+507	Q	2.169	1992.51	C4	C2	215.9	201.1	C2	201.1	0.6	17.1	14.80	0.63	
1547+507	Q	2.169	1994.79	C3	C2	214.0	206.9	C2	206.9	1.2	7.0	7.10	1.22	
1547+507	Q	2.169	1996.71	C4	C3	214.1	212.4	C3	212.4	0.1	10.7	1.70	0.14	
1550+582	Q	1.324	1993.53	C1	C1	163.9	163.9	C1	163.9	0.2				
1550+582	Q	1.324	1995.75	C1	C2	159.7	155.6	C2	155.6	0.5	9.7	4.10	0.64	
1550+582	Q	1.324	1998.20	C1	C2	160.8	156.0	C2	156.0	0.2	11.2	4.80	0.28	
1619+491	Q	1.513	1993.53	C1	C1	10.9	10.9	C1	10.9	0.2				
1619+491	Q	1.513	1995.75	C1	C1	6.1	6.1	C1	6.1	0.2				
1619+491	Q	1.513	1998.20	C1	C1	7.7	7.7	C1	7.7	0.1				
1622+665	G	0.201	1995.73	C1	C1	62.4	62.4	C1	62.4	1.1				
1622+665	G	0.201	1998.20	C1	C1	60.6	60.6	C1	60.6	0.8				
1622+665	G	0.201	1999.96	C1	C1	49.1	49.1	C1	49.1	0.9				
1623+578	G	0.789	1995.75	C2	C3	268.4	252.6	C3	252.6	0.1	16.4	15.80	3.60	
1623+578	G	0.789	1998.20	C1	C3	266.9	250.9	C3	250.9	0.1	24.9	16.00	0.32	
1623+578	G	0.789	1999.96	C1	C3	267.7	249.4	C3	249.4	0.2	25.6	18.30	0.36	
1624+416	Q	2.550	1996.71	C4	C3	306.2	219.8	C3	219.8	0.3	12.2	86.40	3.01	
1624+416	Q	2.550	1999.96	C4	C3	285.8	215.6	C3	215.6	0.2	19.3	70.20	2.01	
1624+416	Q	2.550	2001.03	C4	C3	295.3	221.7	C3	221.7	0.4	7.4	73.60	1.84	
1629+495	Q	0.520	1993.52	C1	C2	247.2	244.7	C2	244.7	2.1	5.7	2.50	2.18	
1629+495	Q	0.520	1995.75	C2	C3	249.1	245.2	C3	245.2	1.2	16.3	3.90	1.70	
1629+495	Q	0.520	1998.20	C3	C1	248.4	237.6	C1	237.6	0.8	30.7	10.80	1.20	
1633+382	Q	1.807	1996.71	C3	C2	293.9	276.1	C2	276.1	0.4	23.4	17.80	0.43	
1633+382	Q	1.807	1999.96	C3	C2	297.4	276.5	C2	276.5	0.1	20.7	20.90	0.22	
1633+382	Q	1.807	2001.03	C1	C2	276.2	274.9	C2	274.9	0.2	10.5	1.30	0.25	
1636+473	Q	0.740	1993.53	C1	C2	341.5	334.5	C2	334.5	1.2	10.8	7.00	2.53	

Continued on Next Page...

Table C.2 – Continued

Source	Type	Redshift	Epoch	Component		P.A. (deg)	Error (deg)	Component Min	P.A. (deg)	Error (deg)	Distance (pc)	Width (deg)	Error (deg)
				Max	Min								
1636+473	Q	0.740	1995.75	C1	C2	338.3	0.1		327.3	0.6	11.1	11.00	0.61
1636+473	Q	0.740	1998.20	C1	C2	337.8			330.8	1.1	10.4	7.00	1.14
1637+574	Q	0.749	1996.71	C2	C1	197.5	0.1		197.3	0.2	12.8	0.20	0.24
1637+574	Q	0.749	1999.96	C1	C2	202.5			199.6	0.1	14.9	2.90	0.10
1637+574	Q	0.749	2001.03	C1	C2	202.0	0.1		200.4	0.1	15.0	1.60	0.14
1638+398	Q	1.660	1990.28	n/a									
1638+398	Q	1.660	1993.53	n/a									
1638+398	Q	1.660	1996.71	n/a									
1638+540	Q	1.977	1993.52	C1	C1	207.9	0.3		207.9	0.3			
1638+540	Q	1.977	1995.75	C1	C1	203.1	0.9		203.1	0.9			
1638+540	Q	1.977	1998.20	C1	C1	207.9	0.2		207.9	0.2			
1641+399	Q	0.595	1996.71	C3	C1	288.4			270.4		27.6	18.00	0.04
1641+399	Q	0.595	1999.96	C3	C0	286.7	0.1		257.8	0.1	31.4	28.90	0.14
1641+399	Q	0.595	2001.03	C3	C1	285.1	0.1		263.5		26.1	21.60	0.10
1642+690	Q	0.751	1996.71	C2	C1	195.5	0.1		177.8	0.4	7.0	17.70	0.41
1642+690	Q	0.751	1999.96	C2	C1	197.5			182.2	0.2	15.3	15.30	0.20
1645+410	Q	0.835	1993.53	C1	C2	134.7	0.6		129.9	0.7	9.5	4.80	0.92
1645+410	Q	0.835	1995.78	C1	C2	132.2	0.4		123.1	2.6	9.6	9.10	2.63
1645+410	Q	0.835	1998.20	C1	C1	126.7	0.3		126.7	0.3			
1645+635	Q	2.379	1992.81	C1	C2	357.2	1.3		21.6	0.8	16.5	24.40	1.52
1645+635	Q	2.379	1994.78	C2	C1	18.7	1.1		0.2	1.5	16.0	18.50	1.86
1645+635	Q	2.379	1996.72	C2	C1	21.8	0.7		8.0	1.1	12.2	13.80	1.30
1652+398	BL	0.034	1996.71	C1	C5	156.0	0.3		113.5	0.1	6.2	42.50	0.32
1652+398	BL	0.034	1998.22	C1	C4	150.2	0.1		114.6	0.1	4.6	35.60	0.13
1652+398	BL	0.034	1999.96	C1	C5	158.1	0.2		106.5	0.1	6.4	51.60	0.22
1656+477	Q	1.622	1990.27	C2	C3	356.8	0.1		334.5	0.4	35.4	22.30	0.41
1656+477	Q	1.622	1992.51	C2	C1	356.2	0.5		0.4	0.7	5.3	4.20	0.86
1656+477	Q	1.622	1996.71	C1	C2	358.1	0.1		350.8	0.3	9.9	7.30	0.32
1656+482	G		1991.80	C1	C2	254.0	0.3		248.0	0.9		6.00	0.95

Continued on Next Page...

Table C.2 – Continued

Source	Type	Redshift	Epoch	Component		P.A.		Distance	Width		Error
				Max	Min	(deg)	(deg)		(deg)	(deg)	
1656+482	G		1993.52	C1	C2	253.4	242.2	1.1	11.20	1.17	
1656+482	G		1996.71	C1	C2	257.2	247.2	0.4	10.00	0.45	
1656+571	Q	1.281	1992.80	C2	C1	58.3	43.5	0.3	33.1	0.42	
1656+571	Q	1.281	1994.78	C1	C1	51.8	51.8	0.7			
1656+571	Q	1.281	1996.72	C1	C1	53.7	53.7	0.4			
1700+685	G	0.301	1992.81	C1	C2	124.4	124.2	1.4	5.3	1.61	
1700+685	G	0.301	1994.78	C1	C2	138.7	121.6	4.6	4.7	4.87	
1700+685	G	0.301	1996.72	C1	C2	139.2	131.0	3.0	5.6	3.45	
1716+686	Q	0.339	1992.51	C1	C2	330.9	327.0	0.4	7.4	0.45	
1716+686	Q	0.339	1994.79	C1	C3	333.9	321.8	0.7	21.4	1.30	
1716+686	Q	0.339	1996.70	C1	C3	331.2	322.7	0.2	21.1	0.45	
1719+357	Q	0.263	1991.80	C1	C2	181.9	178.0	0.1	10.6	0.22	
1719+357	Q	0.263	1993.53	C1	C2	179.1	178.1	0.1	9.9	0.22	
1719+357	Q	0.263	1996.71	C0	C3	180.2	178.1	0.1	21.4	0.51	
1722+401	Q	1.049	1993.53	C1	C1	308.9	308.9	2.1			
1722+401	Q	1.049	1995.75	C1	C2	308.8	300.0	1.3	19.4	1.44	
1722+401	Q	1.049	1998.19	C1	C2	307.9	296.8	0.1	24.9	0.36	
1726+455	Q	0.717	1993.53	C1	C1	283.7	283.7	0.2			
1726+455	Q	0.717	1995.73	C1	C1	276.6	276.6	0.1			
1726+455	Q	0.717	1998.19	C1	C1	273.0	273.0	0.2			
1732+389	Q	0.970	1990.28	C1	C2	125.0	77.7	3.2	5.7	3.72	
1732+389	Q	0.970	1994.79	C3	C2	120.6	98.3	1.8	20.4	2.77	
1732+389	Q	0.970	1996.72	C1	C2	124.6	103.9	0.6	7.2	0.78	
1734+508	G	0.835	1991.79	C1	C2	22.6	18.9	0.2	8.2	0.45	
1734+508	G	0.835	1993.53	C3	C2	19.2	15.6	0.3	10.8	0.30	
1734+508	G	0.835	1996.72	C2	C1	19.5	13.4	0.2	6.3	0.36	
1738+476	BL	0.950	1990.27	C2	C1	263.1	224.4	0.9	5.1	1.14	
1738+476	BL	0.950	1992.51	C3	C1	272.7	220.8	1.0	10.6	1.49	
1738+476	BL	0.950	1996.72	C3	C1	282.3	232.0	0.2	10.2	0.63	

Continued on Next Page...

Table C.2 – Continued

Source	Type	Redshift	Epoch	Component		P.A. (deg)	Error (deg)	Component	P.A. (deg)	Error (deg)	Distance (pc)	Width (deg)	Error (deg)
				Max	Min								
1738+499	Q	1.545	1993.25	C1	C2	44.6	7.0		12.5	1.9	4.8	32.10	7.25
1738+499	Q	1.545	1995.73	C1	C2	40.6	1.3		8.9	1.6	9.8	31.70	2.06
1738+499	Q	1.545	1998.19	C1	C2	41.8	1.0		18.9	0.9	7.2	22.90	1.35
1739+522	Q	1.381	1996.72	C1	C1	9.7	0.9		9.7	0.9			
1739+522	Q	1.381	1999.96	C1	C1	6.8	0.3		6.8	0.3			
1739+522	Q	1.381	2001.03	C1	C1	32.2	0.4		32.2	0.4			
1744+557	G	0.031	1996.72	C5	C4	250.6	0.3		244.9	1.2	5.7	5.70	1.24
1744+557	G	0.031	1998.19	C5	C1	249.5	0.2		243.8	0.3	8.1	5.70	0.36
1744+557	G	0.031	1999.96	C5	C1	249.2	0.2		240.6	0.3	8.0	8.60	0.36
1745+624	Q	3.889	1992.81	C2	C1	216.6	0.8		207.9	0.3	8.4	8.70	0.85
1745+624	Q	3.889	1994.78	C2	C1	213.8	0.9		209.5	1.4	7.0	4.30	1.65
1745+624	Q	3.889	1996.72	C1	C2	216.1	0.9		214.3	0.5	8.0	1.80	1.03
1746+470	na		1993.25	C1	C1	273.2	1.0		273.2	1.0			
1746+470	na		1995.73	C1	C1	298.1	2.8		298.1	2.8			
1746+470	na		1998.19	C1	C1	236.6	5.4		236.6	5.4			
1747+433	BL		1993.52	C1	C3	183.7	0.6		167.2	0.1		16.50	0.61
1747+433	BL		1995.73	C1	C3	186.9	0.6		168.3	0.1		18.60	0.61
1747+433	BL		1998.19	C1	C3	183.9	0.4		168.6			15.30	0.40
1749+701	BL	0.770	1996.88	C2	C1	299.2	0.3		281.8	0.4	14.1	17.40	0.51
1749+701	BL	0.770	1999.96	C2	C1	306.7	0.2		286.8	0.1	13.1	19.90	0.22
1749+701	BL	0.770	2001.03	C2	C1	314.3	0.3		287.7	0.2	14.8	26.60	0.36
1751+441	Q	0.871	1990.27	C1	C1	86.2	0.4		86.2	0.4			
1751+441	Q	0.871	1992.51	C1	C1	86.8	0.3		86.8	0.3			
1751+441	Q	0.871	1996.72	C1	C1	85.5	0.2		85.5	0.2			
1755+578	Q	2.110	1992.81	C1	C1	72.5	2.0		72.5	2.0			
1755+578	Q	2.110	1994.78	C1	C1	77.8	3.9		77.8	3.9			
1755+578	Q	2.110	1995.75	C1	C1	78.6	1.3		78.6	1.3			
1755+578	Q	2.110	1998.19	C1	C1	77.7	0.9		77.7	0.9			
1758+388	Q	2.092	1990.27	C2	C1	263.8	0.8		261.3	0.4	10.5	2.50	0.89

Continued on Next Page...

Table C.2 – Continued

Source	Type	Redshift	Epoch	Component		P.A. (deg)	Error (deg)	Component	P.A. (deg)	Error (deg)	Distance (pc)	Width (deg)	Error (deg)
				Max	Min								
1758+388	Q	2.092	1992.51	C2	C1	266.4	1.1	C1	253.2	0.5	11.6	13.20	1.21
1758+388	Q	2.092	1996.72	C2	C1	263.6	0.5	C1	257.3	0.4	8.8	6.30	0.64
1800+440	Q	0.663	1990.27	n/a	n/a			n/a					
1800+440	Q	0.663	1992.51	n/a	n/a			n/a					
1800+440	Q	0.663	1996.72	n/a	n/a			n/a					
1803+784	BL	0.680	1996.71	C3	C1	271.5	0.3	C1	85.2	0.5	17.0	173.70	0.58
1803+784	BL	0.680	1998.22	C1	C2	272.7	0.1	C2	262.4		5.9	10.30	0.10
1803+784	BL	0.680	1999.96	C1	C2	274.9	0.1	C2	264.3	0.1	7.2	10.60	0.14
1803+784	BL	0.680	2001.03	C3	C1	270.6	0.3	C1	269.7		13.6	0.90	0.30
1807+698	BL	0.051	1996.70	C2	C1	266.2	0.1	C1	261.3	0.1	2.5	4.90	0.13
1807+698	BL	0.051	1999.96	C1	C3	264.6	0.2	C3	260.9	0.2	5.0	3.70	0.31
1807+698	BL	0.051	2001.03	C1	C1	263.3	0.2	C1	263.3	0.2			
1809+568	Q		1992.81	C1	C2	153.3	0.1	C2	144.6			8.70	0.10
1809+568	Q		1994.78	C1	C2	153.6	0.1	C2	144.9	0.1		8.70	0.14
1809+568	Q		1996.70	C1	C2	154.9	0.1	C2	144.9			10.00	0.10
1812+412	Q	1.564	1995.73	C2	C1	82.7	0.3	C1	76.0	1.0	28.9	6.70	1.04
1812+412	Q	1.564	1996.72	C2	C1	83.2	0.4	C1	78.6	1.4	30.3	4.60	1.46
1812+412	Q	1.564	1998.19	C1	C2	84.2	0.8	C2	81.5	0.3	30.2	2.70	0.85
1818+356	Q	0.971	1995.73	n/a	n/a			n/a					
1818+356	Q	0.971	1998.19	C1	C1	127.7	1.4	C1	127.7	1.4			
1818+356	Q	0.971	1999.96	C1	C1	157.9	0.9	C1	157.9	0.9			
1823+568	BL	0.664	1996.70	C1	C2	204.7	0.2	C2	203.8	0.4	7.1	0.90	0.45
1823+568	BL	0.664	1999.96	C1	C2	199.2	0.1	C2	197.3	1.0	8.7	1.90	1.00
1823+568	BL	0.664	2001.03	C2	C1	206.2	0.2	C1	199.4	0.1	8.9	6.80	0.22
1826+796	G	0.224	1992.81	C1	C2	90.4	0.4	C2	48.6	0.1	9.5	41.80	0.41
1826+796	G	0.224	1994.78	C1	C2	71.1	1.4	C2	48.5	0.4	9.1	22.60	1.46
1826+796	G	0.224	1996.71	C1	C2	59.0	0.8	C2	48.1	0.2	7.7	10.90	0.82
1828+399	na		1993.52	C1	C1	301.1	0.6	C1	301.1	0.6			
1828+399	na		1995.73	C1	C1	302.4	0.4	C1	302.4	0.4			

Continued on Next Page...

Table C.2 – Continued

Source	Type	Redshift	Epoch	Component		P.A. (deg)	Error (deg)	Component Min	P.A. (deg)	Error (deg)	Distance (pc)	Width (deg)	Error (deg)
				Max	Min								
1828+399	na		1998.19	C1	303.3	0.2	C1	303.3	0.2				
1834+612	Q	2.274	1992.81	C1	192.9	0.3	C2	183.4	0.3	19.6	9.50	0.41	
1834+612	Q	2.274	1994.78	C1	189.0	1.6	C2	183.3	0.4	19.4	5.70	1.65	
1834+612	Q	2.274	1996.70	C1	194.7	0.4	C2	185.9	0.1	22.2	8.80	0.41	
1839+389	Q	3.095	1993.52	n/a			n/a						
1839+389	Q	3.095	1995.73	C1	358.1	7.9	C1	358.1	7.9				
1839+389	Q	3.095	1998.19	C1	359.6	1.7	C1	359.6	1.7				
1842+681	Q	0.472	1990.28	C3	136.0	1.4	C1	116.5	0.5	12.0	19.50	1.49	
1842+681	Q	0.472	1993.52	C3	140.1	1.1	C1	121.1	0.2	13.1	19.00	1.12	
1842+681	Q	0.472	1995.75	C4	140.9	0.8	C2	125.3	0.1	19.5	15.60	0.81	
1842+681	Q	0.472	1998.19	C4	140.1	0.7	C3	126.9	0.5	10.6	13.20	0.86	
1843+356	G	0.764	1991.79	C1	50.1	0.4	C2	41.4	0.2	31.0	8.70	0.46	
1843+356	G	0.764	1993.52	C1	45.2	0.7	C2	43.3	0.4	29.7	1.90	0.79	
1843+356	G	0.764	1996.72	C1	48.6	0.7	C1	48.6	0.7				
1849+670	Q	0.657	1992.51	C2	307.5	0.3	C1	300.0	0.3	16.0	7.50	0.42	
1849+670	Q	0.657	1994.79	C2	306.5	0.7	C1	304.7	0.7	15.6	1.80	0.99	
1849+670	Q	0.657	1996.70	C1	307.0	0.5	C1	307.0	0.5				
1850+402	Q	2.120	1993.52	C1	249.4	0.4	C2	243.1	0.2	8.4	6.30	0.45	
1850+402	Q	2.120	1995.75	C2	243.5	0.1	C1	235.8	0.2	8.2	7.70	0.22	
1850+402	Q	2.120	1998.19	C1	249.1	0.3	C2	241.8	0.1	9.7	7.30	0.31	
1851+488	Q	1.250	1993.25	n/a			n/a						
1851+488	Q	1.250	1995.75	n/a			n/a						
1851+488	Q	1.250	1998.19	n/a			n/a						
1856+737	Q	0.461	1992.81	C3	37.4	0.2	C1	25.0	0.3	14.9	12.40	0.36	
1856+737	Q	0.461	1994.78	C3	35.9	0.4	C1	25.5	1.1	16.2	10.40	1.17	
1856+737	Q	0.461	1996.70	C3	36.0	0.2	C1	22.4	0.6	20.5	13.60	0.63	
1908+484	Q	0.513	1993.25	C1	47.2	0.9	C1	47.2	0.9				
1908+484	Q	0.513	1995.75	C1	48.8	0.7	C1	48.8	0.7				
1908+484	Q	0.513	1998.19	C1	51.4	0.3	C1	51.4	0.3				

Continued on Next Page...



Table C.2 – Continued

Source	Type	Redshift	Epoch	Component		P.A. (deg)	Error (deg)	Component	P.A. (deg)	Error (deg)	Distance (pc)	Width (deg)	Error
				Max	Min								
1910+375	Q	1.104	1993.52	C2	C1	166.3	0.5	157.6	0.5	10.4	8.70	0.71	
1910+375	Q	1.104	1995.75	C2	C1	162.3	0.4	151.9	0.7	7.8	10.40	0.81	
1910+375	Q	1.104	1998.19	C2	C1	166.3	0.2	150.1	0.3	12.3	16.20	0.36	
1924+507	Q	1.098	1993.52	C3	C1	359.6	0.4	0.2	0.4	17.6	0.60	0.57	
1924+507	Q	1.098	1995.75	C2	C1	359.7	0.2	3.0	4.0	8.7	3.30	4.00	
1924+507	Q	1.098	1998.19	C1	C2	9.6	2.2	0.2	0.1	10.5	9.40	2.20	
1926+611	BL		1990.27	C2	C1	134.4	0.6	114.1	0.3		20.30	0.67	
1926+611	BL		1992.51	C2	C1	138.5	0.8	116.7	0.4		21.80	0.90	
1926+611	BL		1996.70	C2	C1	138.2	0.4	117.0	0.3		21.20	0.50	
1928+738	Q	0.302	1996.71	C1	C2	171.4		164.4	0.1	7.9	7.00	0.10	
1928+738	Q	0.302	1999.96	C2	C1	170.0		153.6	0.1	8.1	16.40	0.10	
1928+738	Q	0.302	2001.03	C3	C1	175.7	0.5	133.2	0.3	15.7	42.50	0.58	
1936+714	Q	1.864	1992.81	C1	C2	199.0	0.4	188.3	0.2	8.7	10.70	0.45	
1936+714	Q	1.864	1994.78	C1	C2	191.5	1.2	184.9	1.1	6.1	6.60	1.63	
1936+714	Q	1.864	1996.71	C1	C2	190.2	0.8	182.4	0.8	7.8	7.80	1.13	
1943+546	G	0.263	1991.79	n/a	n/a								
1943+546	G	0.263	1994.79	n/a	n/a								
1943+546	G	0.263	1995.75	n/a	n/a								
1943+546	G	0.263	1998.19	n/a	n/a								
1946+708	G	0.101	1992.81	C0	C4	49.9	0.6	23.5	0.1	26.4	26.40	0.61	
1946+708	G	0.101	1994.78	C1	C4	46.2	1.1	23.6	0.3	23.8	22.60	1.14	
1946+708	G	0.101	1995.75	C8	C4	46.5	0.2	23.3	0.1	12.2	23.20	0.22	
1946+708	G	0.101	1998.19	C1	C4	43.2	0.2	23.4	0.1	23.0	19.80	0.22	
1950+573	G	0.652	1992.81	C2	C1	79.0	0.5	45.3	1.5	24.8	33.70	1.58	
1950+573	G	0.652	1994.78	C2	C1	82.3	1.7	47.8	1.3	32.9	34.50	2.14	
1950+573	G	0.652	1996.73	C2	C1	80.4	0.9	58.1	0.3	25.9	22.30	0.95	
1954+513	Q	1.223	1996.73	C3	C2	306.9	0.3	306.3	0.1	10.5	0.60	0.32	
1954+513	Q	1.223	1999.96	C3	C2	309.9	0.2	308.4	0.1	12.7	1.50	0.22	
1954+513	Q	1.223	2001.03	C2	C3	307.2	0.1	305.0	0.4	11.1	2.20	0.41	

Continued on Next Page...

Table C.2 – Continued

Source	Type	Redshift	Epoch	Component		P.A. (deg)	Error (deg)	Component	P.A. (deg)	Error (deg)	Distance (pc)	Width (deg)	Error (deg)
				Max	Min								
2005+642	Q	1.574	1992.81	n/a	n/a								
2005+642	Q	1.574	1994.78	n/a	n/a								
2005+642	Q	1.574	1996.73	n/a	n/a								
2007+659	Q	1.325	1992.51	C2	C1	220.7	1.0		208.1	0.7	7.1	12.60	1.22
2007+659	Q	1.325	1994.81	C2	C3	219.5	1.2		210.5	1.4	18.2	9.00	1.84
2007+659	Q	1.325	1996.73	C2	C3	217.6	0.6		207.9	0.5	17.4	9.70	0.78
2007+777	BL	0.342	1992.51	C2	C1	258.0	0.5		250.9	0.2	4.4	7.10	0.54
2007+777	BL	0.342	1994.78	C1	C2	271.6	0.3		263.7	0.1	5.1	7.90	0.32
2007+777	BL	0.342	1996.73	C2	C1	264.4	0.1		262.0	0.3	6.2	2.40	0.32
2010+723	BL		1991.52	C1	C4	328.1	0.3		231.2	0.6		96.90	0.67
2010+723	BL		1993.52	C1	C4	325.8	0.4		233.4	1.0		92.40	1.08
2010+723	BL		1995.74	C2	C4	323.5	0.4		231.1	0.8		92.40	0.90
2017+745	Q	2.187	1992.81	C2	C1	87.9	0.9		81.6	0.3	7.5	6.30	0.95
2017+745	Q	2.187	1994.78	C1	C2	84.4	0.8		79.1	1.6	6.5	5.30	1.79
2017+745	Q	2.187	1995.74	C3	C2	84.8	0.4		81.0	0.5	16.9	3.80	0.64
2021+614	Q	0.227	1996.73	C3	C1	71.9	0.4		33.3	0.1	1.0	38.60	0.41
2021+614	Q	0.227	1999.96	C3	C1	82.4	0.4		34.7	0.1	1.8	47.70	0.41
2021+614	Q	0.227	2001.03	C3	C1	75.8	0.4		33.7	0.1	1.0	42.10	0.41
2023+760	BL		1992.81	C5	C2	224.7	0.6		195.7	0.2		29.00	0.63
2023+760	BL		1994.78	C5	C2	228.1	2.6		195.8	0.5		32.30	2.65
2023+760	BL		1996.73	C5	C2	223.1	1.3		195.9	0.4		27.20	1.36
2054+611	Q	0.864	1992.81	C2	C1	161.9	0.1		144.7	0.7	24.8	17.20	0.71
2054+611	Q	0.864	1994.78	C2	C1	163.1	0.2		149.3	1.0	21.1	13.80	1.02
2054+611	Q	0.864	1995.74	C2	C1	163.9	0.1		151.2	0.2	17.4	12.70	0.22
2054+611	Q	0.864	1998.19	C2	C1	164.5	0.1		150.4	0.1	16.7	14.10	0.14
2116+818	Q	0.084	1995.74	C1	C4	337.5	0.5		331.1	0.2	8.2	6.40	0.54
2116+818	Q	0.084	1996.73	C1	C4	335.5	0.8		331.5	0.3	8.3	4.00	0.85
2116+818	Q	0.084	1998.20	C1	C2	334.6	0.5		331.3	0.5	3.5	3.30	0.71
2136+824	Q	2.357	1992.81	C1	C3	150.0	1.0		135.2	0.2	20.5	14.80	1.02

Continued on Next Page...

Table C.2 – Continued

Source	Type	Redshift	Epoch	Component		P.A.		Component	P.A.		Distance	Width		Error
				Max	Min	(deg)	(deg)		(deg)	(deg)		(pc)	(deg)	
2136+824	Q	2.357	1994.78	C1	C3	150.1	135.2	C3	135.2	0.4	19.6	14.90	1.26	
2136+824	Q	2.357	1995.74	C1	C3	149.4	135.6	C3	135.6	0.2	21.5	13.80	0.82	
2136+824	Q	2.357	1998.20	C1	C2	140.0	137.1	C2	137.1	0.5	15.8	2.90	0.86	
2138+389	na	1.306	1993.25	C2	C1	90.0	83.0	C1	83.0	1.5	14.2	7.00	1.70	
2138+389	na	1.306	1995.73	C1	C2	92.9	86.7	C2	86.7	0.3	14.5	6.20	0.58	
2138+389	na	1.306	1996.72	C1	C2	91.8	86.9	C2	86.9	0.3	15.2	4.90	0.58	
2138+389	na	1.306	1999.98	C1	C2	93.4	86.7	C2	86.7	0.3	13.9	6.70	0.50	
2200+420	BL	0.069	1996.72	C4	C3	354.5	189.9	C3	189.9		2.2	164.60	0.86	
2200+420	BL	0.069	1998.19	C2	C4	192.4	180.7	C4	180.7		3.5	11.70		
2200+420	BL	0.069	1999.96	C1	C4	199.7	184.0	C4	184.0	0.2	5.0	15.70	0.92	
2200+420	BL	0.069	2001.03	C1	C4	197.1	181.9	C4	181.9	0.2	5.4	15.20	0.36	
2214+350	Q	0.510	1990.27	n/a	n/a			n/a						
2214+350	Q	0.510	1993.53	C1	C1	163.3	163.3	C1	163.3	0.9				
2214+350	Q	0.510	1995.74	C1	C1	164.9	164.9	C1	164.9	0.4				
2214+350	Q	0.510	1998.19	C1	C1	164.6	164.6	C1	164.6	0.3				
2229+695	BL	1.413	1990.27	C1	C1	74.2	74.2	C1	74.2	0.2				
2229+695	BL	1.413	1993.52	C1	C1	72.3	72.3	C1	72.3	0.2				
2229+695	BL	1.413	1996.73	C1	C1	68.0	68.0	C1	68.0	0.3				
2235+731	Q	1.345	1992.81	C1	C3	48.1	30.3	C3	30.3	0.3	24.8	17.80	0.58	
2235+731	Q	1.345	1994.78	C1	C3	48.7	31.7	C3	31.7	0.8	28.2	17.00	1.05	
2235+731	Q	1.345	1995.74	C1	C3	46.6	32.2	C3	32.2	0.8	26.7	14.40	1.61	
2238+410	BL	0.726	1994.78	C3	C3	138.1	138.1	C3	138.1	2.9				
2238+410	BL	0.726	1995.74	C1	C3	224.7	142.2	C3	142.2	0.9	27.5	82.50	2.10	
2238+410	BL	0.726	1998.19	C1	C3	229.7	136.5	C3	136.5	1.4	28.2	93.20	1.57	
2253+417	Q	1.476	1990.27	C2	C1	350.5	7.9	C1	7.9	0.5	10.4	17.40	0.58	
2253+417	Q	1.476	1993.52	C2	C1	350.5	1.2	C1	1.2	0.4	9.2	10.70	0.56	
2253+417	Q	1.476	1996.70	C1	C2	354.3	350.8	C2	350.8	0.7	7.3	3.50	0.79	
2255+416	Q	2.150	1990.27	C1	C2	168.8	156.2	C2	156.2	1.0	25.1	12.60	1.02	
2255+416	Q	2.150	1993.52	C1	C1	165.4	165.4	C1	165.4	0.5				

Continued on Next Page...

Table C.2 – Continued

Source	Type	Redshift	Epoch	Component		P.A. (deg)	Error (deg)	Component	P.A. (deg)	Error (deg)	Distance (pc)	Width (deg)	Error
				Max	Min								
2255+416	Q	2.150	1995.74	C2	C1	165.6	0.3	C1	163.5	0.5	27.5	2.10	0.58
2259+371	Q	2.179	1992.81	C1	C4	348.3	0.5	C4	2.8	0.3	29.3	14.50	0.58
2259+371	Q	2.179	1994.78	C1	C4	347.4	0.8	C4	5.1	0.6	24.9	17.70	1.00
2259+371	Q	2.179	1995.74	C1	C4	350.1	0.7	C4	3.8	0.3	27.5	13.70	0.76
2259+371	Q	2.179	1998.19	C2	C4	348.2	0.3	C4	5.2	0.2	13.2	17.00	0.36
2309+454	Q	1.447	1993.25	C1	C1	104.3	0.6	C1	104.3	0.6			
2309+454	Q	1.447	1995.73	C1	C1	114.5	0.6	C1	114.5	0.6			
2309+454	Q	1.447	1998.19	C1	C1	113.3	0.3	C1	113.3	0.3			
2310+385	Q	2.181	1993.53	C1	C1	238.2	0.1	C1	238.2	0.1			
2310+385	Q	2.181	1995.73	C1	C1	239.9	0.1	C1	239.9	0.1			
2310+385	Q	2.181	1998.19	C1	C1	239.7		C1	239.7				
2319+444	G	1.251	1993.53	C1	C1	343.7	0.1	C1	343.7	0.1			
2319+444	G	1.251	1995.73	C1	C1	342.9	0.3	C1	342.9	0.3			
2319+444	G	1.251	1998.19	C1	C1	343.1	0.1	C1	343.1	0.1			
2346+385	Q	1.032	1993.53	C2	C1	331.1	1.4	C1	319.4	3.1	8.7	11.70	3.40
2346+385	Q	1.032	1995.73	C2	C2	333.5	0.6	C1	326.2	0.5	12.7	7.30	0.78
2346+385	Q	1.032	1998.19	C2	C2	334.9	0.6	C1	331.4	1.2	13.1	3.50	1.34
2351+456	Q	1.986	1996.73	C1	C1	281.6	0.1	C1	281.6	0.1			
2351+456	Q	1.986	1999.96	C1	C1	277.8	0.3	C1	277.8	0.3			
2351+456	Q	1.986	2001.03	C1	C1	276.2	0.1	C1	276.2	0.1			
2352+495	G	0.237	1995.74	C5	C5	289.6	0.9	C5	289.6	0.9			
2352+495	G	0.237	1998.19	n/a	n/a								
2352+495	G	0.237	1999.96	C5	C5	291.7	0.4	C5	291.7	0.4			
2353+816	BL	1.344	1992.81	C2	C2	329.7	0.1	C2	329.7	0.1			
2353+816	BL	1.344	1994.78	C1	C2	355.9	0.9	C2	333.6	2.2	6.2	22.30	2.38
2353+816	BL	1.344	1996.73	C2	C2	346.1	1.3	C1	343.2	0.4	7.2	2.90	1.36
2356+385	Q	2.704	1995.73	C2	C1	196.2	1.7	C1	161.7	0.3	3.1	34.50	1.73
2356+385	Q	2.704	1996.72	C2	C1	211.0	1.2	C1	163.9	1.0	8.5	47.10	1.56
2356+385	Q	2.704	1998.19	C2	C1	197.0	0.9	C1	164.3	0.2	4.7	32.70	0.92

Continued on Next Page...

Table C.2 – Continued

Source	Type	Redshift	Epoch	Component Max	P.A. (deg)	Error (deg)	Component Min	P.A. (deg)	Error (deg)	Distance (pc)	Width (deg)	Error
2356+390	Q	1.198	1993.52	C1	231.3	0.6	C1	231.3	0.6			
2356+390	Q	1.198	1995.73	C1	229.8	0.4	C1	229.8	0.4			
2356+390	Q	1.198	1998.19	C1	227.8	0.3	C1	227.8	0.3			

## C CJF Jet Ridge Lines

Table C.3: CJF Jet ridge line width evolution (maximum values). Columns (1)-(3) as in previous tables, Col. (4) gives the maximum value of the jet ridge line width evolution across all available epochs, Col. (5) gives the uncertainty, Col. (6) shows the flag regarding the credibility of the data (see text for details), and Col. (7) shows the number of components used in the calculation.

Source	Type	Redshift	$\Delta P_{max}$ (deg/yr)	Error	Flag	# Comp.
0003+380	G	0.229	2.424	1.344	!	4
0010+405	G	0.255	1.380	0.322	OK	2
0014+813	Q	3.366	0.881	0.377	OK	2
0016+731	Q	1.781			OK	1
0018+729	G	0.821	4.124	1.717	OK	2
0022+390	Q	1.946	4.847	0.236	OK	2
0035+367	Q	0.366			OK	0
0035+413	Q	1.353	1.243	1.078	OK	2
0102+480	G				OK	1
0108+388	G	0.669	2.099	0.044	OK	2
0109+351	Q	0.45			OK	2
0110+495	Q	0.389	3.496	0.147	OK	2
0133+476	Q	0.859	5.895	1.431	OK	2
0145+386	Q	1.442			OK	1
0151+474	Q	1.026	4.024	0.392	OK	2
0153+744	Q	2.388			OK	0
0205+722	G	0.895	3.041	1.846	!	2
0212+735	Q	2.367	13.551	0.613	OK	3
0218+357	G	0.936			OK	0
0219+428	BL	0.444	1.689	0.394	OK	3
0227+403	Q	1.019	6.260	0.368	OK	3
0248+430	Q	1.31	0.711	0.238	OK	2
0249+383	Q	1.122	0.772	0.310	OK	3
0251+393	Q	0.289	3.826	0.797	OK	2
0307+380	Q	0.816			!	1
0309+411	Q	0.134	0.409	10.45	OK	5
0316+413	G	0.018	3.354	0.107	OK	5
0340+362	Q	1.485			!	1
0346+800	Q		2.056	1.099	!	2
0402+379	G	0.055	0.686	0.186	!	5
0444+634	Q	0.781	6.566	0.537	!	4
0454+844	BL	0.112	0.738	0.514	OK	2
0537+531	Q	1.275			OK	1
0546+726	Q	1.555	1.571	0.486	OK	2
0554+580	Q	0.904	3.108	0.581	OK	2
0600+442	G	1.136	3.862	0.287	OK	2
0602+673	Q	1.95			OK	1
0604+728	Q	0.986			OK	0
0609+607	Q	2.702	1.715	0.254	OK	4
0615+820	Q	0.71			OK	0
0620+389	Q	3.469			!	2
0621+446	BL				OK	0
0627+532	Q	2.204	2.439	0.424	OK	3
0633+596	na		0.366	0.234	OK	2
0633+734	Q	1.85	1.465	0.908	!	3

Continued on Next Page...

Table C.3 – Continued

Source	Type	Redshift	$\Delta P_{max}$ (deg/yr)	Error	Flag	# Comp.
0636+680	Q	3.174			OK	0
0641+393	Q	1.266	6.723	0.339	OK	2
0642+449	Q	3.396			OK	1
0646+600	Q	0.455			!	1
0650+371	Q	1.982	1.451	0.518	OK	2
0650+453	Q	0.933			OK	0
0651+410	G	0.022	7.489	0.737	!	2
0700+470	G		0.143	0.210	OK	6
0702+612	Q		2.499	0.759	!	3
0707+476	Q	1.292	6.352	2.120	!	2
0710+439	G	0.518			OK	1
0711+356	Q	1.62			!	1
0714+457	Q	0.94	0.673	0.485	OK	3
0716+714	BL	0.31	4.427	2.742	!	3
0718+793	na				OK	0
0724+571	Q	0.426	0.600	0.420	!	3
0727+409	Q	2.5	0.565	0.584	OK	2
0730+504	Q	0.72	5.208	0.960	!	3
0731+479	Q	0.782	0.779	0.197	OK	3
0733+597	G	0.041	5.068	0.672	OK	6
0738+491	Q	2.32			OK	1
0740+768	G		1.813	0.531	OK	2
0743+744	Q	1.629	1.012	0.262	OK	2
0746+483	Q	1.951	3.648	0.409	OK	3
0749+426	Q	3.59			OK	0
0749+540	BL		3.600	0.435	OK	2
0800+618	Q	3.044	27.109	0.595	!	2
0803+452	Q	2.102			OK	1
0804+499	Q	1.432	2.136	0.240	OK	2
0805+410	Q	1.42	1.682	0.304	OK	2
0806+573	Q	0.611			!	1
0812+367	Q	1.025			OK	2
0814+425	BL	0.53	18.318	0.687	!	2
0820+560	Q	1.409			!	2
0821+394	Q	1.216	0.450	0.765	OK	3
0821+621	Q	0.542			OK	0
0824+355	Q	2.249			OK	0
0831+557	G	0.24	3.313	0.158	!	8
0833+416	Q	1.298	0.822	0.181	OK	2
0833+585	Q	2.101			OK	1
0836+710	Q	2.18	1.999	0.581	!	2
0843+575	G		2.483	0.654	OK	4
0847+379	G	0.407	3.356	1.199	!	2
0850+581	Q	1.322	6.168	0.324	OK	2
0859+470	Q	1.462	2.178	0.061	OK	2
0859+681	Q	1.499	1.806	0.389	OK	2
0900+520	Q	1.537	0.806	1.106	OK	2
0902+490	Q	2.69			OK	1
0917+449	Q	2.18			OK	1

Continued on Next Page...

Table C.3 – Continued

Source	Type	Redshift	$\Delta P_{max}$ (deg/yr)	Error	Flag	# Comp.
0917+624	Q	1.446			OK	1
0923+392	Q	0.699			OK	1
0925+504	BL	0.37	2.317	0.648	OK	2
0927+352	BL		1.341	0.659	OK	3
0929+533	Q	0.595			!	2
0930+493	Q	2.582	3.115	0.389	OK	3
0942+468	G	0.639	11.839	0.462	!	2
0945+408	Q	1.252			OK	1
0949+354	Q	1.875	0.697	0.256	OK	2
0950+748	G	0.695	0.508	0.991	OK	2
0954+556	Q	0.895			OK	0
0954+658	BL	0.368			OK	0
0955+476	Q	1.873			OK	1
1003+830	G	0.322	2.132	0.336	OK	4
1010+350	Q	1.414	3.004	0.709	OK	2
1014+615	Q	2.8			OK	1
1015+359	Q	1.226	6.279	2.350	OK	3
1020+400	Q	1.254	1.787	0.515	OK	2
1030+398	G	1.095	3.812	0.258	OK	2
1030+415	Q	1.12	1.500	0.450	OK	2
1030+611	Q	1.401	4.131	0.781	OK	3
1031+567	G	0.46			OK	1
1038+528	Q	0.677			OK	1
1039+811	Q	1.254	0.669	0.406	!	4
1041+536	Q	1.897	2.915	0.700	OK	3
1044+719	Q	1.15			OK	1
1053+704	Q	2.492			!	2
1053+815	G	0.706			OK	1
1058+629	Q	0.663			OK	1
1058+726	Q	1.46	2.633	0.656	OK	3
1101+384	BL	0.031	1.414	0.619	!	2
1105+437	Q	1.226	4.303	0.931	OK	3
1106+380	G	2.29	3.051	0.219	OK	2
1107+607	na		14.264	1.511	!	2
1124+455	Q	1.811	0.526	0.099	OK	2
1124+571	Q	2.89			OK	1
1125+596	Q	1.779			OK	1
1128+385	Q	1.733			OK	1
1143+590	Q	1.982			OK	1
1144+352	G	0.063	6.290	0.959	OK	5
1144+402	Q	1.088			OK	0
1144+542	Q	2.201	2.400	0.274	OK	2
1146+596	G	0.011	1.980	0.484	OK	3
1150+812	Q	1.25	4.079	0.449	!	4
1151+408	Q	0.916	4.082	0.215	OK	2
1155+486	Q	2.028	8.788	2.674	OK	2
1205+544	na		4.413	0.799	OK	4
1206+415	BL				OK	0
1213+350	Q	0.857			OK	0

Continued on Next Page...



Table C.3 – Continued

Source	Type	Redshift	$\Delta P_{max}$ (deg/yr)	Error	Flag	# Comp.
1216+487	Q	1.076	1.020	0.505	OK	2
1218+444	Q	1.345			OK	1
1221+809	BL		2.082	0.271	OK	4
1223+395	Q	0.623			OK	1
1226+373	Q	1.515			!	1
1239+376	Q	3.818			OK	1
1240+381	Q	1.316			OK	1
1246+586	BL				!	2
1250+532	BL		0.688	0.430	OK	3
1254+571	Q	0.042			OK	0
1258+507	Q	1.561	0.618	0.218	OK	2
1300+580	G	1.088			OK	1
1305+804	Q	1.183			OK	1
1306+360	Q	1.055			!	1
1307+562	Q	1.629	2.995	1.077	OK	2
1308+471	na	1.113			OK	0
1309+555	Q	0.926			OK	1
1312+533	na				!	1
1321+410	G	0.496			OK	1
1322+835	na	1.024			!	1
1323+800	G	1.97	1.421	0.882	OK	3
1325+436	Q	2.073	2.439	0.323	OK	2
1333+459	Q	2.449	0.156	0.368	OK	2
1333+589	G		0.439	0.139	OK	2
1335+552	Q	1.096	5.635	1.123	!	4
1337+637	Q	2.558	5.959	4.276	OK	2
1342+663	Q	1.351			OK	0
1347+539	Q	0.98	7.040	1.153	!	3
1355+441	G	0.646			!	2
1356+478	G	0.23	2.373	0.329	OK	3
1357+769	BL				OK	1
1413+373	Q	2.36			OK	0
1415+463	Q	1.552	1.633	1.454	OK	2
1417+385	Q	1.832			OK	0
1418+546	BL	0.151	0.673	0.174	OK	3
1421+482	Q	2.22	5.520	0.824	OK	2
1424+366	BL	1.091			OK	1
1427+543	Q	2.991			!	2
1432+422	Q	1.24			OK	1
1435+638	Q	2.068	0.500	0.161	!	4
1438+385	Q	1.775	2.249	0.880	!	2
1442+637	Q	1.38			OK	0
1448+762	Q	0.899	1.639	1.186	OK	2
1456+375	G	0.333			OK	1
1459+480	BL	1.059	1.448	0.697	OK	2
1504+377	G	0.672	1.615	0.976	OK	2
1505+428	G	0.587	1.134	0.272	OK	4
1526+670	Q	3.02	1.246	0.416	!	2
1531+722	Q	0.899			OK	0

Continued on Next Page...

Table C.3 – Continued

Source	Type	Redshift	$\Delta P_{max}$ (deg/yr)	Error	Flag	# Comp.
1534+501	Q	1.121			OK	1
1543+480	Q	1.277	11.023	0.406	OK	2
1543+517	Q	1.924	3.846	0.231	OK	2
1547+507	Q	2.169	3.377	0.601	OK	4
1550+582	Q	1.324	0.286	0.286	OK	2
1619+491	Q	1.513			OK	1
1622+665	G	0.201			OK	1
1623+578	G	0.789	1.307	0.272	OK	3
1624+416	Q	2.55	4.985	1.115	OK	4
1629+495	Q	0.52	2.816	0.849	OK	3
1633+382	Q	1.807	18.283	0.312	OK	3
1636+473	Q	0.74	1.649	0.528	!	2
1637+574	Q	0.749	0.833	0.080	!	3
1638+398	Q	1.66			OK	0
1638+540	Q	1.977			OK	1
1641+399	Q	0.595	3.342	0.045	OK	4
1642+690	Q	0.751	0.738	0.141	OK	2
1645+410	Q	0.835	1.911	1.239	OK	2
1645+635	Q	2.379	2.997	1.220	!	3
1652+398	BL	0.034	9.187	0.148	!	5
1656+477	Q	1.622	8.080	0.426	OK	2
1656+482	G		3.023	0.876	OK	2
1656+571	Q	1.281			OK	2
1700+685	G	0.301	8.579	2.604	OK	2
1716+686	Q	0.339	1.885	0.722	!	4
1719+357	Q	0.263	1.676	0.183	OK	3
1722+401	Q	1.049	0.925	0.610	OK	3
1726+455	Q	0.717			OK	1
1732+389	Q	0.97	5.543	1.028	OK	3
1734+508	G	0.835	0.784	0.147	OK	3
1738+476	BL	0.95	5.893	0.836	!	2
1738+499	Q	1.545	3.577	1.001	OK	2
1739+522	Q	1.381			OK	2
1744+557	G	0.031	1.638	0.288	OK	5
1745+624	Q	3.889	2.237	0.942	!	2
1746+470	na				OK	2
1747+433	BL		1.341	0.296	OK	3
1749+701	BL	0.77	6.262	0.397	OK	2
1751+441	Q	0.871			OK	1
1755+578	Q	2.11			OK	1
1758+388	Q	2.092	4.777	0.671	OK	2
1800+440	Q	0.663			OK	0
1803+784	BL	0.68	108.212	0.392	OK	3
1807+698	BL	0.051	0.341	0.104	OK	4
1809+568	Q		0.677	0.090	OK	2
1812+412	Q	1.564	2.121	1.810	OK	2
1818+356	Q	0.971			OK	1
1823+568	BL	0.664	4.579	0.962	OK	2
1826+796	G	0.224	9.746	0.768	OK	2

Continued on Next Page...

Table C.3 – Continued

Source	Type	Redshift	$\Delta P_{max}$ (deg/yr)	Error	Flag	# Comp.
1828+399	na				OK	1
1834+612	Q	2.274	1.930	0.862	!	3
1839+389	Q	3.095			OK	1
1842+681	Q	0.472	1.525	0.618	OK	4
1843+356	G	0.764	3.935	0.530	OK	3
1849+670	Q	0.657	2.500	0.472	OK	2
1850+402	Q	2.12	0.628	0.224	OK	2
1851+488	Q	1.25			OK	0
1856+737	Q	0.461	1.667	0.693	OK	3
1908+484	Q	0.513			OK	1
1910+375	Q	1.104	2.377	0.362	OK	2
1924+507	Q	1.098	2.500	1.873	OK	3
1926+611	BL		0.670	0.502	!	2
1928+738	Q	0.302	24.393	0.553	OK	3
1936+714	Q	1.864	2.081	0.857	OK	2
1943+546	G	0.263			OK	0
1946+708	G	0.101			OK	0
1950+573	G	0.652	6.256	1.200	OK	2
1954+513	Q	1.223	0.279	0.120	OK	2
2005+642	Q	1.574			OK	0
2007+659	Q	1.325	1.565	0.961	OK	3
2007+777	BL	0.342	2.815	0.230	!	2
2010+723	BL		2.25	0.634	OK	4
2017+745	Q	2.187	1.562	1.979	OK	3
2021+614	Q	0.227	2.817	0.181	OK	3
2023+760	BL		2.615	1.526	OK	5
2054+611	Q	0.864	1.701	0.630	!	2
2116+818	Q	0.084	2.424	1.020	OK	4
2136+824	Q	2.357	4.431	0.484	OK	3
2138+389	na	1.306	0.552	0.236	OK	2
2200+420	BL	0.069	104.003	0.588	!	4
2214+350	Q	0.51			OK	1
2229+695	BL	1.413			!	2
2235+731	Q	1.345	2.732	2.006	!	4
2238+410	BL	0.726	4.367	1.070	OK	3
2253+417	Q	1.476	2.276	0.303	OK	3
2255+416	Q	2.15			!	1
2259+371	Q	2.179	4.167	1.309	OK	4
2309+454	Q	1.447			OK	1
2310+385	Q	2.181			!	1
2319+444	G	1.251			OK	1
2346+385	Q	1.032	2.000	1.586	OK	2
2351+456	Q	1.986			OK	1
2352+495	G	0.237			!	0
2353+816	BL	1.344	9.949	1.404	OK	2
2356+385	Q	2.704	9.796	1.234	OK	2
2356+390	Q	1.198			OK	1

## C CJF Jet Ridge Lines

Table C.4: CJF Jet ridge line linear evolution. Columns (1)-(3) as in previous tables, Col. (4) gives the total apparent evolution in the X coordinate,  $\Delta X$ , Col. (5) gives the total apparent evolution in the Y coordinate,  $\Delta Y$ , Col. (6) gives the total linear evolution,  $\Delta \ell$ , Col. (7) gives the uncertainty for  $\Delta \ell$ , Col. (8) gives the time span for which the evolution is calculated, and Col. (9) gives the number of component pairs across epochs used for the calculation.

Source	Type	Redshift	$\Delta X$ (mas/yr/comp)	$\Delta Y$	$\Delta \ell$ (pc/yr/comp)	Error	$\Delta T$ (yr)	# Comp.
0003+380	G	0.229	0.041	0.08	0.346	0.006	3.2	6
0010+405	G	0.255	0.019	0.03	0.146	0.005	6.45	4
0014+813	Q	3.366	0.011	0.03	0.220	0.002	3.9	4
0016+731	Q	1.781	0.021	0.04	0.417		4.31	1
0018+729	G	0.821	0.042	0.05	0.512	0.005	5.2	4
0022+390	Q	1.946	0.033	0.08	0.808	0.011	6.45	4
0035+367	Q	0.366					5.3	0
0035+413	Q	1.353	0.039	0.03	0.473	0.025	4.23	3
0102+480	G		0.025	0.03			6.45	4
0108+388	G	0.669	0.012	0.02	0.182		4.31	4
0109+351	Q	0.45	0.02	0.03	0.228	0.007	4.66	3
0110+495	Q	0.389	0.034	0.04	0.291		4.66	4
0133+476	Q	0.859	0.04	0.02	0.385	0.007	4.31	4
0145+386	Q	1.442	0.03	0.06	0.600	0.001	4.66	2
0151+474	Q	1.026	0.0080	0.05	0.392	0.002	4.66	4
0153+744	Q	2.388					4.31	0
0205+722	G	0.895	0.053	0.08	0.812	0.02	3.91	5
0212+735	Q	2.367	0.044	0.07	0.707	0.001	4.31	6
0218+357	G	0.936					7.64	0
0219+428	BL	0.444	0.029	0.08	0.507	0.003	2.46	6
0227+403	Q	1.019	0.019	0.03	0.269	0.004	6.44	9
0248+430	Q	1.31	0.017	0.02	0.252		3.9	4
0249+383	Q	1.122	0.0080	0.02	0.155	0.002	4.66	3
0251+393	Q	0.289	0.029	0.01	0.135	0.001	4.65	5
0307+380	Q	0.816	0.024	0.04	0.342	0.024	4.67	1
0309+411	Q	0.134	0.031	0.02	0.093	0.434	4.66	13
0316+413	G	0.018	0.342	0.04	0.129		4.32	9
0340+362	Q	1.485	0.028	0.07	0.622	0.002	4.66	2
0346+800	Q		0.04	0.06			3.9	4
0402+379	G	0.055	0.086	0.08	0.135	0.001	6.43	11
0444+634	Q	0.781	0.02	0.11	0.843	0.006	3.9	5
0454+844	BL	0.112	0.021	0.1	0.203	0.001	4.32	4
0537+531	Q	1.275	0.021	0.03	0.306		6.73	3
0546+726	Q	1.555	0.015	0.02	0.230	0.002	5.19	4
0554+580	Q	0.904	0.013	0.02	0.180	0.001	4.94	6
0600+442	G	1.136	0.03	0.04	0.483	0.001	4.23	4
0602+673	Q	1.95	0.0060	0.04	0.309	0.001	6.44	2
0604+728	Q	0.986					7.17	0
0609+607	Q	2.702	0.02	0.03	0.335	0.001	4.94	6
0615+820	Q	0.71					6.44	0
0620+389	Q	3.469	0.017	0.01	0.161	0.001	8.46	3
0621+446	BL						4.21	0
0627+532	Q	2.204	0.021	0.02	0.266	0.004	4.67	6
0633+596	na		0.016				4.94	4

Continued on Next Page...

Table C.4 – Continued

Source	Type	Redshift	$\Delta X$ (mas/yr/comp)	$\Delta Y$	$\Delta \ell$ (pc/yr/comp)	Error	$\Delta T$ (yr)	# Comp.
0633+734	Q	1.85	0.018	0.1	0.860	0.025	3.9	7
0636+680	Q	3.174					4.19	0
0641+393	Q	1.266	0.017	0.02	0.253		6.44	6
0642+449	Q	3.396	0.045	0.02	0.373	0.001	5.18	2
0646+600	Q	0.455	0.013	0.01	0.096		6.67	3
0650+371	Q	1.982	0.035	0.04	0.455	0.004	6.43	4
0650+453	Q	0.933					6.46	0
0651+410	G	0.022	0.047	0.04	0.028		4.67	8
0700+470	G		0.07	0.04			4.66	7
0702+612	Q		0.024	0.02			6.73	6
0707+476	Q	1.292	0.025	0.03	0.314	0.003	9.71	8
0710+439	G	0.518	0.014	0.01	0.105		4.32	2
0711+356	Q	1.62	0.027	0.02	0.295	0.001	4.32	3
0714+457	Q	0.94	0.081	0.08	0.894	0.001	4.67	5
0716+714	BL	0.31	0.025	0.03	0.195	0.006	8.22	10
0718+793	na						3.9	0
0724+571	Q	0.426	0.074	0.12	0.796	0.003	4.94	7
0727+409	Q	2.5	0.016	0.01	0.178	0.001	4.23	4
0730+504	Q	0.72	0.066	0.1	0.905	0.003	4.2	4
0731+479	Q	0.782	0.08	0.01	0.607	0.001	4.67	6
0733+597	G	0.041	0.057	0.1	0.093	0.001	3.25	12
0738+491	Q	2.32	0.028	0.03	0.459	0.004	4.67	2
0740+768	G		0.0090				3.9	4
0743+744	Q	1.629	0.019	0.05	0.475	0.001	4.67	4
0746+483	Q	1.951	0.019	0.02	0.273	0.001	5.19	4
0749+426	Q	3.59					4.22	0
0749+540	BL		0.0080	0.03			4.94	2
0800+618	Q	3.044	0.044	0.05	0.618	0.001	4.21	5
0803+452	Q	2.102	0.044	0.03	0.444	0.004	4.67	2
0804+499	Q	1.432	0.052	0.09	0.996	0.002	4.3	4
0805+410	Q	1.42	0.041	0.02	0.418	0.001	5.21	4
0806+573	Q	0.611	0.03	0.03	0.321	0.001	4.22	2
0812+367	Q	1.025	0.0080	0.05	0.381	0.001	6.46	2
0814+425	BL	0.53	0.089	0.04	0.252	0.001	4.3	5
0820+560	Q	1.409	0.041	0.03	0.450	0.003	6.45	4
0821+394	Q	1.216	0.018	0.03	0.314	0.022	6.46	3
0821+621	Q	0.542					4.22	0
0824+355	Q	2.249					2.46	0
0831+557	G	0.24	0.116	0.07	0.567		4.3	15
0833+416	Q	1.298	0.012	0.03	0.300	0.003	3.23	4
0833+585	Q	2.101	0.081	0.01	0.699		5.47	2
0836+710	Q	2.18	0.013	0.02	0.229		4.3	4
0843+575	G		0.019	0.02			4.94	12
0847+379	G	0.407	0.029	0.12	0.689	0.044	2.46	5
0850+581	Q	1.322	0.018	0.02	0.25		4.33	4
0859+470	Q	1.462	0.02	0.03	0.348		4.33	4
0859+681	Q	1.499	0.0070	0.02	0.186		4.22	4
0900+520	Q	1.537	0.072	0.02	0.670	0.005	4.94	3
0902+490	Q	2.69	0.0090	0.02	0.179		4.67	2

Continued on Next Page...

## C CJF Jet Ridge Lines

Table C.4 – Continued

Source	Type	Redshift	$\Delta X$ (mas/yr/comp)	$\Delta Y$	$\Delta \ell$ (pc/yr/comp)	Error	$\Delta T$ (yr)	# Comp.
0917+449	Q	2.18	0.0090	0.02	0.153		5.18	2
0917+624	Q	1.446	0.0060	0.01	0.134		9.51	3
0923+392	Q	0.699	0.045	0.09	0.721	0.009	4.33	4
0925+504	BL	0.37	0.033	0.03	0.227	0.003	4.66	3
0927+352	BL		0.037	0.02			4.67	6
0929+533	Q	0.595	0.027	0.02	0.249	0.001	4.94	2
0930+493	Q	2.582	0.068	0.05	0.717	0.011	4.67	6
0942+468	G	0.639	0.024	0.02	0.225	0.002	4.67	7
0945+408	Q	1.252	0.072	0.08	0.911	0.009	4.31	2
0949+354	Q	1.875	0.0060	0.03	0.296	0.010	4.67	4
0950+748	G	0.695	0.049	0.04	0.475	0.004	3.89	3
0954+556	Q	0.895					3.26	0
0954+658	BL	0.368	0.039	0.02	0.236	0.003	4.33	4
0955+476	Q	1.873	0.026	0.02	0.28	0.001	5.18	2
1003+830	G	0.322	0.053	0.02	0.281		5.19	8
1010+350	Q	1.414	0.056	0.05	0.790	0.008	4.67	3
1014+615	Q	2.8	0.01	0.01	0.12		3.89	2
1015+359	Q	1.226	0.011	0.07	0.594	0.043	4.92	6
1020+400	Q	1.254	0.065	0.06	0.764	0.001	4.93	4
1030+398	G	1.095	0.016	0.04	0.377		4.67	4
1030+415	Q	1.12	0.023	0.07	0.606	0.007	4.93	4
1030+611	Q	1.401	0.018	0.04	0.068	0.001	3.91	4
1031+567	G	0.46	0.016	0.02	0.159		4.31	2
1038+528	Q	0.677	0.03	0.07	0.53		4.67	2
1039+811	Q	1.254	0.07	0.02	0.62	0.002	3.9	6
1041+536	Q	1.897	0.04	0.02	0.410	0.002	4.67	6
1044+719	Q	1.15	0.02	0.02	0.257	0.001	5.19	2
1053+704	Q	2.492	0.051	0.05	0.616	0.003	5.19	2
1053+815	G	0.706	0.039	0.02	0.329	0.003	5.19	2
1058+629	Q	0.663	0.033	0.07	0.519	0.002	3.91	2
1058+726	Q	1.46	0.019	0.02	0.273	0.002	8.46	9
1101+384	BL	0.031	0.049	0.04	0.038		6.43	4
1105+437	Q	1.226	0.051	0.07	0.790	0.016	4.67	3
1106+380	G	2.29	0.01	0.03	0.253		4.23	4
1107+607	na		0.027	0.1			3.91	4
1124+455	Q	1.811	0.0020	0.05	0.429	0.001	4.68	4
1124+571	Q	2.89	0.043	0.04	0.482	0.002	3.91	2
1125+596	Q	1.779	0.015	0.02	0.219	0.002	3.91	1
1128+385	Q	1.733	0.0060	0.02	0.148		4.4	2
1143+590	Q	1.982	0.049	0.01	0.428	0.001	3.91	2
1144+352	G	0.063	0.125	0.08	0.188	0.001	3.2	10
1144+402	Q	1.088					4.4	0
1144+542	Q	2.201	0.017	0.01	0.194		5.2	4
1146+596	G	0.011	0.136	0.16	0.047		3.91	12
1150+812	Q	1.25	0.058	0.13	1.200	0.002	3.9	7
1151+408	Q	0.916	0.039	0.04	0.525	0.001	2.46	6
1155+486	Q	2.028	0.095	0.07	1.018	0.009	3.2	4
1205+544	na		0.027	0.03			4.68	8
1206+415	BL						4.68	0

Continued on Next Page...

Table C.4 – Continued

Source	Type	Redshift	$\Delta X$ (mas/yr/comp)	$\Delta Y$	$\Delta \ell$ (pc/yr/comp)	Error	$\Delta T$ (yr)	# Comp.
1213+350	Q	0.857					4.39	0
1216+487	Q	1.076	0.044	0.02	0.442	0.002	4.39	4
1218+444	Q	1.345	0.032	0.04	0.414	0.002	4.21	2
1221+809	BL		0.02	0.05			4.67	8
1223+395	Q	0.623	0.027	0.04	0.330	0.005	4.67	2
1226+373	Q	1.515	0.047	0.04	0.555	0.007	4.68	1
1239+376	Q	3.818	0.0090	0.03	0.195		4.68	1
1240+381	Q	1.316	0.035	0.04	0.501	0.001	4.68	2
1246+586	BL		0.0060	0.11			3.91	2
1250+532	BL		0.031	0.02			4.68	4
1254+571	Q	0.042					3.91	0
1258+507	Q	1.561	0.0060	0.01	0.105	0.001	6.45	5
1300+580	G	1.088	0.073	0.05	0.707	0.006	3.91	2
1305+804	Q	1.183	0.03	0.02	0.293	0.001	4.23	2
1306+360	Q	1.055	0.019	0.05	0.415	0.003	4.23	1
1307+562	Q	1.629	0.024	0.03	0.340	0.007	3.91	3
1308+471	na	1.113					4.67	0
1309+555	Q	0.926	0.028	0.02	0.308	0.005	3.91	2
1312+533	na			0.01			4.67	1
1321+410	G	0.496	0.0040		0.028		4.66	2
1322+835	na	1.024	0.054	0.02	0.495	0.021	3.9	3
1323+800	G	1.97	0.071	0.03	0.700	0.009	3.9	6
1325+436	Q	2.073	0.031	0.02	0.337	0.001	4.67	4
1333+459	Q	2.449	0.057	0.03	0.526	0.001	4.2	4
1333+589	G		0.023	0.02			4.19	6
1335+552	Q	1.096	0.044	0.02	0.424	0.006	3.9	6
1337+637	Q	2.558	0.042	0.03	0.469	0.020	3.9	5
1342+663	Q	1.351					5.19	0
1347+539	Q	0.98	0.051	0.05	0.613	0.005	6.43	6
1355+441	G	0.646	0.011	0.02	0.183	0.001	4.25	3
1356+478	G	0.23	0.027	0.01	0.125		4.23	7
1357+769	BL		0.0080	0.04			5.19	2
1413+373	Q	2.36					4.67	0
1415+463	Q	1.552	0.032	0.02	0.355	0.002	4.67	6
1417+385	Q	1.832					4.67	0
1418+546	BL	0.151	0.069	0.06	0.234		6.43	4
1421+482	Q	2.22	0.036	0.03	0.395	0.001	4.67	4
1424+366	BL	1.091	0.03	0.02	0.391		4.67	2
1427+543	Q	2.991	0.039	0.03	0.409	0.001	4.67	2
1432+422	Q	1.24	0.057	0.13	1.224	0.007	4.23	2
1435+638	Q	2.068	0.028	0.02	0.290	0.001	6.44	6
1438+385	Q	1.775	0.016	0.02	0.260	0.006	4.2	4
1442+637	Q	1.38					4.2	0
1448+762	Q	0.899	0.062	0.02	0.515	0.025	4.67	4
1456+375	G	0.333	0.037	0.02	0.198		4.66	3
1459+480	BL	1.059	0.014	0.02	0.206	0.007	4.68	4
1504+377	G	0.672	0.066	0.09	0.788	0.003	4.2	4
1505+428	G	0.587	0.072	0.01	0.515	0.004	4.67	7
1526+670	Q	3.02	0.014	0.01	0.143	0.003	3.9	4

Continued on Next Page...

## C CJF Jet Ridge Lines

Table C.4 – Continued

Source	Type	Redshift	$\Delta X$ (mas/yr/comp)	$\Delta Y$	$\Delta \ell$ (pc/yr/comp)	Error	$\Delta T$ (yr)	# Comp.
1531+722	Q	0.899					3.9	0
1534+501	Q	1.121	0.0070	0.01	0.130	0.001	4.67	2
1543+480	Q	1.277	0.011	0.02	0.177	0.002	6.44	5
1543+517	Q	1.924	0.012	0.04	0.363		5.49	4
1547+507	Q	2.169	0.027	0.03	0.373	0.002	4.2	6
1550+582	Q	1.324	0.018	0.03	0.309	0.003	4.67	3
1619+491	Q	1.513	0.016	0.04	0.365		4.67	2
1622+665	G	0.201	0.0070	0.02	0.063	0.001	4.23	2
1623+578	G	0.789	0.092	0.04	0.785	0.002	4.21	5
1624+416	Q	2.55	0.069	0.08	0.933	0.003	4.32	8
1629+495	Q	0.52	0.094	0.02	0.602	0.011	4.68	5
1633+382	Q	1.807	0.059	0.02	0.578		4.32	5
1636+473	Q	0.74	0.044	0.04	0.472	0.01	4.67	4
1637+574	Q	0.749	0.04	0.07	0.616		4.32	4
1638+398	Q	1.66					6.43	0
1638+540	Q	1.977	0.014	0.04	0.396	0.001	4.68	2
1641+399	Q	0.595	0.047	0.02	0.379		4.32	6
1642+690	Q	0.751	0.078	0.21	1.642		3.25	2
1645+410	Q	0.835	0.079	0.02	0.637	0.046	4.67	3
1645+635	Q	2.379	0.043	0.06	0.640	0.009	3.91	4
1652+398	BL	0.034	0.103	0.1	0.099		3.25	9
1656+477	Q	1.622	0.019	0.11	0.926	0.002	6.44	3
1656+482	G		0.029	0.02			4.91	4
1656+571	Q	1.281	0.044	0.01	0.401	0.001	3.92	2
1700+685	G	0.301	0.05	0.07	0.381	0.018	3.91	4
1716+686	Q	0.339	0.025	0.03	0.212	0.002	4.19	5
1719+357	Q	0.263	0.0050	0.15	0.611	0.005	4.91	6
1722+401	Q	1.049	0.072	0.03	0.653	0.014	4.66	3
1726+455	Q	0.717	0.063	0.02	0.475		4.66	2
1732+389	Q	0.97	0.045	0.05	0.571	0.006	6.44	6
1734+508	G	0.835	0.0080	0.04	0.352	0.001	4.93	6
1738+476	BL	0.95	0.033	0.03	0.355	0.001	6.45	4
1738+499	Q	1.545	0.023	0.05	0.539	0.006	4.94	4
1739+522	Q	1.381	0.063	0.06	0.813	0.001	4.31	2
1744+557	G	0.031	0.041	0.03	0.034		3.24	10
1745+624	Q	3.889	0.026	0.02	0.252	0.005	3.91	4
1746+470	na		0.029	0.08			4.94	2
1747+433	BL		0.023	0.03			4.67	6
1749+701	BL	0.77	0.091	0.1	1.081	0.001	4.15	4
1751+441	Q	0.871	0.028	0.01	0.222		6.45	2
1755+578	Q	2.11	0.069	0.03	0.657	0.020	5.38	3
1758+388	Q	2.092	0.02	0.01	0.206	0.001	6.45	4
1800+440	Q	0.663					6.45	0
1803+784	BL	0.68	0.102	0.03	0.796		4.32	7
1807+698	BL	0.051	0.066	0.02	0.069		4.33	4
1809+568	Q		0.01	0.01			3.89	4
1812+412	Q	1.564	0.056	0.02	0.561	0.009	2.46	4
1818+356	Q	0.971	0.095	0.22	1.910	0.007	4.23	1
1823+568	BL	0.664	0.056	0.1	0.850	0.007	4.33	4

Continued on Next Page...



Table C.4 – Continued

Source	Type	Redshift	$\Delta X$ (mas/yr/comp)	$\Delta Y$	$\Delta \ell$ (pc/yr/comp)	Error	$\Delta T$ (yr)	# Comp.
1826+796	G	0.224	0.025	0.07	0.276	0.001	3.9	4
1828+399	na		0.0090	0.01			4.67	2
1834+612	Q	2.274	0.022	0.04	0.382	0.002	3.89	4
1839+389	Q	3.095	0.0090	0.09	0.717	0.357	4.67	1
1842+681	Q	0.472	0.022	0.04	0.269	0.002	7.91	11
1843+356	G	0.764	0.01	0.05	0.357	0.001	4.93	4
1849+670	Q	0.657	0.091	0.07	0.808	0.001	4.19	3
1850+402	Q	2.12	0.018	0.04	0.364		4.67	4
1851+488	Q	1.25					4.94	0
1856+737	Q	0.461	0.047	0.08	0.537	0.001	3.89	6
1908+484	Q	0.513	0.06	0.04	0.445	0.001	4.94	2
1910+375	Q	1.104	0.0060	0.06	0.474	0.004	4.67	4
1924+507	Q	1.098	0.015	0.05	0.441	0.137	4.67	6
1926+611	BL		0.023	0.03			6.43	4
1928+738	Q	0.302	0.1	0.04	0.522		4.32	6
1936+714	Q	1.864	0.01	0.04	0.375	0.009	3.9	4
1943+546	G	0.263					6.4	0
1946+708	G	0.101	0.073	0.1	0.249	0.002	5.38	27
1950+573	G	0.652	0.138	0.02	0.989	0.015	3.92	4
1954+513	Q	1.223	0.124	0.09	1.308	0.001	4.3	4
2005+642	Q	1.574					3.92	0
2007+659	Q	1.325	0.032	0.05	0.495	0.009	4.22	6
2007+777	BL	0.342	0.03	0.02	0.211		4.22	4
2010+723	BL		0.047	0.04			4.22	7
2017+745	Q	2.187	0.03	0.03	0.414	0.008	2.93	6
2021+614	Q	0.227	0.124	0.08	0.54		4.3	9
2023+760	BL		0.06	0.05			3.92	9
2054+611	Q	0.864	0.02	0.03	0.303	0.002	5.38	6
2116+818	Q	0.084	0.087	0.18	0.311	0.001	2.46	8
2136+824	Q	2.357	0.027	0.02	0.309	0.001	5.39	9
2138+389	na	1.306	0.123	0.09	1.324	0.001	6.73	12
2200+420	BL	0.069	0.074	0.25	0.338		4.31	8
2214+350	Q	0.51	0.0010		0.028	0.005	7.92	2
2229+695	BL	1.413	0.021	0.02	0.233		6.46	2
2235+731	Q	1.345	0.065	0.07	0.799	0.011	2.93	6
2238+410	BL	0.726	0.063	0.05	0.720	0.030	3.41	4
2253+417	Q	1.476	0.011	0.04	0.319	0.002	6.43	4
2255+416	Q	2.15	0.041	0.07	0.678	0.004	5.47	3
2259+371	Q	2.179	0.035	0.05	0.542	0.003	5.38	11
2309+454	Q	1.447	0.056	0.04	0.594	0.002	4.94	2
2310+385	Q	2.181	0.024	1	0.227		4.66	2
2319+444	G	1.251	0.02	0.06	0.518	0.008	4.66	2
2346+385	Q	1.032	0.023	0.08	0.688	0.019	4.66	4
2351+456	Q	1.986	0.038	0.04	0.480	0.001	4.3	2
2352+495	G	0.237	0.055	0.06	0.306	0.019	4.22	1
2353+816	BL	1.344	0.035	0.06	0.634	0.007	3.92	3
2356+385	Q	2.704	0.143	0.07	1.287	0.008	2.46	4
2356+390	Q	1.198	0.0070	0.02	0.193		4.67	2



# D CJF $\gamma$ -rays

Table D.1: CJF sources detected in the  $\gamma$ -rays by Fermi-LAT. Columns (1)-(3) give the IAU name, type, and redshift of the source, Col.(4) gives the  $\gamma$ -ray flux (detections are from the first Fermi-LAT catalog, [Abdo et al. 2010b](#)), Col. (5) gives the uncertainty for the  $\gamma$ -ray fluxes, Cols. (6) and (7) give the  $\gamma$  photon index and its uncertainty, Cols. (8) and (9) give the calculated  $\gamma$ -ray luminosity (in the  $\log \nu L_\nu$  form and in logarithmic scale) and the respective uncertainty, Col.(10) denotes sources with detected variability in  $\gamma$ -rays, and Cols. (11) and (12) show the maximum apparent jet speed for that source and its uncertainty.

Source	Type	Redshift	$F_\gamma$ ( $10^{-8}$ ph cm $^{-2}$ s $^{-1}$ )	$\delta F_\gamma$ ( $10^{-8}$ ph cm $^{-2}$ s $^{-1}$ )	Var						
0003+380	G	0.229	0.60	0.30	2.86	0.13	43.58	0.22	N	4.9	0.0
0110+495	Q	0.389	0.70	0.30	2.29	0.18	44.39	0.19	N	1.0	0.6
0133+476	Q	0.859	9.60	0.60	2.34	0.03	46.39	0.03	Y	11.0	2.8
0212+735	Q	2.367	1.00	0.40	2.85	0.13	46.64	0.17	Y	16.1	7.1
0218+357	G	0.936	6.40	0.50	2.33	0.04	46.31	0.03	Y	n/a	n/a
0219+428	BL	0.444	24.90	1.00	1.93	0.02	46.36	0.02	Y	14.0	5.0
0227+403	Q	1.019	1.40	0.30	2.43	0.13	45.72	0.09	Y	4.0	1.1
0307+380	Q	0.816	0.60	0.30	2.49	0.15	45.08	0.22	Y	4.3	0
0316+413	G	0.018	17.30	0.80	2.13	0.02	43.01	0.02	Y	1.0	0.2
0346+800	Q	n/a	2.00	0.30	2.5	0.08	n/a	n/a	Y	n/a	n/a
0621+446	BL	n/a	1.00	0.30	2.03	0.18	n/a	n/a	N	n/a	n/a
0633+734	Q	1.850	0.60	0.30	2.73	0.17	46.07	0.22	N	21.7	1.0
0650+453	Q	0.933	6.10	0.50	2.32	0.04	46.29	0.04	Y	n/a	n/a

Continued on Next Page...

Table D.1 – Continued

Source	Type	Redshift	$F_\gamma$ ( $10^{-9}$ ph cm $^{-2}$ s $^{-1}$ )	$\delta F_\gamma$ ( $10^{-9}$ ph cm $^{-2}$ s $^{-1}$ )	$\alpha_\gamma$	$\delta\alpha_\gamma$	$\log(\nu L_\nu)_\gamma$ (erg s $^{-1}$ )	$\delta \log(\nu L_\nu)_\gamma$ (erg s $^{-1}$ )	Var	$\beta_{app,max}$	$\delta\beta_{app,max}$
0707+476	Q	1.292	0.90	0.30	2.51	0.13	45.80	0.14	N	4.2	4.4
0716+714	BL	0.310	13.10	0.70	2.15	0.03	45.49	0.02	Y	n/a	n/a
0749+540	BL	n/a	1.20	0.30	1.95	0.16	n/a	n/a	N	n/a	n/a
0800+618	Q	3.044	0.60	0.20	2.83	0.13	46.75	0.14	Y	10.0	9.6
0814+425	BL	0.530	8.70	0.60	2.15	0.04	45.12	0.03	Y	2.7	1.8
0820+560	Q	1.409	0.90	0.30	2.87	0.11	45.92	0.14	Y	5.3	0
0836+710	Q	2.180	1.20	0.30	2.98	0.12	46.65	0.11	N	30.6	4.4
0917+449	Q	2.180	14.00	0.70	2.28	0.02	47.65	0.02	Y	14.2	5.5
0917+624	Q	1.446	1.10	0.30	2.7	0.15	46.02	0.12	N	3.2	1.0
0925+504	BL	0.370	0.70	0.20	1.91	0.23	44.65	0.12	N	n/a	n/a
0954+556	Q	0.895	10.50	0.60	2.05	0.03	46.65	0.02	N	n/a	n/a
0954+658	BL	0.368	0.50	0.30	2.51	0.16	44.09	0.26	N	9.9	0
1015+359	Q	1.226	0.50	0.20	2.71	0.15	45.47	0.17	N	10.3	1.6
1020+400	Q	1.254	0.60	0.20	2.45	0.17	45.60	0.14	N	13.2	5.1
1030+415	Q	1.120	1.10	0.30	2.48	0.12	45.72	0.12	N	4.2	2.4
1030+611	Q	1.401	2.20	0.30	2.46	0.08	44.77	0.06	Y	1.9	1.8
1039+811	Q	1.254	0.90	0.20	2.95	0.13	45.77	0.10	Y	10.1	1.5
1044+719	Q	1.150	1.60	0.30	2.47	0.13	45.92	0.08	N	3.0	0.6
1101+384	BL	0.031	26.10	1.00	1.81	0.02	44.01	0.02	Y	0.2	0.1
1144+402	Q	1.088	1.00	0.30	2.47	0.13	45.65	0.13	N	n/a	n/a
1206+415	BL	n/a	0.50	0.20	1.85	0.22	n/a	n/a	N	n/a	n/a
1221+809	BL	n/a	1.00	0.30	2.27	0.14	n/a	n/a	N	n/a	n/a
1246+586	BL	n/a	4.50	0.40	2.18	0.06	n/a	n/a	N	n/a	n/a
1250+532	BL	n/a	3.00	0.40	2.14	0.07	n/a	n/a	N	n/a	n/a
1306+360	Q	1.055	2.20	0.30	2.3	0.09	46.00	0.06	Y	4.6	0
1322+835	na	1.024	0.50	0.20	2.49	0.22	45.27	0.17	N	n/a	n/a
1357+769	BL	n/a	1.10	0.20	2.25	0.16	n/a	n/a	N	n/a	n/a
1418+546	BL	0.151	0.90	0.20	2.77	0.17	43.35	0.10	N	2.6	0
1432+422	Q	1.240	0.70	0.20	2.25	0.2	45.71	0.12	N	17.7	0.7

Continued on Next Page...

Table D.1 – Continued

Source	Type	Redshift	$F_\gamma$ ( $10^{-9}$ ph cm $^{-2}$ s $^{-1}$ )	$\delta F_\gamma$ ( $10^{-9}$ ph cm $^{-2}$ s $^{-1}$ )	$\alpha_\gamma$	$\delta\alpha_\gamma$	$\log(vL_{v,\gamma})$ (erg s $^{-1}$ )	$\delta \log(vL_{v,\gamma})$ (erg s $^{-1}$ )	Var	$\beta_{app,max}$	$\delta\beta_{app,max}$
1504+377	G	0.672	0.70	0.20	2.59	0.13	44.90	0.12	Y	10.5	1.6
1633+382	Q	1.807	6.80	0.50	2.47	0.04	47.09	0.03	Y	12.2	4.9
1641+399	Q	0.595	5.60	0.50	2.49	0.04	45.68	0.04	Y	6.1	0
1652+398	BL	0.034	8.30	0.60	1.85	0.04	43.54	0.03	Y	0.9	0
1700+685	G	0.301	3.70	0.40	2.28	0.06	44.85	0.05	Y	1.0	1.1
1722+401	Q	1.049	2.90	0.40	2.37	0.07	46.09	0.06	Y	20.9	10.4
1726+455	Q	0.717	1.20	0.30	2.57	0.09	45.21	0.11	Y	5.7	0.8
1732+389	Q	0.970	6.00	0.50	2.22	0.05	46.37	0.04	Y	12.1	1.8
1739+522	Q	1.381	3.40	0.40	2.71	0.05	46.45	0.05	Y	11.5	9.0
1749+701	BL	0.770	2.00	0.30	2.05	0.1	45.74	0.07	N	14.8	5.0
1747+433	BL	n/a	2.30	0.30	2.12	0.09	n/a	n/a	N	n/a	n/a
1803+784	BL	0.680	3.00	0.40	2.35	0.07	45.61	0.06	Y	13.6	3.0
1807+698	BL	0.051	1.90	0.30	2.6	0.08	42.69	0.07	N	0.4	0
1823+568	BL	0.664	2.70	0.40	2.34	0.07	45.54	0.06	Y	9.0	1.5
1849+670	Q	0.657	13.30	0.70	2.25	0.03	46.27	0.02	Y	8.6	0.6
1851+488	Q	1.250	0.90	0.30	2.6	0.12	45.75	0.14	N	n/a	n/a
2007+777	BL	0.342	1.40	0.30	2.42	0.16	44.50	0.09	N	1.9	0.8
2010+723	BL	n/a	1.60	0.40	2.45	0.15	n/a	n/a	N	n/a	n/a
2023+760	BL	n/a	1.10	0.30	2.52	0.18	n/a	n/a	N	n/a	n/a
2200+420	BL	0.069	7.10	0.60	2.38	0.04	43.64	0.04	Y	3.1	0.3



# Erklärung

Ich versichere, daß ich die von mir vorgelegte Dissertation selbständig angefertigt, die benutzen Quellen und Hilfsmittel vollständig angegeben und die Stellen der Arbeit - einschließlich Tabellen, Karten und Abbildungen -, die anderen Werken im Wortlaut oder dem Sinn nach entnommen sind, in jedem Einzelfall als Entlehnung kenntlich gemacht habe; daß diese Dissertation noch keiner anderen Fakultät oder Universität zur Prüfung vorgelegen hat; daß sie - abgesehen von unten angegebenen Teilpublikationen - noch nicht veröffentlicht worden ist sowie, daß ich eine solche Veröffentlichung vor Abschluß des Promotionsverfahrens nicht vornehmen werde. Die Bestimmungen dieser Promotionsverfahrens sind mir bekannt. Die von mir vorgelegte Dissertation ist von Prof. Dr. Andreas Eckart betreut worden.

Köln, den 23.08.2010

Teilpublikationen:

Karouzos, M.; Britzen, S.; Eckart, A.; Witzel, A.; Zensus, A.: Tracing the merger-driven evolution of active galaxies in the CJF sample, *Astronomy and Astrophysics*, in press (2010)





# Curriculum Vitae

## Persönliche Informationen:

**Vor- / Nachname:** Marios Karouzos

**Adresse:** M. Geroulanou, 17-19, GR-16452, Athen, Griechenland

**Wohnungsadresse:** Bonngasse, 11, D-53111, Bonn, Germany

**Telefonnummer(n):** +49 228 525365 +49 228 18414203

*Handy:* +49 178 8053941

**E-mail:** mkarouzos@mpifr-bonn.mpg.de; mkarouzos@gmail.com

**Nationalität:** griechisch

**Geburtsdatum:** 14. August 1984

**Geschlecht:** männlich

## Arbeitserfahrung:

**Datum:** Oktober 2007 - Oktober 2010

**Beruf / Arbeitstelle:** Doktorand der International Max Planck Research School (IMPRS) unter der Betreuung von Priv. Doz. Dr. Silke Britzen, Prof. Dr. Andreas Eckart, und Prof. Dr. Anton Zensus

**Anschrift des Arbeitgebers:** Max-Planck-Institut für Radioastronomie, Auf dem Huegel 69, D-53121, Bonn, Deutschland

## Ausbildung:

- Datum: Oktober 2007 - Oktober 2010  
Titel der Qualifizierung: P.h.D. in Astrophysics  
Institution: Universität zu Köln, Deutschland  
Doktorarbeit: A Multiwavelength Study of the Evolution and pc-scale Kinematics of Active Galactic Nuclei
- Datum: Oktober 2002 - September 2007  
Titel der Qualifizierung: Diplom in Physik  
Institution: National und Kapodistrian Universität Athen, Griechenland

Rheinische Friedrich-Wilhelms-Universität Bonn, Germany (ERASMUS Austauschstudent, März - Juli 2006)

Note: 8.1 (Maßskala: 1-10)

Diplomarbeit: Theoretical Study of Polarized Synchrotron Emission from relativistic jets

- Datum: September 1999 - Juli 2002  
Titel der Qualifizierung: Abitur  
Institution: 1st Gymnasium, Argiroupolis, Athen, Griechenland  
Abschlussnote: 18.5 (Maßskala: 1-20)

### **Forschungsstipendien / Unterstützungen / Auszeichnungen**

- Oktober 2007 - Oktober 2010: MPIfR, Bonn, Deutschland  
IMPRS (International Max Planck Research School) - Stipendium
- März 2006 - Juli 2006: Europäische Union, Bonn / Athen  
ERASMUS / SOCRATES (European Region Action Scheme for the Mobility of University Students) - Unterstützung
- Herbst 2000: Astronomy and Space Society of Bolos, Griechenland  
Hellenic Astronomisches Wettbewerb - Auszeichnung
- Frühling 1998: Europäische Union, Straßburg, Frankreich  
European Youth Parliament - Unterstützung

### **Referenten:**

- Priv. Doz. Dr. Silke Britzen  
Max-Planck-Institut für Radioastronomie  
sbritzen@mpifr-bonn.mpg.de
- Ass. Prof. Dr. Nektarios Vlahakis  
National and Kapodistrian University of Athens, Department of Physics  
vlahakis@phys.uoa.gr
- Prof. Dr. Anton Zensus  
Max-Planck-Institut für Radioastronomie  
azensus@mpifr-bonn.mpg.de
- Prof. Dr. Andreas Eckart  
I. Physikalisches Institut, Universität zu Köln  
eckart@phys1.uni-koeln.de

## Refereed Publications

- Roland, J.; Britzen, S.; Kudryavtseva, N. A.; Witzel, A.; **Karouzos, M.**: Modeling nuclei of radio galaxies from VLBI radio observations. Application to the BL Lac Object S5 1803+784, *Astronomy and Astrophysics*, 483, 125-135 (2008)
- Goyal, A.; Gopal-Krishna; Anupama, G. C.; Sahu, D. K.; Sagar, R.; Britzen, S.; **Karouzos, M.**; Aller, M. F.; Aller, H. D.: Unusual optical quiescence of the classical BL Lac object PKS 0735+178 on intranight time-scale, *Monthly Notices of the Royal Astronomical Society*, 399, 1622G (2009)
- Britzen, S.; Meyer, V.A.; Witzel, A.; Agudo, I.; Aller, M.F.; Aller, H.D.; **Karouzos, M.**; Eckart, A.; and Zensus, J.A.: Non-radial motion in the TeV blazar S5 0716+714. The pc-scale kinematics of a BL Lacertae Object, *Astronomy and Astrophysics*, 508, 1205B (2009)
- Britzen, S.; Kudryavtseva, N.; Witzel, A.; Campbell, R.M.; Ros, E.; **Karouzos, M.**; Mehta, A.; Aller, M.F.; Aller, H.D.; Beckert, T.; Zensus, J.A.: The kinematics in the pc-scale jet of S5 1803+784 revisited, *Astronomy and Astrophysics*, 511A, 57B (2010)
- **Karouzos, M.**; Britzen, S.; Eckart, A.; Witzel, A.; Zensus, A.: Tracing the merger-driven evolution of active galaxies in the CJF sample, *Astronomy and Astrophysics*, in press (2010)  
(<http://adsabs.harvard.edu/abs/2010arXiv1005.2177K>)
- Kudryavtseva, N.; Britzen, S.; Witzel, A., Ros, E.; **Karouzos, M.**; Aller, M.F.; Aller, H.D.; Teraesranta, H.; Eckart, A; and Zensus, J.A.: A possible helical trajectory in a strongly periodic quasar 0605-085, *Astronomy and Astrophysics*, in press (2010)  
(<http://adsabs.harvard.edu/abs/2010arXiv1007.0989K>)
- Liu, Y.; Jiang, D.R.; Zhi-Qiang S.; **Karouzos, M.**: A kinematic study of the compact jet in quasar B3 1633+382, *Astronomy and Astrophysics*, in press (2010)